Optical properties of multi-microgratings, their replication and applications

A Dissertation

Presented to

the faculty of the School of Engineering and Applied Science

University of Virginia

in partial fulfillment

of the requirements for the degree

Doctor of Philosophy

by

Christian A. Rothenbach

December

2016

APPROVAL SHEET

The dissertation

is submitted in partial fulfillment of the requirements

for the degree of

Doctor of Philosophy

AUTHOR

The dissertation has been read and approved by the examining committee:

Mool C. Gupta

Advisor

Joe C. Campbell

Lloyd R. Harriott

Petra Reinke

James M. Howe

Accepted for the School of Engineering and Applied Science:

Craig H. Benson, Dean, School of Engineering and Applied Science

December

2016

Optical properties of multi-microgratings, their replication and applications

---

A Defense

Presented to

the Faculty of the School of Engineering and Applied Science

University of Virginia

In Partial Fulfillment

of the requirements for the Degree

Doctor of Philosophy (Electrical and Computer Engineering)

by

Christian A. Rothenbach

November 2016

Approval Sheet

This Defense is submitted in partial fulfillment of the requirements for the degree of

Doctor of Philosophy (Electrical and Computer Engineering)

Christian A. Rothenbach

This Defense has been read and approved by the Examining Committee:

Mool C. Gupta, Adviser

Joe C. Campbell, Committee Member

Lloyd R. Harriott, Committee Chair

James M. Howe, Committee Member

Petra Reinke, Committee Member

Accepted for the School of Engineering and Applied Science:

Dean, School of Engineering and Applied Science

November 2016

Abstract

Multi-microgratings are defined as arrays of one-dimensional diffraction gratings inscribed inside similarly shaped cells and then arrayed in a two-dimensional periodic fashion. Due to the high number of spatial periodicities, these structures form intricate diffraction patterns. A meticulous understanding on how the diffraction patterns form and what their optical properties are has not previously been studied and it is necessary in order to be able to exploit these properties in a variety of applications. A theoretical model of these properties was formulated through analytical and graphical methods based on Fraunhofer diffraction theory, intensity distribution functions, Fourier Transforms and finite-difference time-domain (FDTD). The diffraction pattern was found to be formed by the individual contributions of the periodic elements in multi-microgratings and their interactions. To validate the theoretical model, multi-micrograting samples with 0.5 and 2 μm periods and 10 and 20 μm sides, arrays of hexagonal apertures and other structures were fabricated via electron beam lithographic method on silicon substrates. A polymer based replication method was demonstrated and PDMS replicas were fabricated from silicon masters. Optical properties of the fabricated structures and their replicas were characterized, their diffraction patterns were measured and explained. The optical diffraction efficiency of these samples was measured to be 32.1%. Finally, a brief study of possible applications of multi-microgratings was carried out in the context of a temperature measurement sensor. Diffracted beam spots were characterized for thermally induced changes in the diffraction angles and intensity. An optical interferometric regime was devised that allowed for a high dynamic range and high resolution temperature measurement that had a theoretical resolution of 300 times better (capable of resolving $<0.1°$C) than using one dimensional gratings. Alternative applications of multi-microgratings are proposed as well as future areas of research.

To my family, my friends, my colleagues and Stig.

Acknowledgements

While I may only be mentioning a few names, I wish to extend my gratitude to everyone who supported me in the pursuit of my doctoral degree in Electrical Engineering. The following individuals left a clear mark in my academic endeavors and they turned my graduate school experience into one I will always remember.

First and foremost, I owe much gratitude to my adviser and mentor, Prof. Mool C. Gupta. Much knowledge was passed down to me throughout my academic career with the countless suggestions and encouragement to continue my progress to finalizing the degree. I had the fortune of working with Prof. Gupta in many different environments, academically and in the lab. Most of all, from him I learned how to tackle many obstacles and become an independent researcher.

Second, to the members of my Ph.D. Committee who provided insightful questions and helped steer my research with their much diverse backgrounds: Prof. Joe Campbell, Prof. Lloyd Harriott, Prof. Jim Howe and Prof. Petra Reinke.

Third, to my countless colleagues I had at Prof. Gupta's research group at UVa, especially B.K. Nayak for providing positive and constructive criticism and endless interesting conversations even after leaving the university to furthen my professional career at Corning, Inc. The rest of my colleagues who provided much needed support in different ways, in no particular order are: Paul Caffrey, Tyson Baldridge, Longteng Wang, Keye Sun, Yang Shen, Vikram Iyengar, Will Bagienski, Jiguang Li, Vaishali Koppolu and Chen-Nan Sun.

Fourth, my colleagues and friends at UVa both in and out of the Electrical Engineering department, who helped diversify my interests and explore different ideas: Dincer Unluer, Kian Keyvanfar, Farhad Omar, Kosta Popovic, Alex Young, Lijun Li, Frank Tseng, Yousef Shakhsheer, Zhi Li, Kiril Simov, Aleks Ontman, Michael Cyberey, Kim Scott and many more.

Fifth, to the incredibly helpful people at Oak Ridge National Labs who made the fabrication of my devices a reality, especially Dr. Ivan Kravchenko for his continuous support.

Sixth, to the incredibly helpful research and professional staff in Electrical Engineering and Materials Science at UVa, especially Dan Fetko, Susan Malone, David Durocher, Joe Beatrice, Alex Lobo, Yadi Weaver, Richard White and many more.

Seventh, to my friends and colleagues at Corning, Inc. whom I met during my internship and my time as a Visiting Researcher and as an Optical Scientist: Anping Liu, David Pastel, Minghan Chen, Alex Streltsov, Joel Carberry, John Himmelreich, Robert Sharps, Johannes Moll, Matt Ross, Andres Covarrubias, Nikolai Streltsov, Sijan Khan, Max Sa Pereira, Margot Romer, Laura Cook and Peter Lezzi.

Last but not least, I couldn't have completed my work without the support of my family: Ligia, Rodolfo, Antonio and Michelle and my grandparents, uncles and aunts and countless cousins and most recently Alena and Max. Thank you for providing the opportunities, strength and encouragement to become a better researcher.

Contents

List of Figures

List of Tables

Chapter 1

Introduction and Motivation

The field of biomimicry examines naturally occurring designs and exploits those designs for beneficial purposes. Natural optical structures have evolved to solve problems, so replicating those designs is highly important [1]. Scientists have studied the wings of the *morpho* butterflies and their brilliant iridescent colors and learned that it is not due to pigments but because their scale structures are periodically arranged [2]. The actual wing structures in *morpho* butterfly scales are very complex and they generate an iridescent, bright blue color at large viewing angles due to their intricate design. Figure 1.1 shows the butterfly and an SEM image of the scale structures in the wings. These repeating Christmas-tree-like structures allow for both diffraction and optical interference to take place, which is what gives the butterflies their unique structural color [3]. The design utilizes the effects of diffraction and interference to generate the color, but it is made up of a complex architecture of 3D microribs and lamellar reflectors that are hard to reproduce.

Several studies have been reported which try to replicate the optical effects found in

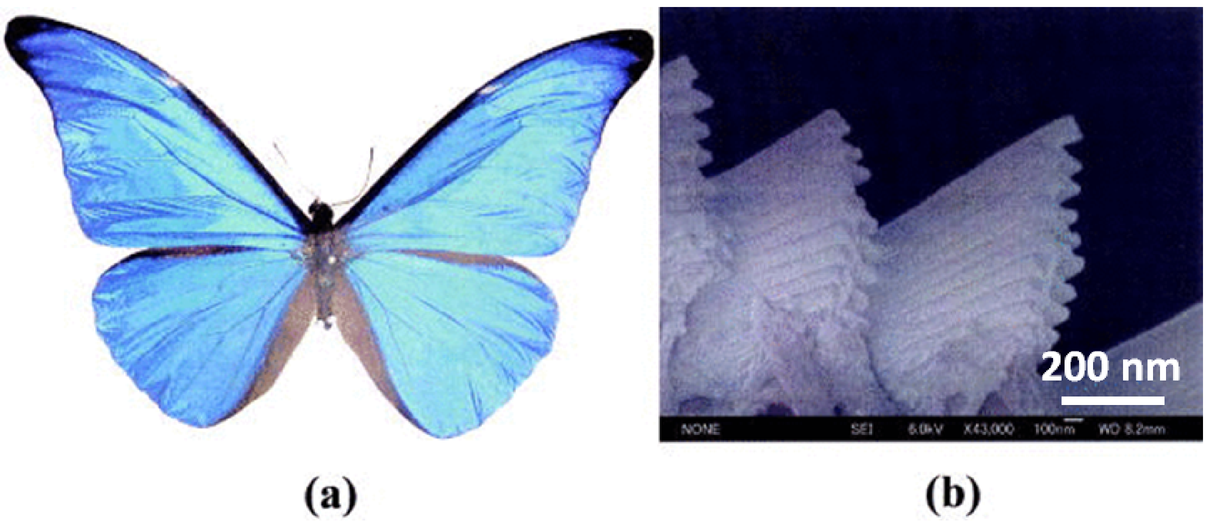

Figure 1.1: (a) Blue *morpho* butterfly and (b) SEM detail of wing structure [3].

morpho butterfly wing scales for sensing and other applications. The wing scales of the *morpho* butterflies can be used as optical gas sensors since they show a highly selective response to closely related vapors, such as water, methanol, ethanol and dichloroethylene. Actual wing scales were used in the experiments and were determined to be very selective in sensing vapors [4]. The same group recently used the wing scales to measure temperature variation, based on the spectral response of these wings to small temperature variations [5]. This type of design will eventually inspire new imaging sensors in the infrared region due to the wings response to heating with MWIR radiation. The spectral response to changes in vapor concentration (for methanol) and temperature are shown in Figure 1.2 [4, 5, 6]. Wing scales have been used as templates for replication. Films of ZnO and alumina were deposited on the wing scales and heated to remove the wings and crystallize the films, producing similar structures. Focused ion beam chemical vapor deposition was used to produce structures similar to those of the butterfly wings [1]. Much work has been done to reverse engineer the sorts of designs found in butterfly wings, some by creating artificial photonic materials that mimic the color generation properties in the wings [7]. Vertically oriented diffraction grating pillars, arrayed in large-scale 2D periodicity have been fabricated in silicon . The 2D pillars, both normally oriented and tilted, were etched with a complex Bosch process to achieve a scalloping effect, which mimic the actual wing structures.

However, these reported methods require complicated equipment and procedures to fabricate the structures. Some also sacrifice actual wing scales, which prohibits them from widespread applications. Also, it is hard to fabricate or reproduce large area devices with similar optical properties to the butterfly wings. Therefore, devices with similar optical properties that can be fabricated more easily are desired.

The work by Wong et al. [8] describes structures that despite being different in their architecture, had similar properties to the wing scales. The study focused on fabricating devices that appeared blue over a wide viewing angle, displaying the effects of diffraction

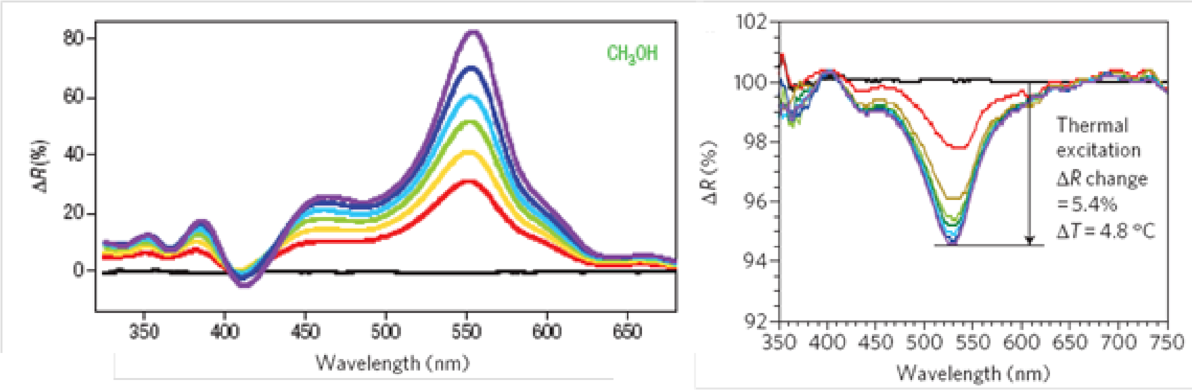

Figure 1.2: Spectral response of *morpho* wing scales to changing methanol concentration and changing temperature [4, 5, 6].

and interference with properties similar to the iridescent wings. They achieved this by fabricating a planar array of micrograting which consisted of hexagonally shaped individual microgratings in different orientations. When illuminated with light, these structures produced blue iridescent colors and complex diffraction and interference patterns. They achieved this by fabricating a planar array of gratings which consisted of hexagonally shaped individual multi-microgratings in different orientations, with a grating period of 440 nm and a depth of 125 nm. This type of structure was selected because replicating the intricate three-dimensional structures of the butterfly wings was very complex. The fabrication method chosen was electron-beam lithography (EBL), with PMMA 495 photoresist of about 150 nm. A dose value of 227 μC/cm^2 and 15 second development time were used. Figure 1.3 (a) shows the hexagonal micrograting design used and Figure 1.3(b) shows an AFM image of a region of the fabricated micrograting array [8].

1.1 The multi-micrograting design

The grating arrays used in the current study contain hexagonally shaped micrograting cells, which contain grating lines with six different orientations, and which are arranged to generate large area patterns. The six micrograting orientations are grouped in a unit cell, shown in Figure 1.4(a), which is repeated to generate large area arrays. The hexagon side

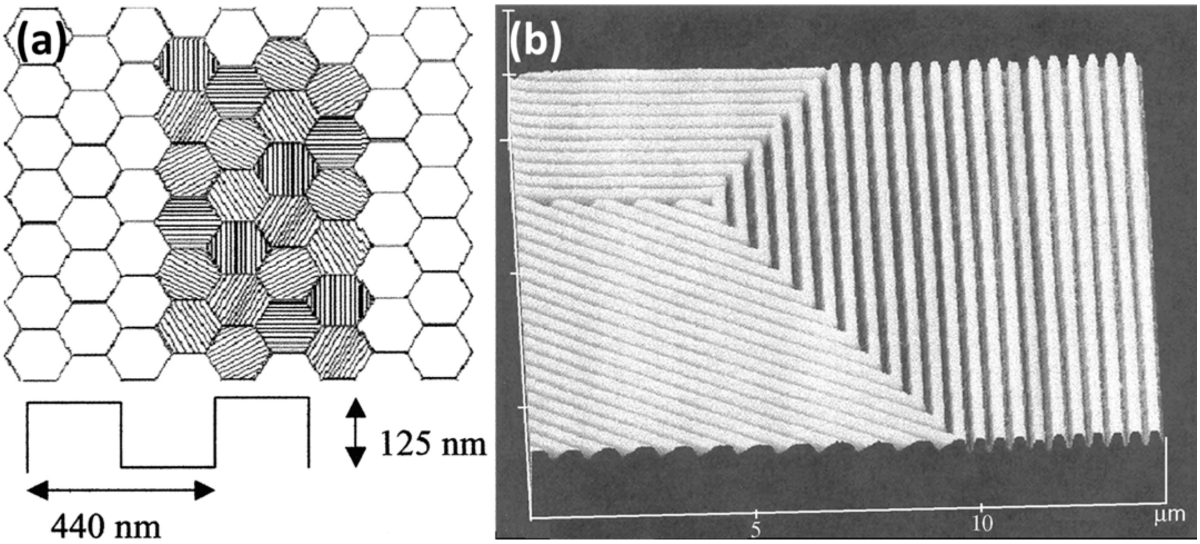

Figure 1.3: (a)Hexagonal micrograting design and (b) AFM image of the fabricated device in Wong et al [8].

is defined as s and micrograting period as d. Figure 1.4(b) shows an array of micrograting cells. The multi-micrograting array is composed of hexagonally shaped micrograting cells, which are arranged to form large area structures.

To fully understand the complex optical diffraction pattern generated by multi-microgratings, it is important to understand the contributions of the different periodicities found in the design. The diffraction pattern of a large area micrograting array is formed by the individual elements seen in Figure 1.5, all of which can produce different diffraction effects. They are listed below:

1. The hexagonal shape of the micrograting apertures.

2. The large area periodic structure produced by the multiple hexagonal apertures.

3. The 1D gratings with different orientations.

4. The lattice produced by the replicating unit cell containing the microgratings.

5. The interaction between elements 1-4.

The first two elements correspond to the hexagonal nature of the micrograting cells. The hexagonally shaped cell, Element 1, acts as an aperture and produce a typical diffraction pattern for a hexagonal aperture. Element 2, the large area structure produced by the hexagonal cell arrays can be considered a honeycomb lattice. Arrays of hexagonal apertures were also chosen for fabrication as they will allow the understanding of the diffraction pattern from the various elements in multi-microgratings.

The periodic micrograting lines oriented at various angles (Element 3) produce diffraction effects like those of a 1D grating. As such, those diffraction effects can be explained with

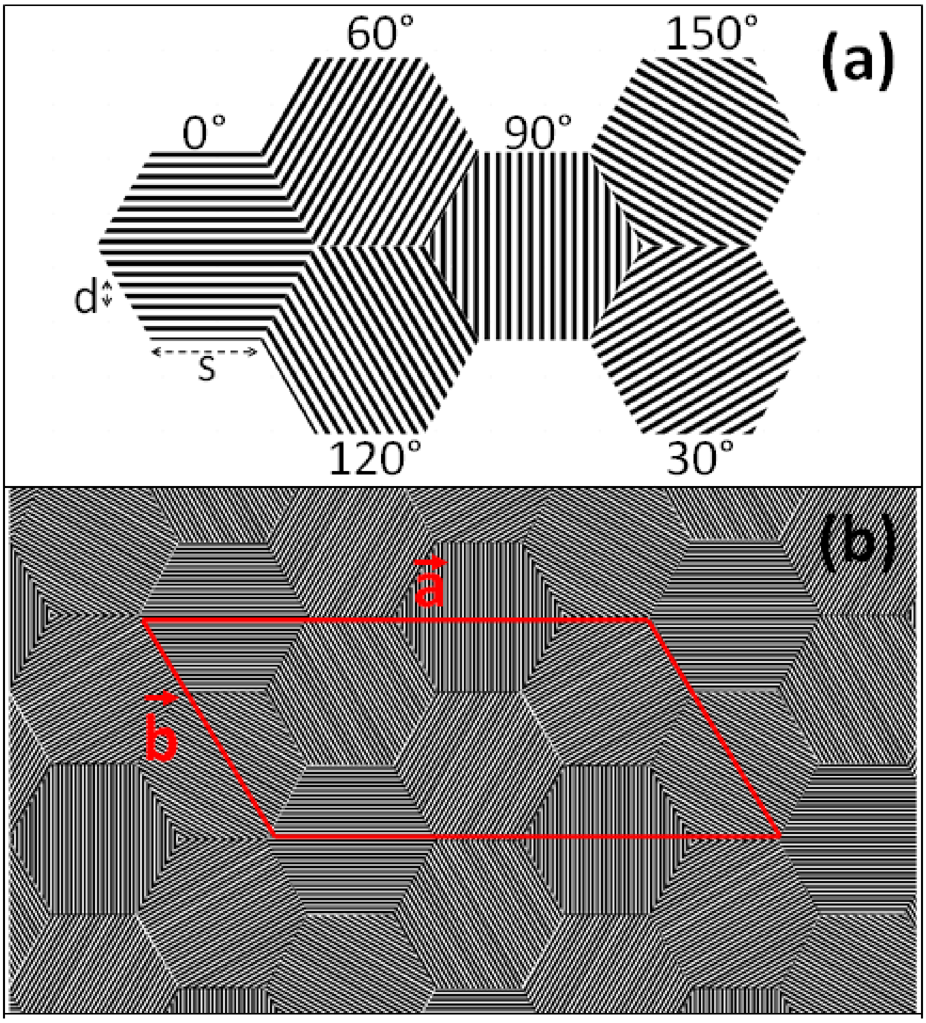

Figure 1.4: (a) Micrograting repeating cell with six different orientations. s is the hexagon side dimension and d is the grating period. (b) Array of multi-microgratings, with the red parallelogram defining the unit cell that was used to form the array, with sides a and b.

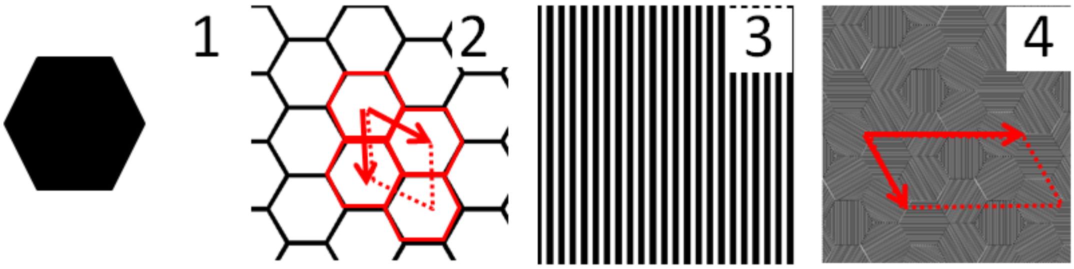

Figure 1.5: The individual elements that form the multi-micrograting arrays. (1) The hexagonal aperture. (2) Periodic hexagonal apertures. (3) 1-D grating with six different orientations. (4) Unit cell.

the grating Equation 1.1, explained in more detail in the following section.

In the grating equation, d is the period of the grating. The angles θ_i and θ_d are the angles of the incident and diffracted beams, respectively, with respect to a surface normal to the grating plane. The integer m represents the mode or order of diffraction and λ is the wavelength of the incident light. By use of this equation it is possible to understand some properties of diffraction from microgratings, for example, the angular position of the diffracted spots and the number of diffracted orders. However, the grating equation only takes the contributions for the 1D component of the micrograting arrays.

Six hexagonal microgratings with different 1D grating orientations are then arrayed into an oblique lattice (Element 4) to form large area patterns. Consequently, the generated lattice also produces diffraction effects. The unit cell, depicted as a red parallelogram in Figure 1.4(b), is used to produce the oblique lattice. The unit cell's sides a and b are related to the hexagon side dimension s. Geometrically, it can be shown that the unit cell dimension $b = 3 * s$ and $a = 6 * s$.

The complex optical properties of the multi-micrograting design explained in this section require a prior understanding of several topics that are covered in the next section.

1.2 Background information

The key characteristics of diffraction gratings are the angular behavior of the diffracted spots with respect to the angle of incident light, which can be described by the grating equation; the relative spot intensity and the efficiency of the diffracted orders. This section discusses prior art as it relates to multi-microgratings, and their status, which will help justify the need for further understanding of the optical properties of multi-microgratings.

1.2.1 The diffraction grating equation

The simplest explanation of a diffraction grating is a periodic set of apertures or slits located on a surface, such as the one described in Figure 1.6, where d is the grating period, a is the slit width and n is the number of slits. Assuming a planar wavefront is incident on the surface at an angle θ_i from the normal of the grating, Ray 1 and Ray 2 are in phase with each other. With θ_d being the angle of the diffracted beam, at wavefront position B the rays will constructively interfere when their difference in path lengths $d\sin(\theta_d) + d\sin(\theta_i)$ is an integer multiple of the wavelength [9]. From this analysis, the grating equation follows and is given below:

$$d(\sin\theta_i + \sin\theta_d) = m\lambda \tag{1.1}$$

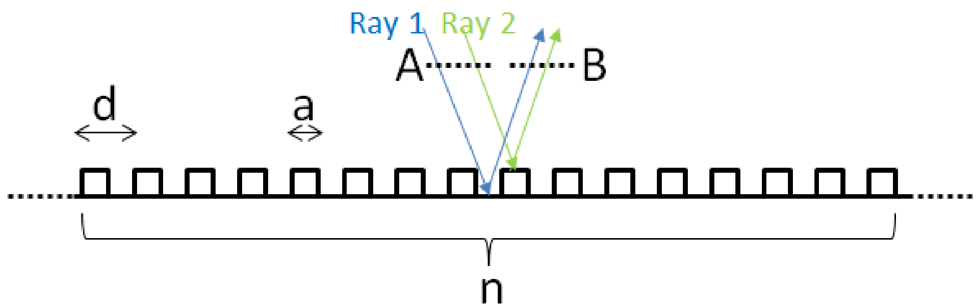

Figure 1.6: 1D representation of a diffraction grating.

The integer m represents the mode or order of diffraction. By analyzing this equation it is possible to understand some properties of diffraction gratings, for example, the angular dependence of the diffracted spots, the number of diffracted orders for a given set of grating parameters.

However, the grating equation falls short when trying to explain more complex systems such as multi-microgratings with different periodicities and orientations. It can only provide very discrete and limited information on the angular distribution of the diffracted spots and no information about their relative intensity. The intensity of the diffracted beams is said to be distributed to discrete orders , but as it will be shown in this study, for systems with increasing numbers of periodicities, those intensities are distributed in a much more complex way.

1.2.2 Formal description of diffraction

In order to have a full understanding of multi-microgratings, a more formal description of diffraction is required. The following sections discuss some key concepts and theorems which are going to be utilized to formulate a complete description of multi-microgratings.

Huygens-Fresnel Principle

Huygens established a method to describe the position of a wavefront in a future time. The assumption states that every point in a wavefront can be considered as new wavefront sources [10]. Diffraction then becomes determining the way that an electromagnetic wave propagates through space and time. In the case of having multiple wavefronts, then the superposition principle applies, which says that electric and magnetic fields at any given point is the vector sum of the individual wavefronts. Thus, depending on the spatial locations of two interfering wavefronts, they can either constructively or destructively interfere forming localized areas of high and low intensities.

The Fresnel-Kirchoff Diffraction Formula

The Fresnel-Kirchoff diffraction equation describes the wavefront as it is diffracted when it encounters an aperture.

In simplified, general form, the Fresnel-Kirchoff diffraction formula describes the intensity distribution of the diffraction pattern of an aperture $I_{Aperture}$ in screen space coordinates given by $\vec{r}$. It is given by Equation 1.2 where $A(\vec{r'})$ is the complex amplitude of the aperture at location $\vec{r'}$.

$$I_{Aperture} \propto \int_{Aperture} A(\vec{r'}) \cdot e^{-\frac{i2\pi}{\lambda}(\vec{r'}-\vec{r})} d\vec{r} \tag{1.2}$$

The Fresnel and Fraunhofer approximations

Using the Fresnel-Kirchoff diffraction formula, certain approximations are made for the near and far fields. For the far field, the distance from the observation screen to the aperture is significantly greater than the wavelength of light. Furthermore, that distance also has to be larger than the size of the aperture itself [11].

The Fresnel number, F, is a useful concept to summarize these approximations. It is given by Equation 1.3, where a is the size of the aperture and L is the distance between the observation screen and the aperture itself.

$$F = \frac{a^2}{L\lambda} \tag{1.3}$$

If the distance to the aperture is much larger than the aperture size, then this becomes Fraunhofer diffraction, and $F << 1$. Otherwise, if $F \sim 1$, then we have the case of Fresnel diffraction. If $F >> 1$, then we have diffraction in the near field.

For the purpose of observing diffraction patterns of microscale diffraction gratings in the visible range, the Fraunhofer approximation is usually sufficient to describe the diffraction of apertures. Known solutions for the diffraction of apertures given by different aperture shapes will be used in subsequent sections to develop an understanding of the formation of the diffraction pattern of multi-microgratings.

The array/convolution theorem

The array theorem, which stems from the convolution theorem that is derived for Fourier Transforms, states that the diffraction pattern of an array of similarly shaped apertures is given by convoluting the diffraction pattern of a single aperture of the same shape with the periodicity of the array, most often given as point sources or delta functions [10]. Extending this further, the diffraction pattern of an array of apertures is the convolution of the Fourier Transform of the aperture shape and the Fourier Transform of the periodic lattice.

In other words, a diffraction grating can be described as an array of similarly shaped apertures that repeat periodically. Thus, the diffraction pattern of a diffraction grating is going to be diffraction pattern of a single slit at each individual location given by the periodicity. Moreover, this theorem also applies to arrays of apertures of any shape. It follows then that the diffraction pattern of an array of hexagons, for example, is going to be the convolution of the diffraction pattern of a hexagonal aperture and that of their periodic array (i.e. honeycomb array).

Babinet's Principle

Babinet's principle states that the diffraction pattern of complimentary diffraction gratings is the same, except in the central area of the aperture [12]. Analogous to Equation 1.2 the intensity distribution of a complimentary aperture I_{Comp} with complex amplitude $1 - A(\vec{r'})$ is given by Equation 1.4.

$$I_{Comp} \propto \int_{Aperture} 1 - A(\vec{r'}) \cdot e^{-\frac{i2\pi}{\lambda}(\vec{r'}-\vec{r})} d\vec{r} \tag{1.4}$$

Thus, Babinet's principle can be described with Equation 1.5 for all values of $\vec{r'} \neq 0$.

$$I_{Aperture} = -I_{Comp} \tag{1.5}$$

For example the diffraction pattern of a rectangular aperture on an otherwise opaque screen is the same as the diffraction pattern of a an opaque rectangle on a transparent screen. This theorem becomes important when understanding the shape of the diffraction patterns of arbitrarily shaped microgratings and their complementary counterparts that can be produced with replication techniques.

1.2.3 Generalized Fraunhofer intensity distributions

With all the given theorems and background information of the theory behind Fraunhofer diffraction, it is now possible to start constructing expressions that better represent the diffraction patterns of gratings.

In the Fraunhoffer approximation, the angular intensity distribution of the diffraction patterns of several types of apertures, such as rectangular or circular apertures and diffraction gratings have been formally described by solving the Kirchoff diffraction integral [11, 13]. The solutions to the diffraction integral, also known as the Fraunhoffer intensity distributions, can be found by integration.

The normalized intensity distribution as a function of the angle θ of a 1D diffraction grating consisting of n slits, is presented in Equation 1.6 and is shown to be the convolution of two terms. The first term, also known as the diffraction factor, is the intensity distribution for a single aperture ($n = 1$) of width a and it acts as an envelope function. The second term, the interference factor, takes into account the contribution of different grating lines separated by the grating period d. Equation 1.6 is plotted in Figure 1.7(a), where the dotted line is the diffraction factor and the solid line is the interference factor for the following parameters: grating period $d = 2$ μm, grating slit width $a = 1$ μm, number of slits n =20 and wavelength $\lambda = 532$ nm.

$$\frac{I(\theta)}{n^2 I_0} = \underbrace{\left[\operatorname{sinc}(a\nu)\right]^2}_{\text{Diffraction factor}} \cdot \underbrace{\left[\frac{\sin(nd\nu)}{\sin(d\nu)}\right]^2}_{\text{Interference factor}} \tag{1.6a}$$

$$\text{where } \nu = \frac{\pi}{\lambda}\sin(\theta) \tag{1.6b}$$

A convolution of the two terms results in the diffraction pattern for a periodic diffraction grating, with the diffraction factor functioning as an envelope that scales the relative intensities. The result of convoluting the diffraction and interference factors can be seen as the solid line in Figure 1.7(b), with the dotted line representing the diffraction factor as reference and to show how it envelopes the convolution and drawn at a different intensity scale to be able to distinguish the features. Often, the diffraction factor is ignored when describing a diffraction pattern in order to be able to clearly distinguish weaker features that would otherwise be obscured by the diffraction factor (envelope function).

Interestingly, the solutions for the local maxima of Equation 1.6 can be found to be the angles described by the grating equation (Equation 1.1), which can be seen as the peaks in Figure 1.7(a) and (b) at $\theta = 0°$, $\pm 15.4°$, $\pm 32.1°$ and $\pm 52.9°$. Also, as mentioned earlier, for $n = 1$, Equation 1.6 reduces to the intensity distribution of a single aperture, which is shown as the dotted envelope in Figure 1.7(b). Moreover, as n increases, the peaks start becoming narrower and narrower and become delta functions at the limit of n=∞.

The Fraunhofer intensity distribution approach is more robust than just using the grating equation. It provides much more detailed information on how the intensity is distributed in a diffraction pattern, and it can be extended even further to explain much more complex systems other than just conventional 1D gratings.

1.2.4 Diffraction efficiency

The diffraction efficiency, η, is defined as the ratio of the diffracted and incident powers of a wave that is incident on a diffraction grating. In other words, the diffraction efficiency is the proportion of the intensity that is distributed to each of the diffracted orders, as it can be seen in Equation 1.7:

$$\eta = P_{diffracted}/P_{incident} \tag{1.7}$$

For a 1D grating, the intensity of the diffracted spots depends upon the substrate or surface material, the quality of the gratings but most of all from the diffraction efficiency

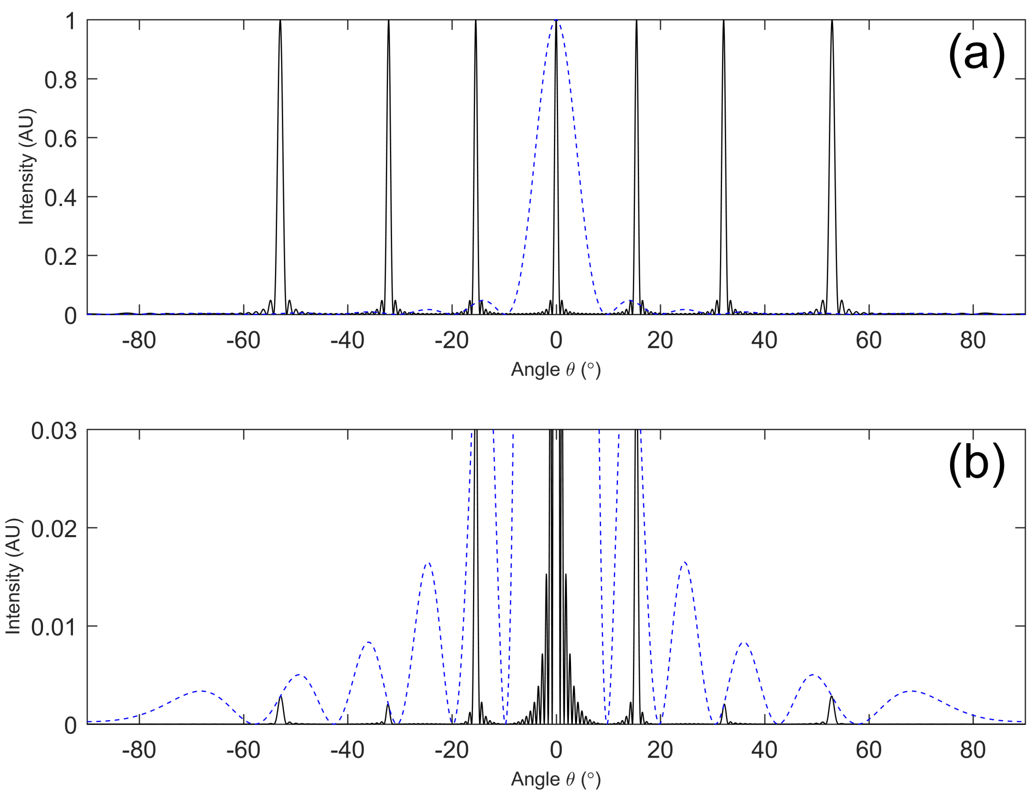

Figure 1.7: Plot of Equation 1.6 for grating parameters period d = 2 μm, grating slit width a = 1 μm, number of slits n =20 and wavelength λ = 532 nm. (a) Diffraction and interference factors (dotted and solid, respectively). (b) Convoluted diffraction (dotted line) and interference (solid line) factors of a magnified region of Figure (a) to visualize relative intensity of envelope diffraction factor.

of that particular order. The diffraction efficiency of each diffracted angle θ_d depends on the grating shape/profile, the period d, duty cycle, light polarization, the incident angle θ_i and the grating depth h [14, 15, 16, 17]. The power of each diffracted order can be measured and compared to the input power and thus the overall efficiency of a diffraction grating can be determined.

Equations 1.1 and 1.7 can provide an explanation for the angular behavior of a simple 1D grating and the relative intensity of the diffracted orders, but for more complex gratings such as 2D gratings or arrays of gratings, a different approach is required since the contributions of other periodicities and the interactions between different components of complex gratings are not treated by the grating equation or described by the defined diffraction efficiency. Scalar and vector diffraction theories are capable of solving simple 1D gratings; however there are two problems with using those theories to understand these micro-multigratings. When the minimum size in an optical element is smaller than a few optical wavelengths, scalar diffraction theory was reported to have significant errors in the calculations [18].

1.3 Prior Art: Multi-microgratings in literature

This section discusses other attempts at describing systems with a high number of periodicities using several methods. In literature, terms that describe systems with two or more periodicities vary, such as sequential and crossed gratings, dual gratings two- and three-dimensional gratings, microgratings, grating arrays, etc. A brief summary of literature providing explanations for these phenomena is provided below.

Two dimensional gratings and aperture arrays

Applications of two dimensional gratings in imaging have a variety of advantages. Gold coated silicon with two dimensional gratings have been used for interferometric, phase and darkfield X-ray imaging. The phase and absorption gratings that were fabricated consisted of high-aspect ratio pillars separated by periods of 2 and 4 μm, respectively. The addition of a second periodicity allows for better phase reconstruction [19]. Lithium niobate 2D arrays of hexagonal apertures with 35 μm period were used for digital holographic microscopy, in order to obtain multiple images of the same target, allowing for lens-less imaging. The diffracted beams happened to overlap as well, producing interference fringes in those regions [20].

Applications of such structures were also proposed for beam splitting, integrated optical circuits, grating spectroscopy, light trapping for solar cells. Femtosecond lasers were used to fabricate a double layer of defects on glass substrates with a 4 μm pitch, in a 2D grating arrangement. The first order diffraction efficiency for these structures was increased from 7.9 to 25.1% when switching from 1D to 2D gratings, since more of the light is coupled into the diffracted orders, rather than transmit through the zeroth order [21]. Self assembled 2D gratings were formed with a solution consisting of colloidally suspended 1 and 3 μm polystyrene spheres in water on a glass substrate. Upon water evaporation, the spheres self assembled into mostly rhomboidal arrangements (hexagonally close packed), forming the 2D gratings that had diffraction patterns similar to those observed for arrays of hexagonal apertures [22]. Two dimensional arrays of cylindrical pillars made of SiO2 were used in a silicon solar cell, allowing for more efficient light trapping as compared to random structures formed by chemical etching. Consequently, short circuit current was increased by 17% as compared to a planar back cell. Furthermore, a lower sensitivity to angle was demonstrated, increasing their light trapping abilities [23].

More intricate, tunable 2D gratings were reported. Thermally actuated square gratings with 100 μm periods on a glass substrate were fabricated and filled with nitrobenzene and placed on a two-side polished silicon substrate. The beam of a CO2 laser, incident on the silicon side, was used to heat the samples. As the temperature of nitrobenzene rises, so does it's refractive index. When the refractive index of the nitrobenzene reaches that of the glass, the grating virtually disappears and just transmits light. Thus, they were able to tune the first order diffraction efficiency of the gratings [24]. Liquid crystal, cholesteric, tunable two dimensional gratings formed by layer undulations, showed that their diffraction patterns were voltage dependent. The possibility of switching from 1D to 2D gratings was also demonstrated, giving their diffraction patterns great flexibility. The diffraction efficiencies of the 2D gratings were reported to be the product of the diffraction efficiencies of their individual 1D gratings [25, 26].

Multi-microgratings

In this context, the term multi-microgratings is defined as a collection of similarly shaped grating cells arrayed in a certain fashion. The closest design to this work's multi-mirogratings that was found in the literature [27] was an array of square shaped cells as a checkerboard grating, with 1D gratings in 2 orientations as it can be seen in Figure 1.8(a). The device was designed to work as a diffractive polarizer with low zeroth order reflectivity for a 1310 nm wavelength. This was achieved by having a subwavelength period for the micrograting (360 nm) and a larger period for the separation between similarly oriented square cells (5 μm). Zeroth order reflection and transmission was shown to be reduced significantly, as more of the light is coupled into the diffraction spots produced by the large period array of square cells. The diffraction pattern that shows this effect is shown in Figure 1.8(b) and (c) where the polarization state is along the pass and block axes, respectively. This is achieved because of the difference in efficiency between the TE and TM polarization efficiencies for the grating parameters, which were chosen so that TE efficiency is maximized while TM efficiency is minimized. Thus, by controling the input polarization the light either is transmitted into the block axis (zeroth order) or to the pass axis (the diffracted orders). Some insight as to how the diffraction patterns of multi-microgratings are formed is becoming apparent, and this will be discussed in the next chapter.

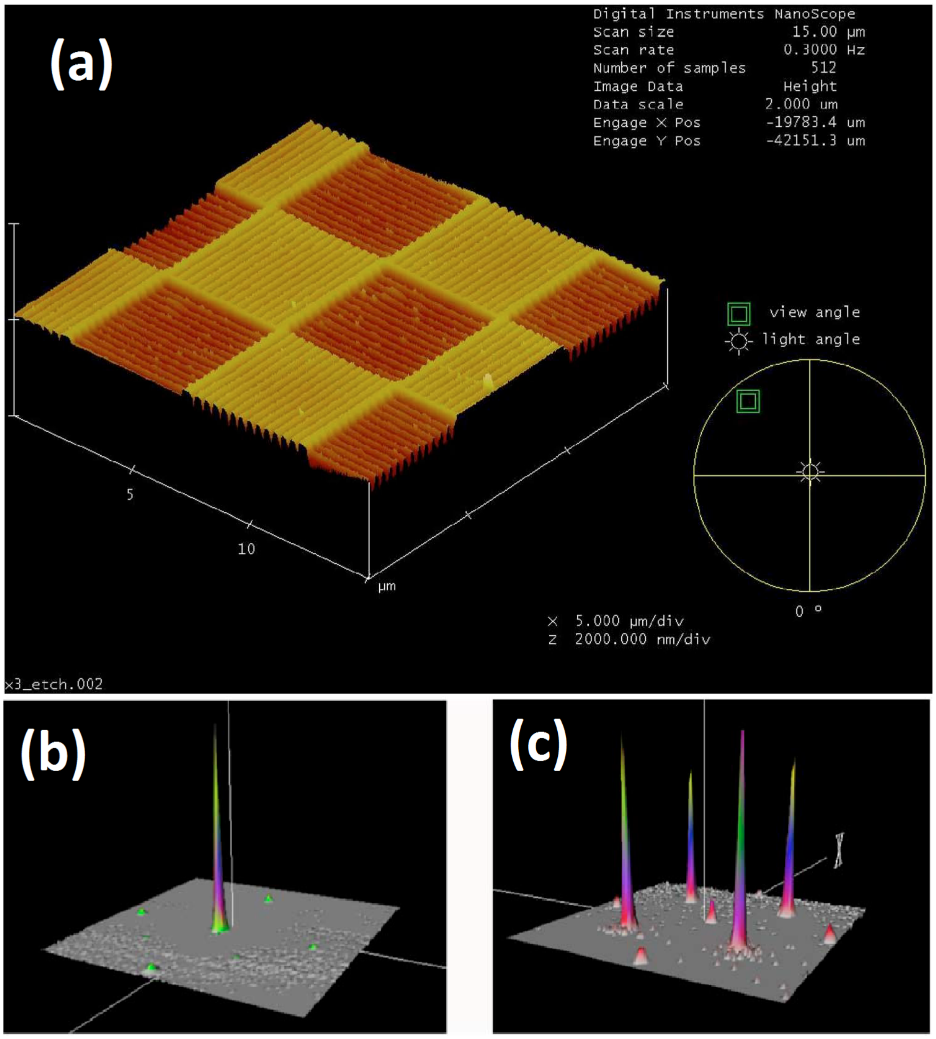

Figure 1.8: (a) Checkerboard multi-microgratings used as diffractive polarizer found in [27]. Figures (b) and (c) show a CCD captured diffraction pattern for polarizations along the pass axis block axes respectively [27].

An array of circular 1D gratings was also reported for sensing zonal wavefronts [28]. A schematic design of the device is presented in Figure 1.9(a), where light is incident from the left into the micrograting device G and focused by a lens L into the detector D. The micrograting device schematic is shown in Figure 1.9(b). The detector plane was divided into 4x4 zones. The position of the diffracted orders was then monitored for different orders and the wavefront aberration was calculated by angular discrimination. Figure 1.9(c) and (d) show first and third order diffracted beams from the detector. In the first order case, it is possible to see cross talk between different detector zones as beams move

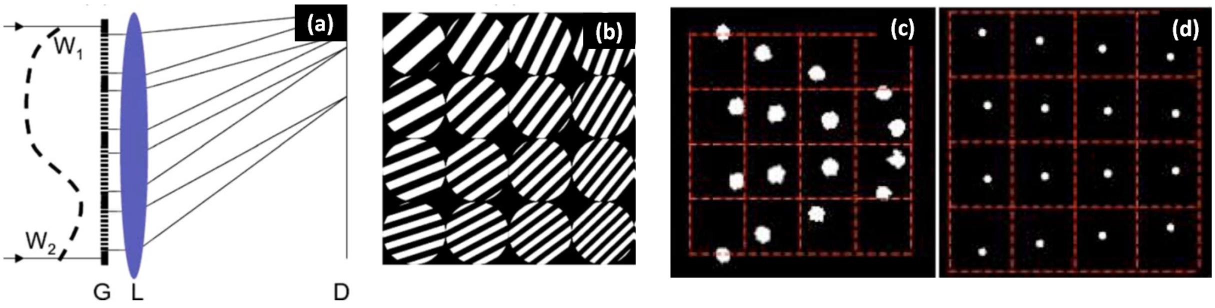

Figure 1.9: (a) Schematic design of zonal wavefront device in [28]. (b) Schematic of the 4x4 circular micrograting device. (c) First order diffracted beams at the detector plane. (d) Third order diffracted beams at the detector plane [28].

to adjacent detector zones. This effect is absent in the third order case.

Multi-microgratings for a multi-directional backlight for 3D displays were recently reported [29] and a 90° field of view was achieved. Circular cells with 1D microgratings with 12 μm periodicity were arrayed in a triangular grid to generate a multiview pixel for prototype LCD panels, as it is shown in Figure 1.10(a). Color discrimination was achieved by grating period design. Three different grating periods were selected for the illuminating LED red, green and blue independent sources, so to only allow first order diffraction at normal incidence. At wider angles, the effects of higher order diffracted beams were blocked off by a liquid crystal front plane. Figure 1.10(b) shows an SEM image of the circular microgratings. It is possible to see the different grating periods for the three independent sources, as well as their arrangement in a triangular lattice. Figure 1.10(c) shows the full wave simulation of the radiation pattern from a red circular micrograting cell when collimated LED light is incident on it. Details of the formation of this diffraction pattern will be revisited.

Talbot and Lau diffraction, Sequential and crossed gratings

Near field effects found in Talbot and Lau diffraction explain the existence of self-imaging planes at distances close to a diffractive optical element [30]. Such effects have been studied for applications in near field lithography, interferometry and they can be extended to

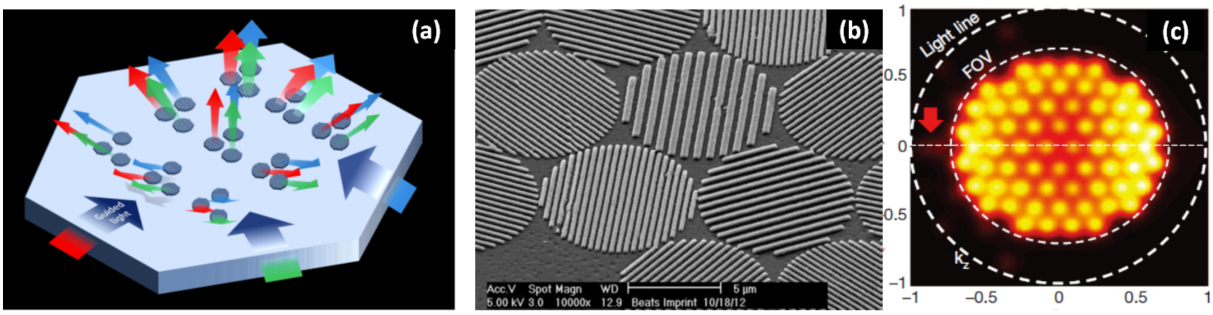

Figure 1.10: (a) Schematic design of multi-directional RGB backlight for 3D displays found in [29]. (b) SEM micrograph of the fabricated circular microgratings on a triangular lattice. (c) FDTD calculated radiation pattern for a red circular micrograting [29].

non-optical wavelengths such as those required to study atom-matter interactions [31, 32]. When an array of apertures, for example a diffraction grating, is illuminated, the near field diffraction pattern shows periodic fringes in the order of the grating spacing. These self images of the gratings occur at multiple distances of what is known as the Talbot length, which are multiples of the ratio of the square of the grating spacing and the wavelength. For optical wavelengths and periods of a few grating periods such as the ones used in this study, these distances occur at very short distances from the grating plane, in the order of a few microns to about a few Talbot lengths. At longer distances beyond that, the diffraction pattern observed transitions to a Fraunhofer diffraction pattern and the self images tend to disappear. Some interesting concepts that arise from studying systems in the Lau configuration that use 2D gratings or sequential, individual gratings separated by fractional Talbot lengths. [32, 33, 34] Far field patterns can be described by the superposition of the Fourier Transforms of the individual gratings at the diffracted order center locations. In the case of 2D gratings, such as 2D array of rectangular apertures, the self imaging distance are also a few microns from the grating itself. When looking at distances longer than a few multiples of the Talbot length, paraxial approximations tend to kick in, therefore, for the purpose of our study, the effects of Talbot and Lau diffraction can be ignored.

Several studies analyzed the effects and applications of the optical phenomena that occur when two or more gratings are used sequentially with relatively large separation distances. The diffraction pattern of rigid and curved gratings [35] is shown to be analogous to the diffraction pattern of a 2D grating. Other studies looked at applications of sequential gratings aligned along their optical axis to suppress diffraction orders or for total light absorption [36, 37].

1.4 Overview of study

As it was explained in this chapter, due to the lack of thorough knowledge on the topic of multi-microgratings, a better understanding of the diffraction pattern of multi-microgratings is necessary for several reasons. The diffraction pattern that is generated is more complex than the grating equation can describe. It is therefore necessary to fully understand what originates the diffraction pattern. The purpose of this study is to understand, through design and experimental fabrication, how the complex diffraction patterns of multi-microgratings are formed and what are their optical properties. Furthermore, a more thorough understanding of these structures would allow for the design and implementation of possible applications of multi-microgratings and similar types of structures that generate complex diffraction and interference patterns. Such applications include applications in vapor sensing [4], temperature sensing [6] and optical nanometrology [38, 39, 40].

In this study, the multi-micrograting structures are composed of an array of hexagonally-shaped grating cells, with six possible orientations. The structures have a complex diffraction pattern, with each grating orientation producing diffracted spots in the direction orthogonal to the lines of the grating. The behavior of the diffracted angle and the number of visible orders depend on the wavelength of the incident light and the incident angle. The overall behavior of these structures appears to be very similar to that of a 1D grating and can be explained using the grating equation. However, in the case of multi-microgratings, the magnitude and distribution of the intensity within each diffracted spot receive contributions from several microgratings.

The main objectives of this study are to:

- Provide understanding of the optical properties of multi-microgratings through modeling, fabrication and characterization.
- Demonstrate a low cost method for replication of multi-microgratings.
- Carry out a feasibility study of various potential applications of multi-microgratings.

In order to fully understand the origin of the complex features in the diffraction patterns of multi-microgratings, Fraunhofer diffraction as it is related to the modeling of multi-microgratings is discussed in Chapter 2. Analytic and graphical methods are used in order to predict the features of the diffraction patterns of multi-microgratings. All the features that form the diffraction patterns of multi-microgratings are successfully explained.

Fabrication of these structures is one of the foremost challenges and is discussed in Chapter 3. The understanding of the optical properties of multi-microgratings is consequently developed through fabrication of different kind of periodic structures, so that the effects of the different components of the micrograting structures can be studied separately.

Characterization of the optical properties of multi-micrograting structures is discussed in Chapter 4. The characterization methods are carefully explained and the results of the characterized samples are presented in detail.

A low-cost, high-fidelity replication method is described in Chapter 5, which allows for quick and easy replication of these and more kinds of structures. The replication method and characterized replicated devices are analyzed in this chapter.

Some applications of multi-microgratings are discussed in Chapter 6 and their working mechanisms explained in order to justify why it would be more beneficial for those applications to use multi-microgratings, rather than conventional one-dimensional gratings.

Concluding remarks and future studies are discussed in Chapter 7.

Additional contributions to different projects during graduate research is discussed in Appendix A, including research carried out at Corning, Inc. with picosecond lasers, the design of a high-resolution, low cost laser lithography system using a Blu-ray optical head assembly, a study of self-organized 2D periodic arrays of nanoprotrusions in silicon formed by nanosecond laser irradiation and nanosecond laser microtexturing of semiconductors and metals. Appendix B contains a list of publications.

Chapter 2

Modeling of the optical properties of multi-microgratings

This chapter outlines the modeling and simulation of the optical properties of multi-microgratings such as the nature of their diffraction pattern and their efficiency. As described in the previous chapter, the multi-micrograting design is composed of several periodic elements, all of which produce diffraction effects that interact with each other to produce the resultant diffraction pattern. Understanding the individual contributions of the different elements through modeling is therefore necessary, and such an understanding is developed in the subsequent sections through an expansion of the theories presented in Chapter 1. The following sections discuss three distinct methods for predicting the diffraction patterns of multi-microgratings as well as a method to predict their diffraction efficiency. The modeling results are then analyzed to establish the fabrication parameters described in Chapter 3.

The main effect that governs the optical properties of multi-microgratings is optical diffraction. Optical diffraction occurs when a beam of light that is incident on an aperture has a wavelength that is comparable to the aperture itself. The intensity distribution of the light after the aperture changes as a function of the size and radial distance. It is no longer just a shadow of the aperture itself, but due to interference effects the distribution has areas of high and low intensity. An array of apertures, separated by a distance d, is also known as a one dimensional diffraction grating. Light is distributed in different orders around a central maximum, and the angular behavior and intensity of the diffracted beams is well understood for such one dimensional gratings. The grating equation, seen in

Equation 1.1, describes a method to calculate the m^{th} order diffraction angle θ_d for a light beam of wavelength λ, incident at an angle of θ_i with respect to the grating normal.

The grating equation offers a very simplified approach to understanding the effects of diffraction from periodic gratings. It only provides the angular behavior of simple 1D grating structures for a given set of parameters, with no information regarding light intensity anywhere on the pattern other than the indicated diffracted angles. Furthermore, it falls short when trying to explain more complicated periodic systems, such as two dimensional arrays of apertures or multi-microgratings.

2.1 Methods

Because of the limiations imposed by the grating equation, a new explanation is needed to describe the intricate diffraction patterns produced by multi-mcirogratings. The current section outlines the methods employed to study the origins of the features found in the diffraction patterns of multi-microgratings. The first one is based on the Fraunhofer intensity distribution approach. The second one is an adapted finite-difference time-domain(FDTD) method which is able to numerically compute the electric and magnetic field distributions for periodic and non-periodic structures. The third method complements the first two, and it uses graphical Fourier Transforms to model the diffraction patterns and other optical properties in multi-microgratings.

2.1.1 Fraunhofer intensity distribution method

As described in Chapter 1, the diffraction pattern of 1D gratings can be obtained by the convolution of the diffraction patterns of a single aperture and by the periodicity introduced by having multiple grating lines. This analogy can be extended to explain systems with more periodicities, in which the intensity distribution functions for the different periodicities can be convoluted with each other to obtain the system's intensity distribution.

2.1.2 Finite-Difference Time-Domain (FDTD) method

The FDTD method is a numerical analysis method that was first proposed by Yee to approximate the time-dependent Maxwell equations for electromagnetic fields [41, 42]. A two-dimensional model is devised, with an electromagnetic wave propagating in the XY plane, with a transverse component H_z [43]. Maxwell's equations for the TM mode are given by Equation 2.1, where H_z is the transverse component of the magnetic field, E_x and E_y are the electric field components and J_{sx} and J_{sy} are the electric current density.

$$\frac{\partial H_z}{\partial t} = -\frac{1}{\mu}\left(\frac{\partial E_y}{\partial x} - \frac{\partial E_x}{\partial y}\right) - \frac{\sigma^*}{\mu} H_z \tag{2.1}$$

$$\frac{\partial E_x}{\partial t} = \frac{1}{\varepsilon}\frac{\partial H_z}{\partial y} - \frac{1}{\varepsilon} J_{sx} - \frac{\sigma}{\varepsilon} E_x \tag{2.2}$$

$$\frac{\partial E_x}{\partial t} = -\frac{1}{\varepsilon}\frac{\partial H_z}{\partial x} - \frac{1}{\varepsilon} J_{sy} - \frac{\sigma}{\varepsilon} E_y \tag{2.3}$$

The XY plane grid is divided into $i * j$ Yee cells, such as the one seen in Figure 2.1(a). The boundaries are defined to be absorbing with a perfectly matched layer (PML). For simplicity, a screen aperture or grating can be defined as a perfect electric conductor (PEC), by setting the electric field components to zero in those regions. A sinusoidal electromagnetic source of a particular wavelength is then defined at a particular location inside the model volume and is allowed to propagate in the XY plane in a particular direction, by iterating over time until steady state is achieved. The sinusoidal source interacts with the aperture that was defined. A simplified schematic of the model is illustrated in Figure 2.1(b).

At each instant in time, the electric field vectors are solved first, followed by the magnetic field vectors in the next time iteration. The result is a time evolution of the

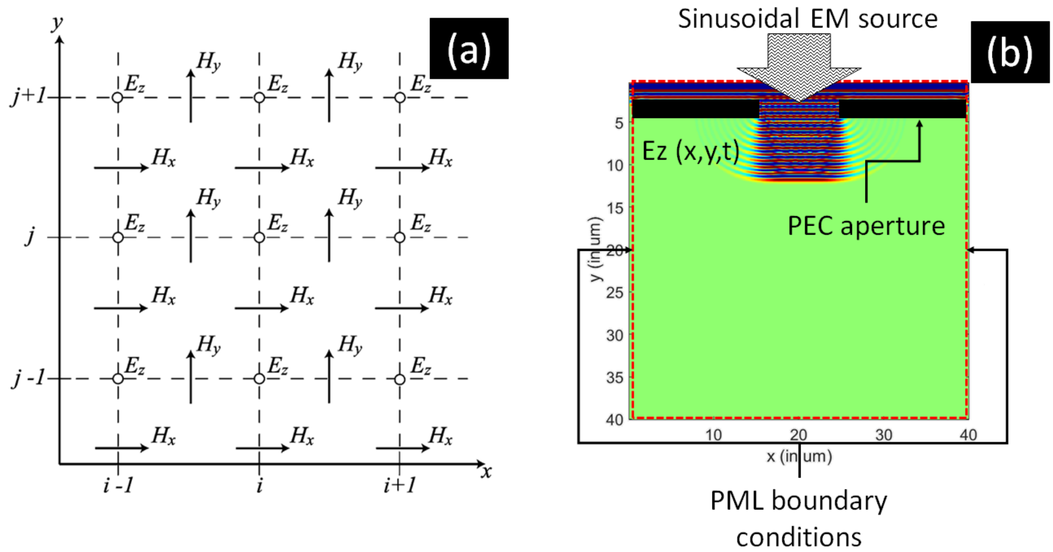

Figure 2.1: (a) Yee cell: representation of FDTD space discretization as seen in [42] (b) 2D FDTD model schematic with sinusoidal source incident on an PEC aperture, with PML boundary conditions and of electric field E_z as it evolves with time.

electric field. Since the electric field is proportional to the intensity of the wave, then it can be used to understand how the electromagnetic wave interacts with the diffraction gratings. For the simulation, because of the short distances, the solved electric fields are in the near field. A spatial Fourier transform of the field is then used to approximate the intensity in the far field.

A MATLAB implementation of this method was created and the results are presented later in this chapter. The FDTD method has advantages and disadvantages. It is computationally and memory intensive, so the size of the grid has to be carefully chosen so as to be able to run the simulations in time-efficient manner. Due to its complexity, only a 1D model of a grating can be solved for. However, the method can be used to observe other optical effects, such as interference between the different microgratings as it is shown later in this chapter. The model can be further specialized to incorporate different materials with distinct refractive indices, different incidence angles, etc. It must be noted that this model is a numerical approximation and must be carefully analyzed as such.

2.1.3 Graphical Fourier Transform method

As apertures become more complex, finding appropriate 2D mathematical descriptions of the apertures becomes cumbersome. However, as mentioned earlier, the solutions to the Kirchoff diffraction integrals can also be obtained by the Fourier Transform method. The diffraction integrals can be thought of as a coordinate transformation between the aperture plane (the functions that describe the apertures or gratings) and the image plane (where the diffraction pattern is projected). In other words, in the Fraunhoffer regime, the diffraction pattern can be described as the Fourier Transform of the aperture plane. The same analogy applies to a graphical representation of the aperture or grating plane, with the resulting graphical Fourier Transform being the simulated diffraction pattern of the aperture plane [10, 44, 45, 46]. Images of different aperture shapes can be manipulated with graphical Fourier Transform techniques to obtain their diffraction patterns. By carrying out a FFT (fast Fourier Transform) of the image of the aperture, the $x - y$ coordinates of the pixel locations in the image are transformed to $\theta_x - \theta_y$ space, obtaining the aperture's diffraction pattern. Spatial distance information from the original aperture image has to be used to calibrate the simulated diffraction pattern in angular space.

2.2 Simulations of diffraction patterns

Using a combination of the aforementioned methods, the following section discusses simulations of the diffraction patterns of different periodic systems that will help to explain how the diffraction pattern of multi-microgratings is formed.

Multi-microgratings, in 1D, can be understood as the combination of the 1D pattern of the microgratings and the 1D pattern of the arrayed apertures, which is basically a larger scale diffraction grating. A 1D multi-micrograting is depicted in Figure 2.2. In the general case, the 1D multi-micrograting intensity distribution function I_{mmg} can be interpreted as the convolution of the intensity distribution functions for the two individual periodic elements, and it can be seen in Equation 2.4.

$$I_{mmg} = I_{microgratings} \cdot I_{apertures} \tag{2.4}$$

The micrograting intensity, I_{mmg}, is simply given by Equation 1.6, derived earlier. For the larger scale aperture array intensity, $I_{apertures}$, a similar function is derived for a system with N apertures with width A, separated by a distance D. Combining all the terms, the normalized Fraunhoffer intensity distribution for 1D multi-microgratings can be seen in Equation 2.5.

$$\frac{I_{mmg}(\theta)}{n^2 N^2 I_0} = [\mathrm{sinc}\,(a\nu)]^2 \cdot \left[\frac{\sin(nd\nu)}{\sin(d\nu)}\right]^2 \cdot [\mathrm{sinc}\,(A\nu)]^2 \cdot \left[\frac{\sin(ND\nu)}{\sin(D\nu)}\right]^2 \tag{2.5}$$

Equation 2.5 is used in the following section for different parameters in order to predict the diffraction patterns of different periodic systems.

2.2.1 Diffraction pattern simulation for 1D gratings

To verify the validity of Equation 2.5, the simple case of 1D gratings is analyzed with it. By setting N and D to 1, Equation 2.5 reduces to the exact solution to the intensity distribution for a 1D grating. The simulation is run for parameters d = 2 μm, a = 1 μm and λ = 532 nm. To understand the effects of the numbers of slits n on a diffraction

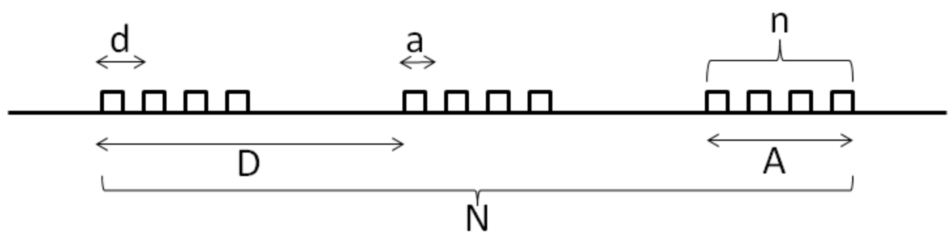

Figure 2.2: 1D array of micrograting cells, with n small apertures with grating period d and N large apertures separated by period D.

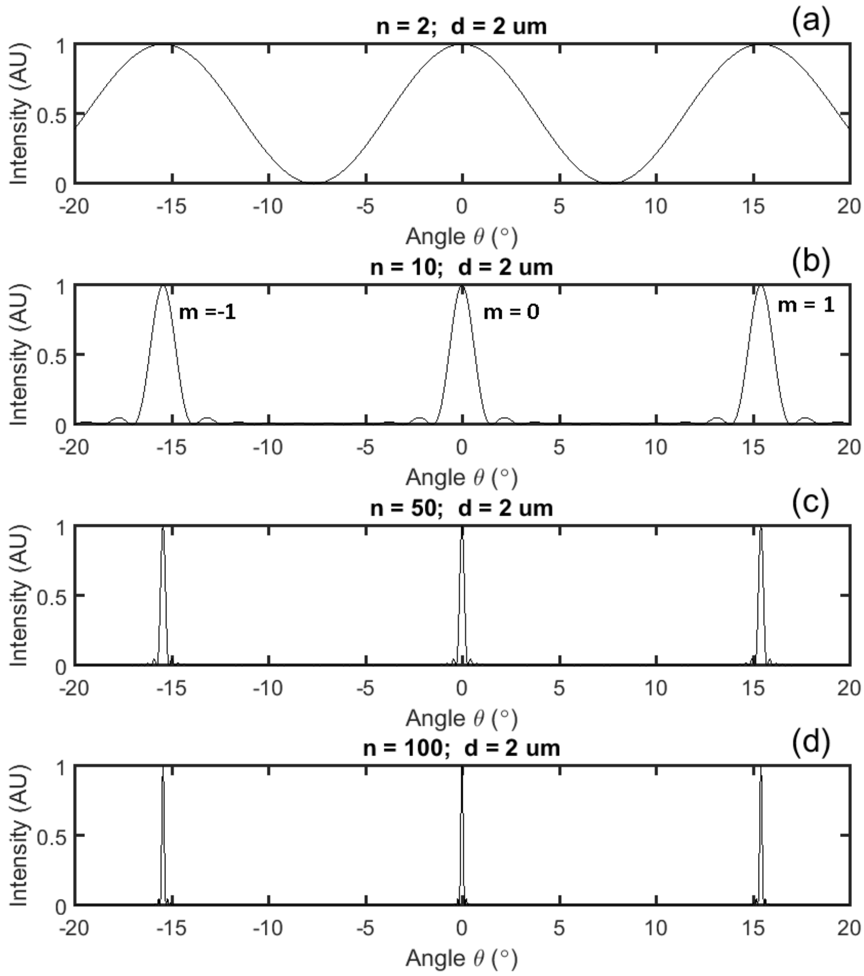

Figure 2.3: 1D grating pattern and effects of number of slits n plotted from Equation 2.5 for parameters $d = 2.0$ μm, $a = 1.0$ μm, $\lambda = 532$ nm; and (a) $n = 2$ slits, (b) $n = 10$ slits, (c) $n = 50$ slits and (d) $n = 100$ slits.

grating, a plot for the 1D grating pattern for these parameters can be seen in Figure 2.3(a) for $n = 2$ slits, (b) $n = 10$ slits, (c) $n = 50$ slits and (d) $n = 100$ slits. The diffraction factor was ignored in the interest of presentation and to normalize the intensity at different angular locations in the patterns.

Figure 2.3(b) has labels for the different diffracted orders. These observed maxima correspond to the locations given by the grating equation. As n increases, the diffracted spots get narrower and narrower, but their angular separation stays constant. In the limit where n approaches infinity, the diffracted spots become Dirac delta functions. Also, the higher n, the more energy gets distributed to the narrow discrete diffracted orders.

2.2.2 Diffraction pattern simulation for 1D multi-microgratings

Equation 2.5 is used to simulate the diffraction pattern of 1D multi-microgratings, for a system with grating lines and large apertures (the micrograting cell shape for example) at wavelength $\lambda = 532$ nm.

The normalized intensity distribution in 1D for the system with grating lines can be seen in Figure 2.4(a), with grating period $d = 2.0$ μm, width $a = 1.0$ μm and $n = 5$ slits. The normalized intensity distribution in 1D for the system with apertures only can be seen in Figure 2.4(b), with aperture period D =34.6 μm, $A = 1.0$ μm, $N = 5$ slits. Combining the two periodicities together, a multi-micrograting is formed and its diffraction pattern is shown in Figure 2.4(c).

As it can be seen, the diffraction patterns of the grating lines in Figure Figure 2.4(a) and aperture array in Figure 2.4(b) can be convoluted together to produce the diffraction pattern of multi-microgratings.

The effects of the number of apertures was (micrograting cells) was studied by varying the N parameter in Equation 2.5 and using the following parameters: $d = 2.0$ μm, $a =$ 1.0 μm, $n = 5$ slits, D =34.6 μm, $A = 1.0$ μm. N was varied and the results are plotted in Figure 2.5 for (a) $N = 2$ apertures, (b) $N = 5$ apertures, (c) $N = 10$ apertures and (d) $N = 20$ apertures.

As a new periodicity is introduced, in this case for the micrograting cell apertures, the diffracted spots are further divided into narrow spots around the maxima expected using the grating equation for 1D gratings. The angular separation of these spots correspond to the angular separation expected for the separation parameter D. As N increases, the spots get narrower and more defined, but their separation stays constant. It is also possible to see that the intensity is no longer distributed to just the discrete order spots given by the

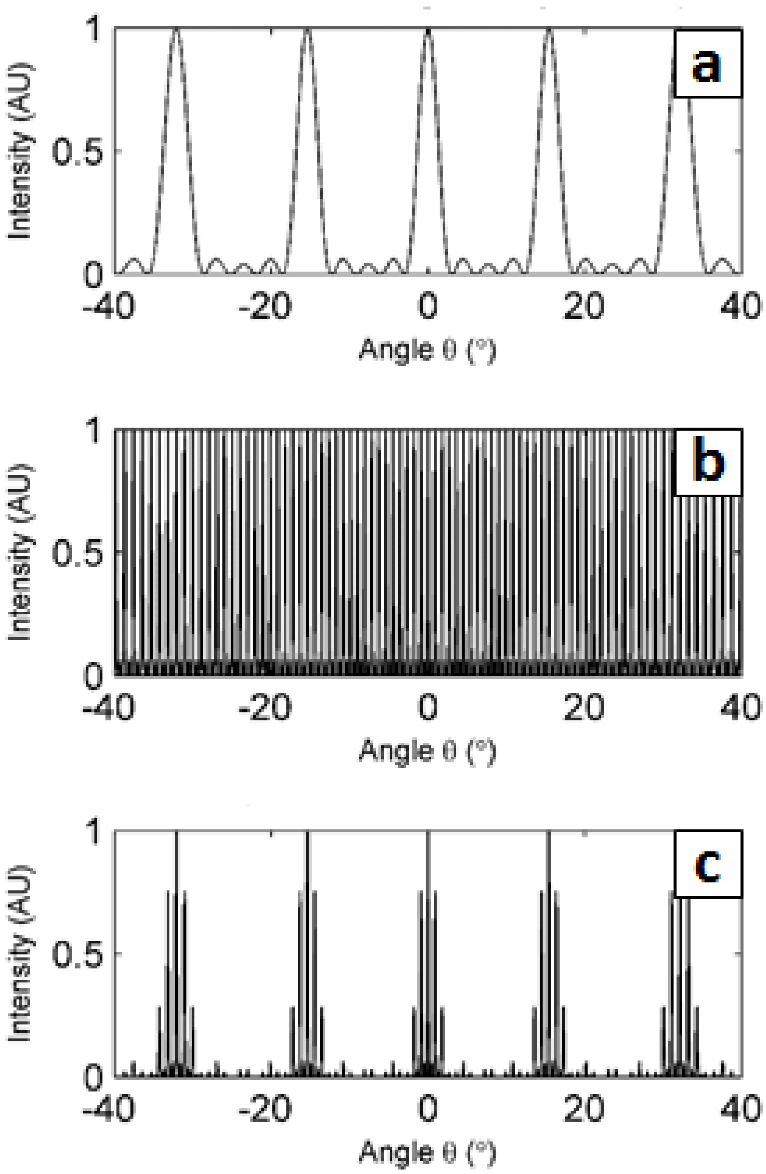

Figure 2.4: Fraunhoffer intensity distribution based simulated diffraction pattern for a 1D array of microgratings with $d = 2.0$ μm, $a = 1.0$ μm, $n = 5$ slits, D =34.6 μm, $A = 1.0$ μm, $N = 5$ slits, $\lambda = 532$ nm. (a) Normalized intensity distribution for grating lines only. (b) Normalized intensity distribution for apertures only. (c) Normalized intensity distribution of combined grating lines and apertures.

grating equation, but also to spots surrounding it corresponding to the newly introduced periodicity.

The same simulation was carried out to understand the effects of the micrograting aperture separation D and the results can be seen in Figure 2.6 for (a) $D = 10$ μm, (b) D

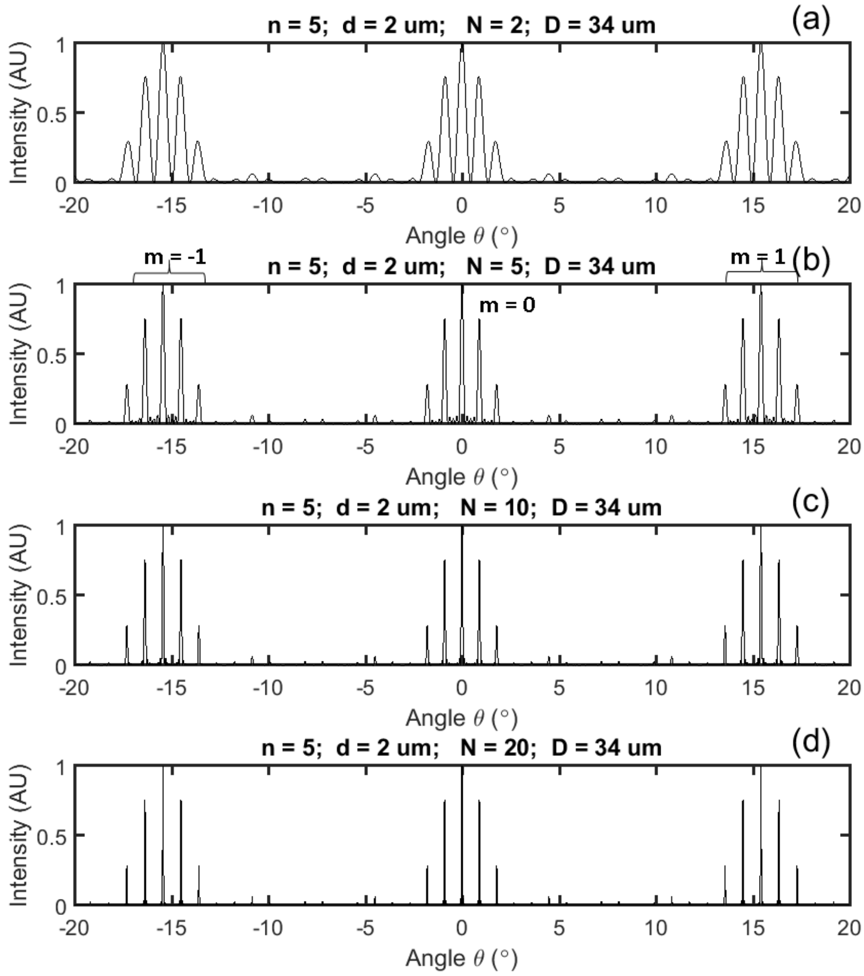

Figure 2.5: 1D multi-micrograting pattern and effects of number of N apertures plotted from Equation 2.5 for parameters d = 2.0 μm, a = 1.0 μm, n = 5 grating lines, D = 34 μm, λ = 532 nm; and (a) N = 2 apertures, (b) N = 5 apertures, (c) N = 10 apertures and (d) N = 20 apertures.

= 20 μm, (c) D = 50 μm and (d) D = 100 μm.

By varying D it is possible to see that as it increases, the separation between the spots gets smaller and the spots get narrower as well.

In the previous 1D models, the effects of the different periodicities present in multi-microgratings have been presented using the Fraunhofer intensity distribution approach, which provides the exact solution to the distribution of the diffracted intensity in the far field.

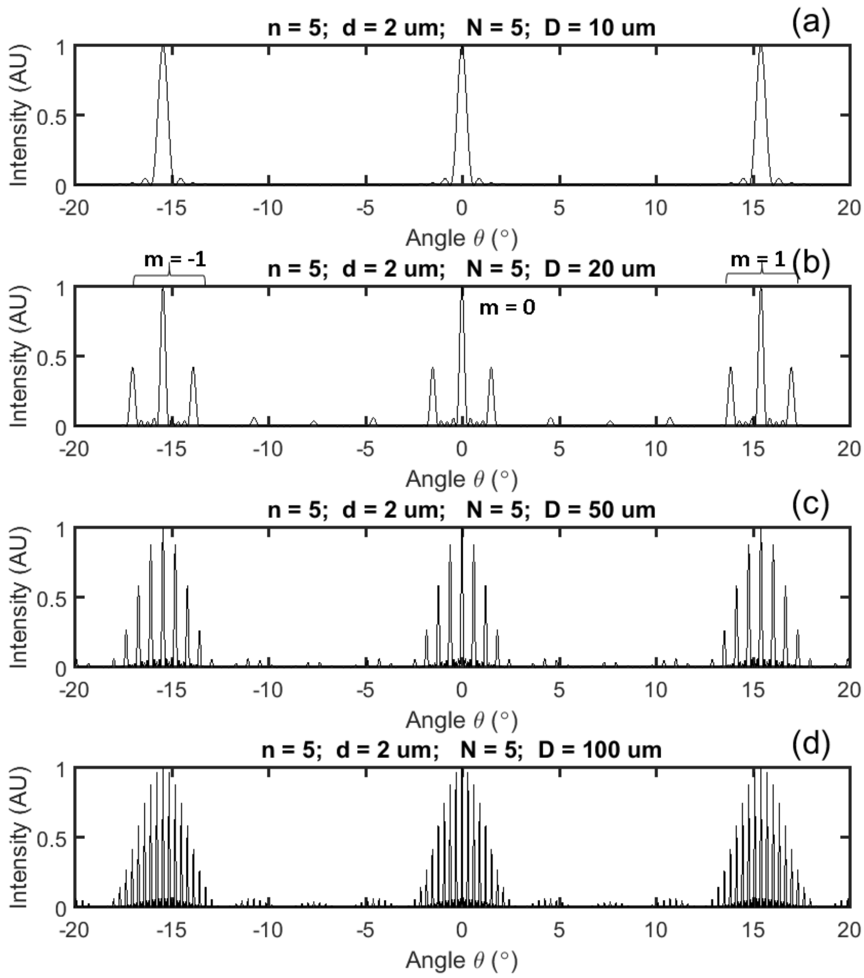

Figure 2.6: 1D multi-micrograting pattern and effects of aperture separation D plotted from Equation 2.5 for parameters $d = 2.0$ μm, $a = 1.0$ μm, $n = 5$ grating lines,$N = 5$ apertures, $\lambda = 532$ nm; and (a) $D = 10$ μm, (b) $D = 20$ μm, (c) $D = 50$ μm and (d) $D = 100$ μm.

2.2.3 Diffraction pattern simulation of 2D apertures

To quickly simulate the effects of the apertures on the diffraction patterns, the Graphical Fourier Transform method was used in this section. Images of different aperture shapes are Fourier transformed to obtain their far field diffraction pattern. Figure 2.7 shows the simulated diffraction patterns using the Graphical Fourier Transform method for (a) a triangular aperture, (b) a square aperture and (c) a hexagonal aperture. The aperture images used are shown in the insets of each case.

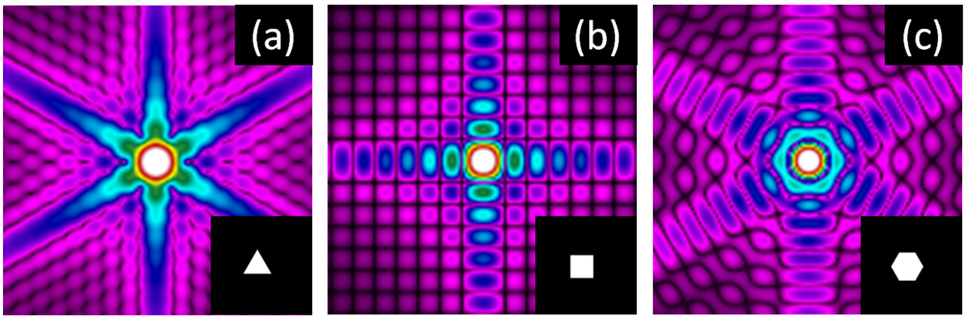

Figure 2.7: Graphical Fourier Transform method to simulate diffraction patterns of different aperture shapes: (a) triangular aperture, (b) square aperture and (c) hexagonal aperture.

A triangular aperture produces three lines. The orientation of these lines are perpendicular to the edges of the triangle (ie. the horizontal edge of the triangle produces the vertical line in the diffraction pattern). Most of the intensity is distributed to the center area, which is shaped like a hexagon, because that is the even distribution of the otherwise odd symmetry. In the case of a square, the center lobe is also shaped like a square, with vertical and horizontal lines extending radially outwards and which are separated into different lobes. These are shaped like sinc^2 functions, as those observed in the 1D patterns of 1D apertures. In the case of the hexagonal aperture, three lines are observed that are all perpendicular to the edges of the hexagon. While the center is shaped as a hexagon, the same as the triangular aperture, the lines that extend outward look different. They are closer in shape to the sinc^2 lines that are observed for the square aperture. This means that because the hexagon sides come in pairs, such as the sides in a 1D aperture, the diffraction along radial lines exhibit that sinc^2 behavior. In the case of the triangle, however, the diffraction lines produced do not have that type of behavior because the aperture sides do not come in pairs. Rather, they act as single edge diffraction patterns instead.

The effects of the aperture size are also studied using this method. A hexagon of different dimensions is plotted in each simulation shown in Figure 2.8 for hexagons of sides with size (a) 10 μm, (b) 30 μm and (c) 60 μm on a 1024 pixel starting grid (1 px = 0.1

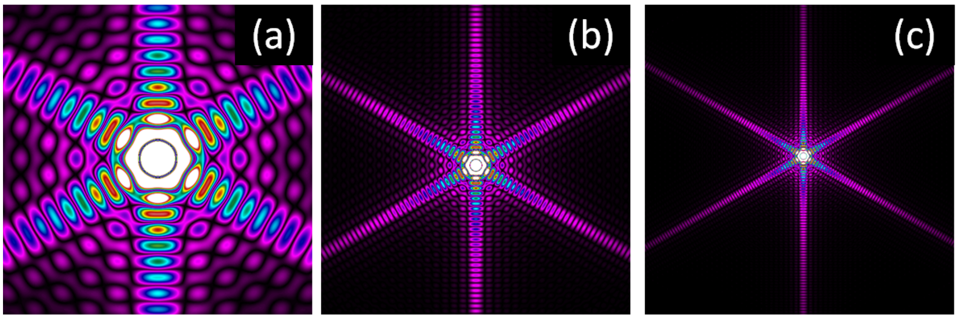

Figure 2.8: Graphical Fourier Transform method to simulate diffraction patterns of different hexagonal aperture shapes: (a) 10 μm sides,(b) 30 μm sides and (c) 60 μm sides.

μm). It is possible to see that the smaller the aperture is, the larger the center area is as well as the wider that the radial lines become. The separation in the lobes in the radial lines also decrease as the hexagon size increases.

The Graphical Fourier Transform method provides a quick way of simulating 2D diffraction patterns by just using images of the apertures. It is limited since it does not scale to wavelenght or real space separations directly, but pixel size can be scaled to calibrate the images. It is a very powerful method, however, since it can accurately estimate the diffraction patterns of apertures, gratings and other periodic structures.

2.2.4 Diffraction pattern simulation of 2D arrays of apertures

The Fraunhofer intensity method is further extended to simulate 2D diffraction patterns of different apertures. As long as the aperture shapes can be described mathematically, it is possible to simulate the diffraction patterns by convoluting the aperture functions in each independent direction. Mathematical descriptions for different types of apertures have been used to simulate their diffraction patterns [47, 48, 49].

Consider a single rectangular aperture in two independent dimensions x and y (with sides oriented at 0° and 90°). Its diffraction pattern is the the 2D intensity distribution given by θ_x and θ_y, and it is the convolution of the 1D intensities in in the x and y directions. This diffraction pattern has a rectangularly shaped central lobe (orthogonally

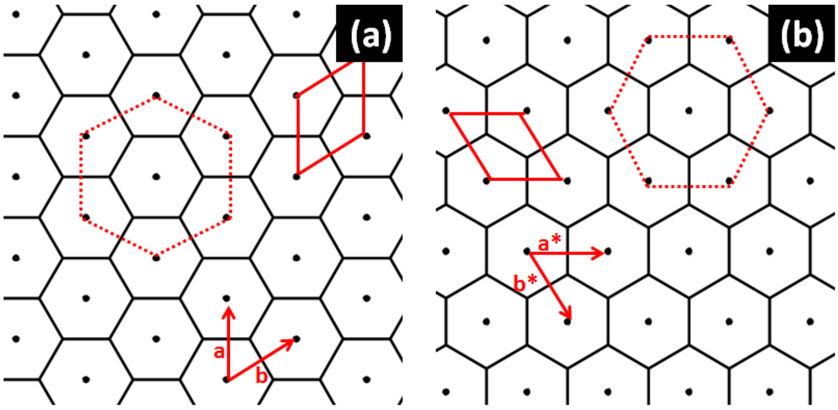

Figure 2.9: (a) Real space hexagonal p3 lattice and (b) its reciprocal lattice.

rotated to the original aperture), and modulated tails that extend past the central lobe sides. The 0° sides of the rectangular aperture cause a modulation in the diffraction pattern of the aperture in the vertical (90°) direction, and the 90° sides of the aperture cause a modulation in the horizontal (0°) direction. Additionally, due to the convolution of the two functions, weaker cross terms appear as well.

Instead, consider a single hexagonal aperture (with sides oriented at 0°, 60° and 120°). Each of the side pairs acts as an aperture in an orthogonal direction (30°, 90° and 150°). Therefore, the diffraction pattern of a hexagonal aperture has a hexagonally shaped center lobe, with tails extending from the center lobe sides in the 30°, 90° and 150° directions.

The honeycomb hexagonal array can be understood as a real space hexagonal or rhomboidal lattice. Figure 2.9(a) shows a typical honeycomb lattice as the one that was used to design the micrograting array design. The centers of the hexagons (black dots) are used as the lattice points, forming the rotated dashed hexagon. Four of the hexagon centers in the honeycomb lattice can be used to form a unit cell that is depicted as the red rhombus in Figure 2.9(a). Vectors $\vec{a}$ and $\vec{b}$ can be defined as the lattice vectors. Figure 2.9(b) shows the reciprocal space lattice of the hexagonal lattice described in Figure 2.9(a). As expected, the lattice vectors $\vec{a}^*$ and $\vec{b}^*$ are perpendicular to those in the real space lattice. The rhomboidal unit cell is used to form the array in reciprocal space. This results in a rotated honeycomb lattice.

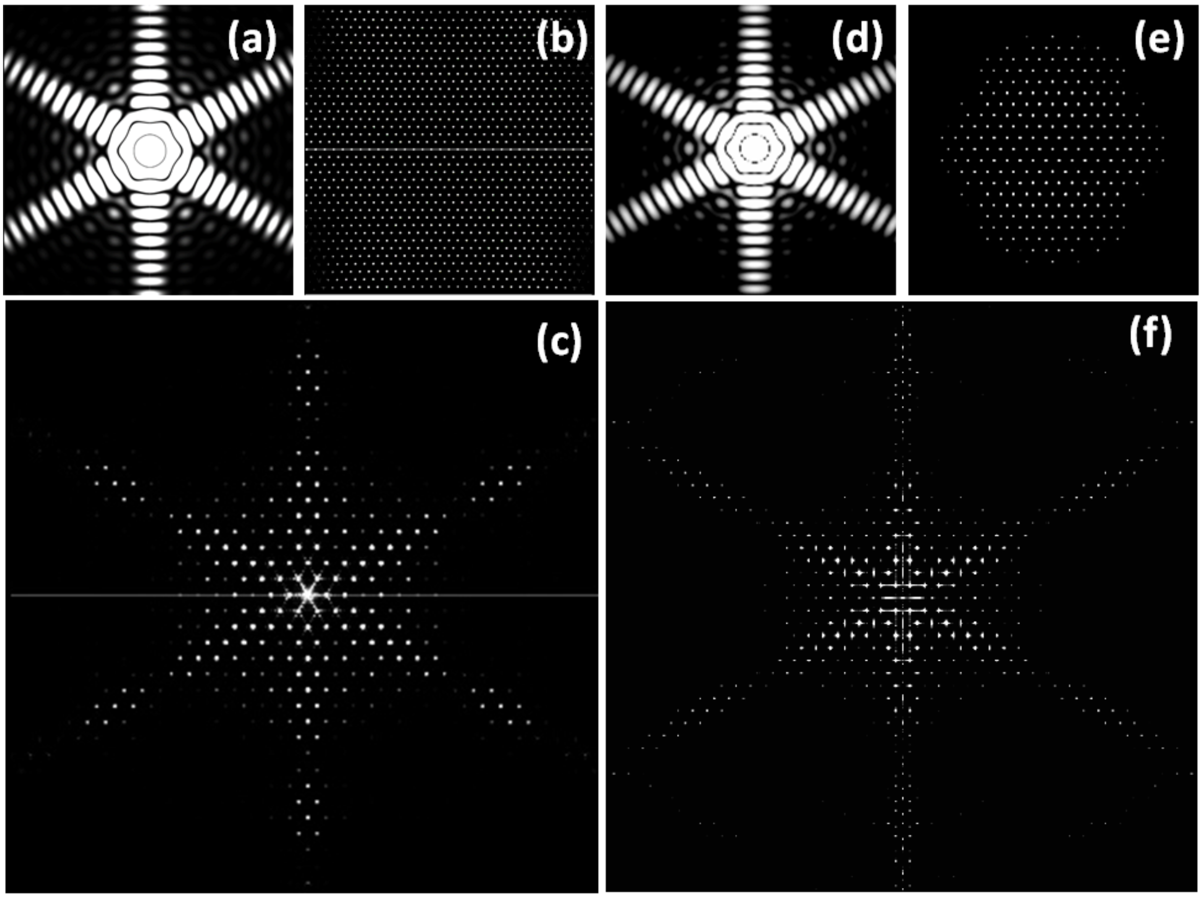

Figure 2.10: Formation of the 2D diffraction patterns from arrays of hexgonal apertures with hexagon side of 20 μm and separation of 34.6 μm. (a-c) show simulations using the Fraunhoffer intensity distribution method and (d-f) using the graphical Fourier Transformform method for a single hexagonal aperture, an array of honeycomb centers, and an array of hexagonal apertures respectively.

The formation of the 2D diffraction pattern of arrays of hexagonal apertures can be seen with the simulation results in Figure 2.10. The patterns were simulated using the Fraunhoffer intensity distribution method and the graphical Fourier Transform method. Hexagonally shaped apertures with 20 μm hexagon side lengths were arrayed in a honeycomb lattice that separated the hexagonal aperture centers by a distance of 34.6 μm.

The diffraction pattern from hexagonal aperture arrays receives two main contributions. The first contribution is from the diffraction effects from the hexagonal aperture itself. Using an adapted mathematical representation of a 2D hexagonal aperture [47, 48, 49], a simulation of a single hexagonal aperture using the intensity distribution approach is shown in Figure 2.10(a). Alternatively, Figure 2.10(d) shows a simulated diffraction pattern using the graphical Fourier Transform approach, which was obtained by plotting the graphical Fourier Transform of the image of a hexagonal aperture. As it can be seen in the figures, the two methods that were used to predict the diffraction patterns of single hexagonal apertures present nearly identical results. A hexagonally shaped center lobe is formed with long, modulated tails emanating from the pairs of hexagon sides. These tails grow dimmer in intensity the further away from the center of the hexagon. They also have areas of high and low intensity. The diffraction effects from the three pairs of sides interact with each other, producing cross terms which exist in between the long diffraction tails.

The second contribution to the diffraction pattern of arrays of hexagonal apertures comes from the honeycomb array. The hexagon centers are located 34.6 μm from each other. Thus, taking just the coordinates of the centers of the each of the hexagons in the array, a rhomboidal unit cell is formed. In turn, when diffracted, they produce an array of equidistant spots in orthogonal directions. Figure 2.10(b) was created by plotting the intensity distribution of a 2D mathematical representation of a honeycomb array. Such array can be formed by convoluting Equation 1.6 in three different angular directions, and letting n become large (n >20), resulting in delta-like points which locate the hexagon centers of the honeycomb array. In the interest of presentation, the simulation in Figure 2.10(b) used $n = 5$. Analogously, Figure 2.10(e) shows the graphical Fourier Transform of a honeycomb array. As it can be seen in both simulated patterns, the rhomboidal unit cell that forms the honeycomb lattice produces a rotated honeycomb lattice in the diffraction pattern.

By combining the two contributing effects of hexagonal apertures and honeycomb array, the diffraction pattern of arrays of hexagonal apertures was simulated and it can be seen in Figures 2.10(c) and (f), respectively via the intensity distribution and graphical Fourier Transform methods. The two simulations appear to be very similar. The diffraction pattern consists of a honeycomb array of spots shaped by the envelope of the hexagonal aperture patterns. Some graphical artifacts are observable in both simulated patterns, but their general shape is very similar.

2.2.5 Diffraction pattern simulation of 2D multi-microgratings

To understand how the diffraction pattern from multi-microgratings is formed, it is necessary to understand how each of the periodicities in the array contributes to the whole diffraction pattern. A graphical Fourier Transform approach was used. Figure 1.4(a) shows the repeating cell used to create the multi-micrograting arrays such as the one in Figure 1.4(b), multi-micrograting parameters are set as follows: hexagon side dimension $s = 20$ μm, micrograting period $d = 2.0$ μm, vector $\vec{a} = 120$ μm at 0° and vector $\vec{b} = 60$ μm at 120°, wavelength $\lambda = 532$ nm.

First, it is necessary to understand the contribution of the micrograting cells. The difraction pattern of each micrograting cell receives contributions from the two elements that form it: the 1D grating element of each micrograting and the hexagonal shape of that micrograting. Figure 2.11 shows the simulated patterns of the apertures shown as the insets via the graphical Fourier Transform approach. Figures 2.11(a) and (b) show the simulated pattern for a micrograting cell with a grating oriented at 90° and 30°, respectively. As expected, the micrograting orientation produces positive and negative

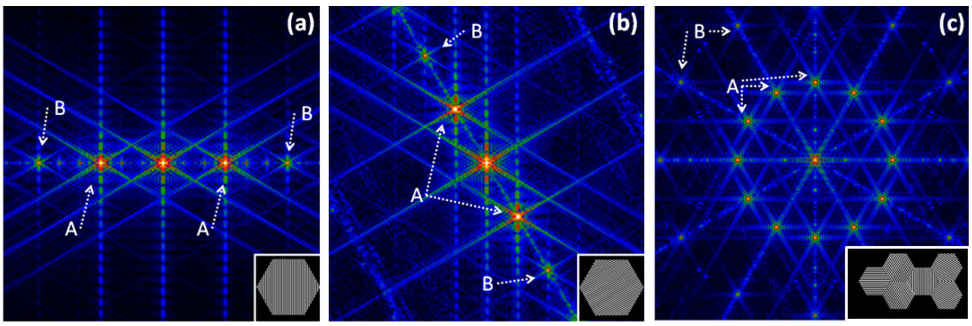

Figure 2.11: Graphical Fourier Transform simulations of micrograting diffraction patterns for (a)single micrograting oriented at 90°,(b)single micrograting oriented at 30° and (c)collection of six microgratings. Insets shown are the images used to simulate diffraction patterns. Labels A and B indicate first and second orders respectively.

orders, arranged radially outward along direction perpendicular to each orientation (0° and 120°). Orders $m = 1$ and $m = 2$, labeled as A and B in Figures 2.11(a) and (b), are found to correspond to the angular position that is described by the grating equation. A and B both have the same shape as the diffraction pattern of a single hexagonal aperture (described earlier in Figure 2.10). Thus, it is shown that the diffraction pattern of each micrograting cell is formed by the convolution of the diffraction patterns of a 1D grating and of a hexagonal aperture.

Figure 2.11(c) shows the simulated diffraction pattern of the six combined micrograting cells. This diffraction pattern has a central spot, surrounded by a ring of 12 first order spots, labeled A. For simplicity, it is possible to refer to the 12 spots as the hours in a clock. Radially outward from each of the 12 spots in the ring are 12 more spots, of lower intensity, forming a second ring, labeled B. Each element in the rings are equidistant to the center spot. The two rings of spots, A and B, correspond to the first and second orders, respectively, for each of the micrograting orientations. Given that there are six possible angular orientations of the grating periods within the micrograting cells, then each angular orientation produces diffracted spots in the corresponding perpendicular direction. For example, for micrograting orientations of 0°, spots are produced in a vertical (90°) direction, or the spots in the 12 and 6 o'clock positions (one being the positive first order, and one the negative). For a grating orientation of 30°, the spots lie in a line that is oriented at 120°, or the 5 and 11 o'clock spots. A similar analysis can be carried out for the other micrograting orientations, thus resulting in the twelve visible spots for the first order (negative and positive) spots and 12 more for the second order if the grating equation is satisfied for that particular order.

Now, in order to generate large area multi-microgratings, the unit cell described by Figure 1.4(b) is used, adding the periodicity of the array itself. Figure 2.12(a) shows the simulated diffraction pattern via graphical Fourier Transform of a large area multi-microgratings. Figure 2.12(b) shows the magnification of one of the 12 spots in Figure

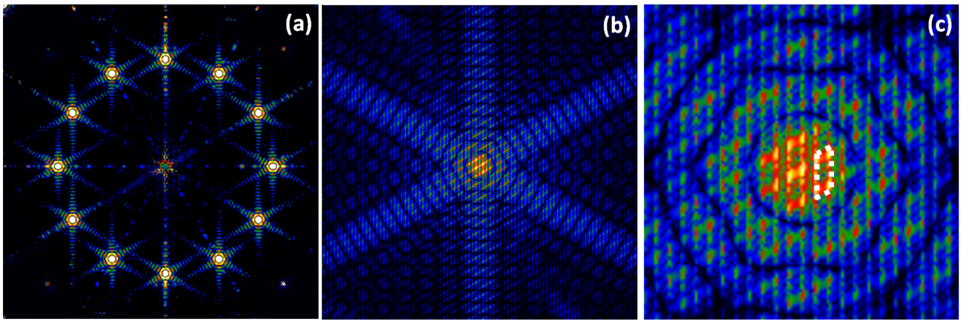

Figure 2.12: Graphical Fourier Transform simulations of micrograting diffraction patterns for (a)single micrograting oriented at 90°,(b)single micrograting oriented at 30° and (c)collection of six microgratings. Insets shown are the images used to simulate diffraction patterns.

2.12(a). Figure 2.12(c) shows detail of one of those spots in 2.12(a). As it can be seen, the diffraction pattern of a large area multi-micrograting design becomes the convolution of the diffraction pattern of a six micrograting array, such as that in Figure 2.11(c), and that of a set of multiple apertures separated by vectors $\vec{a}$ and $\vec{b}$.

The diffraction pattern from the array formed by vectors $\vec{a}$ and $\vec{b}$ is manifested by the white parallelogram inscribed in Figure 2.12(c), which has vectors orthogonal to $\vec{a}$ and $\vec{b}$ at 90 ° and 30° respectively.

2.3 FDTD simulations of multi-microgratings

As described earlier, more complex FDTD simulations were carried out to study the time-dependence of the electric field along the z direction, E_z, for a monochromatic sinusoidal electromagnetic wave incident on diffracting apertures defined by PECs. The electric field E_z is proportional to the intensity of the diffracted wave and is allowed to propagate with time until steady state was achieved.

First, 1D gratings were modeled with this method. A 1D grating with 2.0 μm grating period, 1.0 μm grating aperture and 10 slits is defined with a grid size of 50 nm, to interact with the sinusoidal EM wave with 532 nm wavelength in vacuum with electric permittivity ε_0 of $0.0278 * 10^{-9} F/m$ and magnetic permeability μ_0 of $12.56 * 10^{-7} H/m$. The steady

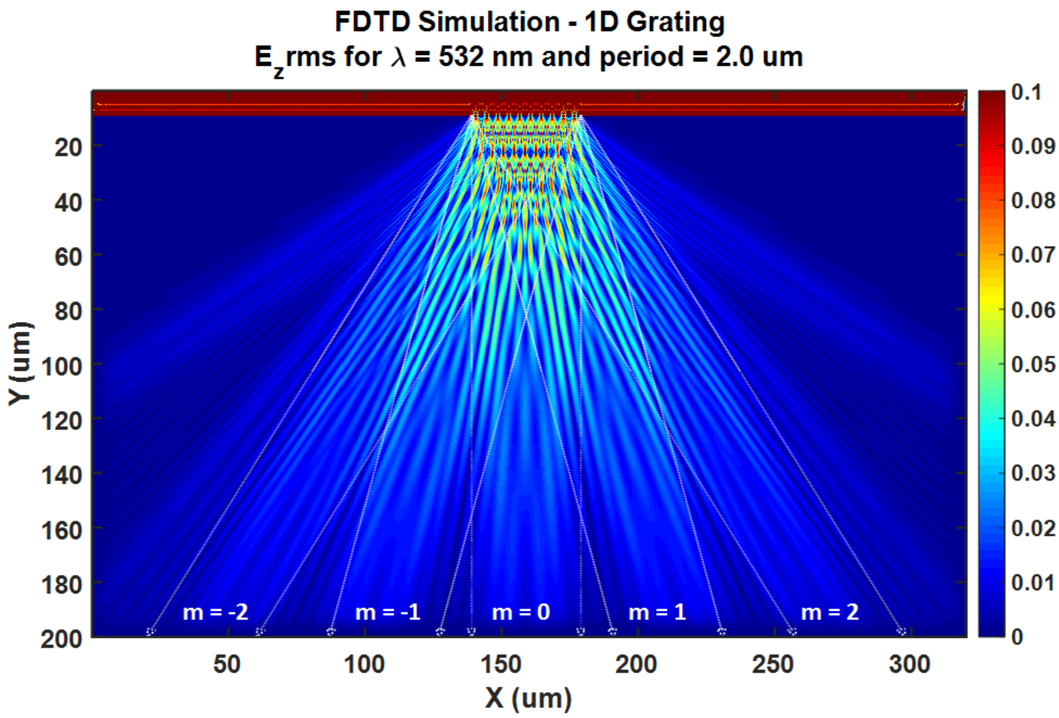

Figure 2.13: FDTD simulation of electric field $E_z rms$ of the interaction of 1D diffraction grating (2.0 μm grating period and 1.0 μm grating width) with EM wave of 532 nm wavelength.

state $E_z rms$ field is shown in Figure 2.13. Arrows denoting the direction of the expected diffracted orders were added for clarity. The intensity can be seen to be condensing and propagating at the angles given by the grating equation. The width of the beams seems to be correlated to the total grating size.

The same parameters were used to simulate the interaction of a multi-micrograting (2.0 μm grating period, 1.0 μm grating width, and 5 slits and 4 micrograting cells separated by 34 μm) with an EM wave of 532 nm wavelength and the results are shown in Figure 2.14. The response is similar to the 1D grating case. A few more observations can be made. Each micrograting produces diffracted beams that travel parallel to the diffracted beams of the other microgratings. Since they are parallel, diffracted beams of a particular order (m = 1 for example) produced by different microgratings will not interfere with each other. However, as it can be seen from the figure, there are areas where the diffracted beam of the

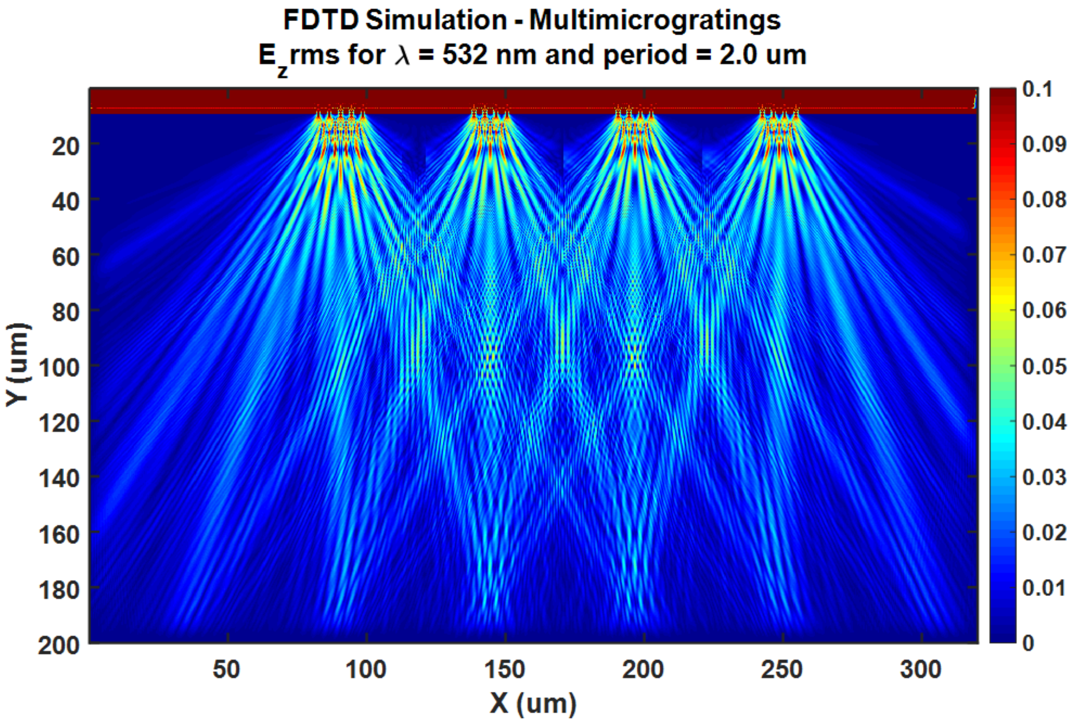

Figure 2.14: FDTD simulation of electric field $E_z rms$ of the interaction of 1D multi-micrograting (2.0 μm grating period, 1.0 μm grating width, and with 34 μm micrograting cell separation) and EM wave of 532 nm wavelength.

left most micrograting interacts with the zeroth order beam from the second micrograting at a Y distance of 200 μm. The same can be said more of the beams at particular distances. In those locations, the interference of those beams would be manifested as interference fringes which will have a fringe period related to the angular separation of the interfering beams. After those regions of interference, the beams continue to propagate to the far field. If one were to place a screen in those locations were the beams overlap, the interference fringes would become visible.

Since the FDTD simulations depict the intensities at the near field, the field distributions of E_z as a function of x for a fixed y are fourier transformed to obtain the far field patterns. These far field patterns are shown in Figure 2.15(a) for a 1D grating and (b) multi-micrograting, centered around the zeroth order max. In the 1D grating case, the intensity can be seen to weakly be distributed to the first order beams. In the case of the multi-

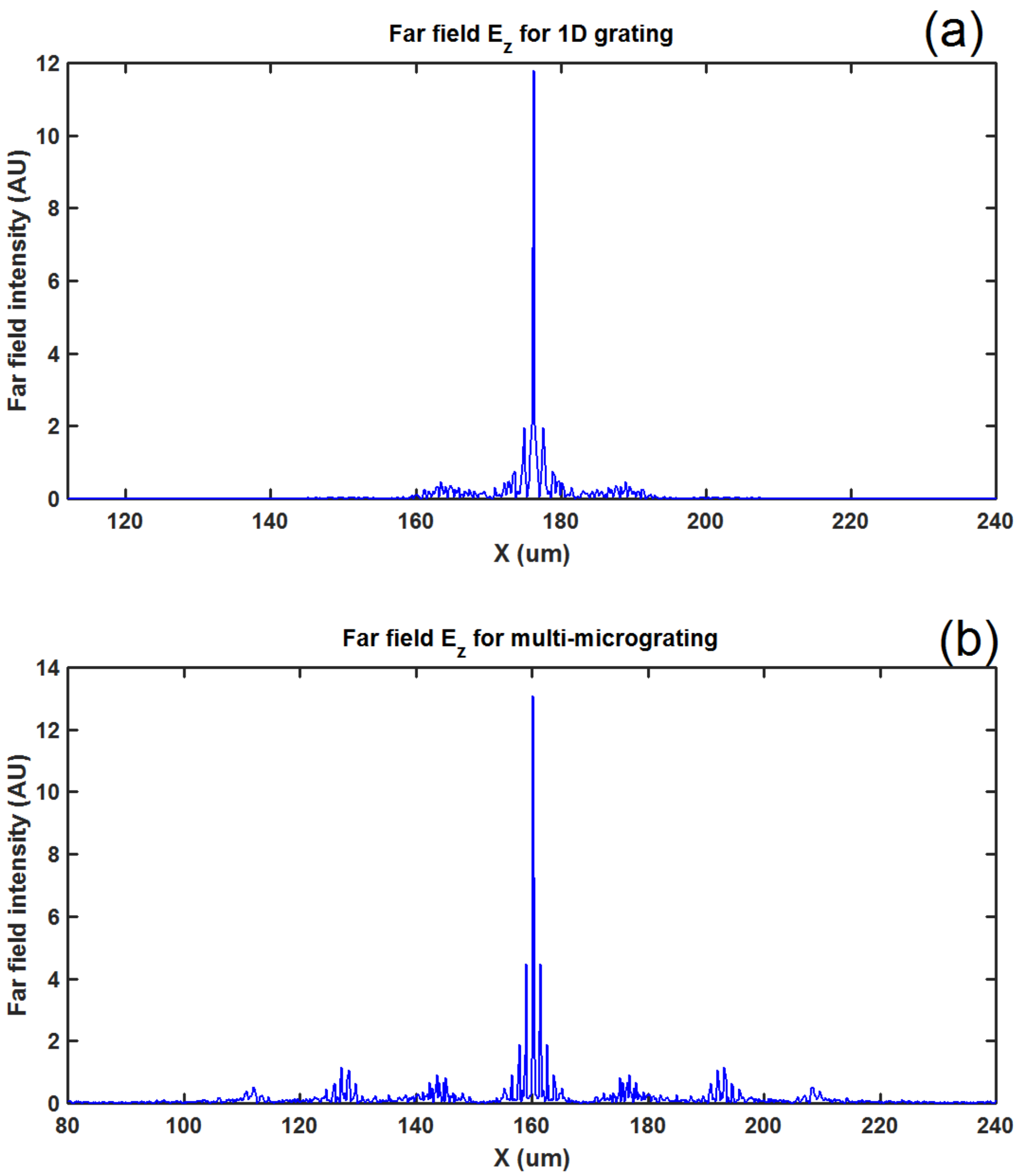

Figure 2.15: Far field distribution of E_z for (a) 1D grating and (b) multi-micrograting.

microgratings, the intensity can be seen to be further distributed to higher orders as well. These far field patterns can be compared to the Fraunhofer intensity distributions shown in Figure 2.4, which are the exact solutions to the multi-micrograting diffraction pattern.

Furthermore, FDTD simulations can help address some of the issues with simulating diffraction patterns when the grating period is smaller than the wavelength of light, such as in the case for 500 nm grating period multi-microgratings. For example, for 500 nm period grating or multi-microgratings, the diffraction equation predicts that no diffracted orders occur at normal incidence. However, if the angle of incidence θ_i is 40°, there exists an m = 1 order that is diffracted at $\theta_d = 24.9°$. An FDTD simulation was created to illustrate this phenomenon. Figure 2.16(a) shows a simulation for multi-microgratings (500 nm grating period, 34 μm micrograting separation) interacting with 532 nm wavelength light at normal incidence($\theta_i = 0°$). Only the zeroth order (transmitted beam) is able to propagate. The three micrograting cells have independent zeroth order beams that will not interact with one another. If instead of normal incidence, the incident angle is changed to $\theta_i = 40°$, then it is possible to see both the transmitted zeroth order beam and the m = 1 order diffracted beam. It is also possible to see that the zeroth order beam of the leftmost micrograting cell will interact with the first order beam of the second micrograting cell.

2.3.1 FDTD simulations of interference

One of the biggest advantages of the FDTD method is that it can also simulate interference effects between plane waves, which is an effect that would happen with multi-microgratings. Referring back to Figure 2.14, it was possible to see that the diffracted beams from a micrograting can interact with the diffracted beam from a different micrograting.

Conceptually, the two diffracted beams can be considered monochromatic plane waves traveling at angles $\pm\theta_{int}/2$ and that intersect at an angle θ_{int}. In the region of intersection, interference fringes would be produced with a fringe period d_f given by Equation 2.6.

$$d_f = \frac{\lambda}{sin\theta_{int}} \tag{2.6}$$

An FDTD simulation was carried out that simulates two interacting beams separated by 30 μm, traveling downwards at angles $\theta_{int}/2 = \pm 20°$ with a wavelength of 532 nm. The steady state electric field E_z field is shown in Figure 2.17(a), and the steady state

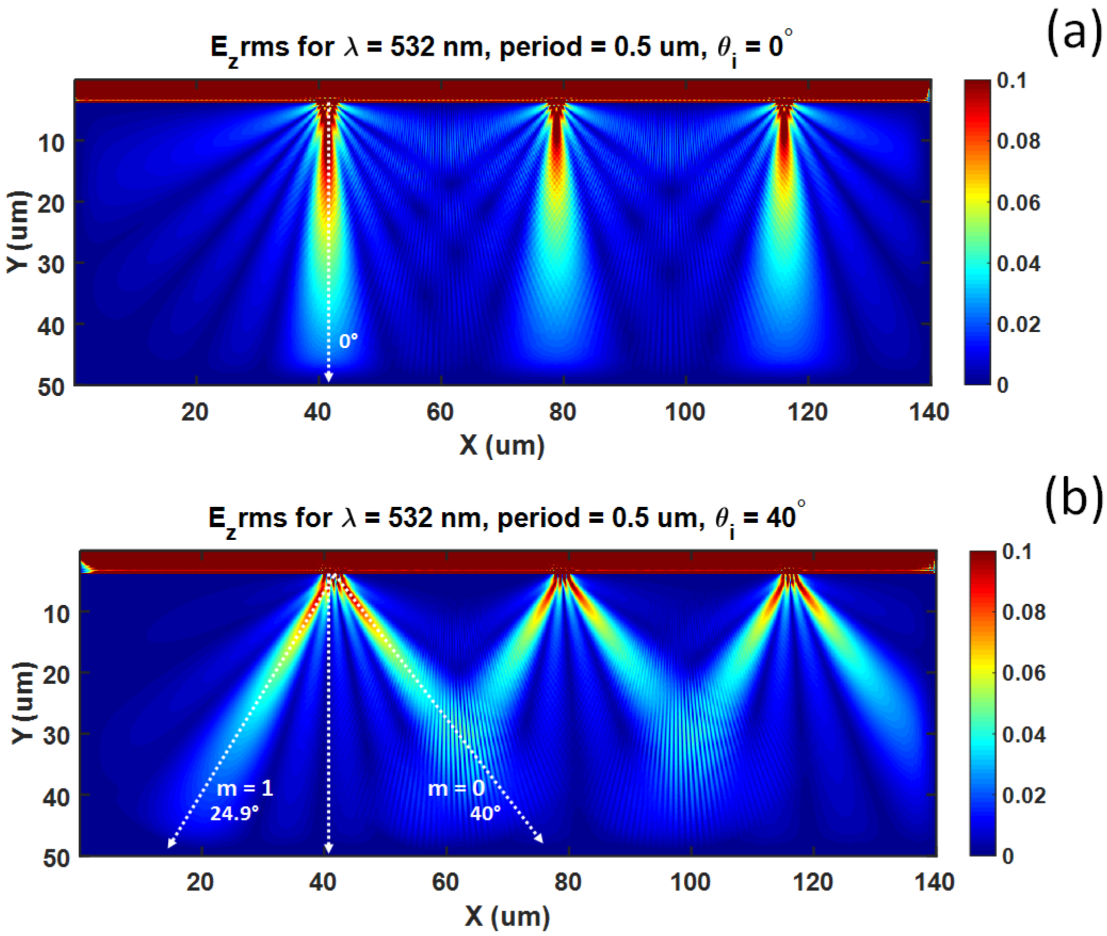

Figure 2.16: FDTD simulation of multi-microgratings (500 nm grating period, 34 μm micrograting separation) interacting with 532 nm wavelength light (a) at normal incidence ($\theta_i = 0°$) showing only the transmitted zeroth order beam propagating and (b) at $\theta_i = 40°$ incidence.

RMS electric field $E_z rms$ is shown in Figure 2.17(b). The beam on the left is traveling at angle $\theta_{int}/2 = 20°$ and the one on the right at angle $\theta_{int}/2 = -20°$ and they intersect at an angle of 40°. As it can be seen from both plots, interference fringes are formed along the white line plotted in Figure 2.17(b). The same simulation was carried out for two beams traveling at angles $\theta_{int}/2 = \pm 40°$. E_z and $E_z rms$ for this case can be seen in Figure 2.17(c) and (d).

As it is seen in Figure 2.17, if the interference angle increases, the fringe period decreases. To better visualize this effect, the profiles of the RMS fields of Figure 2.17(b) and (d) are

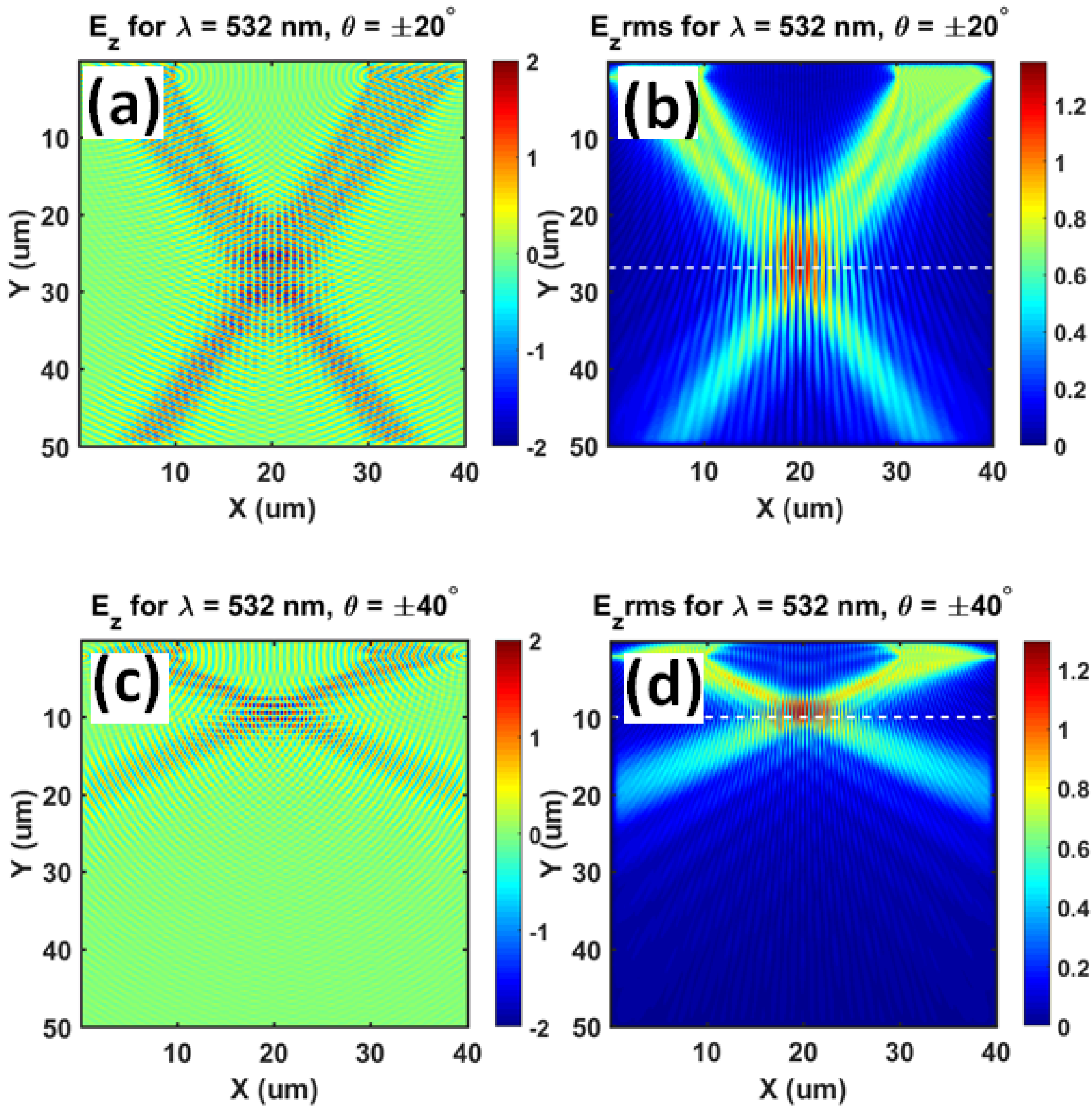

Figure 2.17: FDTD simulation of interfering beams (30 μm separation, 532 nm wavelength). (a) Electric field E_z and (b) RMS electric field $E_z rms$ at angles $\theta_{int}/2 = \pm 20°$. (c) Electric field E_z and (d) RMS electric field $E_z rms$ at angles $\theta_{int}/2 = \pm 40°$.

plotted along the white lines and are shown in Figure 2.18(a) for the 20° case and (b) for the 40° case. It is possible to see how the interference fringe period changes dramatically.

This simulation was repeated for interference angles $\theta_{int}/2$ in the range of 15 to 40°. The fringe period was automatically calculated by counting the number of peaks in the center region and dividing it by the total distance they span to obtain an average fringe

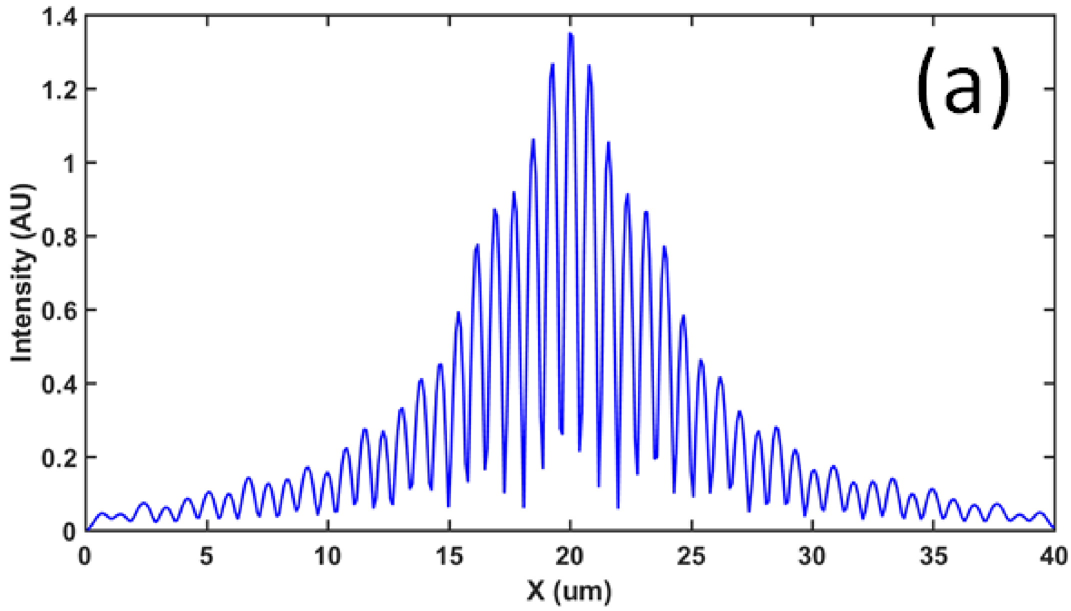

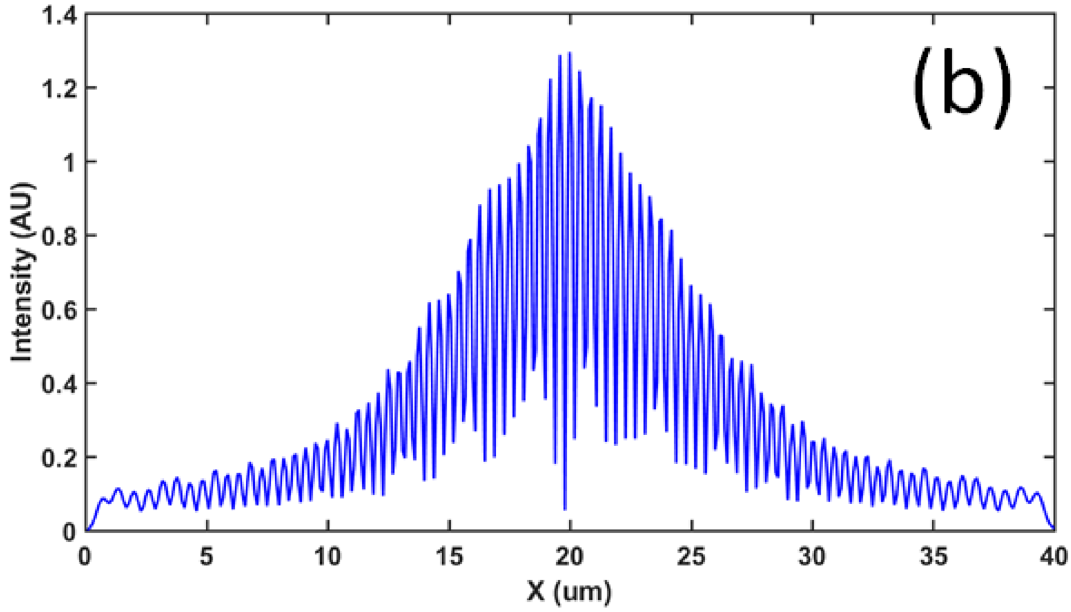

Figure 2.18: Line profiles of the RMS electric fields from Figure 2.17(b) and (d).

period. The average fringe period is plotted in Figure 2.19 as the black line, and for reference Equation 2.6 is plotted as well, using the same parameters. The two lines show to be in agreement, indicating this is a valid method to predict interference fringe periods and other interference effects observable using this FDTD method.

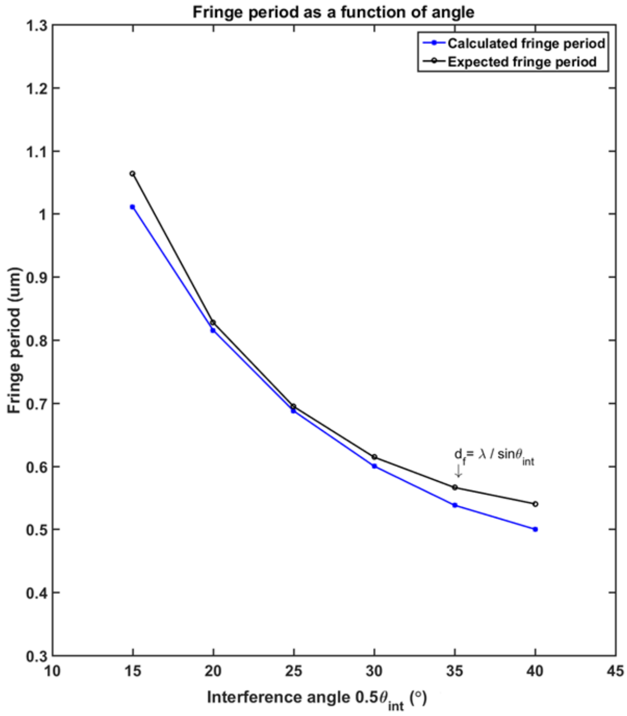

Figure 2.19: Line profiles of the RMS electric fields from Figure 2.17(b) and (d). (a) RMS electric field $E_z rms$ at angles $\theta_{int}/2 = \pm 20°$. (b) RMS electric field $E_z rms$ at angles $\theta_{int}/2 = \pm 40°$.

The FDTD simulations presented complement and corroborate the results shown for the predicted patterns of multi-microgratings that were calculated with the Fraunhofer intensity approach and with the graphical Fourier Transform method. These simulations also predict interference fringes forming in the regions where multi-micrograting diffracted beams overlap with one another. The simulations carried out were compared to other approaches that modeled 3D structures like those found in Morpho butterflies using the FDTD method to understand the diffraction patterns and how their color is being produced [50]. The simulated diffraction studies look very similar to the ones observed in the current study.

2.4 Simulation of diffraction efficiency of multimicrogratings

It has been shown that the diffraction pattern of multi-microgratings is formed by the different contributing elements that form them: the 1D grating element of the microgratings, the hexagonal aperture shape of the micrograting, and the periodicity in the array that forms those apertures. Those elements also contribute to the distribution of power of the incident beam. As described earlier, the ratio of diffracted power to incident power is known as the diffraction efficiency , otherwise referred to as the diffraction efficiency η, and given by Equation 1.7.

$$\eta = P_{diffracted}/P_{incident} \tag{1.7}$$

Diffraction efficiency is a function of several external parameters such as incident light polarization, angle of incidence, wavelength and substrate material; and grating parameters such as depth, shape, period and duty cycle. Very complex relationships exist between the different parameters and their effects on diffraction efficiency, but trench depth seems to have a large impact on diffraction efficiency.

Figure 2.20(a) has a schematic diagram of what happens to a beam that is incident on a sample with 1D diffraction gratings. For simplicity in the diagram, the grating shown is a transmission type grating, rather than reflection type, but the concept remains the same. Due to the periodic nature of the sample, the incident beam is split into a zeroth order transmitted beam and two diffracted orders labeled ±m. All of the diffracted power gets distributed in the 3 orders shown. If instead of a 1D grating sample, the beam were to be incident on a sample with periodic apertures, then the beam would get distributed to many different ±M orders as it can be seen with the schematic diagram in Figure 2.20(b). If the beam is incident on a sample with multi-microgratings, then the light would interact with both the 1D grating lines and the periodic hexagonal apertures.

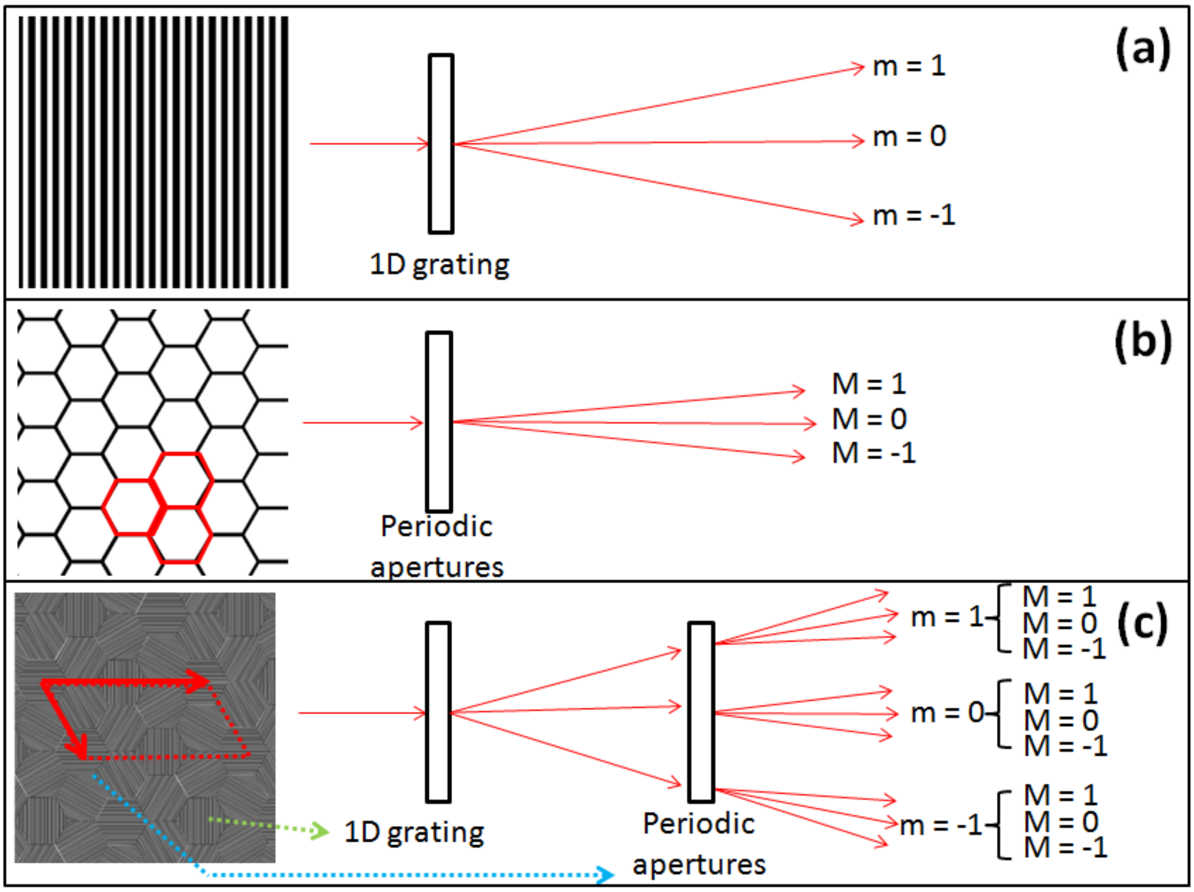

Figure 2.20: (a) Distribution of light in a sample with 1D diffraction grating. (b) Distribution of light in a sample with periodic apertures.(c) Distribution of light in a sample with multi-microgratings.

We can conceptualize this idea as follows. First, the beam sees the periodic lines within the micrograting cells and gets distributed into m orders 0 and ± 1. Each, in turn, then encounter the aperture shape of the microgratings, thus reshaping them. One can think of this step as the beam intensity getting distributed with the intensity of the single aperture diffracted pattern. In turn, each of the diffracted beams as well as the zeroth order transmitted beams all encounter the periodic array of apertures, thus, acting like a grating again, further separating each of the beams into M orders 0 and ± 1. It is possible to see that the zeroth order transmitted beam has lost more intensity to the increased number of diffracted spots. It can be expected then, that the total diffraction efficiency for multi-microgratings would be higher than that for 1D gratings.

Much research has been done to understand the optimal profile for diffraction gratings (sinusoidal, square, triangular shapes for the grating facets) [14, 15, 16, 17], but due to the ease of fabrication, a rectangular profile was selected. It is expected then that the efficiency of multi-microgratings will have contributions from the different contributing elements. Therefore, simulations to explain the diffraction efficiency of gratings with similar parameters to the ones in our design were carried out.

Simulations focused on maximizing diffraction efficiency as a function of trench depth. Due to the large possible combination of parameters, some of the parameters were fixed. Incident beam polarization was fixed to TE mode. A wavelength of 532 nm was selected. The angle of incidence was selected to be 0° with respect to the grating normal (ie. normal incidence), but for patterns with grating periods lower than the wavelength of 532 nm, the simulations were estimated at a 45° angle of incidence. Furthermore, for 1D gratings, duty cycle was chosen to be 50% as it also maximizes the diffraction efficiency. Therefore, Square gratings with 50% duty cycle on a silicon substrate were simulated with commercial software (GSolver V52 Demo, Grating Software Development, Co.) to determine the optimal depth of the gratings.

2.4.1 Diffraction efficiency simulation results

As it was mentioed earlier, the several designs were selected for fabrication: 1D gratings with periods of 0.5 and 2 μm, periodic hexagonal aperture arrays with 10 and 20 μm sides, and multi-microgratings with 0.5 μm period and 10 μm hexagonal sides and 2 μm period and 20 μm sides. However, the simulation software is only capable of running simulations of 1D gratings, not 2D complex designs of aperture arrays or multi-microgratings.

Calculated diffraction efficiency plots for 1D gratings of 2.0 μm period with rectangular facets are shown in Figure 2.21. The effects of trench depth on diffraction efficiency are shown in Figure 2.21(a) and (b) for TE and TM incident polarizations. To maximize first order TE diffraction efficiency for the 1D gratings, a grating depth of around 0.95 μm was selected to be optimal for the grating period of 2 μm at a 532 nm wavelength, resulting in a 1D grating TE diffraction efficiency of 14.1% for the first order, and a total diffraction efficiency of 31.5%. Due to the duty cycles being optimal, for these 1D grating samples most of the power is expected to be distributed to the first few diffracted orders, with a great majority of that power to be distributed exclusively to the $\pm$ 1 order.

Similar plots were obtained for 1D gratings with 0.5 μm periodicity and it was verified that the selected trench depth of 0.95 μm would work as well. For 0.5 μm period samples, only the m = 1 order is allowed at 45° incidence, so all the diffracted power goes to that order. Total TE calculated diffraction efficiency for 1D gratings with 0.5 μm was 10.4%.

To understand the effects of the material covering the gratings and their diffraction efficiency, simulations were carried out for gratings made of different materials. Figure 2.21(c-d) show simulations for gratings made of silicon, aluminum and silicon with 100 nm coating of aluminum.

For the pattern with hexagonal apertures, the same software was used to calculate the diffraction efficiency of arrays of hexagonal apertures. With a 20 μm hexagon cell size, the period between adjacent hexagons is calculated to be 34.67 μm. Similarly for a 10 μm hexagon cell size, the period between adjacent hexagons is calculated to be 17.3μm. A linewidth of 3.0 μm was selected for the width of the hexagon lines. The distance between adjacent hexagons and the linewidth is used to approximate the hexagonal apertures as 1D gratings with a duty cycle of 0.17 % for 10 μm hexagons and 0.087% for 20 μm hexagons. Due to the longer period, the incident light is diffracted into several spots. The efficiency of individual diffracted spots is considerably reduced. Additionally, due to a non-ideal duty cycle, efficiency is further decreased. A depth of 1.95 μm was selected since it provided a local maximum in the efficiency calculations. The total diffraction efficiency for periodic hexagonal apertures is calculated to be 16.8% for 10 μm hexagons and 8.7% for 20 μm hexagons. As there also exist cross-terms due to the combined effect of the different hexagon apertures, the total intensity of the diffracted spots will be distributed even further.

The diffraction efficiency of multi-microgratings is expected to behave as a combination of the 1D and hexagonal aperture array diffraction efficiencies. However, since the majority of the pattern surface consists of 1D gratings in several orientations, the contributions of the hexagonal apertures to the total diffraction efficiency is not as large as that of the 1D gratings. The majority of the light is distributed to the 1D grating orders, therefore the same grating depth of 0.95 μm was selected for multi-micrograting samples.

A compilation of calculated diffraction efficiencies is summarized in Table 2.1.

This chapter has outlined the simulation methods used to predict the diffraction patterns of multi-microgratings, presented simulated results, calculated the diffraction efficiency of multi-microgratings. These simulated optical properties of multi-microgratings will be compared in subsequent chapters to those measured from fabricated samples.

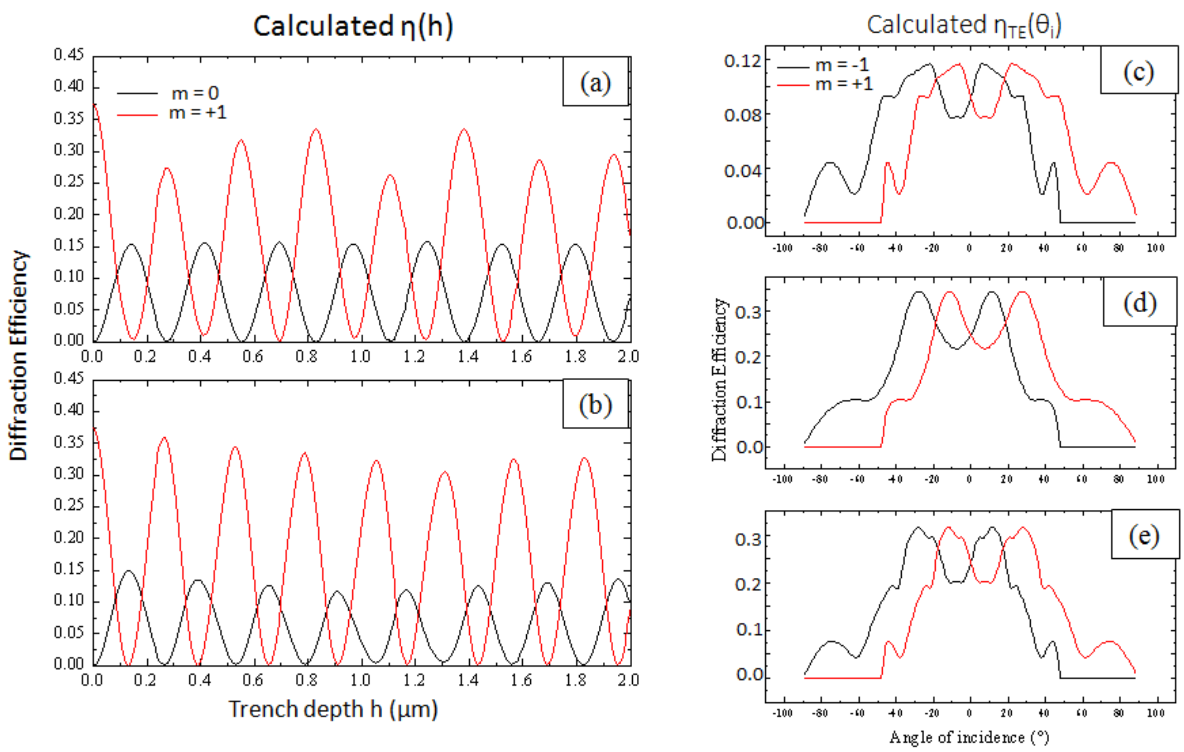

Figure 2.21: Calculated efficiency for square, 50% duty cycle 2 um gratings at a wavelength 532 nm and normal incidence. Effects of (a) TE and (b) TM polarization. TE diffraction efficiency effects for (c) silicon, (d) aluminum, (e) 100 nm Al on Si.

Table 2.1: Calculated diffraction efficiencies

Design type	Grating period or cell size (μm)	Minimum feature size (μm)	Etch depth (μm)	Calculated total TE diffraction efficiency (%)
1D grating	0.5	1.0	0.95	10.4
1D grating	2.0	1.0	0.95	31.5
Hexagon array	10.0	3.0	1.95	16.8
Hexagon array	20.0	3.0	1.95	8.7
Multi-micrograting	0.5	1.0	0.95	10.4
Multi-micrograting	2.0	1.0	0.95	31.5

Chapter 3

Fabrication of multi-microgratings

This chapter discusses fabrication methods for multi-microgratings as well as a discussion of their limitations, which reveals why only some of them were selected for the experimental implementation. The effects of the individual optical elements described earlier can be observed by the fabrication and characterization of three designs: array of hexagonal apertures, 1D gratings, and multi-microgratings. The following grating parameters were selected for fabrication. For 1D gratings and microgratings, grating periods of 0.5 and 2.0 μm (0.25 and 1.0 μm feature sizes, respectively) were chosen. The grating period, which is comparable to the wavelengths, allows for observation of the diffraction effects of the 1D grating component of the micrograting arrays. For the hexagonal aperture patterns and the micrograting cell sizes, the hexagons were chosen to be 10 (for microgratings with period of 0.5 μm) and 20 μm (for microgratings with period of 2.0 μm), so as to have enough grating lines contained within each hexagon. The total area of the patterned samples was chosen to be 1.5 mm x 1.5 mm to have an area large enough for experimental characterization. The design parameters are summarized in Table 2.1.

3.1 Overview of suitable fabrication technique

The fabrication of periodic patterns can be carried out with a variety of techniques, depending on the required feature density and dimensions, the type of substrate used and the necessity for replication of the generated structures. A few criteria must be met by these fabrication methods, which are:

1. Must be accessible to our research group.

2. Must be resource-effective (cost and time).

3. Must be able to generate complex designs of small feature sizes.

4. Must be able to fabricate multi-orientation gratings.

5. Must be able to generate close to high aspect ratio, vertical sidewalls in the interest of matching with simulations; and of precise depths, as trench depths greatly affect the diffraction efficiency.

Among the most common methods are mechanical ruling, holographic (interference lithography), optical and laser lithography, laser ablation and ion and electron beam lithography [9] and these methods are described below.

3.1.1 Optical lithography

One of the most common lithography systems is optical projection, which uses an advanced optical design to expose a pattern onto a photoresists using a mask. It is capable of exposing large areas of resist and offers great repeatability, but its resolution is limited by the wavelength of light being used. Excimer lasers are the current standard, and feature sizes have reached dimensions below 100 nm [51].

Similar dimensions have been fabricated using X-ray sources instead of coherent light as the source of energy for these systems [52]. Masked systems are capable of producing complex designs, but the cost for an intricate optical mask with very small feature sizes can be prohibitive. Masked, optical lithography can in fact be used for fabrication of multi-microgratings, but in order to fabricate microgratings with submicron periods, expensive high-density masks and advanced optical lithography equipment would be necessary.

3.1.2 Interference lithography

Laser interference lithography is a cost-effective technique used to fabricate large area periodic patterns such as 1D gratings and 2D arrays of features, with sub-micron line widths. A low-cost ($ 1,000) interference lithography system with a 405 nm GaN semiconductor laser diode in a Lloyds mirror configuration has been reported to be able to generate periodic patterns with a 300 nm period using PFI-88 photoresist [53]. A similar, cost-effective ($ 15,000) setup using an AlInGaN 405 nm diode was used to make periodic patterns with periods between 290-750 nm over a large area on AZ5214-E resist [54]. More advanced methods that produce periodic and quasiperiodic nanostructures using EUV lithography showed that high resolution is achievable with interfering beams [55, 56, 57]. While interference lithography systems are low-cost and simple, the periodicity of the patterns is determined by the interference effects of multiple laser beams and such technique is not suitable to fabricate microgratings of different orientations and complex architectures as the one required for this study.

3.1.3 Direct laser writing lithography

Another way of fabricating devices using mask-less lithography is to use a laser source and scan it across the photoresist covered sample, known as direct laser writing (DLW). The minimum resolution that can be achieved with this technique is in the range of 0.5 to 1 μm depending upon the wavelength and focusing optics, and it has a high throughput and relatively low cost. Direct-laser lithography can fabricate large-area, arbitrary patterns but its main limitation is the resolution which is larger than the critical dimensions required for this study. This technique would have been viable, but it was not readily available at the University of Virginia and it would have not allowed for the fabrication of patterns with sub-micron features easily.

3.1.4 Ion and electron beam lithography

Ion and electron beam lithography have been shown to produce features on the order of 10 nm, but their high complexity, high cost and low throughput limit their wider applications [58]. This technique could potentially satisfy all the criteria described earlier, so it was chosen as the ideal fabrication method. Electron-beam lithography (EBL) systems were available at the University Of Virginia, but they had a high cost of operation and maintenance. They were also not able to generate large area (1.5 mm) size samples in a time efficient manner. Some sample microgratings were fabricated at UVa, but the pattern area was limited to around 0.5 x 0.5 mm at about an 8 hour exposure time.

Fortunately, a collaboration with Oak Ridge National Laboratory and the Center for Nanophase Materials Sciences (CNMS) was established in order to use their EBL and clean-room facilities for the fabrication of multi-microgratings.

3.2 Sample fabrication at ORNL

After careful consideration of possible fabrication techniques and discussion with the CNMS group at ORNL and due to equipment availability as well as sample requirements in terms of minimum feature size, two fabrication techniques were employed at their facilities. Samples that had fine features such as multi-microgratings (250 and 1000 nm features) were selected to be exposed with a state of the art JEOL JBX-9300FS EBL system. For samples with hexagonal apertures, since the minimum feature size was not critical (larger than 1 μm), optical contact lithography was selected. The techniques and fabrication procedures for both are explained in the following subsections.

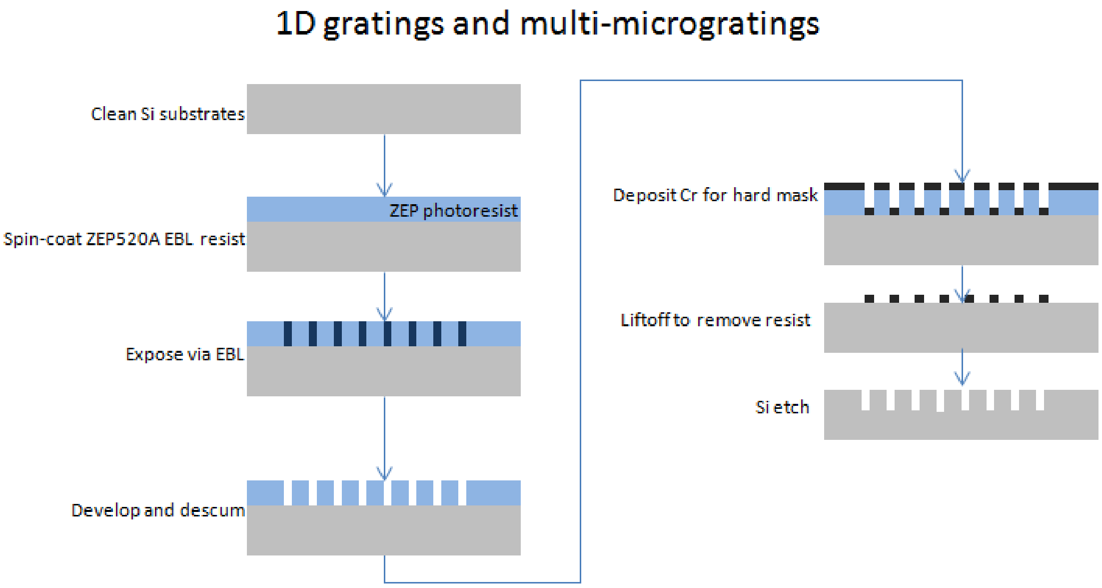

Figure 3.1: Flow chart of the EBL fabrication procedure used to fabricate samples with multi-micrograting patterns and 1D gratings.

3.2.1 EBL fabrication of multi-microgratings

The EBL fabrication procedure is summarized in the schematic shown in Figure 3.1 and is described in detail below.

For the fabrication of 1D gratings and micrograting arrays, adhesion promoter P20 was spin coated on silicon wafers (p-type, <100>, 100 mm) at 3000 rpm for 45 s. ZEP520A electron-beam resist was then spin-coated at 3000 rpm for 45 s for a desired thickness of approximately 400 nm. The wafers were then baked at 100 °C for 2 minutes.

Patterns were designed with CAD software and transferred to a JEOL JBX-9300FS EBL system (Energy = 100 keV, Current = 2 nA, Base dose = 250-290 $\mu C/cm^2$). Samples were loaded into exposure cassettes and the system automatically loads the cassettes, seen in Figure 3.2(a) into the electron beam exposure column as shown in Figure 3.2(b). Patterns were adjusted for proximity effect correction (PEC) and dimension biases (-25 to -75 nm corrections) to expose features with the desired dimensions and duty cycle. An example of a PEC corrected pattern is shown in Figure 3.2(c), where it can be seen that a

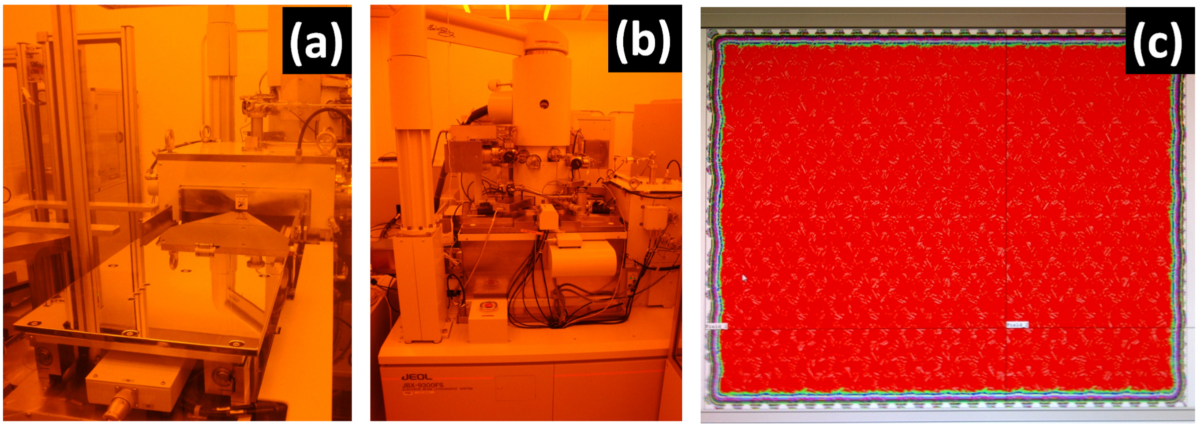

Figure 3.2: JEOL JBX-9300FS EBL system used to expose patterns with high density features. (a) Loading cassette mechanism. (b) Electron beam exposure column. (c) Example of PEC corrected pattern, where red areas denote features that required feature size corrections due to electron beam overexposure due to proximity to other features.

great majority of the center area of the pattern (seen in red) required the PEC correction to avoid overexposure of features, while the edges did not need a large correction. Exposed patterns were then developed in Xylenes for 35 s, rinsed with isopropyl alcohol (IPA) and dried with N_2.

A descum step with 0_2 plasma (200 sccm) was performed in an IonWave10 Microwave Plasma System for 15 s to remove particulates left over from the resist development steps.

For all fabricated patterns (high and low feature density), a 20 nm chromium hard mask was deposited on the wafers with an electron-beam evaporator to transfer the pattern from the resist to the silicon substrates. Metal liftoff was performed by placing samples in an acetone ultrasonic bath. Then the wafers were submerged in resist stripper and cleaned again with 15 s of O_2 plasma.

To enhance diffraction efficiency of the patterns, trenches were etched via plasma etching of the silicon in accordance with the efficiency simulations described earlier. Etching was done with an Oxford Plasmalab System 100 with a recipe that was originally designed for vertical sidewall etching of silicon waveguides (Pressure = 15 mTorr, RF-Power = 30 W, ICP = 1200 W, 25 sccm of SF_6, 60 sccm of C_4F_8 and 5 sccm of Ar), at an approximate rate of 180 nm/min for 5-10 minutes depending on the required depths for each pattern.

For the purpose of optical characterization of patterns, samples were metallized with 70-80 nm of aluminum with an E-beam evaporator, which should increase their reflectivity from approximately 36% to approximately 90%, and diffraction efficiency by a factor of 2 - 2.5.

3.2.2 Fabrication of samples with hexagonal apertures using optical contact lithography

Due to limited availability of the EBL system, for patterns with low density of features (hexagonal apertures only), since the critical dimensions were 3 μm for the borders, contact lithography was chosen for their fabrication. Their fabrication procedure is summarized in Figure 3.3 and is described below.

A quartz mask coated with chromium and photoresist was exposed with a direct-laser write Heidelberg Mask Writer (DWL66). The mask was then developed and a chrome etching step was added to transfer the patterns from the developed resist to expose the quartz substrate.

The mask was used with a contact lithography aligner and was used to expose AZ photoresist coated wafers. After exposure, the samples were developed in AZ 300 MIF Developer, rinsed with IPA and dried with N_2. The subsequent steps were identical as those for EBL fabrication from the development step.

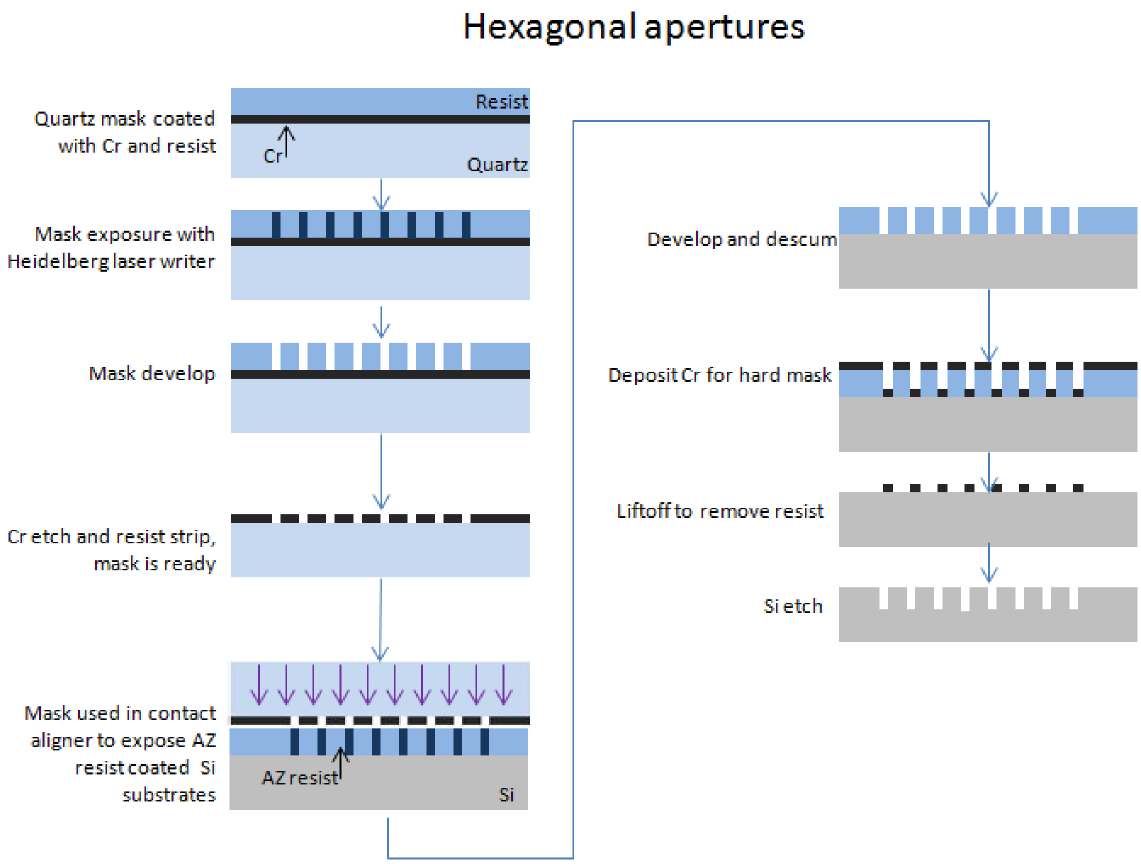

Figure 3.3: Flow chart of the EBL fabrication procedure used to fabricate samples with hexagonal apertures.

Chapter 4

Surface characterization and optical diffraction properties of multi micro-gratings

This chapter discusses the surface characterization and optical properties of the fabricated samples such as morphology, diffraction patterns and their efficiency. The characterization methods are explained in each section. Figure 4.1 shows a multi-micrograting sample with 2 μm periodicity fabricated using EBL, before being diced into individual samples and before aluminum deposition. It is possible to see each individual multi-micrograting sample as the diffracted color varies depending on the incident angle.

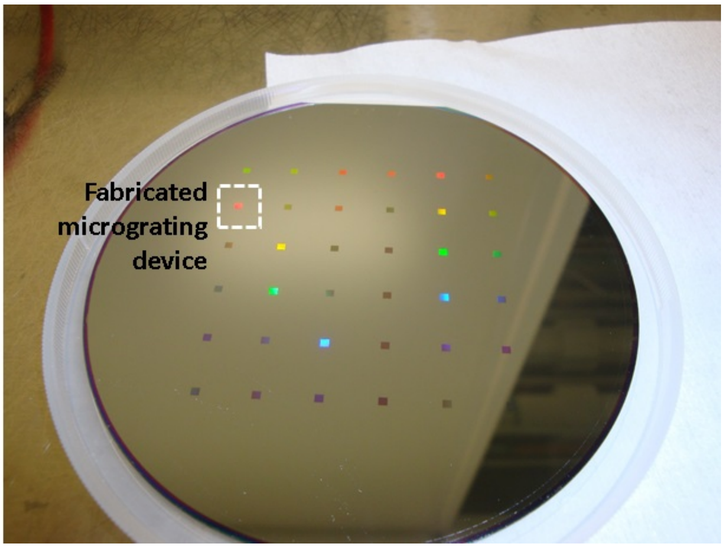

Figure 4.1: Photograph of fabricated multi-micrograting sample with 2 μm periodicity before dicing and metal deposition.

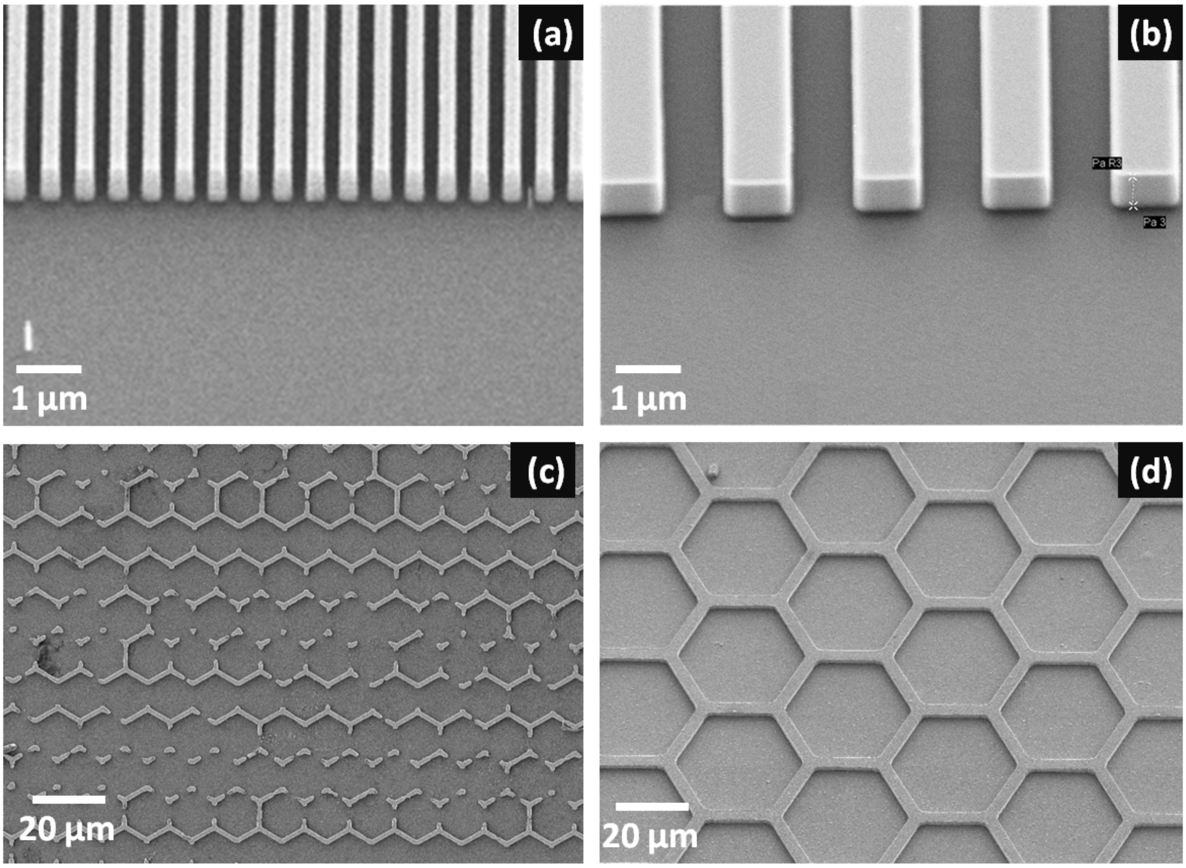

Figure 4.2: SEM micrographs of fabricated silicon samples with (a) 1D grating with period of 0.5 μm, (b) 1D grating with period of 2.0 μm, (c) array of hexagonal apertures with hexagon side dimension of 10 μm and (d) array of hexagonal apertures with hexagon side dimension of 20 μm.

4.1 Surface characterization

In order to examine the surface morphology of the fabricated silicon samples, scanning electron micrographs of the patterns were obtained. Figure 4.2(a) shows a SEM micrograph of the fabricated sample with the 1D grating pattern (at a 30° tilt) for grating period of 0.5 μm. Figure 4.2(b) shows an SEM micrograph of the fabricated sample with the 1D grating pattern for grating period of 2.0 μm. Figure 4.2(c)and (d) show SEM micrographs of fabricated samples with the pattern of hexagonal apertures for cells with side dimension of 10 and 20 μm respectively.

Unfortunately, as it can be seen in Figure 4.2(c), the 10 μm side dimension hexagon

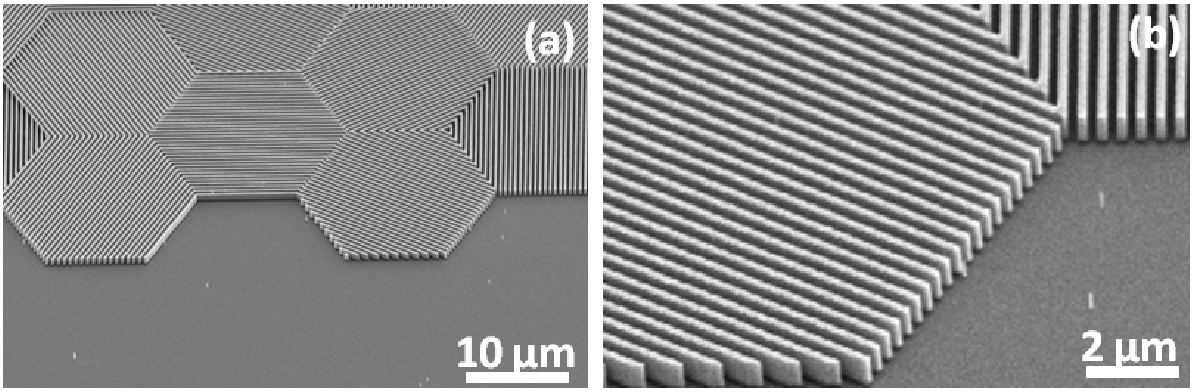

Figure 4.3: (a) SEM micrograph of fabricated silicon sample with multi-micrograting array with grating periods of 0.5 μm. Magnified details of regions around the edge of (a) are shown in (b).

aperture patterns did not turn out as expected. As described in the fabrication chapter, the hexagonal aperture patterns were fabricated via a contact aligner and a mask that was exposed with a DLW system. The system did not have a resolution good enough to properly expose the 1 μm features in the mask, therefore, some lines did not connect properly. However, as it will be discussed later, this error in fabrication did not significantly affect the generated diffraction pattern.

Figure 4.3(a) shows an SEM micrograph of a multi-micrograting sample with 0.5 μm grating period and 10 μm hexagon side dimension and Figure 4.3(b) shows a magnified area of (a) near one of the edges to be able to see the sample features clearly. With features of 500 nm grating period and 0.95 μm trench depth, it is possible to see their high aspect ratio. Due to the etching process, vertical sidewalls were achieved. Similarly, Figure 4.4(a) shows SEM micrographs of the combined multi-micrograting patterns with a 2.0 μm grating period and 20 μm hexagon side dimension. Figures 4.4(b) and (c) shows images of (a) at higher magnifications.

From the SEM micrographs it is possible to see that the samples were fabricated to the desired specifications. For patterns with high feature density, sample critical dimensions had to be adjusted in the EBL exposure step for PEC and for dimension bias, resulting in 50% duty cycles and precise grating periods with no spatial variation of these dimensions

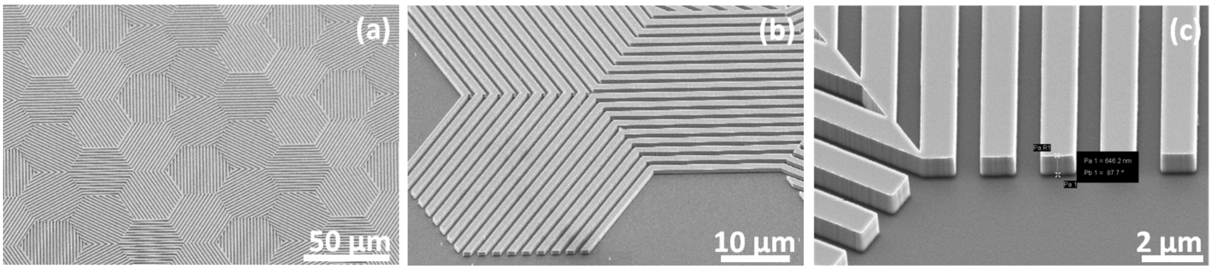

Figure 4.4: (a) SEM micrograph of fabricated silicon sample with multi-micrograting array with grating periods of 2.0 μm. Magnified details of regions around the edge of (a) are shown in (b) and (c).

in different parts of the 1.5 mm x 1.5 mm areas of the samples. The edges are well defined and the sidewall profiles are straight, which indicates that the recipe that was used for the etching process was appropriate. Feature shape, periodicty and regularity are very important in determining the quality of the samples' diffraction patterns, especially when it comes to diffraction efficiency.

The depth of the trenches can be extracted from the 30° tilted SEM micrographs. It was determined that they were very close to the specified depths of 0.95 and 1.95 μm, respectively for samples with micrograting arrays and with hexagonal apertures. These measurements were also in agreement with profilometer data. Additionally, to verify the depth measurements, Figure 4.5(a) shows a laser confocal micrograph of multi-micrograting sample with 2.0 μm grating period, which shows a typical grating profile for the fabricated samples. To show the grating profile, Figures 4.5(b) and (c) show a 3D profile of the captured laser confocal micrograph and a linescan profile of a selected area. Similarly, the grating depths of samples with 1D gratings and hexagonal apertures was measured with laser confocal microscopy and were found to be in agreement with the other measurements.

4.2 Optical diffraction study of fabricated structures

The diffraction patterns from arrays of hexagonal apertures and multi-microgratings were obtained by illuminating the samples with a laser beam with λ = 532 nm at normal

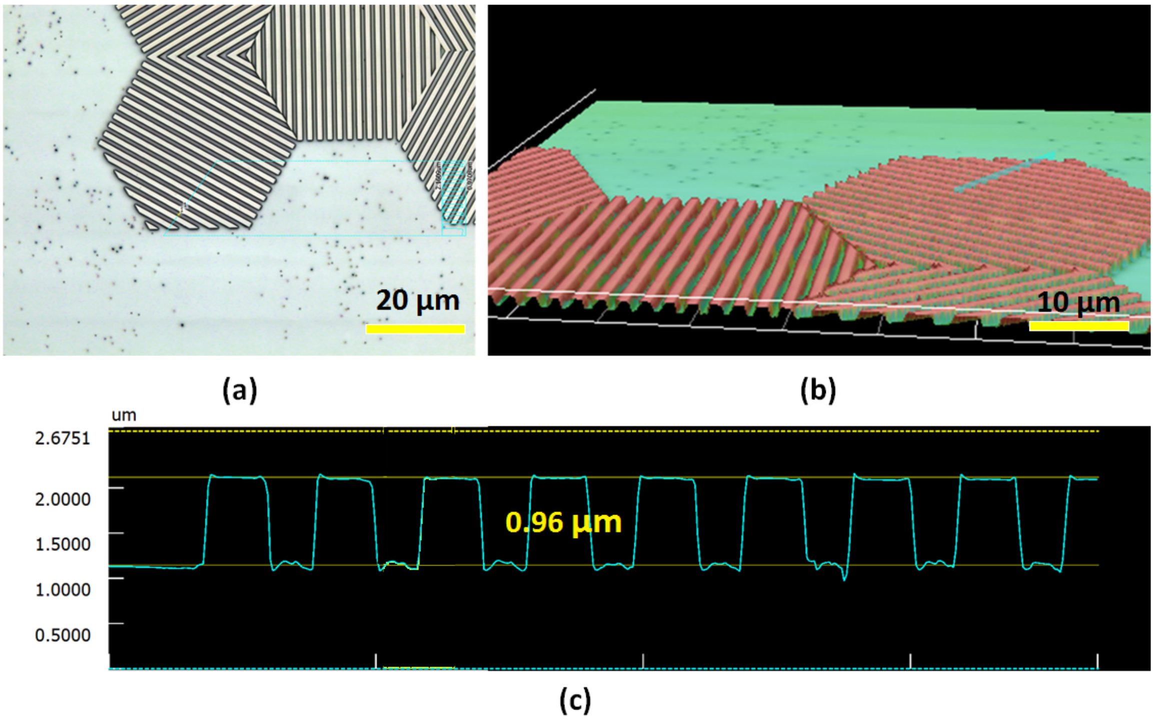

Figure 4.5: Laser confocal micrographs of micrograting pattern with 2.0 μm periodicity. (a) Top view. (b) 3D height profile. (c) Linescan profile.

incidence. The reflected diffraction patterns were projected onto a screen 20 cm away and photographed. Due to the variation in intensity distribution in the diffraction pattern, the areas of high intensity tend to saturate the camera sensor used to take the images and low intensity features are not well captured. A photographic technique called High Dynamic Range photography (HDR) has been used to overcome the issue of having to capture a wide range of exposures [59, 60, 61]. Images of diffraction patterns were captured at several exposure levels and then recombined to produce a more uniform intensity distribution allowing the capture of both high and low intensity details without saturation. This technique was applied in order to obtain high quality images of the diffraction pattern.

4.2.1 Optical diffraction patterns from arrays of hexagonal apertures

The diffraction patterns of arrays of hexagonal apertures with side dimensions of 10 μm and 20 μm, such as the ones in Figure 4.2(c) and (d), are shown in Figure 4.6(a) and (b). The two diffraction patterns look very similar with respect to overall intensity distribution, but the separation between individual diffraction spots is different due to the different hexagon side dimensions. The inset in Figure 4.6(b) shows details of the center area of the pattern projected on a screen 300 cm away.

As described earlier, the arrays of hexagonal apertures receive contribution from the hexagonally shaped aperture and periodic arrangement of the cells (Elements 1 and 2). The diffraction patterns of the fabricated patterns with two side dimensions both have three main features. First, the center area of the diffraction pattern is shaped as the hexagon, which arises from the hexagon shape acting as an individual aperture.

Second, there are three lines oriented at 30°, 90° and 150°. The hexagonal cells act as individual apertures, and thus, they diffract light. The hexagon has two sides oriented at 0°, which can be considered as an aperture in 1D space. That aperture, when illuminated with planar electromagnetic radiation, diffracts the incoming wave in the shape of a sinc^2 function in the direction perpendicular to the edges of the aperture. Thus, the illuminating light would produce a sinc^2 intensity distribution in a direction normal to the apertures. In this case, the 0° aperture produces an intensity distribution in the vertical direction. The other two pairs of hexagon sides (60° and 120°) produce two intensity distributions (at their respective normals of 150° and 30°). Combining all three 1D apertures (with a convolution of the three aperture functions describing the three hexagon edges) generates the three lines. The three lines in Figure 4.6(a) appear to be dimmer than those in Figure 4.6(b) because of fabrication errors described earlier.

Third, as seen in the inset in Figure 4.6(b), the individual lattice spots are observed.

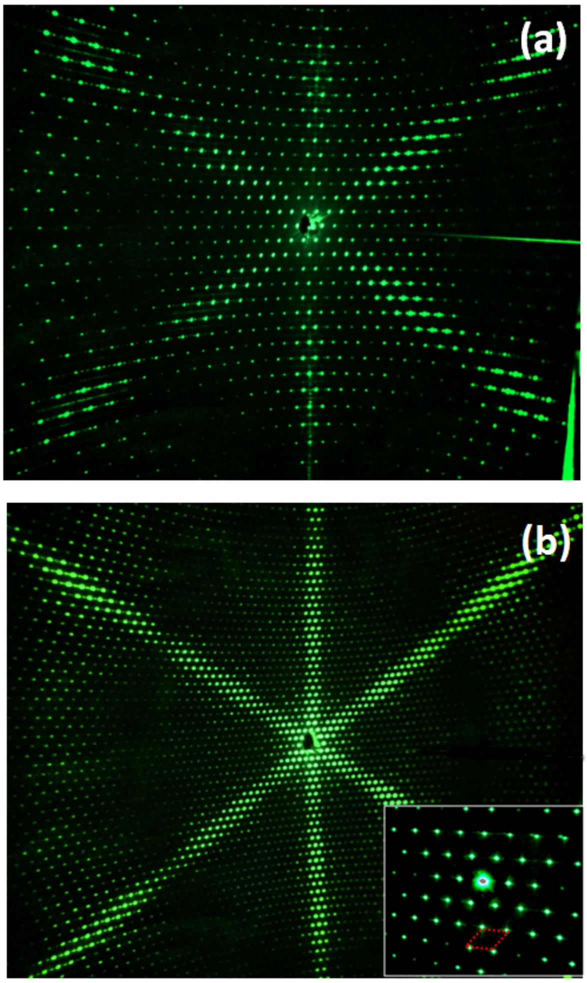

Figure 4.6: Observed diffraction pattern of sample with arrays of hexagonal apertures with hexagon side dimensions (a) 10 μm and (b) 20 μm with laser light with $\lambda = 532$ nm. Inset in (b) shows center area of diffraction pattern projected on a screen 300 cm away, to obtain details.

They are originated by the honeycomb lattice that was used to array the hexagons. The red parallelogram in the inset shows a lattice that exists in the diffraction pattern. Each of the spots are all measured to be equidistant to each other, indicating that the lattice that produced these spots had two vectors that were equal in dimensions. The angular separation of the lattice spots is measured to be in accordance with that one of the generating lattice of hexagonal apertures. Even though the 10 μm sample that originated the diffraction pattern in Figure 4.6(a) had fabrication errors, its diffraction pattern still appears as predicted. Due to the periodic nature of the hexagon aperture centers, it

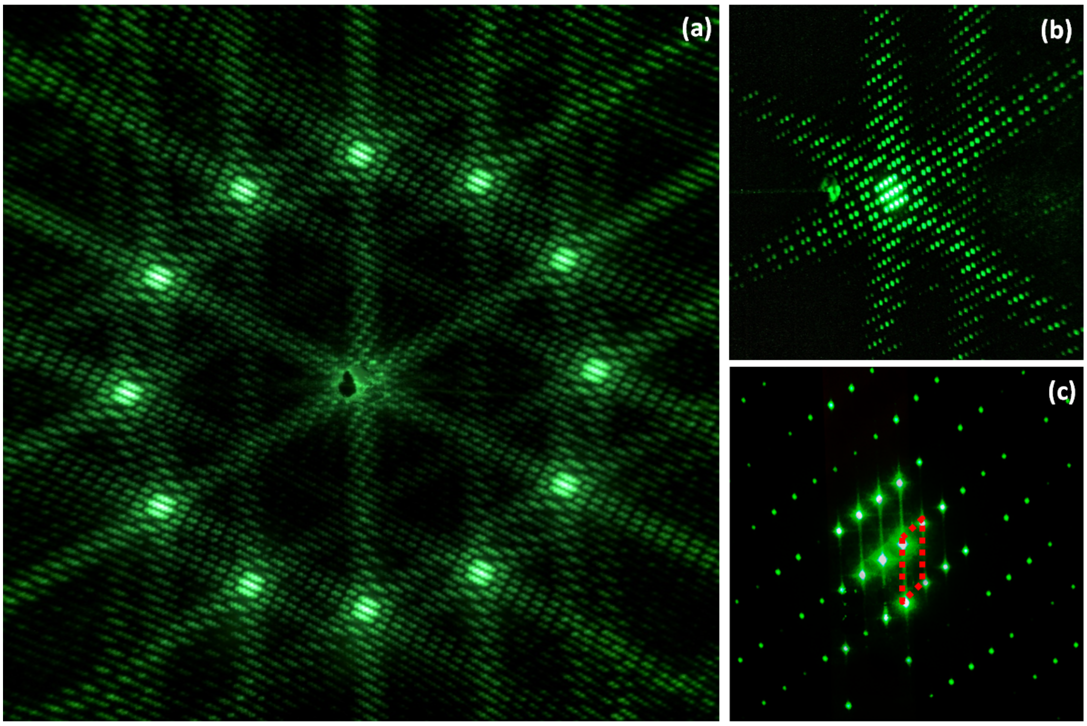

Figure 4.7: (a) Observed diffraction pattern for multi-micrgorating silicon master with 2.0 μm period illuminated with laser with $\lambda = 532$ nm projected on a screen 20 cm from the reflecting sample at normal incidence. (b) Detail of one of the spots from (a)at a further distance. (c) The same spot in (b) but projected on a screen 300 cm away, to obtain details.

is concluded that the observed lattice in the diffraction pattern to be reciprocal to the honeycomb lattice that originated the hexagonal aperture arrays.

4.2.2 Diffraction patterns of arrays of multi-micrograting

The multi-micrograting samples with grating period of 2.0 μm produced a very unique diffraction pattern as it can be seen in Figure 4.7(a). Figure 4.7(b) shows details of the diffraction pattern in 4.7(a). To examine the small details seen in Figure 4.7(b), the screen was moved to a distance of 300 cm and a photograph was taken and results are shown in Figure 4.7(c).

The diffraction pattern of the multi-micrograting structures is composed of several prominent features which are a result of the multi-micrograting constituting elements described earlier. The first feature can be seen in Figure 4.7(a) as a set of twelve bright annular spots surrrounding the central beam. For simplicity, these features are named after the hour hands of a clock. They are originated by periodic lines at six different orientations (Element 3). Consequently, these spots behave in accordance to the 1D grating equation. Each of the periodic micrograting orientations produces diffracted spots in a direction perpendicular to the grating lines, such as they do in a 1D grating. Given that there are 6 possible angular orientations of the periodic grating lines within the micrograting cells, then each angular orientation produces diffracted spots in the corresponding perpendicular direction. For example, for micrograting orientations of 0°, diffraction spots are produced in a vertical (90°) direction. For a grating orientation of 30°, the spots lie in a line that is oriented at 120°. Furthermore, just as 1D gratings, each of the micrograting cells can produce positive and negative orders. Thus, the 0° microgratings produces the 12 and 6 o'clock spots around the central reflected spot. A similar analysis can be carried out for the other micrograting orientations, thus resulting in the twelve visible spots for the first order (negative and positive) spots. Higher order spots extend radially outward from the center beam but are not shown in the photographs.

The second feature, seen in Figure 4.7(b), is produced by individual hexagons and their periodicity (Elements 1 and 2) and it is seen at a higher magnification of the individual annular spots of Figure 4.7(a). Each of the twelve annular spots (1D diffraction grating spot locations) has the same features. The three lines and hexagonal shape of the spot observed in Figure 4.7(b) are very similar to the diffraction pattern observed for hexagonal apertures only, as seen in Figure 4.6. The 1D diffraction grating spot locations act as centers for individual hexagonal diffraction patterns. In other words, a convolution of the diffraction patterns of 1D grating and hexagonal aperture arrays is observed in Figure 4.7(b). These cross terms now exist in the diffraction pattern that would otherwise not appear.

The third feature, seen in Figure 4.7(c), is formed by the oblique lattice that is formed from the unit cell that was used to generate the large area micrograting arrays, as it can be seen from the red parallelogram drawn in Figure 4.7(c). The six hexagonal microgratings were broken down into a unit cell that had dimensions a and b (related to the hexagon side dimension s), as it can be seen in Figure 1.4. The unit cell itself is skewed, as a is twice as long as b. Therefore, the periodicity of the unit cell is expressed in the diffraction pattern as a lattice depicted by the red parallelogram.

In other words, the diffraction pattern of arrays of multi-microgratings can be explained as the convolution of the different periodicities that form the arrays and it appears to have a spatial hierarchy for the existence of these cross terms. The smallest observable features in the diffraction pattern (the lattice described by the red parallelogram in Figure 4.7(c)) corresponds to the largest feature in the micrograting array design (the unit cell that forms the arrays). This lattice is convoluted with the diffraction pattern of individual hexagonal apertures, thus creating the pattern seen in Figure 4.7(b). In turn, the pattern seen in Figure 4.7(b) is then convoluted with the 1D diffraction grating spot locations, creating the large and complex diffraction pattern of multi-microgratings seen in Figure 4.7(a).

For comparison, Figure 4.8(d-f) show experimental diffraction patterns captured for multi-microgratings at similar magnifications.

It can be seen that the experimentally observed diffraction patterns of multi-microgratings are very similar to their simulated patterns, confirming that their diffraction pattern is formed by the different periodicities found in the arrays. The micrograting period forms positive and negative orders around the central spot. Due to the hexagonal shape of the micrograting, each of the positive and negative spots are shaped like the diffraction pattern of a hexagonal aperture. Finally, the vectors used to create the multi-microgratings appear in the diffraction pattern, giving rise to an array of spots in a grid like fashion, described by a rhomboidal unit cell.

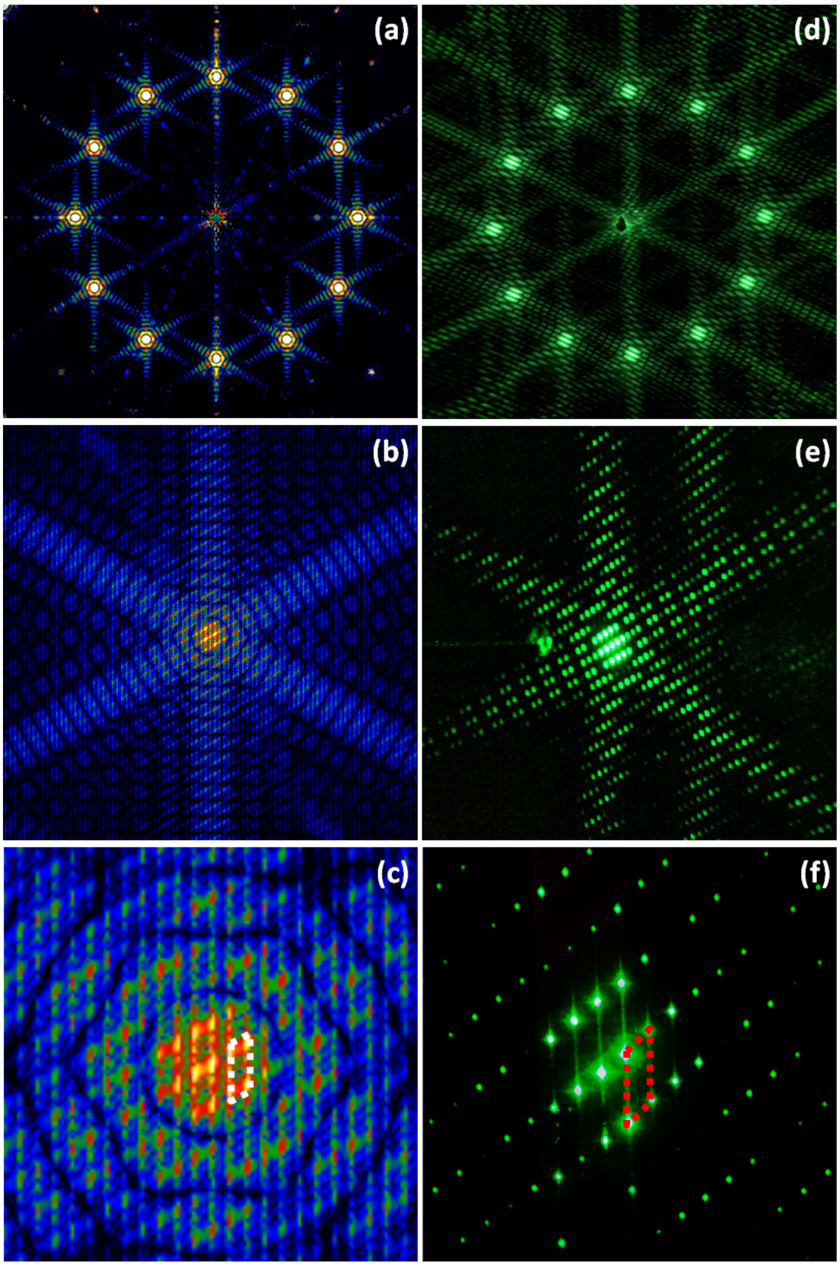

Figure 4.8: Simulated via graphical Fourier Transform and observed diffraction patterns of an array of hexagonally shaped microgratings with $s = 20$ μm, $d = 2.0$ μm, vector $\vec{a} = 120$ μm at 0° and vector $\vec{b} = 60$ μm at 120°, wavelength $\lambda = 532$ nm.(a) The 12 calculated spots shown correspond to the positive and negative orders of each micrograting orientation. (b) shows a magnified image of one of the 12 spots seen in (a). (c) Higher magnification of a spot in (a), showing the periodic nature of the small features produced by the large area array. (d-f) show experimentally observed diffraction patterns at similar magnifications as those in (a-c).

4.3 Beam profile measurements of diffracted spots

Beam profiles of samples with 1D gratings and multi-microgratings are an important measurement that help exemplify the advantages of using multi-microgratings over traditional 1D gratings. Measurements of diffracted beam profiles were carried out using two techniques, with a scanning pinhole and with a commercial CCD camera sensor. The measurement techniques are described in this section.

4.3.1 Beam profile measurement using pinhole scanning technique

Beam profiles were measured experimentally using a pinhole scanning technique. The experimental setup for the measurement can be seen in Figure 4.9(a). A 1 mm pinhole aperture was mounted on a linear translation stage and the power transmitted through the aperture was measured with a power meter. While it provides an integrated measurement of the sample beam profiles, this technique is valid since it was used both for samples with 1D gratings and multi-microgratings with 2 μm periodicities. Because a 1D grating spot was of much higher intensity than a multi-micrograting spot, a linear polarizer was used after the laser to ensure that similar power levels were measured by the power meter and to eliminate any overall intensity related phenomena in the power meter.

Measurements were carried out to understand the differences between 1D grating and multi-micograting beam profiles using the aforementioned setup. Maximum intensity in the sensor was approximately 15-20 μW for both samples. The aperture was scanned along the diffracted beams at 127 μm intervals using the linear stage. OriginPro was used to normalize the intensity of the acquired data with respect to the maximum intensity measured and also centered with respect to the same maximum intensity location. Figure 4.9(b) shows the beam profiles as captured by this technique. An OriginPro filter was

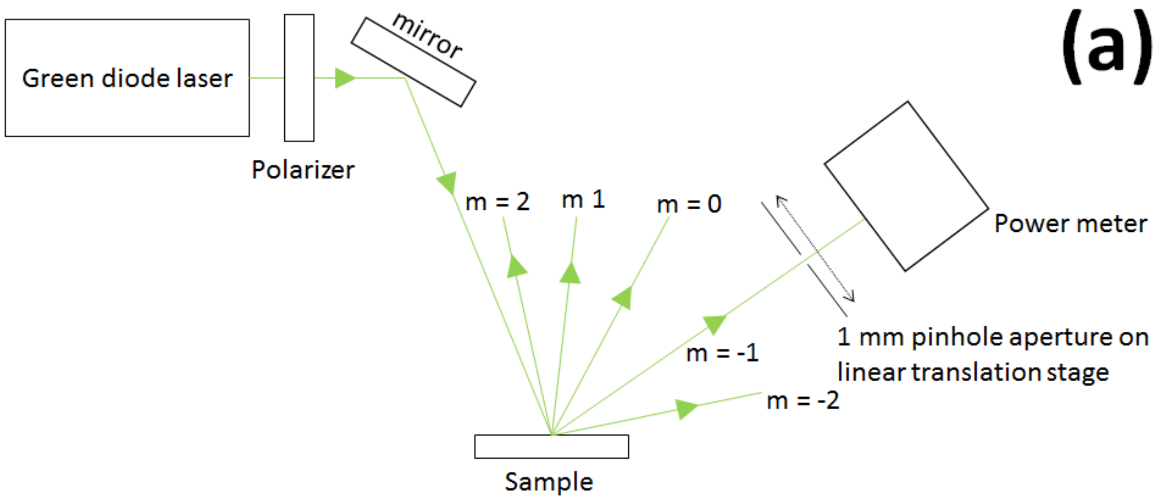

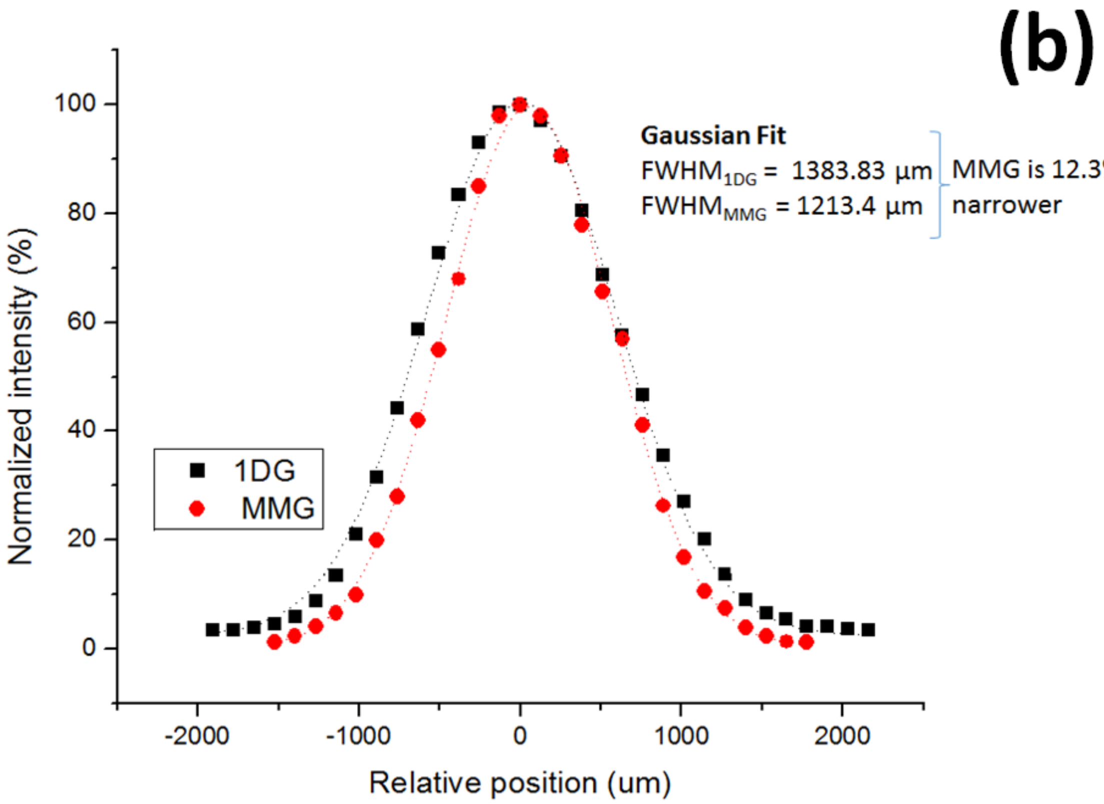

Figure 4.9: (a)Experimental setup for beam profile characterization using pinhole scanning technique. (b) Beam profiles for 1D grating and multi-microgratings as captured by this technique.

used to calculate the beam widths. These were found to be 1383.83 μm and 1213.4 μm respectively. Using this technique it was possible to determine that the multi-micrograting beams appear to be 12.3% narrower.

4.3.2 Beam profile measurements using CCD camera

Commercial CCD beam profilers tend to be expensive, but a cost-effective technique using the CCD sensor found in a webcam was reported to produce accurate measurements of laser beam profiles [62]. The experimental setup for this technique can be seen in Figure 4.10(a). Samples were illuminated with a green laser diode with 532 nm wavelength, under two conditions: with a narrow probing beam and with a 10x expanded beam. This was done to understand the effects of input beam width on diffracted beam profiles. For the first condition, the 1.2 mm laser beam width was not modified. For the second condition the beam was magnified by 10x to 12 mm using a removable 10x ThorLabs beam expander. The intensity of the beams was attenuated with combinations of neutral density (ND) filters and polarizer to prevent saturation on the sensor, which can capture intensity values between 0 and 255. A bandpass notch filter (ThorLabs, 550-40) was used to prevent any unwanted light from entering the sensor and to enhance contrast ratio.

A commercial webcam (Intel CS110), seen in Figure 4.10(b) was used for these measurements. The housing and lens of the webcam were removed to reveal the CCD sensor, seen in Figure 4.10(c). The active area of the sensor is shown inside the white dashed rectangle. The CCD sensor had a resolution of 352 x 288 pixels, for a total sensor area of 2.84 x 2.33 mm. Pixel pitch was measured via an optical microscope and was found to be 8.08 μm, and an optical image of the sensor array is shown in Figure 4.10(d). Images of the beams were then captured with freeware program QFocus. Intensity profiles were extracted from the captured images using ImageJ software. Beam profile data was then normalized and fitted to a Gaussian profile using OriginPro to obtain measurements of the FWHM of the beams.

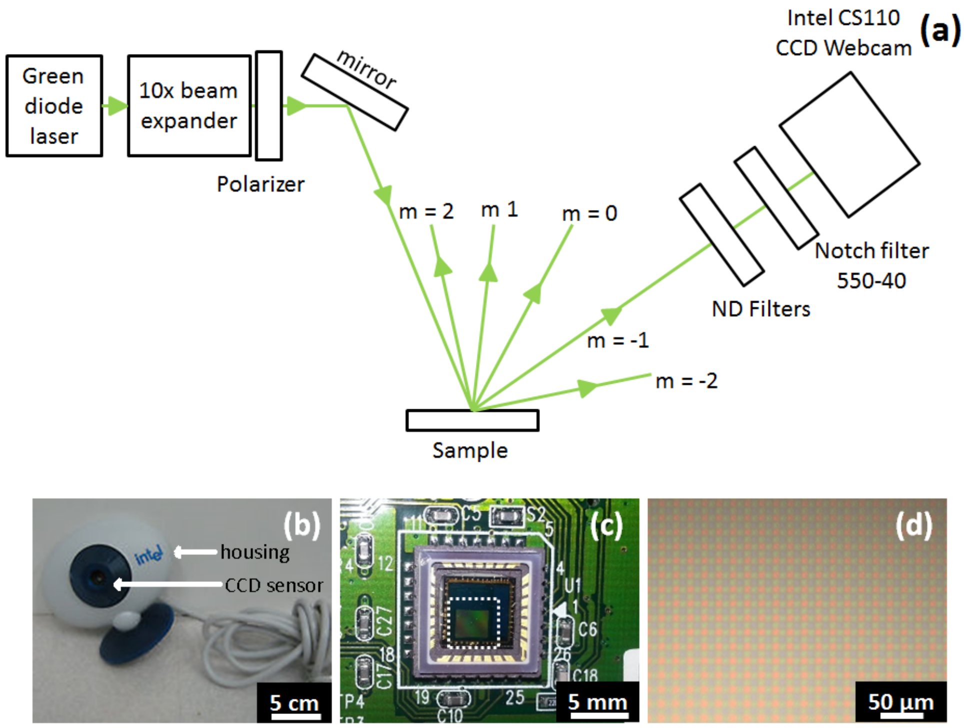

Figure 4.10: (a) Experimental setup for beam profile characterization using CCD webcam. (b) Intel CS110 Webcam used as a beam profiler. The housing and lens were removed to reveal the CCD sensor. (c) Picture of CCD sensor area. Active area, shown inside dashed rectangle, has dimensions of 2.84 x 2.33 mm and a resolution of 352 x 288 pixels. (d) Optical microscope image of CCD pixel array. Pixel pitch is measured to be 8.08 μm.

For the first condition, for a probing beam with 1.2 mm width, the total pattern size (1.5 x 1.5 mm) is larger than the probing beam. Figure 4.11 shows images of the beam profiles captured with the CCD sensor at a sample to sensor distance of 30 cm for the first condition. Figure 4.11(a) shows the beam profile captured for a 1D grating sample, and the slice of the profile along the blue dotted line is shown in Figure 4.11(b). Several images (5) were captured and fitted to a Gaussian profile to calculate an average FWHM for 1D grating beams of 562.1 μm, which is comparable to the input beam that was measured using the same technique to have a FWHM of 563 μm. Figure 4.11(c) shows an image of a captured beam profile for a sample with a multi-micrograting pattern, specifically from the red rectangle shown in the inset. The captured image shows almost 3 of the individual beams that were seen in that area of the diffraction pattern, and their separation on the

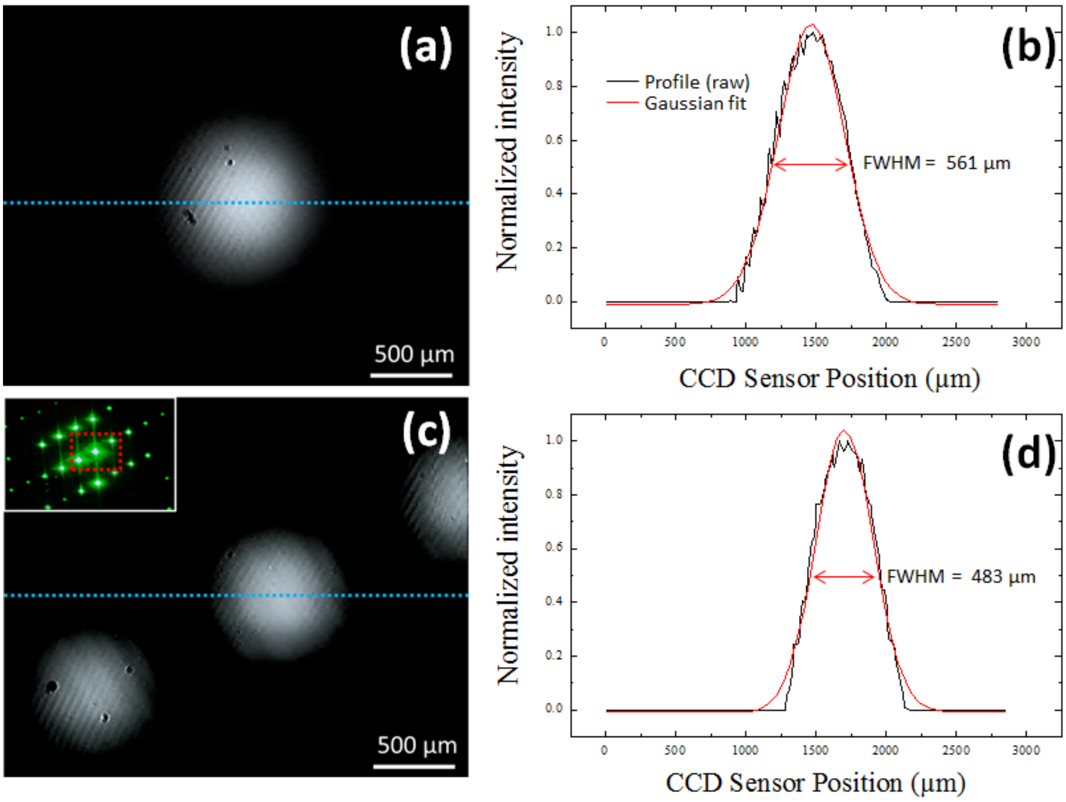

Figure 4.11: Beam profiles obtained with CCD sensor at a sample to sensor distance of 30 cm and with a probing beam of 1.2 mm. (a) Beam profile for a sample with a 1D grating pattern. (b) Slice along blue dotted line of (a) to show raw beam profile and Gaussian fit to obtain FWHM. (c) Beam profile for a sample with multi-micrograting pattern. For clarity, inset shows a photograph of the area of the diffraction pattern that was captured. (d) Slice along blue dotted line to show beam profile and Gaussian fit to obtain FWHM.

sensor of 1.25 mm corresponds to the expected separation (0.27°) of the beams at a sample to sensor distance of 30 cm. Figure 4.11(d) shows the profile along the blue dotted line in Figure 4.11(c), with its corresponding Gaussian fit. Several images (5) were used to compute an average FWHM of 482.4 μm, which is about 14.1% narrower than the FWMH for a 1D grating beam. For this first condition, the beams from 1D grating samples are observed to have a Gaussian profile of similar characteristics to the input laser beam, but for the micrograting, they are found to be slightly narrower.

For the second condition, for a probing beam with 12 mm width, the total pattern size is smaller than the probing beam, which becomes important as the probing beam now encounters the aperture shape of the total pattern size. Beam profiles captured with the CCD sensor for an expanded probing beam can be seen in Figure 4.12, at a sample to sensor distance of 30 cm. Figure 4.12(a) shows the profile of a 1D grating sample when illuminated with an expanded probing beam. The sample had a pattern size of about 1.5 x 1.5 mm, and it acts as an aperture, causing the light to diffract into the pattern observed. The pattern corresponds to the Fresnel diffraction from a square aperture rather than Fraunhofer diffraction, as it would be expected for this wavelength, aperture size and sample to sensor distance (Fresnel number $F = 14.09$). The beam is square shaped, as the aperture, and was observed to have the same size of 1.5 x 1.5 mm at sample to sensor distances between 10 cm and 50 cm. Figure 4.12(b) shows the beam profile of a sample with multi-micrograting patterns at a sample to sensor distance of 30 cm. The image now shows three separate micrograting beams all incident on the sensor at the same time. They have a rectangular shape due to the expanded beam encountering the total pattern shape as an aperture and producing Fresnel type diffraction. Due to the fact that three micrograting beams are incident on the CCD sensor, it causes them to interact with each other, which produces the high contrast areas of high and low intensity fringes in the areas where the beams overlap. A slice profile of the interference fringes along the red line in Figure 4.12(b) is shown in Figure 4.12(c). The interference fringes are fitted to a $cos^2(x)$ function, having a period between 90 - 100 μm at a sample to sensor distance of 30 cm. The three micrograting beams have an angular separation (0.27°) that causes them to separate as the distance from the sample increases, but at sample to sensor distances between 10 and 35 cm such interference fringes were observed. At longer distances, the beams separate enough as to not interfere with each other on the CCD sensor. It is important to note that similar interference fringe effects could be achieved with the same expanded probing beam but with a much larger total pattern size, which would produce no additional Fresnel aperture effects from the total pattern size as the diffracted beams would still have a Gaussian profile. Such interference fringes provide very

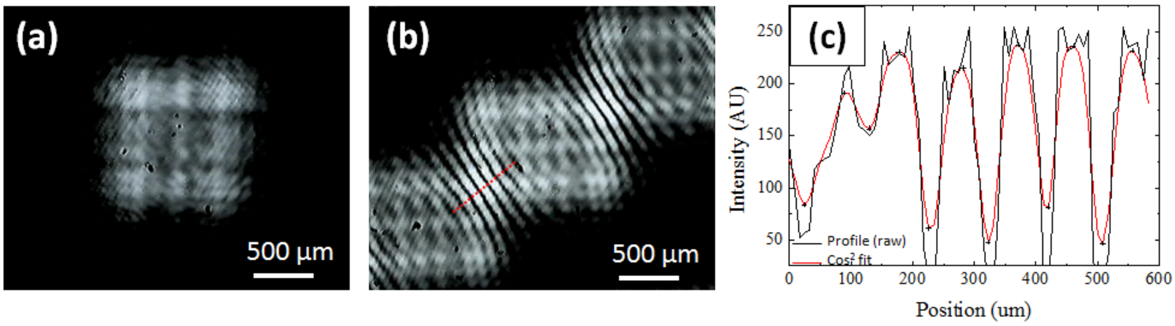

Figure 4.12: Beam profiles captured with a CCD sensor with an expanded probing beam for a sample to sensor distance of 30 cm. (a) For a sample with 1D grating pattern. (b) For a sample with a multi-micrograting pattern. (c) Slice profile of the interference fringes observed in (b).

sharp, resolvable features that can be further exploited for increased resolution in sensing applications, which would otherwise be challenging with 1D gratings.

4.4 Efficiency measurement of fabricated samples with an integrating sphere

In order to measure the total diffraction efficiency of the samples, typically a laser beam of known power is incident on the grating sample. The power for each of the diffracted orders is then measured individually and the total efficiency can be calculated as the sum of the power of the diffracted beams (excluding the reflected zeroth order beam). Such measurement is simple for 1D gratings, however, when you have multiple diffracted orders or very complex diffraction patterns, capturing all the diffracted light becomes complicated. To overcome this obstacle, samples were positioned at the output port of an integrating sphere (Labsphere, Inc), as it can be seen in Figure 4.13. Light incident from a green diode laser with 1.5 mm beam width and 7.3 mW power at a 532 nm wavelength enters the integrating sphere via the input port and is incident on the samples. Samples were placed on a tilt mount, to adjust the direction of the reflected beam and to cause it to escape the

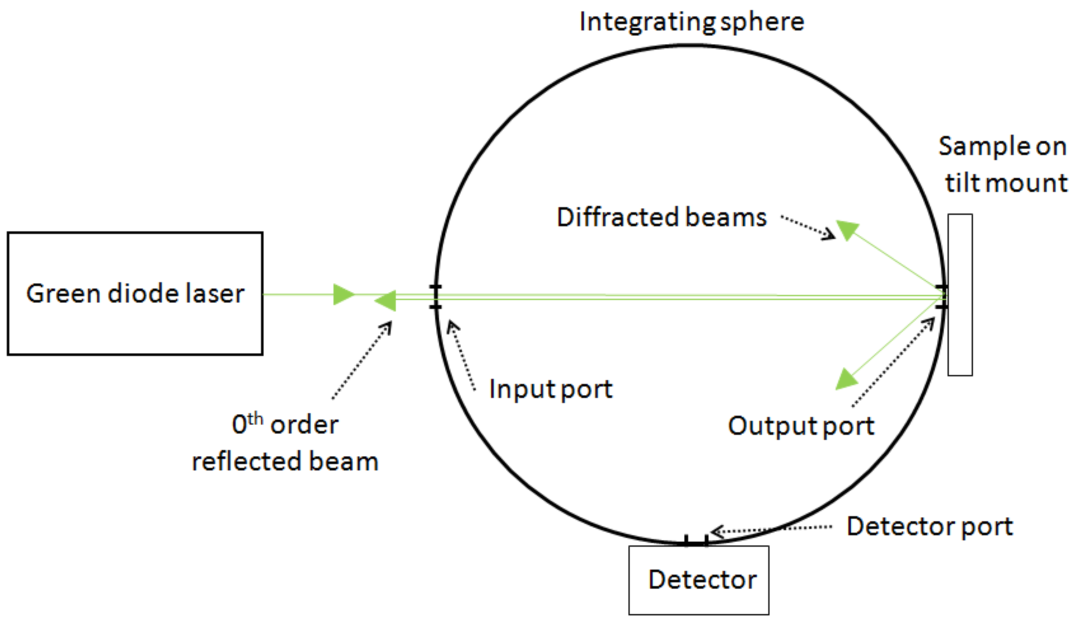

Figure 4.13: Total diffraction efficiency measurement using integrating sphere.

integrating sphere back through the input port. All the light beams that get diffracted then get captured inside the integrating sphere, and bounce off the highly reflective walls until they are collected by a detector. Total efficiency can then be calculated for any sample by finding the ratio of the total diffracted power as measured by the detector and the input laser power. The zeroth order power was measured separately to ensure all the power is accounted for.

Measurements were calibrated with three standard reflectors: a gold standard, a plain silicon wafer and a silicon wafer coated with 80 nm aluminum film. Expected reflectivities for the different materials at 532 nm were obtained with a tool called Reflectance Calculator (Filmetrics) and compared to the measured values using the integrating sphere technique. The results are summarized in Table 4.1. Measured values are found to be slightly lower than the expected reflectivities within a 5.1% error.

Table 4.2 shows the measured total diffraction efficiency for the fabricated samples, measured with the described integrating sphere technique. Diffraction efficiency was optimized for 1D grating parameters of 0.95 μm trench depth, $\lambda = 532$ nm. Therefore, the

Table 4.1: Calibration of integrating sphere measurement at $\lambda = 532$ nm

Reflector material	Expected Reflectivity (%)	Measured Reflectivity (%)
Gold	76.4	73.0
Silicon	37.4	36.3
80 nm Al on Silicon	92.2	87.0

Table 4.2: Measured Total Diffraction Efficiency of fabricated samples

Sample	**Reflected 0th order power (%)**	**Total TE diffraction efficiency (%)**
1D Grating	2.9	33.7
1D Grating w/ 80 nm Al	3.7	76.7
Micrograting	1.8	32.1
Micrograting w/ 80 nm Al	7.4	70.1
Hex. apertures w/ 80 nm Al	52.6	23.7

measured total diffraction efficiency for silicon samples with 1D grating patterns of 33.7% is comparable to the calculated 31.5% that was obtained with simulations. Efficiency values were measured to be slightly higher than the calculated efficiencies by about 2%. The addition of an 80 nm layer of Al to increase reflectivity also increased diffraction efficiency by over a factor of 2.3 to 76.7%. Samples with micrograting patterns in silicon were measured to have a total diffraction efficiency of 32.1%, which is nearly as high as the measured 1D grating diffraction efficiency. Micrograting samples with an 80 nm layer of Al show an increased efficiency by a factor of 2.2, to 70.1%. Samples with hexagon arrays only, with an 80 nm layer of Al were measured to have a 23.7% total diffraction efficiency, which corresponds to the same rate of increase as compared to a simulated 8.7%. The total diffraction efficiency of 1D gratings plays the biggest role in the multi-micrograting diffraction efficiency, rather than the total diffraction efficiency of the array of apertures. Diffraction efficiency properties can be tailored to increase it at a particular wavelength, diffraction order and angle depending on the requirements.

Chapter 5

Replication of multi-microgratings

After successful fabrication of multi-micrograting structures, a quick, high-fidelity, high-accuracy replication process was implemented for several reasons. This chapter justifies the need for a replication process, outlines a replication procedure and characterizes replicated structures.

Patterning and microtexturing of surfaces are important methods to change surface properties of materials for several applications, such as antireflective coatings, hydrophobic and hydrophilic surfaces among others. Typical processes use a variety of techniques to fabricate the structures on substrates like silicon and metals, but are typically multi-step, expensive processes that can fabricate only a few specimens at a time [63]. Nanoimprinting technologies have recently been developed that utilize previously patterned substrates to emboss soft polymers [64, 65, 66]. Polymers such as polymethyl methacrylate (PMMA) and polydimethylsiloxane (PDMS) are commonly used in the nanoimprint techniques.

The replication process can be used on the previously fabricated silicon masters to generate nearly identical polymer replicas which share very similar optical properties in terms of how diffraction patterns are formed, but in a different substrate. The silicon masters can be used many dozens of times with no degradation to the fabricated structures, making this a very inexpensive, quick and reliable method for replication. The process can produce similar, small feature sizes in a simple fashion, with no surface preparation. Since the PDMS replicas are elastomeric, it expands the possibilities of further applications that require such properties by being more responsive to external perturbations. PDMS is also transparent to visible wavelengths and can be used to fabricate transmission diffraction gratings. The PDMS embossing method was chosen because of the versatility that it allows when trying to form accurate replicas of the previously fabricated multi-microgratings.

5.1 Experimental PDMS embossing method

Silicon master samples were used to replicate their structures onto PDMS substrates. A flow chart describing the experimental procedure is outlined in Figure 5.1 and described in this section.

The PDMS polymer was obtained as Sylgard 184 Silicone Encapsulant (Dow-Corning). The polymer is a two part polymer mixture of a base agent and a hardener.

The base and hardener are poured together in a glass container at a 10:1 weight ratio. The mixture is carefully mixed with a glass or plastic rod to prevent excessive air bubble

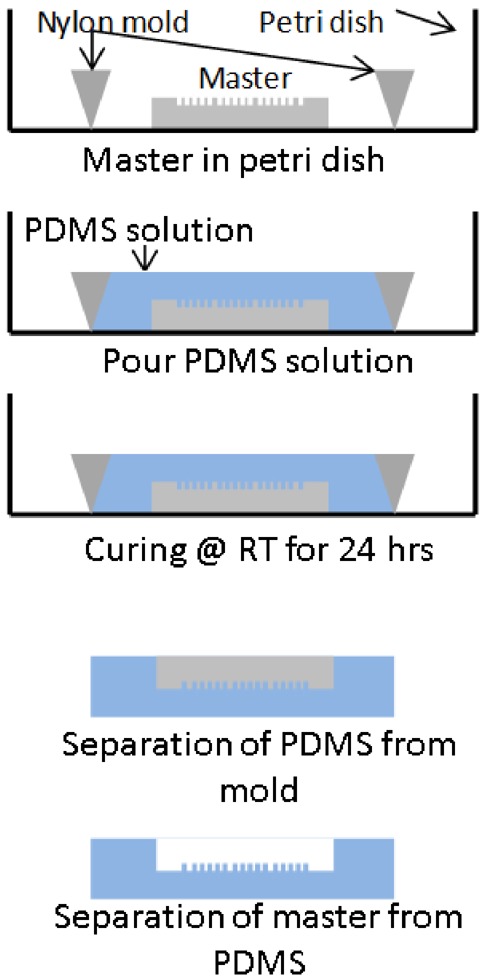

Figure 5.1: Flow chart depicting replication process using PDMS embossing method.

formation. The mixture is then placed in a vacuum desiccator for 10 minutes to remove any formed bubbles.

Silicon masters are placed on a Petri dish, face up, inside a nylon washer to serve as a mold for the replication process. The PDMS mixture is dispersed on top of the silicon master to form approximately 3 mm thick samples.

The Petri dishes are placed on a hot plate at 80-100 °C for 90 minutes to initiate the curing process. To ensure proper curing, the samples were cooled down to room temperature for an additional 3-5 hours, which helped in the separation step. Alternatively, proper curing and separation was achieved with a curing period of 24 hours at room temperature.

After the curing and cooling steps are completed, the 3 mm thick replicas are carefully peeled from the silicon masters with tweezers as to not induce cracking of the PDMS replicas and to prevent the polymer from breaking and permanently filling the gaps of the fabricated silicon masters. Afterwards, samples are inspected with an optical microscope for possible polymer residues. If necessary, samples are quickly submerged in Dynasolve 190 polymer coating remover (Dynaloy) to remove any left over PDMS.

5.2 Characterization of optical properties of replicated microgratings

5.2.1 Surface morphology

The replicated samples were examined using SEM. To prevent charging under SEM image acquisition, the PDMS replicas were coated with 12 nm of gold-palladium via a sputter coater. As it can be seen, the replicas are high quality inverse patterns of the masters. Instead of having protruding gratings and structures from the surface of the silicon, the patterns are recessed below the surface of the PDMS, thus making them more robust.

Figure 5.2 shows SEM micrographs of PDMS replicas fabricated using this method. Figure 5.2(a) shows a 1D grating sample with 0.5 μm periodicity. Due to the high aspect ratio and small feature size (950 nm depth, 250 nm width), the PDMS was found to be strongly bound to the substrate, making the separation and replication process not feasible for samples with critical dimensions smaller than 500 nm, such as multi-microgratings with 0.5 μm period. This limitation of the replication procedure can be overcome with certain surface treatment techniques, however, they were not available. However, for samples with larger critical dimensions, the replication process worked very well as it can be seen in the rest of the SEM micrographs. Figure 5.2(b) shows a replicated 1D grating sample with 2.0 μm periodicity. Figure 5.2(c) and (d) show replicated samples with hexagonal apertures of 10 and 20 μm respectively. The 10 μm hexagon aperture replica turned similar to its silicon counterpart, as the silicon master originally had defects during its fabrication process. Figure 5.2(e) and (f) show replicated multi-microgratings with 2.0 μm periods. Areas close to the center of 5.2(e) can be seen to have edges that are bending due to the elastomeric property of PDMS, but that does not seem to have a strong effect on the optical properties of the fabricated structures as it will be shown below.

To compare the fidelity of the replicated structures, Figure 5.3 shows the silicon masters and their replicas in PDMS. Figure 5.3 are SEM micrographs of (a) a fabricated 1D grating with period of 2.0 μm in silicon and (b) its replica in PDMS; (c) a fabricated array of hexagonal apertures with hexagon side dimension 20 μm in silicon and (d) its replica in PDMS; and (e) a fabricated array of microgratings with period of 2.0 μm in silicon and (f) its replica in PDMS. Depths were measured for replicated samples using the SEM technique and it was found to be 950 nm as well.

5.2.2 Diffraction patterns of replicated structures

Figure 5.4 shows the optical diffraction patterns for (a) 10 μm hexagonal apertures, (b) 20 μm hexagonal apertures and (c) multi-microgratings with 2 μm period. Their respective

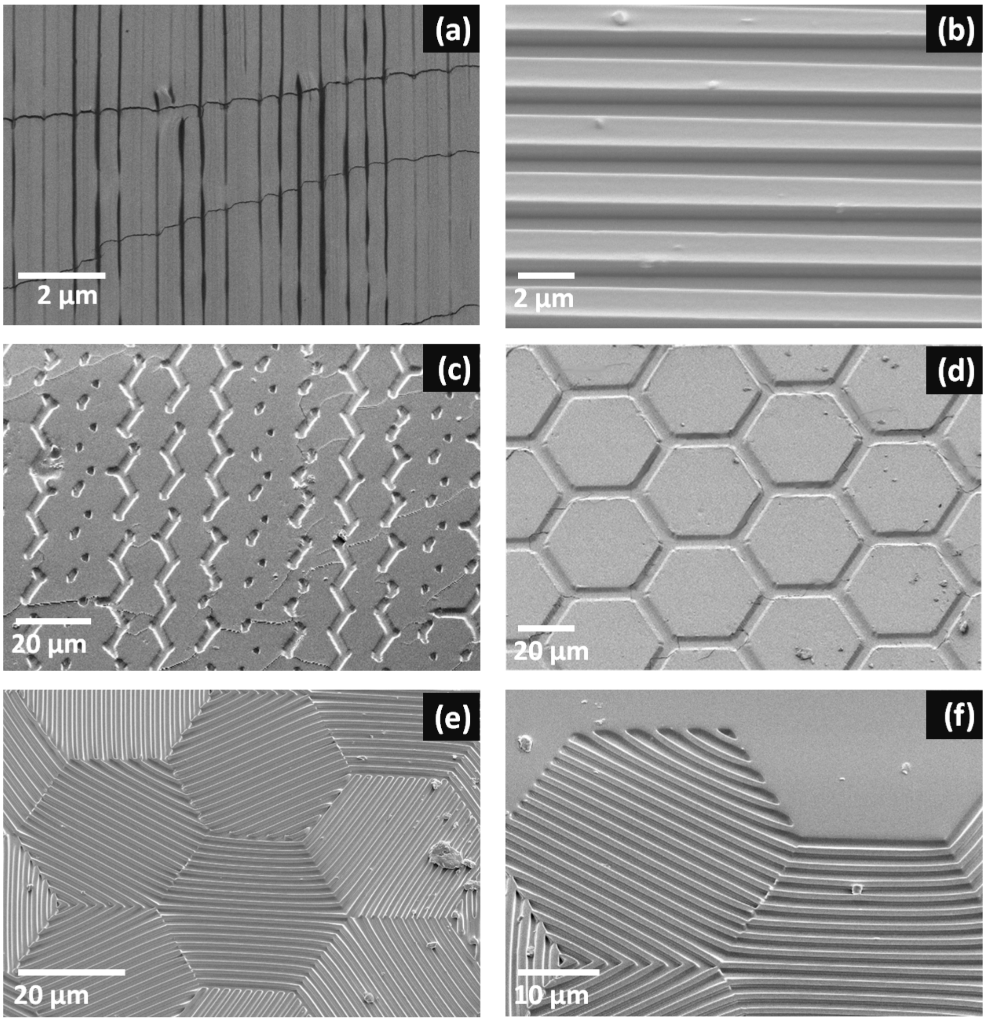

Figure 5.2: PDMS replicas of samples. 1D grating replicas with periods of (a) 0.5 μm and (b) of 2.0 μm. Hexagon aperture replicas with side dimension (c) 10 μm and (d) 20 μm. (e) and (f) Replicas of multi-micrograting samples with 2.0 μm period.

silicon master diffraction pattern counterparts are shown in (d)-(f). As expected, the replicated 3D structures look like the original masters but inverted. As per Babinet's Principle [67, 68], the diffraction patterns of an aperture plain and its complimentary (inverted) plane are the same. As it can be seen in Figure 5.4, which shows the diffraction patterns obtained from PDMS replicas and Si masters, the diffraction patterns are very similar. In the case for replicas with the 10 μm sides, the pattern seems to lack the vertical line that would be originated from the horizontal edges from the hexagonal apertures/ The vertical line can be seen to be missing from the SEM from PDMS replicas shown in

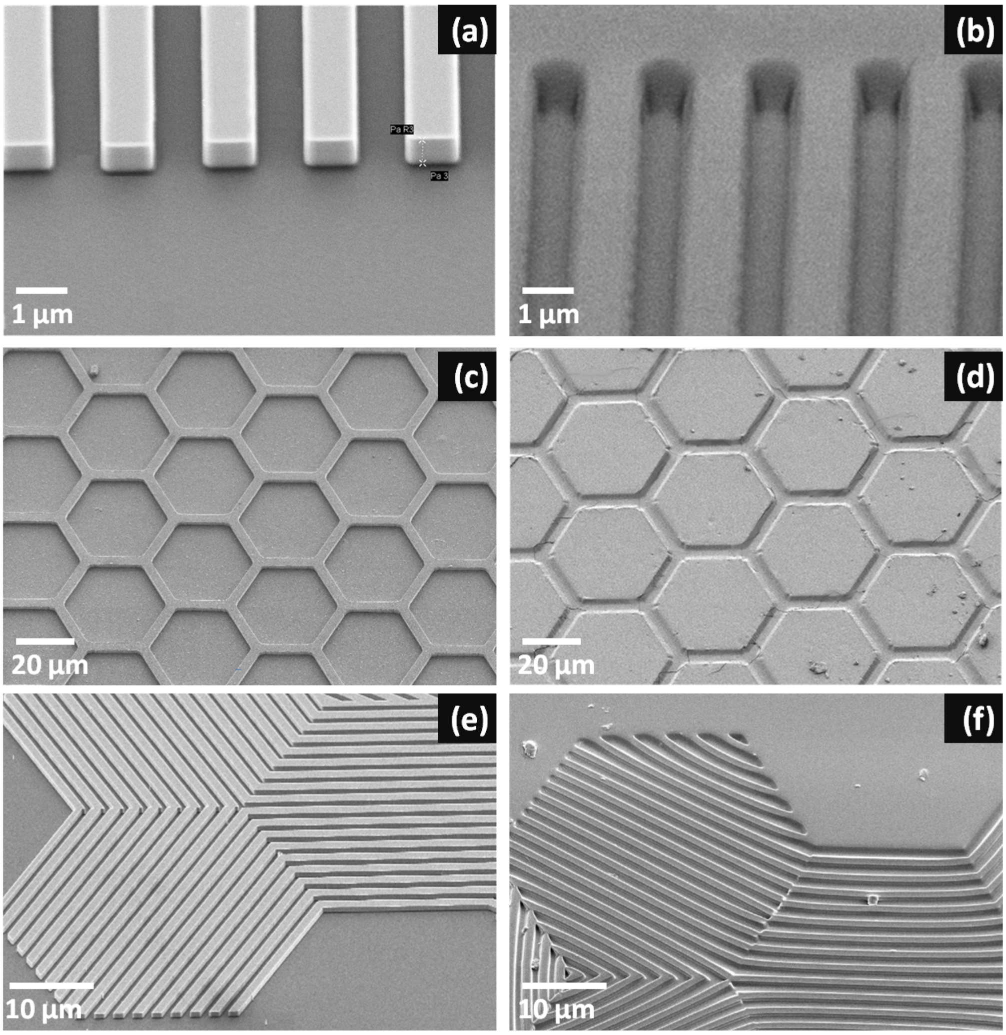

Figure 5.3: Silicon masters and their PDMS replicas. (a) 1D grating with period of 2.0 μm in silicon and (b) its replica in PDMS. (c) Array of hexagonal apertures with hexagon side dimension 20 μm in silicon and (d) its replica in PDMS. (e) Array of micrograting with period of 2.0 μm in silicon and (f) its replica in PDMS.

Figure 5.2. The zeroth order, transmitted beam does not seem to have such high intensity as that found in Si masters, so it was not necessary to let that go through a hole in the screen where the diffraction patterns were projected.

5.2.3 Total TE Diffraction Efficiency

Using the integrating sphere method in transmission mode, the diffraction efficiencies for samples with 1D gratings and multi-microgratings with 2 μm periods were determined.

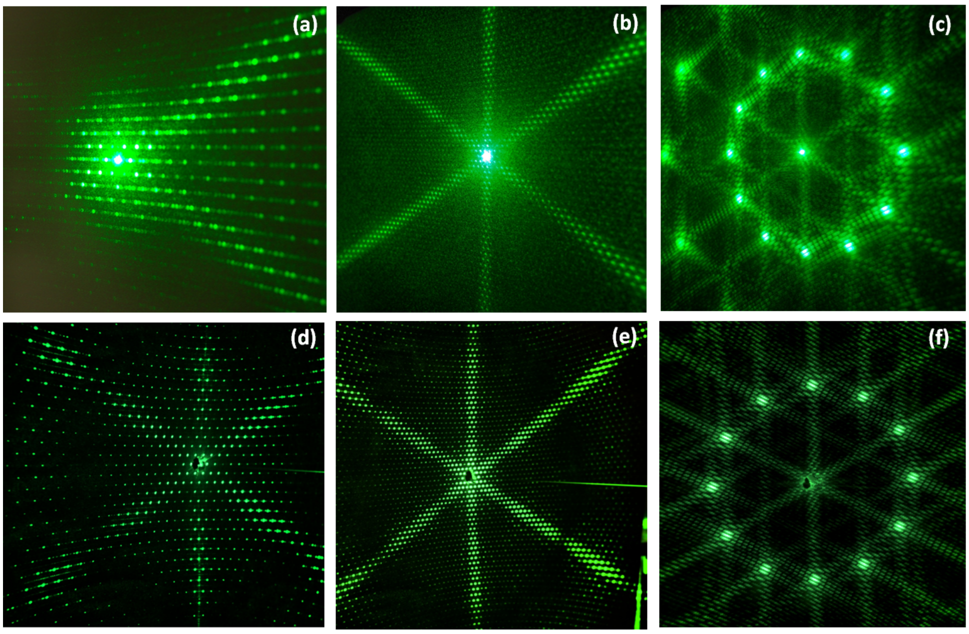

Figure 5.4: Diffraction patterns produced from PDMS replicas with patterns (a) 10 μm hexagonal apertures, (b) 20 μm hexagonal apertures and (c) multi-microgratings with 2 μm period. Diffraction patterns of Si masters for (d) 10 μm hexagonal apertures, (e) 20 μm hexagonal apertures and (f) multi-microgratings with 2 μm period.

Samples were placed at the entrance port of the integrating sphere, allowing reflected and backscattered light to leave the integrating sphere. The zeroth order transmitted beam and diffracted beams were allowed to be collected by the integrating sphere. Then the zeroth order power was measured independently and subtracted from the integrated measurement to obtain total TE diffraction efficiency for the PDMS replicas.

Total TE diffraction efficiency was calculated for PDMS (n = 1.41) for 532 nm wavelength light and at normal incidence, and was calculated to be 92.1%. The zeroth order beam intensity was expected to have 4.9% of the total intensity of the incident beam. Zeroth order beams were measured to be 5.6% and 7.8% for 1D grating and multi-micrograting replicas, respectively. The zeroth order beams were subtracted from the integrating sphere measurement and a total TE diffraction efficiency of 90.3% and 88.4% for 1D grating and multi-micrograting replicas were calculated respectively. Both values were slightly lower than the expected diffraction efficiency and it can be attributed to measurement error. Also, transmitted zeroth order beams were found to be slightly higher than expected, suggesting that some efficiency could have been lost in the replcation process due to areas not being completely separated as well as possibly from stretching of certain high density features in the multi-micrograting case. The measured diffraction efficiencies in PDMS were higher than for Si samples because of material properties and because of limited reflection losses.

A novel PDMS embossing method was adapted to replicate the fabricated structures, which created high fidelity replicas for patterns that had higher critical dimensions. For samples with high aspect ratios or very small dimensions (sub micron), surface treatments may be necessary to facilitate PDMS/master separation. Imprinting the patterns onto a flexible, optically transparent substrate such as PDMS opens up the possibility for further applications.

Chapter 6

Feasibility study of applications of multi-microgratings

It was shown earlier that multi-microgratings have complex diffraction patterns that arise from the interaction of the multiple periodic elements that are present in the multi-micrograting design. These diffraction patterns are formed by the combination of the effects of periodic grating lines, single and multiple apertures as well as the arrangement of those apertures containing grating lines. Hence, the diffraction patterns contain information regarding the interaction between the individual elements that form the multi-microgratings. These cross-term interactions between the different periodicities opens the opportunity for novel sensor applications.

In 1D gratings, the intensity is distributed between the 0th order and a few higher order diffracted beams, which occur at very localized and discrete angular positions. In the case of multi-microgratings, a significant portion of the intensity is also distributed into multiple higher order diffracted beams, into the diffraction due to apertures and into the periodic nature of the apertures.

Thus, by monitoring the position and intensity of the diffracted beams, the overall diffraction pattern characteristics and intensity distribution from multi-microgratings can be shown to be more sensitive to changes. Furthermore, as it was shown earlier, multi-micrograting beams tend to be slightly narrower than their 1D grating counterparts. Also, depending on the sensing configuration, they also interfere with each other at the sensor plane, producing highly defined interference patterns.

Overall, the purpose of this chapter is to describe a feasibility study of possible applications of multi-microgratings which exploit the differences between 1D gratings and multi-microgratings. Some phenomena presented earlier are revisited in order to use the acquired knowledge to provide an explanation, such as the examples of multi-microgratings in literature, color generation over wide angles. Also, a method that utilizes the complex multi-micrograting diffraction pattern and their interference is described in the framework of temperature sensing, which can also be further extended for other sensor applications such as strain/stress sensing, vapor concentration detection and nanometrology, etc.

6.1 Application of multi-micrograting theory

6.1.1 Color generation over wide angles

An interesting problem to revisit is the idea that multi-microgratings can be used to generate blue color over a wide range of angles, as it was theoretically implied in [8], such as in Morpho butterfly wing scales. The wing scales are made up of periodic structures that when interacting with white light, produce blue iridescent colors that arise from the combination of diffraction and multi-layer interference from the periodic structures that form them. The diffractive structures found within those scales demonstrated to have a periodicity in the range between 400-500 nm. Assuming a periodicity of 440 nm, only light with wavelength lower than 440 nm will be allowed to diffract at normal incidence. This means that there would be a ± 1 order for wavelengths below 440 nm. If the wavelength is longer than 450 nm, then there would be no diffracted beams at normal incidence. As the incident angle increases, however, longer wavelengths are allowed to diffract as well.

The same thinking can be applied to multi-microgratings with 440 nm period, where the micrograting period produces the diffractive effects and the interfering multi-micrograting beams produce the interference effects. To help visualize this concept, an FDTD simulation was carried out using similar parameters as above (440 nm period multi-microgratings illuminated with 450 nm wavelength light) at different incident angles. Figure 6.1(a)

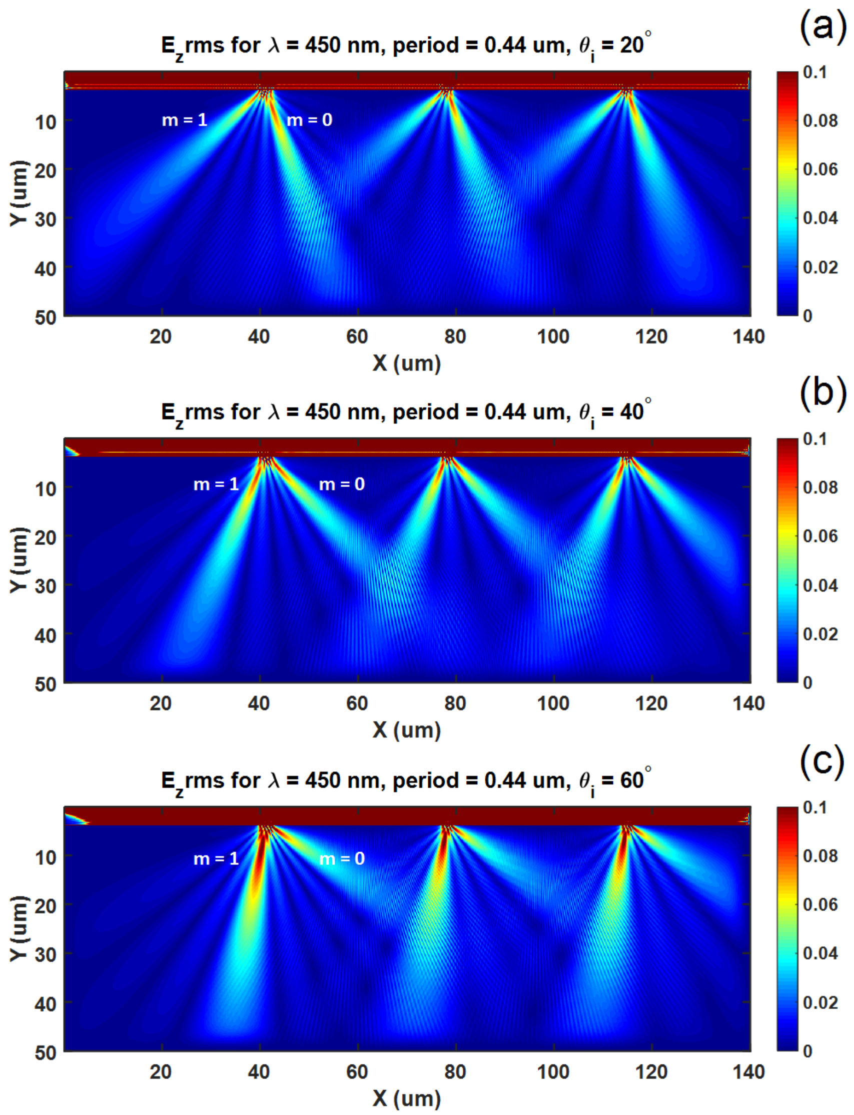

Figure 6.1: Demonstration of color generation over wide angles: FDTD simulation of multi-microgratings (440 nm grating period, 34 μm micrograting separation) interacting with 450 nm wavelength light (a) $\theta_i = 20°$, (b) $\theta_i = 40°$ and (c) (b) $\theta_i = 60°$.

through (c) show multi-micrograting response at 20, 40 and 60° respectively. If incident with white light, at normal incidence (not shown), only wavelengths of 440 nm or below will produce diffraction.

The diffracted orders are labeled for guidance. As θ_i increases, both orders are seen to rotate to the right. At lower angles, the dominant light is produced by the zeroth order beam, while at higher angles, the light diffracted into the first order is dominant.

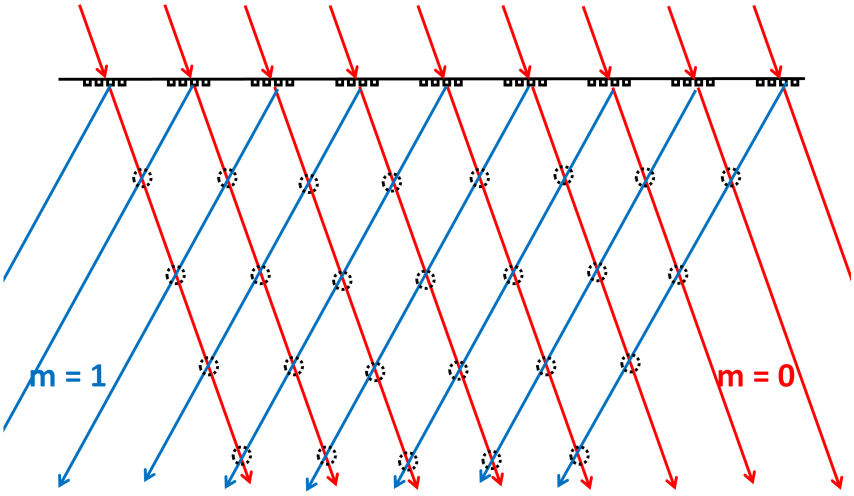

Figure 6.2: Schematic diagram that illustrates multiple interference locations of first order diffracted beams and zeroth order beams .

Furthermore, as it can be readily observed in Figure 6.1(b) interference fringes are being formed by the interaction of the zeroth order of one micrograting and the first order another one. It can be shown that with an arbitrarily long patterned sample, the diffracted beam from one micrograting would interfere with the zeroth order of several other microgratings. A schematic diagram of this concept is shown in Figure 6.2. The paths for the zeroth order and first diffracted order are shown and their intersections are marked to illustrate the regions where the beams would interfere.

To show that blue color is primarily generated, FDTD simulations were carried out for multi-microgratings of 440 nm period, at a 30° incident angle as shown in Figure 6.3(a)-(c) for wavelengths of 400 nm, 500 nm and 600 nm, respectively. The angles at which the m = 1 diffracted orders occur are seen to be increasing. The intensity of the m = 1 diffracted beams seem to be decreasing as wavelength increases. This example shows, qualitatively, that the blue wavelengths would be more dominant if the devices were illuminated with white light, thus producing brighter blue colors.

Additionally, the effects of wavelength on the diffraction efficiency were studied by numerically computing the efficiencies for 440 nm period gratings using GSolver (which uses the RCWA method) as it is shown in Figure 6.3(d). Silicon gratings were modeled with

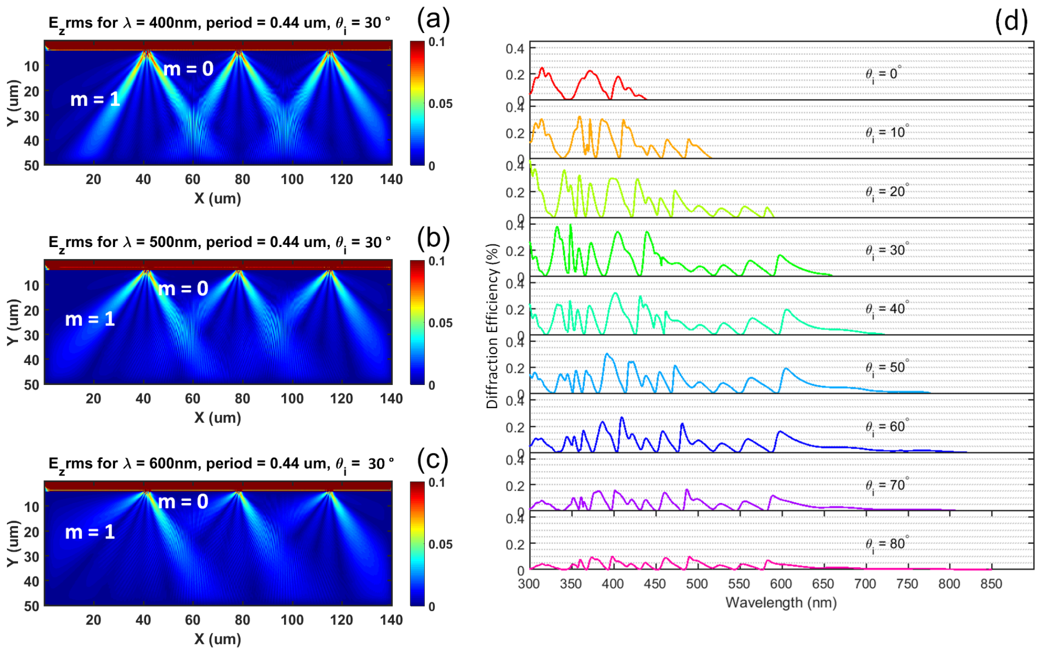

Figure 6.3: Simulated diffracted beams to understand the effects of wavelength on 440 nm period multi-microgratings for incident angle of 30° and for wavelengths of (a) 400 nm, (b) 500 nm and (c) 600 nm. (d) Calculated first order diffraction efficiency for multi-microgratings of 440 nm period at different angles of incidence.

square facets and 200 nm deep trenches and the incident angle was varied. It is possible to see that as the incident angle increases from 0° to 80°, longer and longer wavelengths are allowed to diffract. However, the highest efficiencies were achieved at shorter wavelengths between 300 and 500 nm. At higher angles of incidence, light with wavelengths between 500 nm and 700 nm is allowed to diffract, but their diffraction efficiencies are much lower than those in the blue wavelengths.

A special note regarding diffracted beam divergence must be discussed. In the case of multi-microgratings, each micrograting cell acts as an aperture. When diffracting through an aperture, a plane wave will have a divergence half angle that can be calculated from the first minimum of the single slit envelope function, which can be derived from Equation 1.6. By finding the solutions where the intensity drops to zero, it is possible to calculate the divergence half angle for a plane wave that encounters an aperture of size D [69]. This divergence is given by Equation 6.1:

$$sin\theta \approx \theta \approx \frac{\lambda}{D} \tag{6.1}$$

It can be seen as D decreases, then the minima angular location increases. That is to say, when incident on smaller apertures, the divergence would be larger. The diverging nature of the diffracted beams has some consequences. In the far field, the diffracted beams from multi-microgratings will spread out enough so that they will overlap, producing a uniform blue color. For example, when a multi-micrograting with 440 nm period, 10 μm hexagon side and 34 μm micrograting cell separation interacts with light of 450 nm wavelength incident at 30 degrees, the divergence half angle can be calculated to be 4.5 mrad. This means that a distance of 10 cm, the beam would have a diameter of 9 mm. Referring back to the schematic diagram in Figure 6.2, it is possible to see that the diffracted beams from a micrograting travel parallel to the diffracted beam of other microgratings. Thus, in the far field, the separation between those beams would be the same separation as the micrograting separation. For this example that would mean that the diffracted beams from adjacent microgratings would be 34 μm apart from each other, and thus can be clearly shown to be interacting with one another at a diameter of 9 mm. This results in a uniform distribution of color. With 1D gratings, this would not occur as the divergence would be much smaller, and there would only be one diffracted beam, rather than several from different micrograting cells. Furthermore, the diverging nature of the diffracted multi-micrograting beams means that as white light is incident on them, the zeroth order light will diffuse in the far field, while due to the short period of the multi-microgratings, would only allow blue colors to be diffracted. The resulting effect is that the white light gets diffused, leaving behind the diffracted blue light, thus accentuating the blue color.

6.1.2 Multi-microgratings in literature

Three particular cases in the literature presented in Chapter 1 refer to having used some form of multi-microgratings. The knowledge that has been acquired for multi-micrograting theory in this study was applied to those examples.

The first one was an array of circular zonal plates, with different grating periods inside each circular cell and oriented at different angles using 4x4 cells [28]. An image of the device was used to simulate the diffracted pattern using a Graphical Fourier Transform approach. The device can be seen in Figure 6.4(a) and the simulated diffraction pattern in Figure 6.4(b). Because each of the cells had a different period and different angles, the diffracted spots are unique for each grating. There are no contributions from different micrograting cells into the total pattern. There are several orders, each consisting of 4x4 matrices of diffracted spots. The first order beam in the simulated pattern is the really bright area located near the center of the pattern. The second order is easier to distinguish as the spots are not so close together. The circular diffracted spots take the shape of the circular cell from which they originate. The study had issues differentiating between certain orders of diffracted beams and it is possible to see why there was crosstalk between different diffracted beams. Also, since there is empty space between cells as they cannot be packed efficiently in this manner, it is possible to see a lot of scattered light around the diffracted orders. For reference, the actual diffraction pattern observed by the study can be seen in Figure 1.9.

The second example was found in [29] where circular microgratings of different periods were arranged in different patterns to be used as color pixels for 3D displays. Figure 6.4(c) shows an SEM micrograph from one of the devices in the study. It's image was used to simulate its diffraction pattern using the Graphical Fourier Transform method and the results are shown in Figure 6.4(d). The circular microgratings had several periods, which is why the diffracted orders are manifested in a similar grid. A considerable amount of

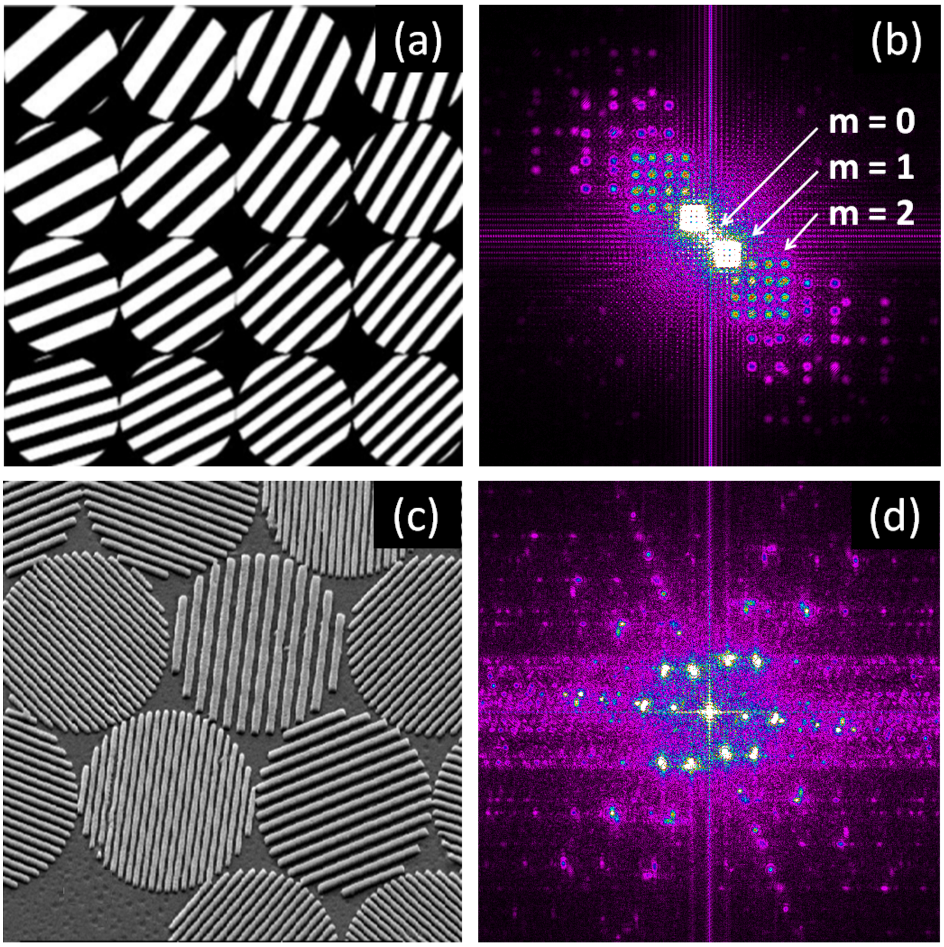

Figure 6.4: (a) Circular micrograting cells in a square 4x4 grid for zonal wavefront sensing seen in [28] and (b) its simulated diffraction pattern using the Graphical Fourier Transform method. (c) Circular microgratings of different periodicities arranged in a triangular grid used for a backlight illuminator found in [29] and (d) its simulated diffraction pattern using the Graphical Fourier Transform method.

scattered light can be seen and that arises from the poor quality of the image used and due to the space that exists between the circular microgratings. One more thing to note, this simulation method cannot differentiate between aperture sizes being larger or smaller than the wavelength. In the case of the reported study, the periods used were subwavelength, therefore the effects of the diffracted beams at normal incidence would be non existent. Only the center area would see the effects of the periodicities larger than the wavelength, in this case, the separation between different apertures, and this is manifested by the grid-like pattern observed in the simulations carried by the study using the the FDTD

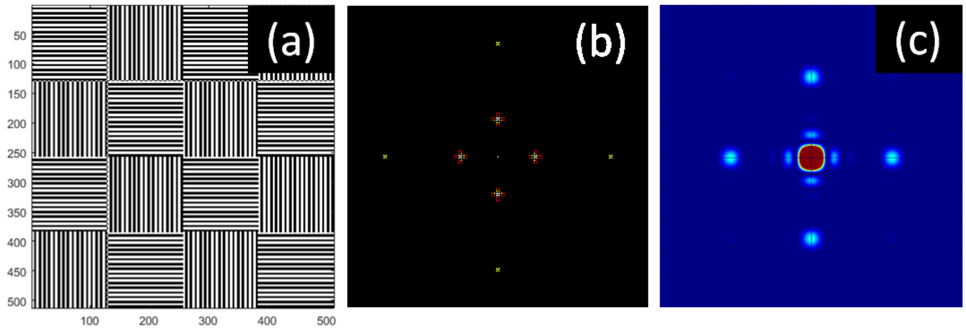

Figure 6.5: (a) Array of square multi-microgratings used in [27]. (b) A simulated diffraction pattern using Graphical Fourier Transform method. (c) The exact solution using intensity distribution functions.

technique, seen in Figure 1.10.

The third one was an array of square microgratings of different orientations, stitched together to form a large area pattern [27] used for a grating based polarizer. First, a Graphical Fourier Transform simulation is carried out using the pattern seen in Figure 6.5(a) and the result is shown in Figure 6.5(b). It is possible to see that the light is being distributed to a zeroth order beam, as well as first order beams in the vertical and horizontal directions. Due to the cells being arranged in a square array, the diffracted orders separate into smaller beams, also arranged in a square grid. Because of the simplicity in this design, the exact solution can be found in 2D using Equation 2.5, and it is used to simulate the diffraction pattern and plotted in Figure 6.5(c). It is much easier to see the first order beams that appear in the vertical and horizontal directions. For comparison, Figure 1.8 shows the captured diffraction pattern by that study.

The device was used as a selective polarizer by allowing most light to be distributed to the zeroth order beam or to the first order beams by means of controlling the etching depth. An optimal depth was found to offer highest diffraction efficiency in one polarization and lowest in the perpendicular polarization. Then by controlling the incident beam polarization it was possible for the team to control the distribution of diffracted light, which is an interesting application of multi-microgratings for polarization selection.

6.1.3 Applications in beam splitting

As it was just presented, a possible application for multi-microgratings is in beam splitting, for example for interconnects. If a particular arrangement is desired, it is possible to use the theory that was discussed in this study. If a 4 beam arrangement is required, square microgratings in a square grid can be used to separate the light into strong diffracted beams, using a similar arrangement as that observed in Figure 6.5. An important consideration in this case is the size of the incident beam. While it would be possible to use just 2 micrograting cells in a 2x1 grid or 4 micrograting cells in a 4x4 grid, those cells would have to be relatively large (approximately the size of the diameter of the incident beam divided by 2 or 4), very careful alignment would be critical so as to evenly control the power being distributed to each of the 4 beams. If the incident beam is not exactly centered, then different amounts of power would be distributed to the different orders. To mitigate that effect, instead of using just 4 mirograting cells, by adding more cells, the device would act as if it had multiple more periodic apertures and since the cell size is large, then the diffracted spots generated by the aperture would be close enough to the expected location and thus coupled in a more evenly distributed intensity.

Similarly, if a 3-beam arrangement was required, it would be best to use an array of large triangular microgratings arranged in a triangular grid with 3 different periods, parallel to one of the three sides of the triangle. Since 3 is an odd number. However, 3 micrograting orientations would produce 6 diffracted spots. A unit cell that could be used is shown in Figure 6.6(a), with the different colored numbers used to differentiate the three different periods. The unit cell was used to form a large area pattern such as the one shown in Figure 6.6(b). The predicted diffracted pattern, showing the six diffracted spots is shown in Figure 6.6(c). One possible solution to obtain 3 diffracted spots would be to use a subwavelength period for the micrograting, and set the incident angle so that only one of the diffracted orders is visible.

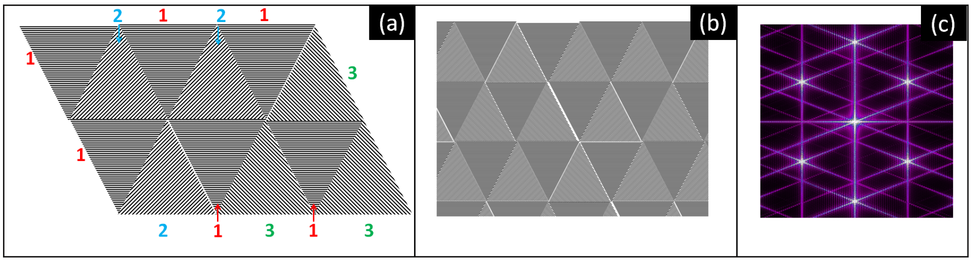

Figure 6.6: Triangular array of microgratings. (a) Possible unit cell showing three different orientations. (b) Large area pattern formed by repeating the unit cell. (c) Predicted diffraction pattern showing six visible orders.

6.2 Temperature sensing with multi-microgratings

There are several temperature measurement techniques. The most common ones are direct contact measurements such as those with thermocouples, which require physical contact between the probe and the material being measured. Physical contact is not always feasible in certain processing configurations and thermocouples are highly susceptible to contamination. Conventional, optical noncontact measurement techniques such as pyrometers, which measure blackbody radiation from a surface are relatively inaccurate, as they are highly dependent on surface and material properties (i.e. emissivity, roughness) and offer poor spatial resolution [70].

Newer methods for temperature sensing, such as microbolometers, thermal bimorphs, thermal buckling based sensor arrays, Fabry-Perot structures and cantilevers have poor spatial resolution and poor broadband operation [5]. Some novel designs such as thermally actuated interferometric sensors have been reported based on device fabricated with PDMS [71], long period grating fiber sensors with high temperature sensitivity [72, 73] and designs with photonic crystals [74, 75] and plasmonic nanostructures [76]. These novel designs are complicated to fabricate and may not be suitable for a simple, quick temperature measurement.

6.2.1 Temperature sensors based on thermal expansion of 1D gratings

One dimensional gratings have been proposed as method for temperature measurements, using diffracted beam angular measurement changes due to thermal expansion of the grating substrates, like PDMS, silicon carbide, silicon and gallium arsenide [77, 78, 79]. Results are promising, but they lack a high spatial resolution and sensitivity.

Low-cost, simple methods such as those described in [71, 78] based on thermal expansion of diffraction gratings offer a fast method to measure temperature. The angular deflection of diffracted beams was monitored due to increases in temperature in Si-C ($\alpha = 6.5\cdot 10^{-6}$ °C^{-1}) and PDMS ($\alpha = 277\cdot 10^{-6}$ °C^{-1}) and reported sensor configurations capable of resolving $\Delta T = 5$°C and 0.01°C, respective, have been reported. While α plays a big role in the sensitivity of the system, for a Si ($\alpha = 2.6\cdot 10^{-6}$ °C^{-1}) [80] based sensor, sensitivity in the order of a few °C can be expected.

To obtain better sensitivity (0.3-0.6°C), more complicated configurations can be used, such as those described in [70, 77]. Two independent probing beams at different incident angles are incident on Si substrates with diffraction gratings, so that their diffracted beams travel parallel to each other to a sensor. The difference in centroid position of the individual beams is monitored and used to measure changes in temperature and rotation. While this configuration offers a higher sensitivity, it has a complicated optical configuration that is very sensitive to alignment.

Interferometric measurement methods using expansion of gratings can obtain further improvements in sensitivity, which also require complicated setups with critical alignment, cost and operation [81, 82, 83, 84]. It follows that using interferometric measurements would then improve the sensitivity of optical temperature measurement using thermal expansion of gratings.

6.2.2 Temperature sensing with multi-microgratings

As the temperature of a solid is changed its physical dimensions are also affected. The coefficient of thermal expansion (CTE), α, is a characteristic of each material and it is a measure of the magnitude of the thermally induced change in dimensions [85]. This coefficient is also dependent on temperature itself. The change of dimensions in an object, ΔL, is given by Equation 6.2. The equation states that the change in length of an object ΔL is proportional to the change in temperature ΔT, where L is the initial length and the proportionality constant α is the coefficient of thermal expansion.

$$\Delta L = \alpha * L * \Delta T \tag{6.2}$$

When surface relief gratings are present on a substrate, thermal expansion of the substrate can induce changes in the periodicity of the gratings. A change in this periodicity will result in a change in the diffracted angles, and thus, this technique can be used to measure changes in temperature. The change in the periodicity (Δd) of a grating with period d is given in Equation 6.3.

$$\Delta d = \alpha * d * \Delta T \tag{6.3}$$

A change in temperature of the substrate will induce a change in the periodicity of the micro-multigratings, and it will be dependent on the material itself (by means of the coefficient of thermal expansion) and the change in temperature. If the grating periodicity is changed, then it follows that the diffraction angle will also have to change. The accuracy at which that angular deflection can be measured determines the measurable resolution of the temperature change.

The mechanism showing the thermally induced changes in the diffracted angles is shown in Figure 6.7. If temperature increases from T to T', this will cause a linear expansion in

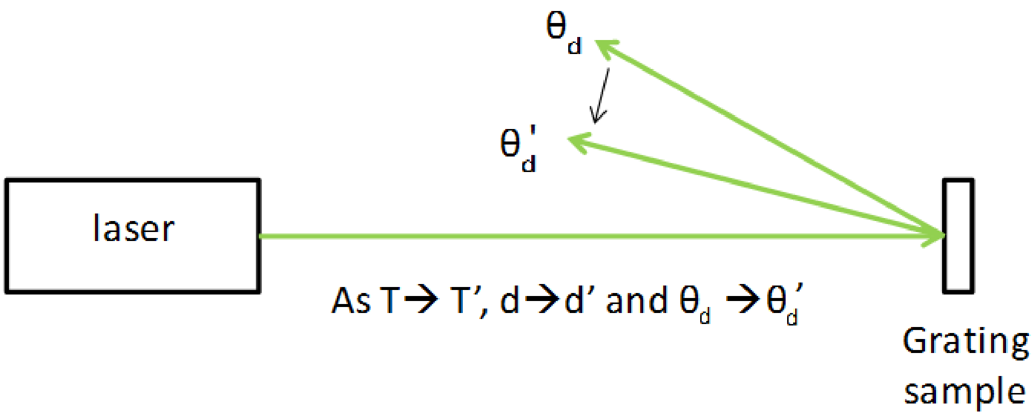

Figure 6.7: Visualization of changes in diffracted angle caused by thermally induced periodiciy changes that affect the diffracted angle.

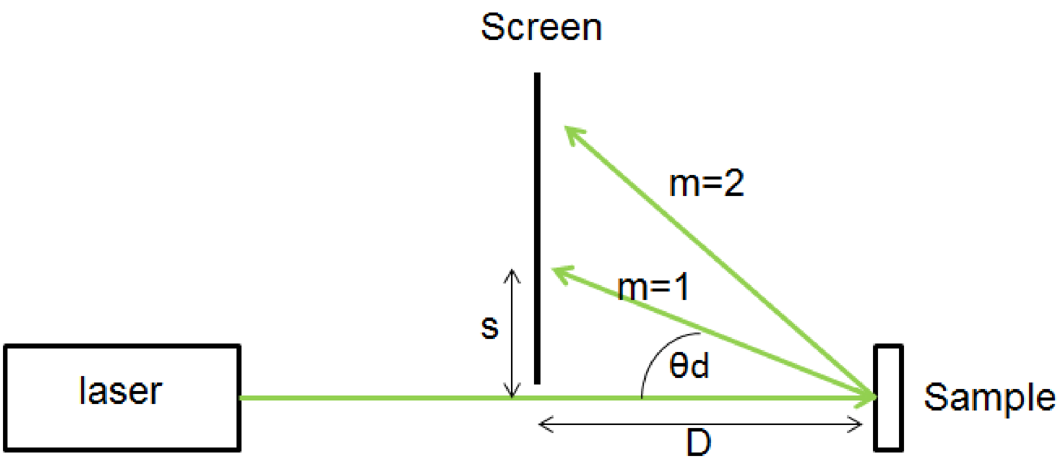

Figure 6.8: Schematic of screen projection of diffraction patterns.

the grating periodicity from d to d'. In other words, as ΔT increases, Δd will also have to increase. An increase in the grating periodicity will mean that the diffracted beams will shift towards the 0th order. Since the thermally induced changes in the grating periodicity will be relatively small, accurate measurement of the position of diffracted beams becomes very important.

In order to measure the changes in the diffracted angles, $\Delta\theta$, a screen can be placed at a distance D from the grating sample as seen in the schematic diagram in Figure 6.8.

The diffracted orders will be projected onto the screen, and the distance between the zeroth order beam and the first diffracted spot will be given by s. The relationship between the diffracted angle θ_d, the distance to the screen D and the separation between the 0th order and the diffracted order can be described by $tan(\theta_d) = s/D$. As the distance to the screen D is moved further away, the separation of the diffracted order and the 0th order on the screen, s, will also increase. Thus, the measurements will be more accurate as D increases.

The change in displacement Δs can be measured, and an accurate way of measuring that change is by monitoring the displacement using a CCD camera. The resolution of the system is going to depend on the resolution of the optics and the ability of the system to resolve measurements of displacement. Arbitrarily long sample to sensor D distances can be used to measure a small change in the diffracted angle. Angular shift, $\Delta\theta_d$, is however fixed. It is good practice to normalize the measurement with respect to sample distance. Angular shift is also proportional to the change in temperature and the reference angular position, so for a given change in temperature, a larger θ_d is preferable, which can be achieved by using higher order diffracted beams or large angle of incidence θ_i of the probing beam.

As an example, a simulated change in dimensions Δd is introduced to the diffracted patterns of multi-microgratings as seen in Figure 6.9. The unaltered, $\Delta d = 0\%$ pattern is shown in Figure 6.9(a)-(f), where (a) is the contribution of the periodic aperture and (b) its line profile; (c) is the contribution of the aperture shape and (d) its line profile; (e) is the combined effect of the prior patterns to form the multi-micrograting pattern and (f) is its line profile. A simulated change of $\Delta d = 10\%$ is introduced, and the altered diffraction patterns are shown on the right side of Figure 6.9. Figure 6.9(g)-(l) correspond to similar patterns to those found in (a)-(f) but with the added $\Delta d = 10\%$. As Δd is increased, the individual lattice spots seen in Figure 6.9(b) shift slightly to the left as it can be seen in Figure 6.9(h) due to the increased distance between neighboring apertures. Additionally, the added Δd causes the aperture to also change in dimensions, and the cross term showing

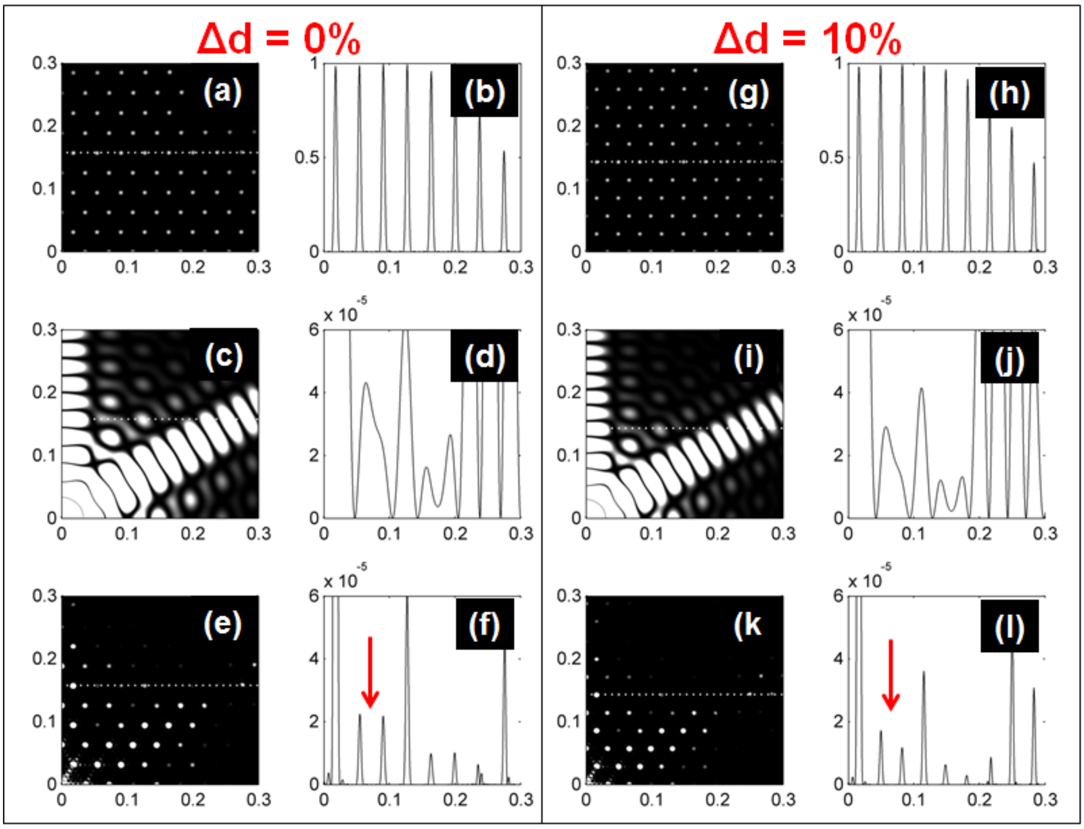

Figure 6.9: Simulated diffraction pattern for an unaltered $\Delta d = 0\%$ pattern (left) and altered $\Delta d = 10\%$ (right) pattern. (a) The lattice of spots formed by diffraction pattern of periodic apertures and (b) Its line profile. (c) The aperture shape diffraction pattern and (d) Its line profile. (e) The convolution of (a) and (b), which is the resulting multi-micrograting pattern and (f) Its line profile. (g) through (l) show similar patterns and line profiles for the altered pattern with $\Delta d = 10\%$. Red arrows are added for clarity.

interaction (marked with the red arrow in Figure 6.9(f) and (l)), are also affected by the change in dimensions. They interact differently with the lattice of spots formed by the periodic apertures. The net result is a change in not only the maximum position of the diffracted spots but also their intensity. While the simulated 10% change in dimensions is rather drastic, the principle still holds. Such an effect that arises from the cross term interactions in multi-microgratings can potentially be used to monitor dimensional changes in the diffraction pattern.

Peak to peak ratios can be used to monitor changes in intensity. Figure 6.10(a) corresponds to a simulated diffraction profile where the first four peaks along a fixed θ_y

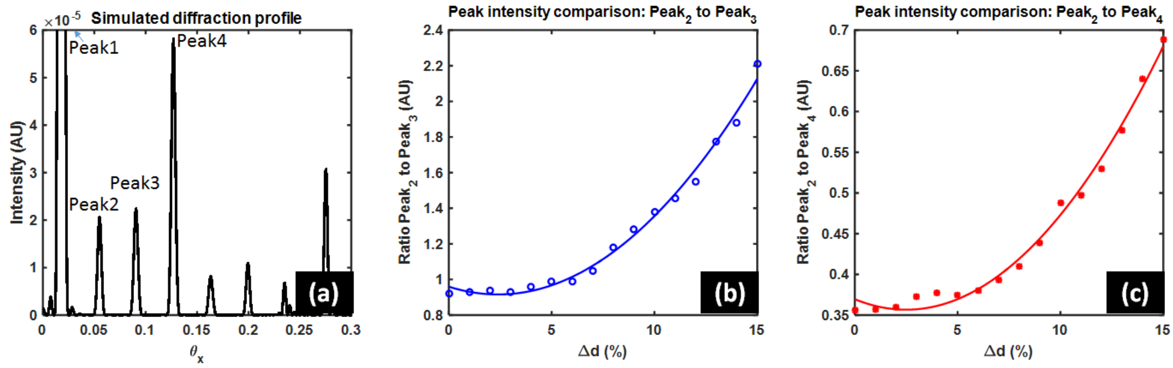

Figure 6.10: (a) Profile of a simulated diffraction pattern showing Peak 1 through Peak 4. (b) Ratio of Peak 2 to Peak 3. (c) Ratio of Peak 2 to Peak 4.

have been labeled Peaks 1 through 4. A simulation was coded to monitor the peak to peak ratios. Figure 6.10(b) shows the peak intensity comparison between Peak 2 and Peak 3 and Figure 6.10(c) shows the peak intensity comparison between Peak 2 and Peak 4. Both ratios were fitted to second order polynomials. It can be seen that they follow a similar trend, albeit the Peak 2/Peak 3 ratio changes more dramatically as Δd increases. The interaction between the lattice spots and the hexagonal aperture can be seen to cause intensity variations that can be used for different applications.

Use of multi-micogratings allows measurement of several parameters. If multi-micogratings are present on the surface of a substrate, the absolute temperature of a substrate can be determined if the CTE of the substrate and the periodicity of the multi-micograting are known. Changes in the angular position of the diffracted orders can then be used to determine changes in the periodicity, which in turn can be used to determine the overall change in temperature of the substrate. This can be realized with gratings of single orientations, but there are advantages to having multi-micogratings of multiple orientations. By monitoring the diffracted angles, in the case of multi-micogratings, it is possible to determine the spatial variation of temperature.

The size of the probing beam has a large impact on the measurement of this method. If the probing beam is large in diameter but smaller than the overall size of the multi-micrograting pattern, the diffraction pattern will be the result of the contribution of all the multi-micogratings. However, a smaller beam can probe the area covered by the repeating unit of six hexagons. This pattern provides local information on the scale of the repeating cell. If the probing beam is even smaller in diameter, it can be focused to only be incident on a single hexagon, thus being able to determine the temperature of that particular area. The spatial resolution of this method will be in part dependent on the individual size of the hexagonal gratings. For probing beams that are larger than the muti-micrograting pattern itself, and at the right sample to detector position, interference effects were observed which create sharp, highly defined features.

An important characteristic of a sensor is its efficacy at resolving adjacent measurement points, i.e. the resolution of the system. It is dependent on several factors such as the sensor resolution, the range of measurement but most importantly the signal to noise ratio (SNR). The SNR is tied to the contrast of the measurement (or fringe visibility) [86, 87], and it is defined as the ratio of the signal value compared to the average noise of the sensor. Features with high contrast can be more easily resolved, where contrast C is defined as the interferometric visibility of the system as seen in Equation 6.4. One way to improve SNR is to have a high contrast in the measurement as to compared to the noise level, but what ultimately determines the resolution of a system is going to be the spatial dimensions of the high contrast features. Assume two Gaussian features of equal intensity of 200, ideal contrast of 1, but with different FWHMs as seen in Figure 6.11, where the blue curve has a FWHM that is half of the black curve. For a given change in displacement along the X axis of both curves, since the blue curve is sharper it will more readily be able to resolve that particular change, as long as it is higher than the SNR of the system.

$$C = \frac{I_{max} - I_{min}}{I_{max} + I_{min}} \tag{6.4}$$

Prior, in Chapter 4, it was shown that the measured FWHM of a multi-micrograting diffracted beam was narrower than that for a 1D grating, which suggests that carrying out the measurement with a multi-micrograting beam would provide better results.

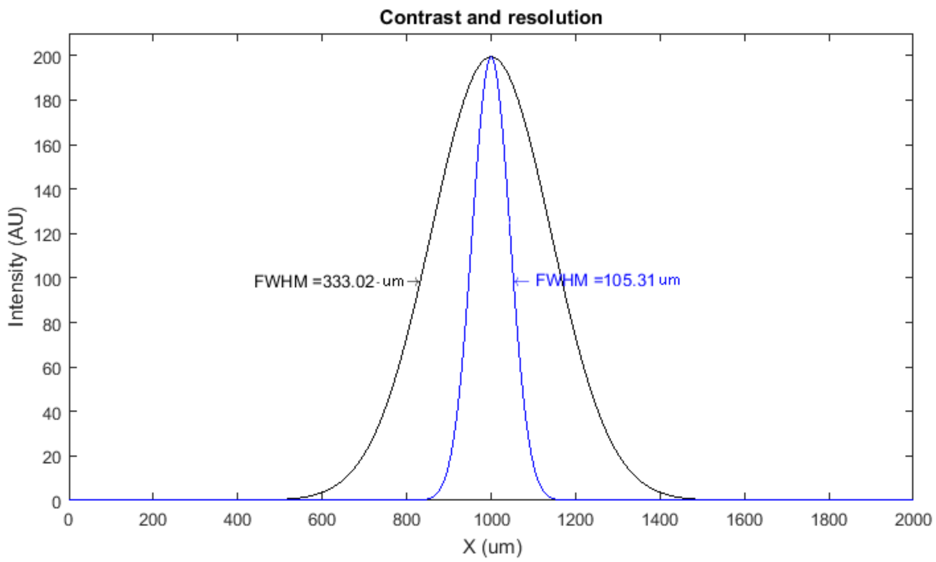

Figure 6.11: Comparison of resolution of Gaussian features of similar intensity, contrast but different feature size.

Sensing with interference effects in multi-microgratings

In addition to being narrower, under certain conditions, the multi-micrograting diffracted beams can be allowed to interfere at the sensor plane, producing high contrast, sharp fringes. Figure 6.12 illustrates this effect. If we assume the diffracted beam from a 1D grating of FWHM = 560 μm such as the one previously observed for a 1D grating seen as the black line in Figure 6.12(a), a typical 45 μm displacement that causes it to shift to the red line can be measured. One way to quantify that measurement is to look at the differential signal DS given by Equation 6.5, where T1 and T2 are the original and shifted signals respectively. The differential signal of Figure 6.12(a) can be seen in Figure 6.12(b). A maximum change of around ±11% is observed in the differential signal.

$$DS = 100\% * (\frac{T2}{T1} - 1) \tag{6.5}$$

For comparison, if the beam were instead narrower, that maximum change in the differential signal would be greater, such as in the case for multi-microgratings. However, as shown earlier, if the beam that is probing the grating sample is expanded so that it

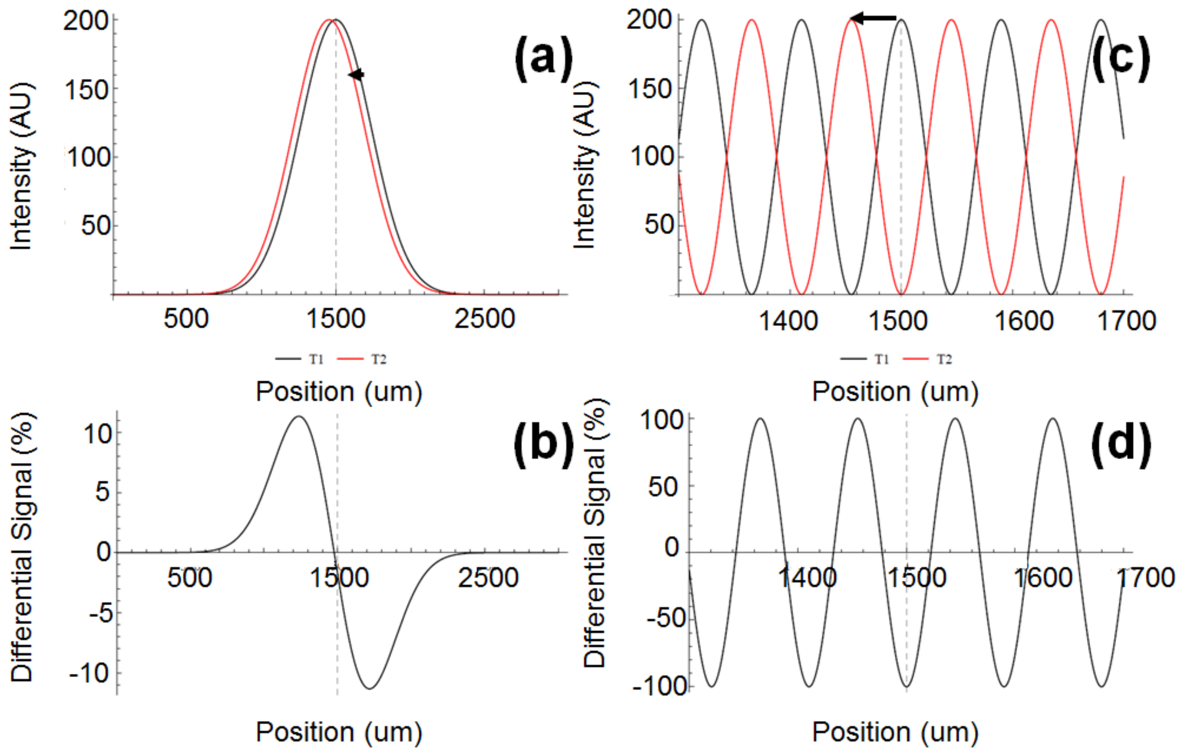

Figure 6.12: Simulated 45 μm displacement in (a) 1D grating Gaussian signal and (c) multi-micrograting signal with interferometric fringes with 90 μm periodicity. (b) and (d) represent differential changes in the signal to visualize strength of measurement.

is larger than the total grating size, at a similar sample to sensor distance and due to their proximity, multi-micrograting beams were observed to interfere with one another, producing fringes. Figure 6.12(c) simulates interference fringes with equal contrast but much sharper than the beam of Figure 6.12(a) and of 90 μm period. It is represented by the black T1 line, noting the difference in spatial scales. In the ideal case, a half period displacement of 45 μm exemplified by the red curve would produce the maximum change in the system's differential signal, as it can be seen in Figure 6.12(d). The differential signal can be found to have a maximum change of 100%. While this is an ideal case scenario, it is clearly observable how utilizing the interference effects observed on multi-micrograting diffraction patterns, which do not appear on 1D grating diffraction patterns, can much more readily utilized to carry out measurements.

Interference sensing with phase changing method

To more accurately measure changes in displacement using interference fringes, a phase can be calculated for the reference image at T1 and at T2 for the example seen in Figure 6.12. The computed phase difference, $\Delta\phi$, can be used as a metric for calibration or measurement. As it can be seen from Figure 6.12(c) and (d), since a half period was chosen as the displacement, the phase difference between T1 and T2 is π. A short simulation was written in MATLAB that calculates the phase difference $\Delta\phi$ [88]. To obtain the phase, Fourier Filters were applied to isolate one of the periodic frequencies of curves T1 and T2, a wrapped phase is calculated and unwrapped and the difference in phase between the reference image and the changed image are calculated. Since the fringe period was chosen to be displaced by a half period, the calculated phase is π.

A much more sensitive case would be when directly looking at the interference of two diffracted multi-micrograting beams and having the angle they intersect, as if by induced by temperature changes. The idea was previously discussed in Chapter 2, where it was proposed that by counting the number of fringes and calculating the fringe period when the diffraction angles were changing. We can utilize the phase change technique just presented and run an FDTD simulation of interfering beams. Two micrograting diffracted beams, separated by 30 μm, are allowed to interfere and form interference fringes. They are diffracting at angles of $\pm 32°$. The selected parameters are typical for the devices in this study. The illuminating source was light with 532 nm wavelength. The diffracted angle θ_d (or interference half-angle $\theta_{int}/2$, as they can be shown to be the same angles) was simulated to increase from 32° to higher angles at different increments, as if temperature were decreasing in the sample. As a reminder, as temperature in a sample decreases, the sample dimensions decrease. Inherently, the grating separation decreases, which in turn cause the diffracted angles to increase.

The FDTD simulations were allowed to run and reach steady state. Instead of looking

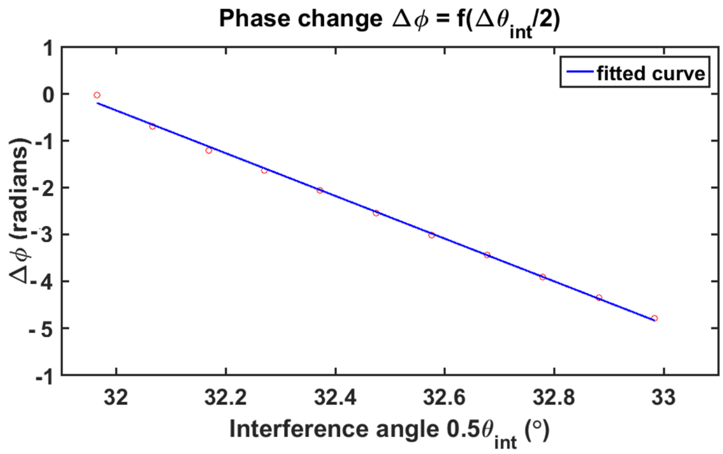

Figure 6.13: Effects of decreasing temperature, causing an increase in the diffracted angle (or interference half-angle) from 32 to 33°, shown as red circles fitted to a blue best fit line.

at how much the fringes are moving, the phase change $\Delta\phi$ is calculated with respect to the reference beams at 32.0° ($\Delta\phi$=0). The phase change is calculated for each increment of 0.1° up to 33.0°. The plot for the phase change $\Delta\phi$ as a function of the interference half-angles is shown in Figure 6.13 as the red circles fitted to a blue linear trend. The initial condition at a half-angle of 32° is on the top left corner of the plot, and as temperature decrease is simulated, the phase change moves downwards to the right.

While the trend shown is very clearly linear, a change in the interference half-angle of a whole degree, and assuming a silicon sample, corresponds to a change in temperature ΔT of over 1100°C, which is not very useful. However, this technique can be shown to be very sensitive. Different increments in interference half-angles $\Delta\theta_{int}/2$ were selected to understand the sensitivity of the phase change technique and the results are plotted in Figure 6.14 for increments (a) $\Delta\theta_d$ = 1x10$^{-4\circ}$, (b) 1x10$^{-5\circ}$ and (c) 1x10$^{-6\circ}$. The R^2 values for the fitted curves are shown as well. The linear trend remains for all cases. The R^2 are for the two increments in Figure 6.14(a) and (b) are very high, indicating a good fit of the trend to the data. It can be said that differentiating two adjacent measurements at these deltas would accurately differentiate them from one another. In the third case, for $\Delta\theta_{int}/2$=1x10$^{-6\circ}$, the actual captured values (red circles) are seen to be deviating from the linear trend. At this point, it is still possible to differentiate two adjacent measurements.

Table 6.1: Summary of phase changing technique sensitivity

$\Delta\theta_d$ (°)	ΔT (°C)	$\Delta\phi$ per step (rad)	R^2
10	1100	-0.4	1
$1*10^{-4}$	1.1	-0.0004	0.99929
$1*10^{-5}$	0.11	-0.00004	0.99792
$1*10^{-6}$	0.011	-0.000004	0.94576

At lower values of $\Delta\theta_{int}/2$, the ability to distinguish two adjacent measurements would be lost. The resolving capabilities of this method are summarized in Table 6.1.

Due to the nature of the process, an ambiguity as to the direction of the phase shift is introduced since the phase shift is periodic and a 2π shift is the same as a 0 π shift. Due to that ambiguity, errors can be made when calculating the phase. In this example, a 2π shift corresponds to a full 90 μm shift, but the calculated phase can result to be multiples of $\pm 2\pi$.

A solution is proposed, which uses both the high dynamic range and low resolution of 1D grating displacements and also the low dynamic range, high resolution of the phase change mechanism of the interference fringes caused by the multi-microgratings to obtain a high dynamic range, high resolution sensing method that would otherwise be impossible with just 1D gratings.

Using 1D gratings in sensing applications was shown earlier to have some advantages. Because multi-micrograting optical properties are the combined effect of the elements that compose them, the sensing current method shares some of the conventional 1D grating advantages as well as helps mitigate some of the issues. The advantages of using multi-microgratings is summarized below, which set them apart from other optical temperature measurement techniques.

1. Noncontact.

2. Real-time.

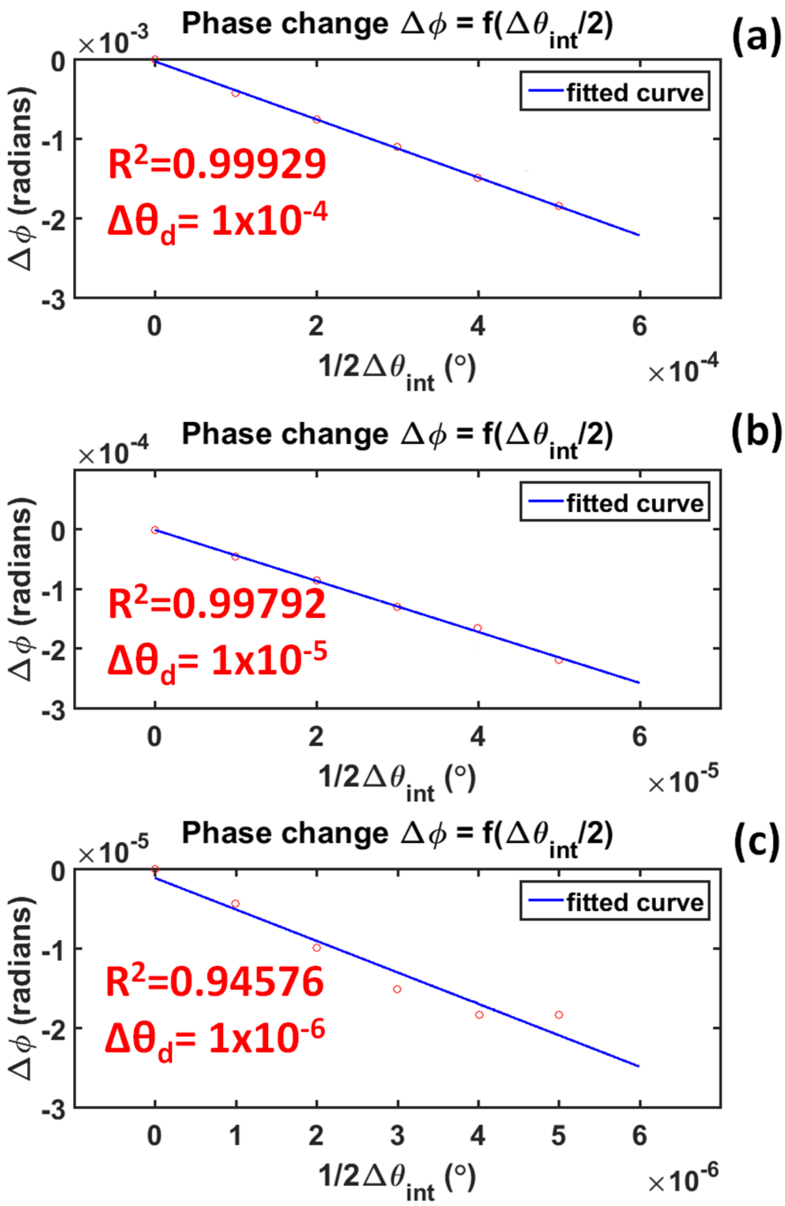

Figure 6.14: Simulation of effects of decreasing temperature, causing an increase in the diffracted angle (or interference half-angle) at three different $\Delta\theta_{int}/2$ separating each measurement step, of (a) 1x$10^{-4\circ}$, (b) 1x$10^{-5\circ}$ and (c) 1x$10^{-6\circ}$.

3. High dynamic range/ high resolution by combining displacement measurements of large features that behave as 1D grating spots and sharp features present from allowing multi-micrograting beams to interfere with each other.

4. Capable of localized micron scale measurements by probing different areas of multi-microgratings.

5. Simple architecture and alignment, requiring only a laser, a substrate with multi-micrograting patterns and a camera.

6. Capable of measuring changes in variety of substrates such as transparent and opaque with low or no susceptibility to surface emissivity or conditions, flat or curved as long as periodic elements can be fabricated.

7. Analogous technique can easily be adapted for stress/strain, displacement or rotation measurements.

6.2.3 Experimental description of multi-microgratings in temperature sensing

To test the feasibility of temperature sensing using multi-microgratings, the experimental setup shown in Figure 4.10 was slightly modified to include a hot plate and is shown in Figure 6.15. The incident angle and sample to sensor positions were estimated from photographs of the experimental setup. 1D grating and multi-micrograting samples with 2 μm periodicities were placed and slowly heated to different temperatures to observe changes in the diffraction pattern as a function of temperature. The optional beam expander was used to modify the incident beam size so that adjacent beams in multi-microgratings could interfere with each other.

The diffracted beams were captured by the CCD sensor and analyzed for changes. Average RMS noise of the CCD sensor was measured using MatLab by analyzing the mean and standard deviations of several captured signals and it was found to be 5.9%, with a range between 4.5% to 10.4%. It is established that if a measured signal is below the average noise of the sensor (SNR$\leq$1), then a change cannot be resolved.

Temperature of the hot plate (Corning Digital Hot Plate) was calibrated to the nominal reading in the device controls with a k-type thermocouple over several cycles, and such calibration can be seen in Figure 6.16. Additionally, a pyrometer based infrared ther-

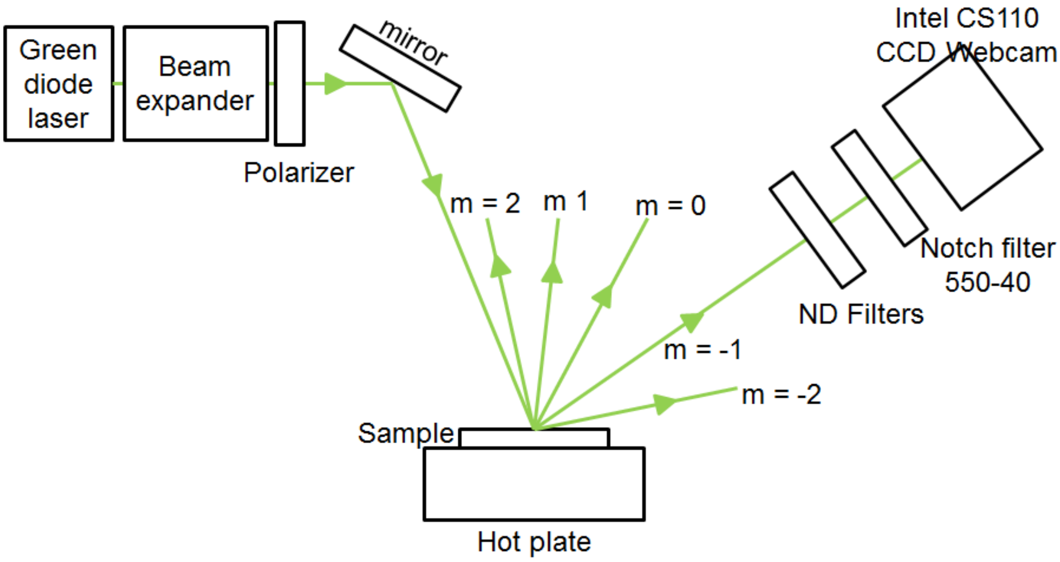

Figure 6.15: Experimental setup for temperature change experiments.

mometer (Fluke 568) was used on the hot plate to verify temperature readings. During experiments, temperature was carefully monitored with the attached thermocouple and infrared thermometer.

6.2.4 Results of temperature sensing with multi-microgratings

For proof of principle, thermally induced changes in diffraction patterns were observed for different sensor configurations. A silicon sample with 1D grating with 2 μm periodic lines was exposed to temperature variations between room temperature and 133°C. The sensor was placed 48 cm away. The first order diffraction pattern area near the first order was monitored. Typically 5 measurements were carried out for each temperature and the centroid position of the diffracted beam was measured. A plot of these changes can be seen in Figure 6.17(a). The changes in the diffracted angle induced by the changes in temperature can be seen to closely related to the expected changes, calculated by using the parameters given earlier for Si samples. A linear regression fit to the data shows an expected change of 4.09 μm/°C for this sample to sensor distance of 48 cm. This kind

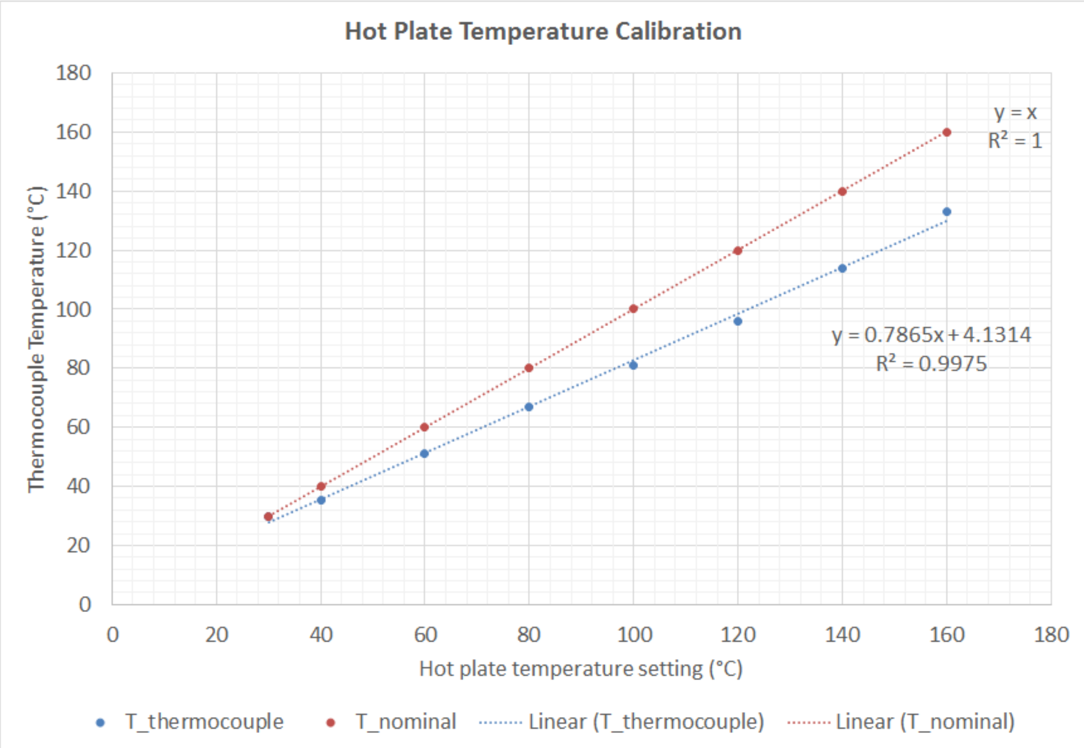

Figure 6.16: Calibration for hot plate setup for temperature experiments. Thermocouple measurements were compared with infrared thermometer to ensure proper calibration.

of measurement exemplifies the range and resolution of the system and it serves as the standard to which sensor configurations with multi-microgratings can be compared.

A similar measurement was carried out for a sample with multi-microgratings of the same periodicity at a sensor distance of 35 cm. The observed changes can be seen in Figure Figure 6.17(b) and results closely agree with the expected change of 2.93 μm/°C. When normalized to a sensor distance of 48 cm by a ratio comparison, the expected change is calculated to be 4.07 μm/°C , it is possible to see that the changes induced by both 1D gratings and multi-microgatings to be similar in magnitude, however, as explained earlier, multi-micrograting features were shown to be slightly narrower in diameter, so carrying out the measurement with multi-micrograting beams can offer better resolution.

In order to calculate system resolution and to visualize how using multi-microgratings would be beneficial in the described sensor configuration, images of displaced diffraction beams are shown in Figures 6.18 and 6.19 for two cases. Case 1 is with a measurement

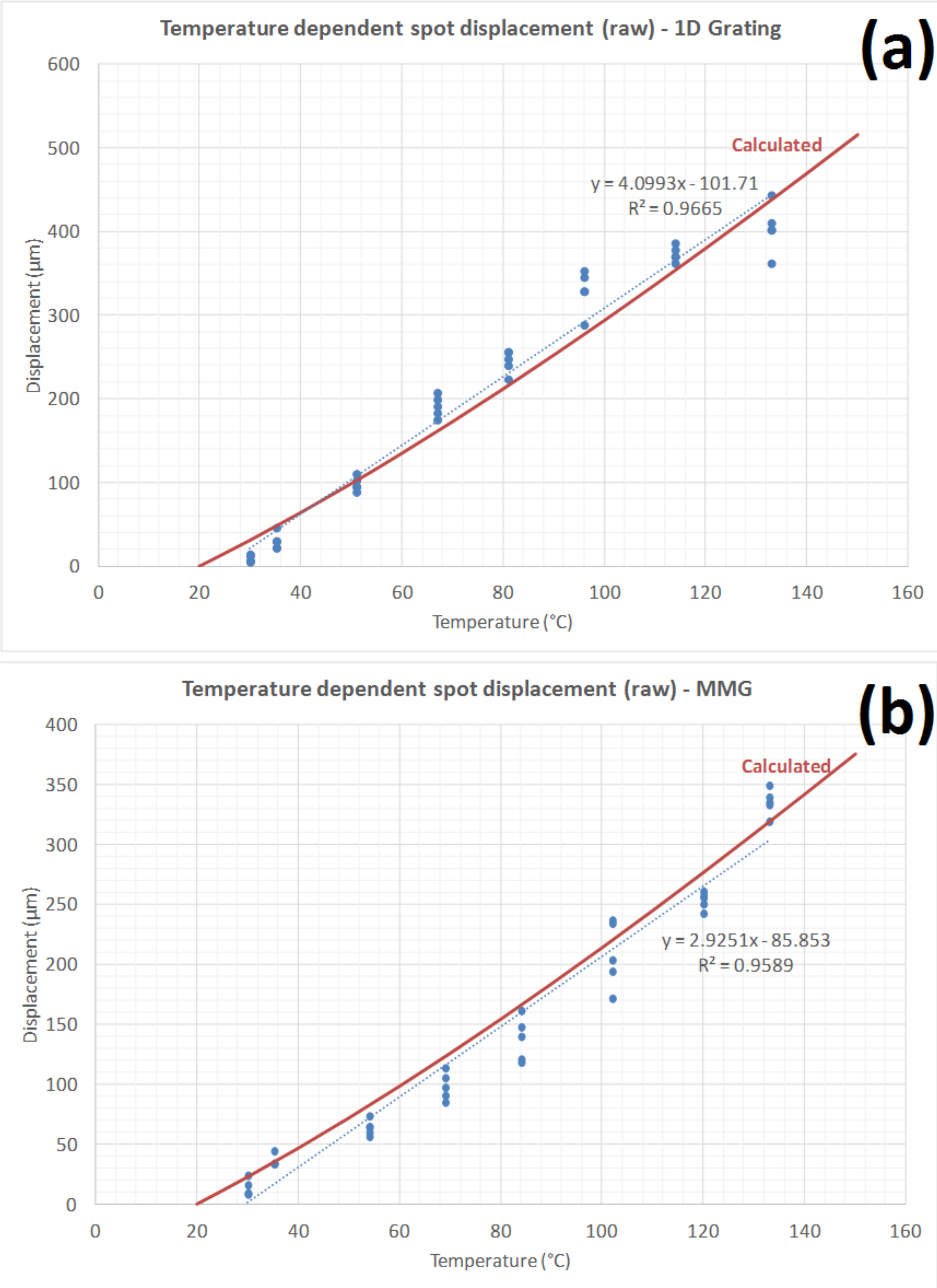

Figure 6.17: Measured and calculated changes in first order diffraction spot for (a) 1D gratings and (b) multi-microgratings.

using a 1D grating and Case 2 is using multi-microgratings. Displacement in both cases is measured to be 65 μm. It should be noted that the sample to sensor distances was different for each of the two cases, as it will be discussed below.

Case 1: 1D gratings (beam not expanded)

Figure 6.18(a) and (b) shows the first order diffracted beam positions at temperatures of 30°C and 60°C for a sample with 1D gratings at a sample to sensor distance of 48 cm. The reference (30°C) beam is shown as the solid line in Figure 6.18(c). A contrast value of 0.988 (I_{max} = 175, I_{max} = 1) is calculated using Equation 6.4. The displaced beam profile is plotted in Figure 6.18(d) as the solid line and the reference beam appears as the dotted line. The differential change produced by the measurement can be seen in Figure 6.18(e). A maximum change of 12.6% was observed, which is still above the measured 5.9% average noise in the sensor. The effective observed change which can be seen to be high enough to resolve the measurement when compared to the average noise (5.9%) of the sensor. The SNR is calculated to be 2.13. Under the current parameters, a minimum displacement of 30.43 μm would be necessary in order to resolve the change, which corresponds to a 14.04°C minimum resolvable temperature.

Case 2: Multi-microgratings (expanded beam)

A sample with multi-micrograting pattern was exposed to temperature variations and the first order diffracted beam using an expanded probing beam was measured as shown in Figure 6.19(a) for room temperature (30°C) and (b) 100°C at a sample to sensor distance of 20 cm. As it can be seen, diffraction fringes that are produced by expanding the probing beam cause the diffracted beams to interfere with each other, producing the high contrast lines in the regions of overlap. The contrast of the fringes is calculated to be 0.990 (I_{max} = 203, I_{max} = 1), which is of similar magnitude to that in the case of the sample with 1D gratings. However, due to the sharpness of the feature, a smaller change can be more

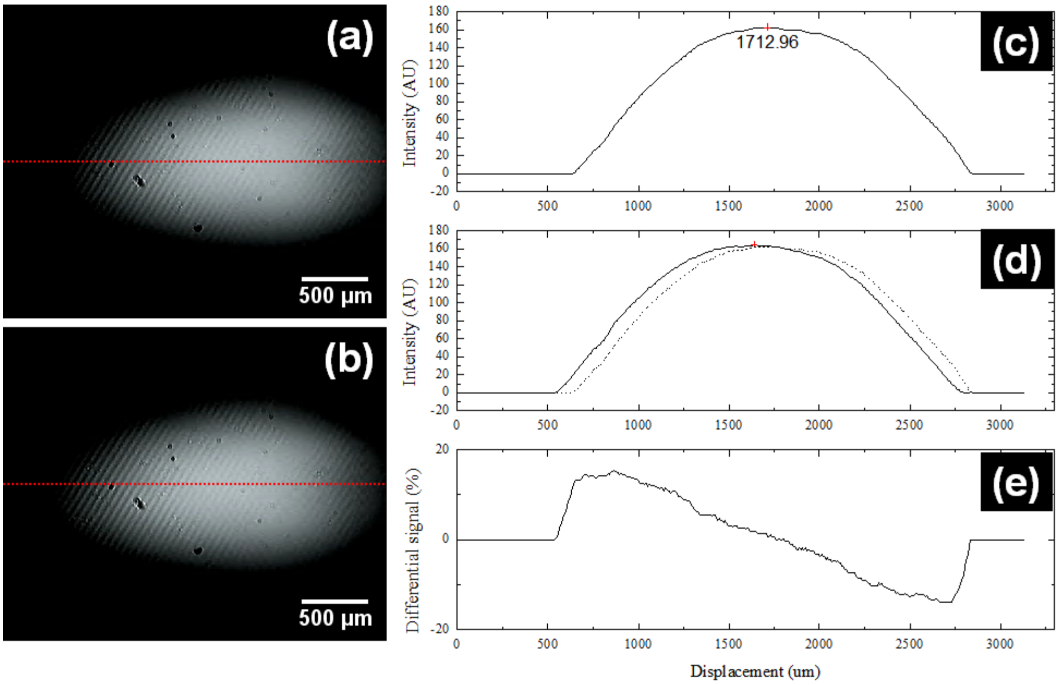

Figure 6.18: Diffracted beam displacement for 1D gratings at (a) 30°C (reference) and (b) 60°C. (c) shows the reference beam profile and (d) shows the displaced beam as the solid line and reference as the dotted line for clarity. (e) shows the differential signal that results.

readily resolved. Figure 6.19(c) shows the profile of the room temperature measurement as the solid line, which has been smoothed (Gaussian filter) to more easily visualize the fringes and their periodic nature. Figure 6.19(d) shows the displaced diffracted beam at a temperature of 100°C as the solid line, while the dotted line represents the room temperature reference measurement. Arrows are added to clarify how the displacement occurred. The differential signal produced by this measurement is shown in Figure 6.19(e), where the maximum observable change can be seen to be produced at a position around 300 μm in the sensor, and it is around 51%. The SNR is calculated to be 8.6, which is much higher than that for 1D gratings. Under this configuration, the sensor would be able to resolve a minimum displacement of 7.5 μm, which corresponds to a minimum ΔT of 8.07°C. A phase change $\Delta\phi$ is calculated to be 1.52, which corresponds to the expected $\pi/2$

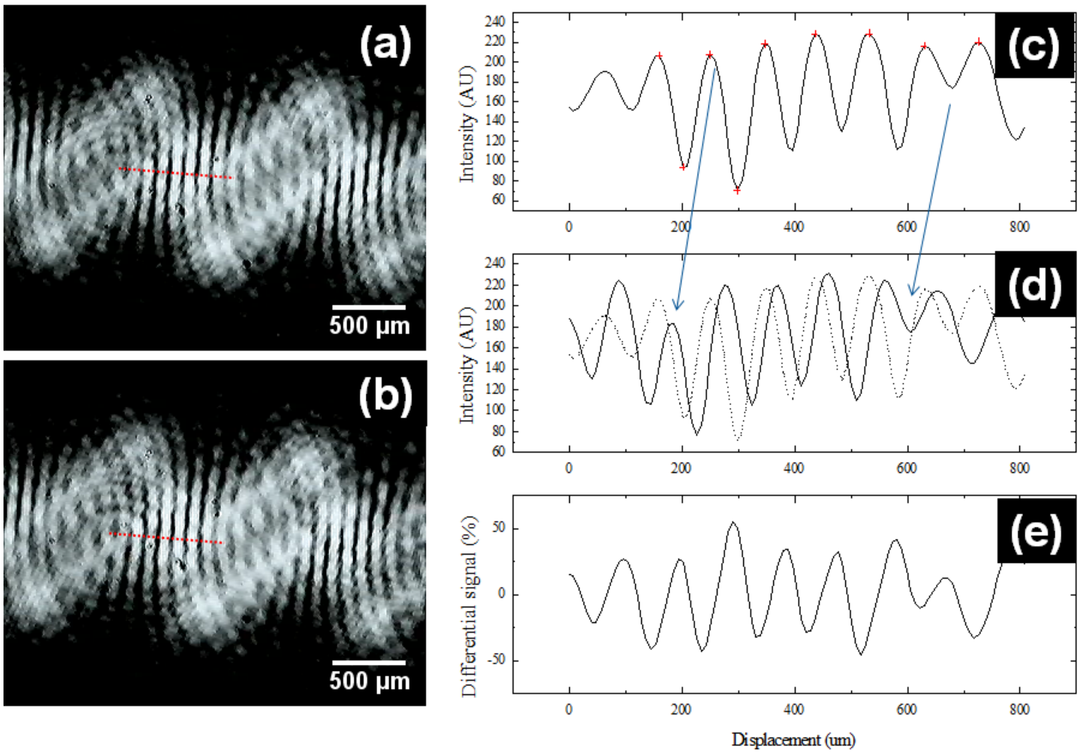

Figure 6.19: Diffracted beam displacement for multi-microgratings at (a) 30°C (reference) and (b) 100°C. (c) shows the reference beam profile and (d) shows the displaced beam as the solid line and reference as the dotted line for clarity. (e) shows the differential signal that results.

shift for this particular displacement. A phase calculation can easily assign a numerical value to the displacement and can be used for alignment and characterization purposes.

Due to the different sample to sensor distance in Case 1, the resolution measurement of Case 1 is normalized to the sample to sensor distance of 20 cm and it is calculated to be 33.6°C, while for Case 2 it remains as 8.07°C. Case 2 shows a resolution that is 4.2 times higher than that for Case 1. The range of such a system under this configuration, normalized to a sensor to sample distance of 20 cm, is between 30 and 140 °C.

A third case is considered, using multi-microgratings with interfering multi-micrograting beams. As shown earlier in this chapter, this phase changing technique is very sensitive to changes in angular displacement and fringe periodicity. The current equipment (camera

Table 6.2: Summary for 1D gratings and multi-microgratings

Parameters	Case 1 (1D Gratings)	Case 2 (Multi-microgratings)	Case 3 (Multi-microgratings with interference)
Contrast (AU)	0.988	0.990	0.990
SNR (AU)	2.13	8.6	8.6
Sample-sensor distance (cm)	48	20	10
ΔT (°C)	30	70	<0.1
Adjusted min. resolvable ΔT (°C)	33.6	8.07	<0.1
Improvement (AU)	NA	4.2x	300x

with poor resolution, setup) and sample size (1.5 mm samples) prevent from experimentally demonstrating this effect. With the current samples of 2 μm grating period, 34 μm separation between multi-microgratings and 1.5 mm in size, the maximum distance at which beams would interfere would be about 5.6 mm, which is not ideal to position a sensor to observe the interference patterns. At that distance it would be difficult to differentiate between beams, and even less to be able to resolve any interference effects. A more usable sensor distance would be in the order of 100 mm, which would correspond to samples with dimensions up to 27 mm if maintaining grating period, micrograting separation, contrast, SNR and range. It was proven however, through simulation, that it would be possible to use the interference effects of multi-microgratings to resolve up to 0.011°C. That ability to resolve such small changes in temperature would be over 3054 times better than with 1D gratings at a 0.011°C change in temperature.

Table 6.2 summarizes the parameters and results for Cases 1 and 2 and the theoretical limit using interference effects (Case 3).

6.3 Discussion

A method that uses the thermal expansion of 1D gratings and multi-microgratings was described to measure temperature changes. Several key aspects show these clear improvements. Beams that are narrower for multi-microgratings allow for a better sensor resolution. High contrast fringes that are produced only in the case of multi-micrograting diffraction patterns can be used to increase the resolution of the system by 4.2 times. The improvement in resolution can be achieved without a decrease in the dynamic range of the sensor configuration. With 1D gratings, in order to improve the resolution of a system with a similar configuration it would require the sample to sensor distance to be increased, at the cost of a reduced field of view (range). In the case of the interferometric measurement using multi-microgratings, the same range can be achieved but at a much higher resolution.

Furthermore, the tested configuration is simple and cost-effective. A simple webcam is sufficient to capture the diffracted beams. No critical alignment is necessary, which is often the case with interferometric setups requiring multiple beams. A low power laser beam (5 mW) can be used as the probing light source. One can argue that instead of using multi-microgratings, a large period 1D grating could be used in order to have multiple diffracted beams. A 1D grating with a period of 10-20 wavelengths ((i.e. d = 50-100 μm) would produce multiple diffracted orders that could be interfered on the sensor plane, but since the diffraction efficiency of higher order 1D grating beams is much lower, a higher power laser may be necessary for proper sensor operation. One of the key advantages of multi-microgratings is the fact that the diffraction efficiency can be tailored to be enhanced for larger angles because of the multi-micrograting low period (i.e. 2 μm) and diffraction efficiency that distributes most of the power to the area of the pattern. This corresponds to first order diffracted beam, but which is further separated into more spots because of the periodic nature of the apertures.

Further improvements could be made by using a better, lower noise camera with a larger sensor and higher dynamic range or by using better alignment techniques. The thermal expansion method measures changes in the diffracted angle due to induced changes in dimensions by temperature differences. The method can easily be extended for sensing displacement, stress/strain and rotation. Micro-multigratings can be incorporated into substrates using different methods. Using photolithography, for example, these structures could be made out of photoresist or etched onto the substrates surface and the temperature could easily be determined. Also, the probing area could be made out of polymers that contain the micro-multigratings, such as PDMS, that could be glued or attached to the surface of the substrates easily, and temperature measurements could be carried out.

Chapter 7

Conclusions and Future Work

7.1 Conclusions

The objective of this work was to understand the fundamental optical properties of multi-microgratings. In Chapter 1, it was established that the theory to explain the complex optical properties of multi-microgratings was incomplete. The diffraction patterns produced by structures with multiple periodicities had not been properly understood in previous work. In order to better understand the possible applications of multi-microgratings, other effects such as interference and parameters like efficiency, beam characteristics among others were required to be studied.

Proper simulation of optical properties of multi-microgratings like their diffraction patterns, efficiency and interference effects was of critical importance. In Chapter 2, through analytical and graphical techniques the diffraction patterns of multi-microgratings were found to form from the contribution of the different periodic elements that form the multi-microgratings, which are the periodic lines (1D gratings), the hexagonal aperture shapes of the multi-micrograting cells and the arrays that periodically arranged those apertures into large area patterns. By deconstructing the different periodic elements that form the multi-microgratings it was possible to understand how each of those elements contribute to the final diffraction pattern. In short, the interaction of the incident light and the multi-microgratings can be understood as follows: the light first encounters the periodic 1D grating lines and gets separated into diffracted orders as they would in a 1D grating. Second, the light then interacts with the hexagonal apertures. Third, the light then interacts with the periodic apertures. The resulting diffraction pattern has high intensity arrays of diffracted spots near the 1D grating locations, their intensity is tailored by the envelope function that comes from the interaction with hexagonal apertures and further separated into periodic spots that are formed from the lattices that form the large area arrays. It was also shown that complex periodic structures can be broken down into their constituting elements for easier understanding of how their diffraction patterns are formed, but suggesting that there is a strong interaction between the different periodic elements. The interaction gives rise to areas of high intensity appearing as highly defined, sharp features. These features could prove to be very sensitive to changing conditions in the samples themselves. Such idea can be exploited in multiple applications such as strain or temperature sensing where both anisotropic and isotropic changes in the sample dimensions could lead to very defined changes in a diffraction pattern. Two simulation approaches were presented. A Fraunhofer intensity distribution approach was developed in order to mathematically explain structures with multiple periodic elements. This approach is useful when mathematical expressions of the apertures can be easily derived, such as regularly shaped aperture arrays. Also, the simulations can be targeted to only selected areas of interest with great detail, allowing for high resolution images of any area of the simulated diffraction pattern. This first approach provides the exact solution to multi-microgratings. A different method, a graphical Fourier Transform approach, was implemented to simulate the diffraction patterns of more complex structures. Diffraction patterns of such structures can be simulated by obtaining their graphic Fourier Transform, but the diffraction patterns must be spatially calibrated. Furthermore, such technique only applies to square images with pixel counts that are in powers of 2. Memory limitations can prevent simulating diffraction patterns for very large images. This graphical approach can be further optimized to run in parallel environments to overcome the memory limitation issues. It has proven to be a very useful tool to explain the formation of diffraction patterns of complex periodic structures like arrays of hexagonal microgratings, but it is also possible to use such approach to simulate the diffraction patterns of quasi-periodic and non-periodic structures as well. However, both approaches were only able to explain the interaction of light with multi-microgratings in the far field, as both provide solutions to the far field patterns. In order to better understand near field patterns and other optical effects such as interference between beams, an FDTD method was used. This method is ideal to study the optical interactions between light and matter by studying the time-evolving EM fields. The FDTD technique can be developed for very specific applications, such as to model diffraction efficiency in these structures, but it was found that the best technique to model diffraction efficiency of multi-micrograting was using the RCWA technique. This technique solves light interaction with periodic structures, although it works better with fully periodic structures or at best 2D systems with only a few periodicities such as square gratings. In the case of multi-microgratings, the technique worked well since the majority of the contribution to the diffraction efficiency arises from the 1D grating portion of the structures, which correspond to most of the area that the multi-microgratings encompass. To summarize, by studying all the various techniques it was possible to divide the problem of explaining the optical properties of multi-microgratings into smaller problems. The correct choice of technique would depend on the final use of the structures. Different multi-microgratings can be tailored for different applications. The exact distribution of light intensity can be carefully controlled by means of controlling etching depth, substrate choice, grating period, micrograting cell size, coatings, etc.

In Chapters 3 to 5, presented work was focused on experimentally fabricating and characterizing the optical properties of multi-microgratings and their respective polymer replicas. Electron-beam fabrication of 1D grating structures, periodic hexagonal apertures and multi-microgratings was carried out to individually characterize the contributiuons of the different elements that make the multi-microgratings. High quality samples were fabricated on Si using the fabrication procedure provided by Oak Ridge National Laboratory facilities. The complex optical diffraction pattern generated from multi-microgratings has been explained using an understanding of the optical principles that govern the diffraction from periodic structures. In summary, the diffraction pattern of multi-microgratings is formed by convoluting the individual diffraction patterns of the individual periodic elements that describe it: the hexagonal shape of the cells, the lattice that is formed with the periodic hexagons, the 1D periodic grating lines oriented at six different orientations. This convolution produces cross terms that have been explained. The micrograting diffracted beam size seem to be slightly narrower than those for a similar 1D grating. Furthermore, depending on the plane of observation, multi-micrograting diffracted beams can interact with each other, producing high contrast interference fringes. Diffraction efficiency of multi-micrograting samples was measured to be highly dependent on 1D grating parameters. Low-cost method of replication has been demonstrated, and optical properties of replicas have been compared to masters and found to be in agreement. The overall diffraction pattern formation is independent of substrate, however, substrate selection was found to be very important if maximum effifiency is required to go to a particular order or for a particular application. Limitations with the presented replication method, for example limitations on minimum feature size that can be replicated, could be overcome by studying different replication schemes. A possible candidate would be nanoimprint lithography, which has been used to replicate fine features in three dimensions and would be an ideal way to generate large area substrates for certain applications of multi-microgratings.

Chapter 6 explored the application of multi-microgratings in a temperature measurement scheme that improves on earlier optical, non-contact methods of temperature measurement using 1D gratings. These methods use the idea that as a sample with 1D gratings is heated, the induced thermal expansion shifts the diffracted position of the beams. One of the limitations of such a configuration is that in order to increase the resolution of the system, measurement range is often sacrificed since the detection plane must be moved further away from the surface being sensed. Because of the profiles of multi-micrograting beams, it is possible to increase the resolution of this method. Furthermore, due to the possibility of having interfering beams, the resolution is increased by a factor of 300 (

compared to making the measurement using ordinary 1D gratings, without sacrificing the measurement range in the system) and would allow to resolve tenths of degrees of changes in temperature. This measurement method was intended as a proof of principle example on how these multi-micrograting structures can be utilized for measurements of temperature, stress/strain, rotation and other forms of optical metrology of samples. The method presented requires simple alignment and equipment, making it an attractive option to a measurement where high speed, non-contact optical measurements are required. Using the interference effect found inherent in multi-micrograting diffraction patterns, it was shown that the resolution could be significantly increased to be able to resolve temperature changes to tenths of degrees, without the need for special alignment or complicated setups. This effect was shown to be existent at short distances to the substrates. To extend the distance at which these interference effects are observable, multi-microgratings must be arrayed to cover larger areas. The patterns studied were smaller than 1.5 mm in dimensions, but having much larger patterns would be useful to see interference effects at longer distances. Furthermore, to experimentally verify the resolution with the interference effects, it would be necessary to have very stable equipment. With the equipment available, it was found that small changes were difficult to identify due to variations in ambient temperature. The CCD sensor that was used was very inexpensive, and because of that it had poor optical resolution, framerate and stability.

There are several industrial processes that would benefit from sensors made with multi-microgratings. There are two processes in glass manufacturing where temperature control is extremely difficult but that highly affect the quality of the fabricated materials. One of them is during glass etching in acidic and aqueous solutions. The etching process is exothermic, and the etching rate is highly related to local sample temperature. Etching times are typically in the order of seconds or minutes, but there is no way of inserting a thermocouple or relying on processing parameters such as etch bath temperature to properly extract localized sample temperatures. Furthermore, samples are submerged in acid. An optical method to accurately, quickly and capable of resolving sample temperatures in this environment is very promising. Having multi-micrograting structures patterned into glass before etching could be very valuable. Just by illuminating the structures when samples are submerged in the etching bath, withouth complicated alignment it would be possible to measure localized changes in temperature. This would ensure etching uniformity. Analogously, another process that requires clever control of temperature is during ion exchange to fabricate strengthened glasses. Ion exchange layers are formed by submerging samples into dopant baths. Careful control of the ion exchange thickness layer is paramount, especially with typical ion exchange glasses becoming thinner and thinner. These are just two real world examples that would benefit from using multi-microgratings patterned into samples in order to measure temperature.

For the first time, a thorough understanding of the optical properties and diffraction and interference effects in multi-microgratings has been provided, which can be used to tailor properties for different applications. These optical properties were simulated. Samples with multi-micrograting structures were fabricated, characterized and replicated. Experimentally observed interference of micrograting beams, producing sharp interference fringes. Monitoring position and intensity of fringes allows for sensing applications, otherwise not likely with 1D gratings. This simple method for temperature measurement was presented, which increased resolution of the method by a factor of 4.2 (without sacrificing measurement range). Sensing can be achieved at a micron scale level with capability of simultaneous multi-point detection, applicable to both isotropic and anisotropic changes. Possible extensions of the current work are described in the following section.

7.2 Future Work

Further research needs to be done in order to study the various applications of these structures, for vapor, temperature and strain sensing and for nanometrology, optical telecommuncations and spectroscopy. Key parameters that need to be well understood include polarization dependent losses, dispersion, spectral resolution for such applications.

Spectroscopic studies of vapor and temperature sensing using multi-microgratings

Morpho butterfly wing scales have been used in vapor and temperature sensing applications due to their unique optical properties [4, 5, 6]. These properties allowed for the possibility of systematic monitoring of their reflectance spectra, as it was shown in Figure 1.2, when illuminated with white light and exposed to different vapor concentrations and different temperatures. The authors concluded that changes in the reflectance spectra due to vapor concentration variations were due to a change in effective refractive index as analyte molecules get trapped in the structures. Similarly, changes in reflectance spectra due to temperature variations were thought to be caused by changes in the multi-layer interference effects. Signature signals were observed for different vapors and different heating regimes.

Preliminary studies were carried out with multi-micrograting samples using white light illumination in the experimental setups shown in Figure 7.1(a) and (b). White light from a halogen source was used to illuminate samples and reflectance spectra were captured using a USB Ocean Optics fiber spectrometer. Multi-microgratings were exposed to different vapor concentrations from nitrogen vapor infused with different analyte molecules. A systematic change was observed when the concentration of the analyte vapors was changed. These effects are summarized in Figure 7.2(a) for 2 μm multi-micrograting samples subject to differing methanol concentrations. The graph shows wavelength vs. differential spectra at different vapor concentrations. The different curves represent changes from the reference case (flow of methanol 0 sccm) to increasing methanol flow (20 sccm, 40 sccm, etc). One possible explanation is due to the change in the effective refractive index in the structures when different flow conditions are changed or changes in efficiency due to changes in the effective trench depths. More work is required to properly understand this phenomenon.

Analogously, when multi-micrograting samples were subject to temperature changes when placed on a thermoelectric heater, reflectance spectra was observed to change dramatically. Some preliminary results are shown in Figure 7.2(b). In this case, the differential spectra was calculated for the difference between the reference case response at room temperature to increasing temperatures up to 120°C. Again, it is theorized that a change in efficiency could be the cause of the different responses at different temperatures, but more studies are required to confirm this idea.

In both vapor and temperature sensing experiments, the changes were observed to be repeatable when cycled through different iterations. Signatures from these two experiments must be further analyzed to understand precisely what causes the changes but it would be possible to use these structures in such applications. Furthermore, sensitivity and resolution must be determined for such experiments in order to prove their validity. A better spectrometer with higher dynamic range and resolution would be required in order to more accurately monitor the changes. Furthermore, simulation of these spectral signatures would be a possible area for future work, either using the FDTD method described here or other methods to solve for the optical properties of periodic structures (such as RCWA). Understanding the proper interaction between the different periodic structures and vapor analytes can be modeled to be able to design better structures suited to a particular application.

Polarization dependence

Similar structures to our hexagonal multi-microgratings composed of square micrograting cells with 2 orientations were described in the literature review section in Chapter 1. Those structures were used as a low reflectivity, low loss polarizer, and this was achieved by having a subwavelength period for the microgratings and a larger than the cell separation. Structures fabricated in our study had similar features, multi-microgratings with 500 nm period and 10 μm sides. This type of structure may work well for low IR wavelength polarizer applications since even a greater majority of the light is distributed to the diffracted beams rather than the zeroth order. Further research is required in order to prove these effects.

Strain/stress sensing

A temperature measurement method was devised earlier which relied on the shift of diffraction angles induced by temperature changes in samples with multi-microgratings. Analogously, such technique can be extended for stress/strain sensing. The angular deflection occurs in near real-time , making this method useful for situations where the need for an in-situ stress/strain measurement is required. For example, as theorized in [89], these structures could be placed in high stress areas on the wings of aircraft to monitor wing deformations accurately and quickly.

Nanometrology

A series of works cited in [38, 39, 40] utilized the diffraction patterns of penrose quasi-periodic structures for nanometrology applications. The intricate diffraction patterns produced by those structures had a high number of periodic and quasiperiodic elements that produced very intricate, densely populated diffraction patterns. By monitoring those patterns using sensitive CCD cameras, they were able to generate algorithms that can use the diffraction patterns as optical rulers. Only diffraction effects were considered for that study, but multi-beam interference fringes could be further used to refine these optical rulers. A similar study could be carried out using multi-microgratings as they incorporate diffraction patterns of multiple periodicities that can be tailored to have very densely populated features.

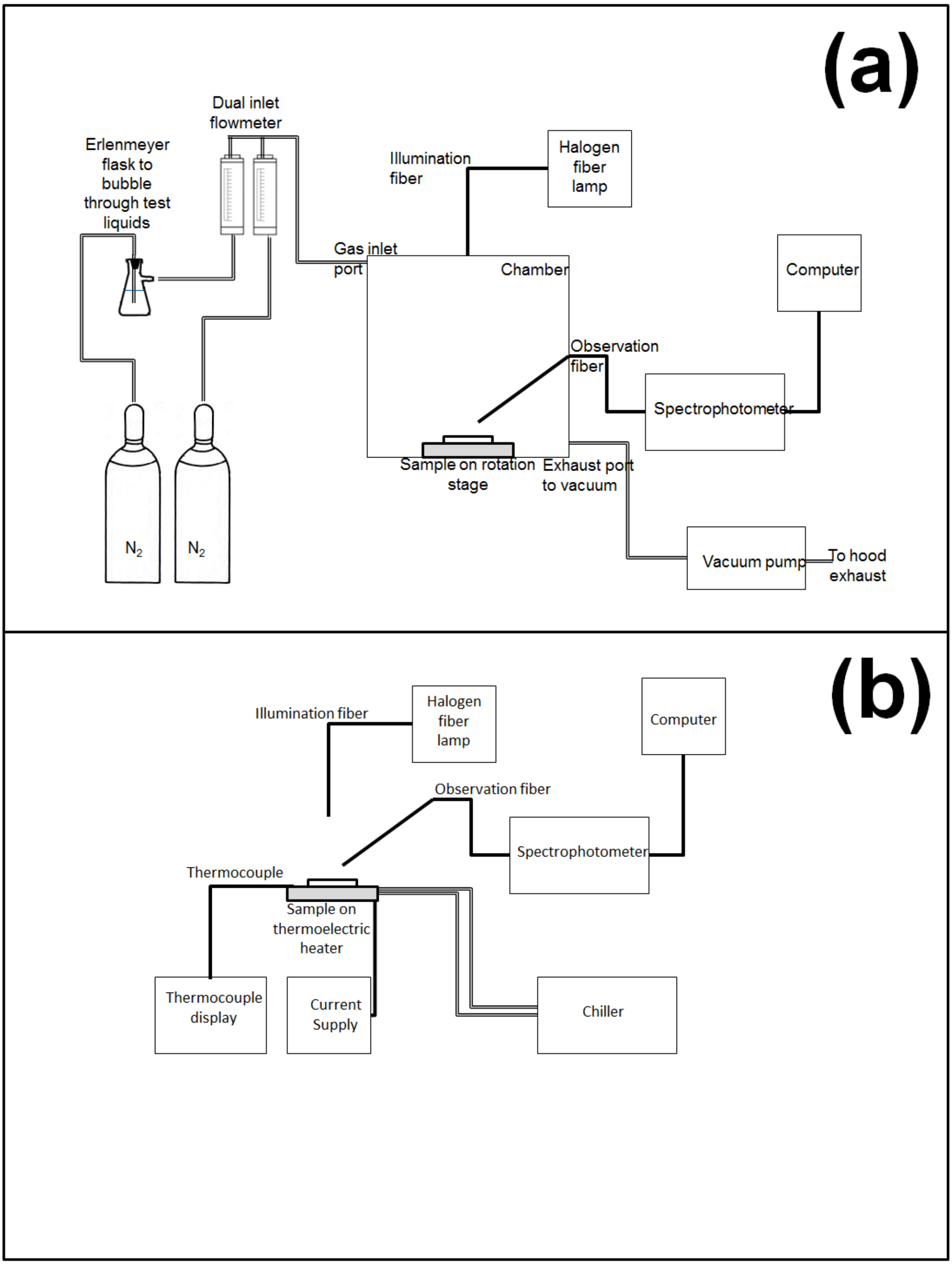

Figure 7.1: Experimental setups for monitoring changes in reflectance spectra of multi-microgratings (a) due to vapor concentration variations and (b) due to changes in temperature.

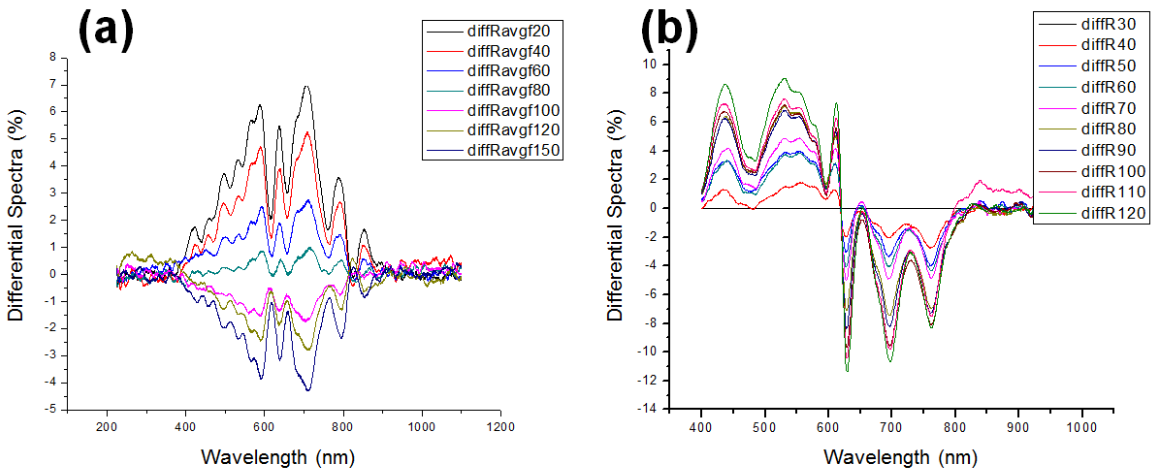

Figure 7.2: Preliminary results demonstrating changes in reflectance spectra of multi-microgratings (a) due to methanol concentration variations and (b) due to changes in temperature.

Appendix A

Authored publication manuscripts

This appendix includes the full manuscripts of authored publications in the topic of multi-microgratings:

1. Optical diffraction properties of multimicrogratings

2. Simulation of optical diffraction properties of multi-microgratings

3. Multi-microgratings for high sensitivity temperature sensing

Optical diffraction properties of multimicrogratings

Christian A. Rothenbach,[1] Ivan I. Kravchenko,[2] and Mool C. Gupta[1,*]

[1]Department of Electrical and Computer Engineering, University of Virginia, Charlottesville, Virginia 22904, USA

[2]Center for Nanophase Materials Sciences, Oak Ridge National Laboratory, Oak Ridge, Tennessee 37831, USA

*Corresponding author: mgupta@virginia.edu

Received 25 August 2014; revised 22 December 2014; accepted 28 December 2014; posted 6 January 2015 (Doc. ID 221682); published 27 February 2015

This paper presents the results of optical diffraction properties of multimicrograting structures fabricated by e-beam lithography. Multimicrograting consist of arrays of hexagonally shaped cells containing periodic one-dimensional (1D) grating lines in different orientations and arrayed to form large area patterns. We analyzed the optical diffraction properties of multimicrogratings by studying the individual effects of the several periodic elements of multimicrogratings. The observed optical diffraction pattern is shown to be the combined effect of the periodic and non-periodic elements that define the multimicrogratings and the interaction between different elements. We measured the total transverse electric (TE) diffraction efficiency of multimicrogratings and found it to be 32.1%, which is closely related to the diffraction efficiency of 1D periodic grating lines of the same characteristics, measured to be 33.7%. Beam profiles of the optical diffraction patterns from multimicrogratings are captured with a CCD sensor technique. Interference fringes were observed under certain conditions formed by multimicrograting beams interfering with each other. These diffraction structures may find applications in sensing, nanometrology, and optical interconnects.

OCIS codes: (070.2575) Fractional Fourier transforms; (050.1950) Diffraction gratings; (050.1960) Diffraction theory.

http://dx.doi.org/10.1364/AO.54.001808

1. Introduction

The field of biomimicry examines naturally occurring designs and exploits these designs for beneficial purposes. Natural optical structures have been used for several applications, so low-cost methods to replicate these designs is important [1]. Several studies have been reported that try to replicate the optical effects found in *morpho* butterfly wing scales for sensing and other applications [2–4].

The actual wing structures in *morpho* butterfly scales are very complex and they generate an iridescent, bright blue color at large viewing angles due to their intricate design. The design uses the effects of diffraction and interference to generate the color, but it is made up of a complex architecture of three-dimensional (3D) microribs and lamellar reflectors that are hard to reproduce. Wing scales have been used as templates for replication. Transparent metal oxides were deposited on the wing scales and heated to remove the wings and crystallize the films, producing similar structures [5]. They were used to make chemical sensors. Focused ion beam and chemical vapor deposition were used to produce 3D structures similar to those found in the butterfly wings [6]. However, these reported methods require complicated equipment and procedures to fabricate the structures. They also sacrifice actual wing scales, which prohibits them from widespread applications. It also is hard to fabricate or reproduce large area devices with optical properties similar to the butterfly wings. Therefore, more easily fabricated devices with optical properties similar to these wing structures are needed.

Wong *et al.* [7] describes structures that, despite being different in their architecture, had optical properties similar to the wing scales. Their study

1559-128X/15/071808-11$15.00/0

focused on fabricating devices that appeared blue over a wide viewing angle, displaying the effects of diffraction and interference with properties similar to the iridescent wings. They achieved this effect by fabricating a planar array of micr: gratings that consisted of hexagonally shaped individual microgratings in different orientations. When illuminated with light, these structures produced blue iridescent color and complex diffraction and interference patterns.

A more thorough understanding of the diffraction properties of multimicrogratings is necessary for several reasons. The diffraction pattern generated is more complex than the simple grating equation can describe. It is therefore necessary to fully understand what causes the diffraction pattern from multimicrograting structures. The purpose of this study is to understand, through design and experimental fabrication, the optical properties of complex diffraction patterns and how they are formed. Furthermore, a more thorough understanding of these structures would allow the design and implementation of possible applications of multimicrogratings and similar types of structures that generate complex diffraction and interference patterns. Such applications include vapor sensing [2], temperature sensing [3], strain sensing, and optical nanometrology [8–10].

2. Theory and Design of Multimicrogratings

The grating arrays used in the current study contain hexagonally shaped micrograting cells, which contain grating lines with six different orientations, and are arranged to generate large area patterns. The six micrograting orientations are grouped in a unit cell, shown in Fig. 1(a), that is repeated to

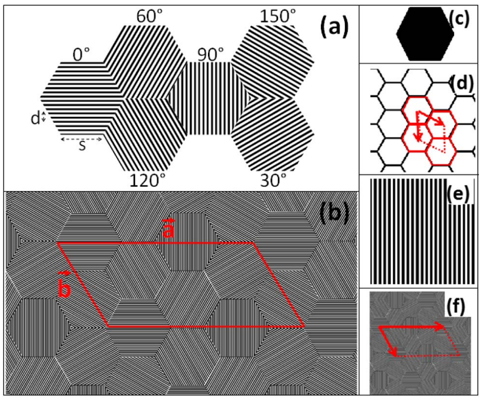

Fig. 1. (a) Micrograting repeating cell with six different orientations. s is the hexagon side dimension and d is the grating period. (b) Array of multimicrogratings, with the red parallelogram defining the unit cell used to form the array, with sides a and b. (c) Hexagonal shape of the micrograting apertures. (d) Large area periodic structure produced by the multiple hexagonal apertures. (e) 1D gratings with different orientations. (f) Lattice produced by the replicating unit cell containing the microgratings.

generate large area arrays. The hexagon side is defined as s and micrograting period as d. Figure 1(b) shows an array of micrograting cells, also referred to as multimicrogratings. The multimicrogratings are composed of hexagonally shaped micrograting cells, which are arranged to form large area structures.

To fully understand the complex optical diffraction pattern generated by multimicrogratings, it is important to understand the contributions of the different periodicities found in the design. The diffraction pattern of large area multimicrogratings is formed by the following individual elements, all of which can produce different diffraction effects:

1. The hexagonal shape of the micrograting apertures, as seen in Fig. 1(c).
2. The large area periodic structure produced by the multiple hexagonal apertures, as seen in Fig. 1(d).
3. The 1D gratings with different orientations, as seen in Fig. 1(e).
4. The lattice produced by the replicating unit cell containing the microgratings, as seen in Fig. 1(f).
5. The interaction between elements 1-4, as displayed in Figs. 1(c)–1(f).

The first two elements correspond to the hexagonal nature of the micrograting cells. The hexagonally shaped cells, Element 1, act as apertures and produce a typical diffraction pattern for a hexagonal aperture. Element 2, the large area structure produced by the hexagonal cell arrays can be considered a honeycomb lattice. Arrays of hexagonal apertures also were chosen for fabrication because they will help us understand the diffraction pattern from the various elements in multimicrogratings.

The periodic micrograting lines oriented at various angles (Element 3) produce diffraction effects like those of a 1D grating. As such, those diffraction effects can be explained by this grating equation:

$$d(\sin\theta_i + \sin\theta_d) = m\lambda. \tag{1}$$

In this equation, d is the period of the grating. The angles θ_i and θ_d are the angles of the incident and diffracted beams, respectively, with respect to a surface normal to the grating plane. The integer m represents the mode or order of diffraction and λ is the wavelength of the incident light. Using this equation, we can understand some properties of diffraction from microgratings; for example, the angular position of the diffracted spots and the number of diffracted orders. However, the grating equation only takes the contributions for the 1D component of the multimicrogratings.

Six hexagonal microgratings with different 1D grating orientations are then arrayed into an oblique lattice (Element 4) to form large area patterns. Consequently, the generated lattice also produces diffraction effects. The unit cell, depicted as a red parallelogram in Fig. 1(b), is used to produce the oblique lattice. The unit cell's sides a and b

are related to the hexagon side dimension s. Geometrically, it can be shown that the unit cell dimension $b = 3 * s$ and $a = 6 * s$.

As it will be discussed below, the diffraction patterns from hexagonal apertures and their arrays, 1D gratings and multimicrogratings would lead to some cross interaction with each other (Element 5). This interaction is manifested as cross-term spots that would otherwise not exist if one of the previous four elements were not present. This property of multimicrogratings is should be useful for sensing and other applications.

3. Experimental

A. Fabrication of Multimicrogratings Using Electron-beam Lithography

The effects of the individual optical elements described earlier can be studied by the fabrication and characterization of three designs: array of hexagonal apertures, 1D gratings, and multimicrogratings. The following grating parameters were selected for fabrication. For 1D gratings and multimicrogratings, a grating period of 2.0 μm (1.0 μm feature size) was chosen. This grating period, which is longer than visible wavelengths, allows for observation of the diffraction effects of the 1D grating component of the multimicrogratings. For the hexagonal aperture patterns and the micrograting cell sizes, the hexagons were chosen to be 20 μm, so as to have enough grating lines contained within each hexagon. The total area of the patterned samples was chosen to be 1.5 mm × 1.5 mm to have an area large enough for experimental characterization.

Much research has been done to understand the optimal profile for diffraction gratings (sinusoidal, square, triangular shapes for the grating facets) [11–14], but due to the ease of fabrication, a rectangular profile was selected. Furthermore, for 1D gratings, duty cycle was chosen to be 50% because it also maximizes the diffraction efficiency. To maximize first order transverse electric (TE) diffraction efficiency for the 1D gratings, simulations were carried out with commercial software (GSolver V52 Demo, Grating Software Development Co.). A grating depth of 0.95 μm was selected to be optimal for the grating period of 2 μm at a 532 nm wavelength. This setup resulted in a 1D grating TE diffraction efficiency of 14.1% for the first order, and a total TE diffraction efficiency of 31.5% for all diffraction orders.

Total transverse electromagnetic (TM) diffraction efficiency for a 1D grating also was calculated for the given parameters and was found to be 20.2%. For the pattern with hexagonal apertures, the same software was used to calculate the total TE diffraction efficiency of arrays of hexagonal apertures and it was calculated to be 8.7%, while TM diffraction efficiency was 5.9%. Because cross-terms also exist due to the combined effect of the different hexagon apertures, the total intensity of the diffracted spots will be lowered even further. The diffraction efficiency of multimicrogratings is expected to behave as a combination of the 1D and hexagonal aperture array diffraction efficiencies. The majority of the light is distributed to the 1D grating orders; therefore the same grating depth of 0.95 μm was selected for micromultigrating samples. Table 1 summarizes the design parameters. We will publish more details on diffraction efficiency simulations separately.

Table 1. Design Parameters and Calculated Diffraction Efficiencies

Design Type	Grating Period or Cell Size (μm)	Minimum Feature Size (μm)	Etch Depth (μm)	Calculated Total TE Diffraction Efficiency (%)
1D grating	2.0	1.0	0.95	31.5
Hexagon array	20.0	3.0	1.95	8.7
Multimicrograting	2.0	1.0	0.95	31.5

Periodic patterns can be fabricated using a variety of techniques. Laser interference lithography is typically used to fabricate large area periodic patterns such as 1D gratings and two-dimensional (2D) arrays of features. However, the periodicity of the patterns is determined by the interference effects of multiple laser beams and this technique is unsuitable to fabricate micrograting of different orientations and complex architectures such as the one required for this study. Although direct-laser lithography can fabricate large area, arbitrary patterns, its main limitation is the resolution is larger than the critical dimensions required. Masked, optical lithography can be used for fabrication of multimicrogratings, but to fabricate microgratings with submicron periods, expensive high-density masks and advanced optical lithography equipment is necessary. A high-energy electron-beam lithography (EBL) system was chosen for large area fabrication of arbitrary patterns. Figure 2 shows a flow chart for the fabrication process and details are below.

For the fabrication of 1D gratings and multimicrogratings, adhesion promoter P20 was spin coated on silicon wafers (p-type, ⟨100⟩, 100 mm) at 3000 rpm for 45 s. ZEP520A electron-beam resist was then spin-coated at 3000 rpm for 45 s for a desired thickness of approximately 400 nm. The wafers were then baked at 180°C for 2 min.

We used CAD software to design patterns and transferred them to a JEOL JBX-9300FS EBL system (energy = 100 keV, current = 2 nA, base dose = 250–290 $\mu C/cm^2$). Patterns were adjusted for proximity effect correction (PEC) and dimension biases (−25 to −75 nm corrections) to expose features with the desired dimensions and duty cycle. Exposed patterns were then developed in Xylenes for 35 s, rinsed with isopropyl alcohol (IPA) and dried with N_2.

Alternatively, for patterns with low density of features (hexagonal apertures only), contact lithography was chosen for the fabrication since the critical dimensions were 3 μm for the borders. A chrome mask was fabricated with a direct-laser write

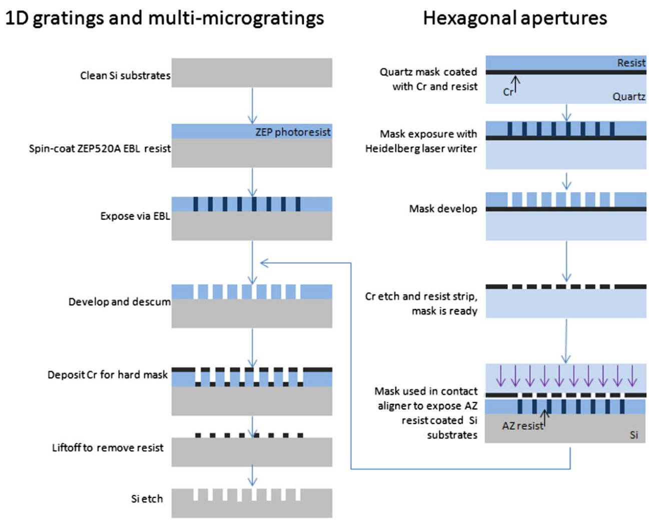

Fig. 2. Fabrication flow charts for samples with 1D and multimicrograting patterns and for samples with hexagonal apertures.

Heidelberg Mask Writer and a contact lithography aligner was used to expose AZ photoresist coated wafers. The samples then were developed in AZ 300 MIF developer, rinsed with IPA and dried with N_2.

A descum step with O_2 plasma (200 sccm) was performed in an IonWave10 microwave plasma system for 15 s to remove resist residue after the development step.

For all fabricated patterns (high and low feature density), a 20 nm thick chromium hard mask was deposited on the wafers with an electron-beam evaporator to transfer the pattern from the resist to the silicon substrates. We performed metal liftoff by placing samples in an acetone ultrasonic bath. Then the wafers were submerged in resist stripper and cleaned again with 15 s of O_2 plasma treatment.

To enhance diffraction efficiency of the patterns, trenches were etched via plasma etching of the silicon. Etching was done with an Oxford Plasmalab System 100 with a recipe that was originally designed for vertical sidewall etching of silicon waveguides (pressure = 15 mTorr, RF-Power = 30 W, ICP = 1200 W, 25 sccm of SF_6, 60 sccm of C_4F_8 and 5 sccm of Ar), at an approximate rate of 180 nm/min for 5–10 min, depending on the required depths for each pattern.

For optical characterization of patterns, samples were metallized with 70–80 nm of aluminum with an E-beam evaporator.

B. Characterization of Optical Diffraction Patterns

The diffraction patterns from arrays of hexagonal apertures and multimicrogratings were obtained by illuminating the samples with a laser beam with $\lambda = 532$ nm at normal incidence, passing through a small aperture on a screen located at 20 cm from the samples. The reflected diffraction patterns were projected onto the screen and photographed by a camera oriented at approximately 10° from the normal direction of the screen. Due to the variation in intensity distribution in the diffraction pattern, the areas of high intensity tend to saturate the camera sensor used to take the images and low intensity features are not well captured. A photographic technique called high dynamic range (HDR) photography has been used to overcome the issue of having to capture a wide range of exposures [15–17]. Images of diffraction patterns were captured at several exposure levels and then recombined to produce a more uniform intensity distribution allowing the capture of both high and low intensity details without saturation. This technique was applied to obtain high-quality images of the diffraction pattern.

C. Beam Profile Measurement Technique Using a CCD Camera

Commercial CCD beam profilers are expensive, but a cost-effective technique using the CCD camera found in a webcam was reported to produce accurate measurements of laser beam profiles [18]. To obtain the beam profile characteristics of the diffracted spots, samples were illuminated with a green laser diode with 532 nm wavelength, under two conditions: with a narrow probing beam size and with a 10× expanded beam. We did this to understand the effects of input beam width on diffracted beam profiles. For the first condition, the 1.2 mm laser beam width was used.

For the second condition, the beam was magnified by 10× to 12 mm in size using a beam expander. The lens of a commercial Intel CS110 webcam was removed to image the diffracted spots directly onto the CCD camera sensor. The intensity of the beams was attenuated with combinations of ND filters and polarizer to prevent saturation of the sensor. The CCD sensor had a resolution of 352×288 pixels, for a total sensor area of 2.84×2.33 mm. Pixel pitch was measured via an optical microscope and was found to be 8.08 μm. Images of the beams were then captured with freeware program QFocus. Intensity profiles were extracted from the captured images using ImageJ software. Beam profile data was then normalized and fitted to Gaussian beams using OriginPro to obtain measurements of the FWHM of the beams.

D. Diffraction Efficiency Measurements Using an Integrating Sphere

To measure the total diffraction efficiency of the samples, typically a laser beam of known power is incident on the grating sample. The power for each of the diffracted orders is then measured individually and the total efficiency can be calculated as the sum of the power of the diffracted beams (excluding the reflected zeroth order beam). Such measurement is simple for 1D gratings; however, for multiple diffracted orders or very complex diffraction patterns, capturing all the diffracted light is more complicated.

To overcome this obstacle, samples were positioned at the output port of an integrating sphere (Labsphere, Inc.), as shown in Fig. 3. Light incident from a green diode laser with 1.5 mm beam width and 7.3 mW measured power at 532 nm wavelength enters the integrating sphere via the input port and is incident on the sample. Samples were placed on a tilt mount, to adjust the direction of the reflected beam and to cause it to escape the integrating sphere back through the input port. All the light beams that get diffracted then get captured inside the integrating sphere, and bounce off the highly scattering walls until they are collected by a power meter located at the detector port. We can then calculate the total efficiency for any sample by finding the ratio of the total diffracted power as measured by the detector and the input laser power. The zeroth order power was measured separately to ensure all the power was accounted for.

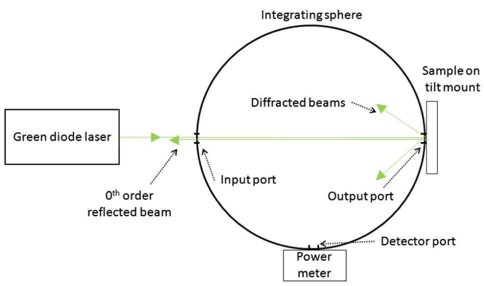

Fig. 3. Side view of experimental setup for diffraction efficiency measurement using integrating sphere.

Table 2. Integrating Sphere Measurement Calibration

Reflector Material	Expected Reflectivity at 532 nm (%)	Measured Reflectivity at 532 nm (%)
Gold	76.4	73.0
Silicon	37.4	36.3
80 nm Al on Silicon	92.2	87.0

Measurements are calibrated with three standard reflectors: a gold standard, a plain silicon wafer, and a silicon wafer coated with 80 nm aluminum film. Expected reflectivities for the different calibrated materials at 532 nm are obtained with a tool called a reflectance calculator (Filmetrics) and compared to the measured values using the integrating sphere technique. Table 2 summarizes the results. Measured values are found to be slightly lower than the expected reflectivities within a 5.1% error.

4. Results and Discussion

A. Morphology Results of Fabricated Samples

To examine the surface morphology of the fabricated silicon samples, scanning electron micrographs of the patterns were obtained. Figure 4(a) shows a SEM

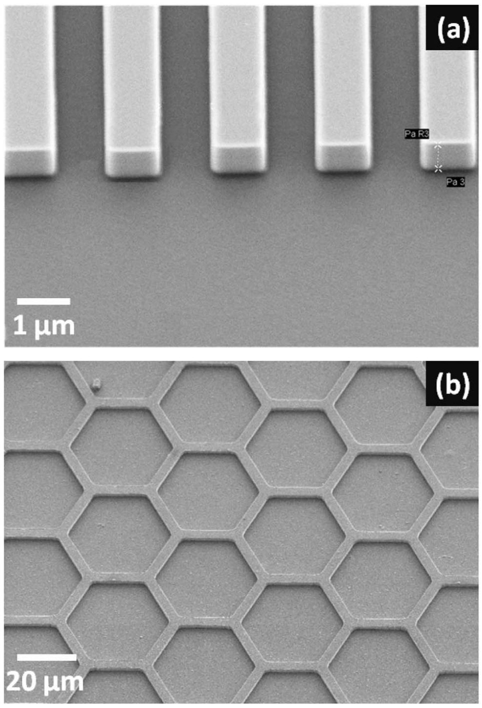

Fig. 4. SEM micrographs of fabricated samples with (a) 1D grating with period of 2.0 μm and (b) array of hexagonal apertures with hexagon side dimension of 20 μm.

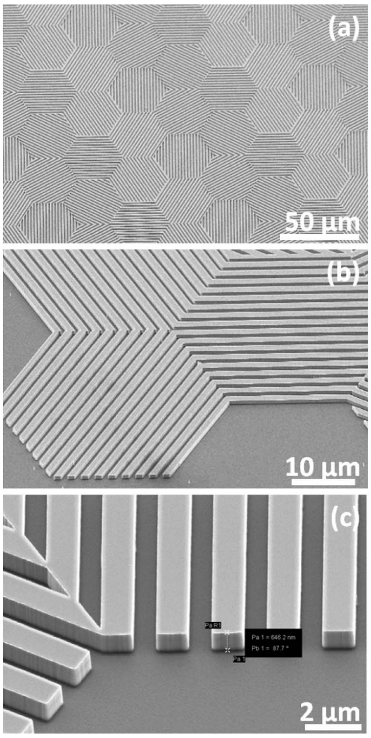

Fig. 5. (a) SEM micrograph of fabricated silicon sample with multimicrogratings with grating periods of 2.0 μm. Magnified details of regions around the edge of (a) are shown in (b) and (c).

micrograph of the fabricated sample with a 1D grating pattern (at a 30° tilt) for grating period of 2.0 μm. Figure 4(b) shows a SEM micrograph of the fabricated sample with the pattern of hexagonal apertures for cells with side dimension of 20 μm. Figure 5(a) shows SEM micrographs of the combined multimicrograting patterns with a 2.0 μm grating period and 20 μm hexagon side dimension. Figures 5(b) and 5(c) show images of (a) at higher magnifications.

From the SEM micrographs, it is possible to see that the samples were fabricated to the desired specifications. For patterns with high feature density, sample critical dimensions had to be adjusted in the EBL exposure step for PEC and for dimension bias, resulting in 50% duty cycle and precise grating period with no spatial variation of these dimensions in different parts of the 1.5 mm × 1.5 mm areas of the samples. The edges are well defined and the sidewall profiles are straight, which indicates that the recipe used for the etching process was appropriate.

The depth of the trenches can be extracted from the 30° tilted SEM micrographs. It was determined that they were very close to the specified depths of 0.95 and 1.95 μm, respectively, for samples with multimicrogratings and with hexagonal apertures. These measurements were also in agreement with profilometer data. Additionally, to verify the depth measurements, Fig. 6(a) shows a laser confocal micrograph of multimicrograting sample with 2.0 μm grating period, which shows a typical grating profile for the fabricated samples. To show the fabricated profile, Figs. 6(b) and 6(c) show a 3D profile and a linescan profile of a selected area. Similarly, the grating depths of samples with 1D gratings and hexagonal apertures were measured with laser confocal microscopy and were found to be in agreement with the other measurements.

B. Optical Diffraction Results

We will now discuss the details of the observed diffraction patterns of arrays of hexagonal apertures and microgratings. Details on the simulation of the diffraction properties of arrays of hexagonal

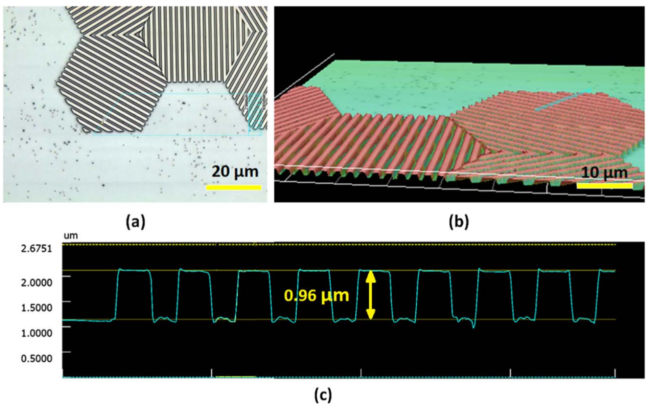

Fig. 6. Laser confocal micrographs of micrograting pattern with 2.0 μm periodicity. (a) Top view. (b) 3D height profile. (c) Linescan profile.

apertures, microgratings and other arbitrary designs will be published separately.

1. Optical Diffraction Pattern from Arrays Of Hexagonal Apertures

The diffraction pattern for arrays of hexagonal apertures, such as the one depicted in Fig. 4(b), is shown in Fig. 7(a). Figure 7(b) shows details of the center area of the pattern projected on a screen 300 cm away. Figure 7(c) shows a simulated diffraction pattern from the single hexagon shown in the inset. As described earlier, the diffraction from arrays of hexagonal apertures is contributed by the hexagonally shaped apertures and their periodic arrangement (Elements 1 and 2).

There are three main features observed in the diffraction pattern of hexagonal apertures. First, the center area of the diffraction pattern is shaped as the hexagon. Second, there are three lines oriented at 30°, 90°, and 150°. The central hexagon and lines can be seen in Fig. 7(c). The hexagonal cells act as individual apertures, and thus, they diffract light. In the vertical direction, the hexagon, comprised of two sides oriented parallel to each other, can be considered as an aperture in 1D space. That aperture, when illuminated with planar electromagnetic radiation, diffracts the incoming wave in the shape of a sinc^2 function in the direction perpendicular to the edges of the aperture. Thus, the illuminating light would produce a sinc^2 intensity distribution in a direction normal to the apertures. In this case, the 0° aperture produces an intensity distribution in the vertical direction. The other two pairs of hexagon sides (60° and 120°) produce two patterns (at their respective normals of 150° and 30°). Combining all three 1D apertures oriented at different angles generates the three lines. The central hexagon and lines do not appear as continuous features, as we describe below. Rather, they serve as an intensity envelope for the smaller individual diffraction spots.

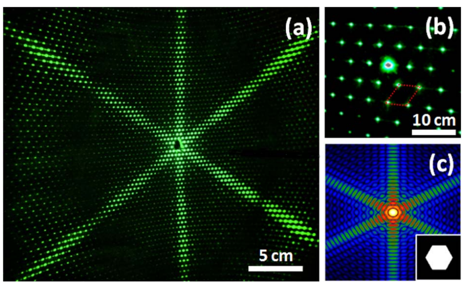

Fig. 7. (a) Observed diffraction pattern of sample with arrays of hexagonal apertures with hexagon side dimensions 20 μm and laser light with $\lambda = 532$ nm projected on a screen located 20 cm from the sample. The dark area in the center corresponds to the hole on the screen. (b) Details of the center area of the diffraction pattern are projected on a screen 300 cm away. (c) Simulated diffraction pattern for a hexagon, such as the one shown in the insert.

Third, as seen in Fig. 7(b), we observed small diffraction spots. They originated from the honeycomb lattice used to form the array of hexagons. The red parallelogram in Fig. 7(b) shows a periodic element that exists in the diffraction pattern. Each of the spots are all measured to be equidistant to each other, indicating that the lattice that produced these spots had two periodic elements of equal dimensions. The angular separation of the lattice spots is measured to be about 0.26° and is found to be in accordance with the calculated angle from the generating lattice of hexagonal apertures. Therefore, we concluded that the observed periodic elements in the diffraction pattern is reciprocal of the honeycomb lattice that originated the hexagonal aperture arrays. These lattice spots in the diffraction pattern also have varying intensity.

2. Optical Diffraction Results from Multimicrogratings

Figure 8(a) shows that the multimicrograting samples with grating period of 2.0 μm produced a very unique diffraction pattern. Figure 8(b) shows details of the diffraction pattern indicated in 8(a). To examine the finer details seen in Fig. 8(b), the screen was moved to a distance of 300 cm and a photograph was taken. Figure 8(c) shows results.

The diffraction pattern of the multimicrograting structures is composed of several prominent features that are a result of the multimicrograting constituting elements described earlier. The first feature can be seen in Fig. 8(a) as a set of 12 bright annular spots surrounding the central beam. For simplicity, these features are named after the hour hands of a clock. They originated from the periodic grating lines at six different orientations (Element 3). Consequently, these spots behave in accordance to the 1D grating

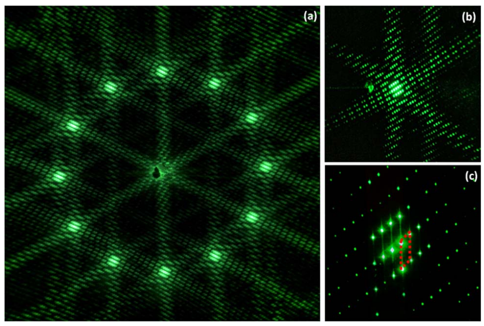

Fig. 8. (a) Observed diffraction pattern for multimicrograting on silicon with 2.0 μm period illuminated with laser with $\lambda = 532$ nm and projected on a screen 20 cm from the diffracting sample at normal incidence. The irregularly shaped area in the center corresponds to the hole in the screen onto which the diffraction pattern was projected. (b) Detail of one of the twelve spots shown in (a). (c) The same spot in (b) but projected on a screen 300 cm away, to show finer details.

equation. Each of the periodic micrograting orientations produces diffracted spots in a direction perpendicular to the grating lines, similar to a 1D grating. For example, for micrograting orientations of 0°, diffraction spots are produced in a vertical (90°) direction. For a grating orientation of 30°, the spots lie in a line oriented at 120°. Furthermore, similar to 1D gratings, each of the micrograting cells can produce positive and negative orders. Thus, the 0° microgratings produces the 12 and 6 o'clock spots around the central reflected spot. A similar analysis can be carried out for the other micrograting orientations, thus resulting in the twelve visible spots for the first order (negative and positive) spots.

The second feature, seen in Fig. 8(b), is generated by individual hexagons and their periodicity (Elements 1 and 2) and is observed at each of the individual annular spots in Fig. 8(a). Each of the 12 annular spots has the same features as shown in Fig. 8(b). The three lines and hexagonal shape of the spot observed in Fig. 8(b) are very similar to the diffraction pattern observed for hexagonal apertures, as seen in Fig. 7. The 1D diffraction grating spots act as centers for display of individual hexagonal diffraction patterns. The diffraction pattern from individual microgratings appears to be the superposition of diffraction patterns generated from individual periodic grating lines and hexagonal apertures.

The combined diffraction effect observed in microgratings happens when the incident light beam is diffracted by periodic grating lines, then the diffracted beams pass through the hexagonal apertures where additional diffraction occurs. So, it is like putting two optical elements—periodic gratings and hexagonal apertures—in sequence. The overall diffraction efficiency will depend upon the diffraction efficiency from the periodic grating lines and hexagonal apertures. It is clear that the diffraction spots occur as expected from the grating equation for periodic lines, but are transformed into patterns governed by the hexagonal apertures, which is a clear indication that there is an interaction between the two patterns.

The third feature, seen in Fig. 8(c), is formed by the oblique lattice formed from the unit cell that was used to generate the large area multimicrogratings, as shown by the red parallelogram drawn in Fig. 8(c). The six hexagonal microgratings were broken down into a unit cell that had dimensions a and b (related to the hexagon side dimension s), as shown in Fig. 1(b). The unit cell itself is skewed, as a is twice as long as b. Therefore, the periodicity of the unit cell is expressed in the diffraction pattern as a lattice depicted by the red parallelogram.

In other words, the diffraction pattern of multimicrogratings can be explained as the convolution of the different periodicities that form the arrays. It appears to have a spatial hierarchy for the existence of these cross-terms. The smallest observable features in the diffraction pattern [the lattice shown by the red parallelogram in Fig. 8(c)], which corresponds to the largest feature in the multimicrograting design (the unit cell that forms the arrays), is convoluted with the diffraction pattern of individual hexagonal apertures, thus creating the pattern seen in Fig. 8(b). In turn, the pattern seen in Fig. 8(b) is then convoluted with the 1D diffraction grating spot locations, creating the large and complex diffraction pattern of multimicrogratings seen in Fig. 8(a).

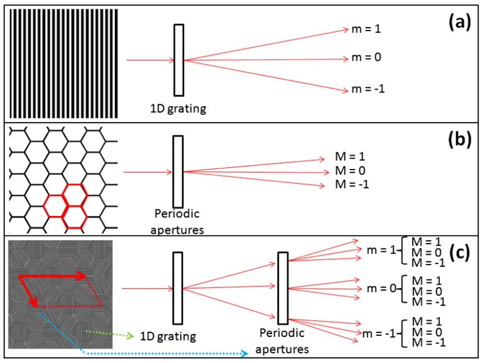

Fig. 9. Schematic of light distribution from fabricated samples for (a) 1D gratings, (b) arrays of hexagonal apertures, and (c) multimicrogratings.

To summarize, Fig. 9 shows a schematic diagram of what happens when light is diffracted from the fabricated samples. For 1D gratings, as it is depicted in Fig. 9(a), the incident beam encounters the periodic lines and thus is diffracted into a $m = 0$ beam and a positive and negative orders $m = \pm 1$. In the case of an array of hexagonal apertures, as it is portrayed in Fig. 9(b), the light is first incident on the periodic hexagonal apertures, depicted by the red hexagons in Fig. 9(b). This interaction both reshapes the beam into the shape of the diffraction pattern of a hexagonal aperture and diffracts the beam into orders $M = 0$ and ± 1, which due to the longer period between periodic hexagons, are closer together. Finally, when a light beam is incident on multimicrogratings, as shown in Fig. 9(c), the light first encounters the 1D grating and is separated into orders $m = 0$ and ± 1 and because the microgratings are hexagonally shaped, the diffracted beams are reshaped to look like the diffraction pattern of a hexagonal aperture. Each of those diffracted orders then interact with the periodicity of the nearest similarly oriented microgratings [depicted as the red parallelogram in Fig. 9(c)], and is further diffracted into $M = 0$ and ± 1.

C. Beam Profile Results

For a probing beam size of 1.2 mm, the total pattern size (1.5 × 1.5 mm) is larger than the probing beam. Figure 10 shows images and profiles of the beam captured with the CCD sensor at a sample-to-sensor distance of 30 cm. Figure 10(a) shows the beam image captured for a 1D grating sample, and the slice of the profile along the blue dotted line is shown in

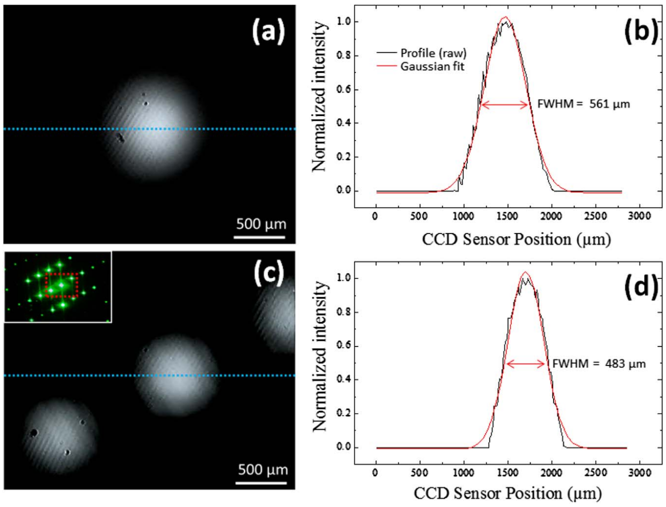

Fig. 10. Beam profiles obtained with CCD sensor at a sample-to-sensor distance of 30 cm and with a probing beam of 1.2 mm. (a) Beam profile for a sample with a 1D grating pattern. (b) Slice along blue dotted line of (a) to show raw beam profile and Gaussian fit to obtain FWHM. (c) Beam profile for a sample with multimicrograting pattern. (d) Slice along blue dotted line to show beam profile and Gaussian fit to obtain FWHM.

Fig. 10(b). Several images were captured and fitted to Gaussian beams to calculate an average FWHM of 562.1 μm, which is comparable to the input beam measured using the same technique to have a FWHM of 563 μm. Figure 10(c) shows an image of a captured beam for a sample with a multimicrograting pattern, specifically from the red rectangle region shown in the inset. The captured image shows almost three of the individual beams that were in the diffraction pattern, and their separation on the sensor of 1.25 mm corresponds to the expected separation (0.27°) of the beams at a sample to sensor distance of 30 cm. Figure 10(d) shows the profile along the blue dotted line in Fig. 10(c), with its corresponding Gaussian fit. Several images were used to compute an average FWHM of 482.4 μm, which is about 14.1% narrower than the FWMH for a 1D grating beam. The beams from 1D grating samples are observed to have a Gaussian profile of similar characteristics to the input laser beam, but for the micrograting, they are found to be slightly narrower. In the case of 1D grating samples, the incident Gaussian beam encounters one set of periodic apertures, distributing the light into diffracted beams each with a sinc^2 distribution. In the case of the multimicrograting samples, the incident beam encounters the periodic 1D grating lines and the periodic apertures, producing a sinc^4 distribution that is narrower.

For a probing beam with 12 mm width, the total pattern size is smaller than the probing beam, which becomes important as the probing beam now encounters the aperture shape of the total pattern size. Figure 11 shows beam profiles captured with the CCD sensor for an expanded probing beam, at a sample-to-sensor distance of 30 cm. Figure 11(a) shows the profile of a 1D grating sample when illuminated with an expanded probing beam. The

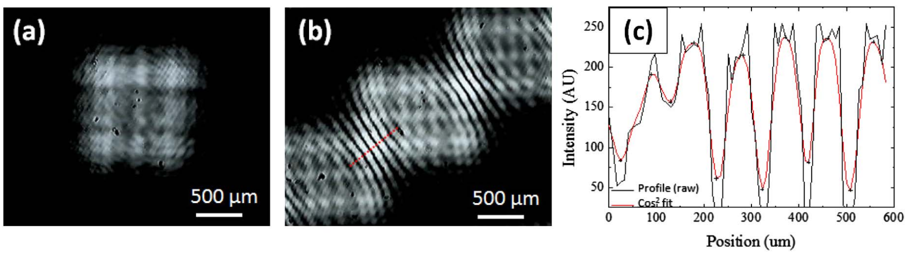

Fig. 11. Beam profiles captured with a CCD sensor with an expanded probing beam for at a sample-to-sensor distance of 30 cm. (a) For a sample with 1D grating pattern. (b) For a sample with multimicrogratings. (c) Slice profile of the interference fringes observed in (b).

sample had a pattern size of about 1.5×1.5 mm, and its sharp boundaries can cause the light to diffract into the pattern observed. The pattern corresponds to the Fresnel diffraction from a square aperture rather than Fraunhofer diffraction, as it would be expected for this wavelength, aperture size and sample to sensor distance (Fresnel number $F = 14.09$). The beam is square shaped, as the aperture, and was observed to have the same size of 1.5×1.5 mm at sample to sensor distances between 10 and 50 cm. Figure 11(b) shows the beam profile of a sample with multimicrograting patterns at a sample-to-sensor distance of 30 cm. The image now shows three separate diffracted beams from micrograting all incident on the sensor at the same time. They have a rectangular shape due to the expanded beam encountering the total pattern shape as an aperture and producing Fresnel type diffraction. Because three micrograting beams are incident on the CCD sensor, it causes them to overlap with each other, which produces the high contrast fringes. A slice profile of the interference fringes along the red line in Fig. 11(b) is shown in Fig. 11(c). The interference fringes are fitted to a $\cos^2(x)$ function, having a period between 90 and 100 μm at a sample to sensor distance of 30 cm. The three micrograting beams have an angular separation (0.27°) that causes them to separate as the distance from the sample increases, but at sample to sensor distances between 10 and 35 cm such interference is observed. At longer distances, the beams separate enough and no interference can be expected. For the particular beam profiles described in Figs. 11(b) and 11(c), bright areas of interference fringes are observed to have an average intensity of approximately 225 (arbitrary units), which drops to 10–15 between the fringes. In areas of non-interfering beams, the average highest intensity drops to 130. This change provides a large intensity contrast. The interference fringes provide very sharp, resolvable features that can be further exploited for increased resolution in sensing applications, which would otherwise be challenging with 1D gratings.

D. Diffraction Efficiency Results

Table 3 shows the measured total diffraction efficiencies for the fabricated samples, measured with the described integrating sphere technique. Reflected power is the measured power reflected from the zeroth order beam; that is, the light that does not undergo diffraction from the samples. Diffraction efficiency was optimized for 1D grating with trench depth of 0.95 μm, at $\lambda = 532$ nm. The total TE diffraction efficiency for silicon samples with 1D grating patterns was measured to be 33.7%. The addition of an 80 nm layer of Al on Si to increase reflectivity also increased TE diffraction efficiency by a factor of 2.3 to 76.7%. Samples with micrograting patterns in silicon were measured to have a total TE diffraction efficiency of 32.1%, which is nearly as high as the measured 1D grating diffraction efficiency. Micrograting samples with an 80 nm layer of Al on Si show an increased efficiency by a factor of 2.2, to 70.1%. Samples with hexagon arrays only, with an 80 nm layer of Al on Si were measured to have a 23.7% total TE diffraction efficiency. For clarity, only total TE diffraction efficiency measurements are shown, but total TM diffraction efficiencies also were measured and found to be in accordance with calculated values. The total diffraction efficiency of 1D gratings plays the biggest role in the multimicrograting diffraction efficiency, rather than the diffraction efficiency of the array of apertures. Diffraction efficiency can be tailored to increase it at particular wavelengths, orders and angles, depending on the application.

Table 3. Measured Total Diffraction Efficiency of Fabricated Samples

Sample	Reflected Power (%)	Total TE Diffraction Efficiency (%)
1D Grating	2.9	33.7
1D Grating w/80 nm Al	3.7	76.7
Micrograting	1.8	32.1
Micrograting w/80 nm Al	7.4	70.1
Hex. apertures w/80 nm Al	52.6	23.7

5. Conclusions

The optical properties of multimicrogratings have been characterized through electron-beam fabrication of 1D grating structures, periodic hexagonal apertures and multimicrogratings. We explained the complex optical diffraction pattern generated from multimicrogratings using an understanding of the optical principles that govern the diffraction from periodic structures. In summary, the diffraction pattern of multimicrogratings is formed by convoluting the individual diffraction patterns of the individual periodic elements that describe it: the hexagonal shape of the cells, the lattice that is formed with the periodic hexagons, and the 1D periodic grating lines oriented at six different orientations.

This convolution produces cross-terms that we have explained. The micrograting diffracted beam size seems to be slightly narrower than those for a similar 1D grating. Furthermore, depending on the plane of observation, multimicrograting diffracted beams can interact with each other, producing high-contrast interference fringes. Diffraction efficiency of multimicrograting samples was measured to be highly dependent on 1D grating parameters. For what we believe is the first time, we have provided a thorough understanding of the optical properties and diffraction and interference effects in multimicrogratings, which now can be used to tailor those properties for different applications. Further research must be done to study the various applications of these structures—for vapor, temperature, and strain sensing; and for nanometrology, optical telecommunications, and spectroscopy. Key parameters to understand include polarization-dependent losses, dispersion, and spectral resolution for such applications.

The authors would like to thank NSF I/UCRC and NASA Langley Professor programs for the partial financial support to this project. A portion of this research was conducted at the Center for Nanophase Materials Sciences, which is sponsored at Oak Ridge National Laboratory by the Scientific User Facilities Division, Office of Basic Energy Sciences, U.S. Department of Energy.

References

1. A. R. Parker and H. E. Townley, "Biomimetics of photonic nanostructures," Nat. Nanotechnol. **2**, 347–353 (2007).
2. R. A. Potyrailo, H. Ghiradella, A. Vertiatchikh, K. Dovidenko, J. R. Cournoyer, and E. Olson, "Morpho butterfly wing scales demonstrate highly selective vapour response," Nat. Photonics **1**, 123–128 (2007).
3. R. A. Potyrailo, Z. Ding, M. D. Butts, S. E. Genovese, and T. Deng, "Selective chemical sensing using structurally colored core-shell colloidal crystal films," IEEE Sens. J. **8**, 815–822 (2008).
4. A. D. Pris, Y. Utturkar, C. l. Surman, W. G. Morris, A. Vert, S. Zalyubovskiy, T. Deng, H. T. Ghiradella, and R. A. Potyrailo, "Toward high-speed imaging of infrared photons with bio-inspired nanoarchitectures," Nat. Photonics **6**, 195–200 (2012).
5. S. Zhu, D. Zhang, Z. Chen, J. Gu, W. Li, H. Jiang, and G. Zhou, "A simple and effective approach toward biomimetic replication of photonic structures from butterfly wings," Nanotechnology **20**, 315303 (2009).
6. K. Watanabe, T. Hoshino, K. Kanda, Y. Haruyama, T. Kaito, and S. Matsui, "Optical measurement and fabrication from a morpho-butterfly-scale quasistructure by focused ion beam chemical vapor deposition," J. Vac. Sci. Technol. B **23**, 570–575 (2005).
7. T. H. Wong, M. C. Gupta, B. Robins, and T. L. Levendusky, "Color generation in butterfly wings and fabrication of such structures," Opt. Lett. **28**, 2342–2344 (2003).
8. N. Yoshimizu, A. Lal, and C. R. Pollock, "MEMS diffractive optical nanoruler technology for tipbased nanofabrication and metrology," in *IEEE 22nd International Conference on Micro Electro Mechanical Systems (MEMS 2009)*, Sorrento, 2009, pp. 547–550.
9. N. Yoshimizu, A. Lal, and C. R. Pollock, "Nanometrology optical ruler imaging system using diffraction from a quasiperiodic structure," Opt. Express **18**, 20827–20838 (2010).
10. N. Yoshimizu, A. Lal, and C. R. Pollock, "Nanometrology using a quasiperiodic pattern diffraction optical ruler," J. Microelectromech. Syst. **19**, 865–870 (2010).
11. M. C. Gupta and S. T. Peng, "Diffraction characteristics of surface-relief gratings," Appl. Opt. **32**, 2911–2917 (1993).
12. M. G. Moharam and T. K. Gaylord, "Rigorous coupled-wave analysis of planar-grating diffraction," J. Opt. Soc. Am. **71**, 811–818 (1981).
13. M. G. Moharam and T. K. Gaylord, "Rigorous coupled-wave analysis of metallic surface-relief gratings," J. Opt. Soc. Am. A **3**, 1780–1787 (1986).
14. M. G. Moharam and T. K. Gaylord, "Diffraction analysis of dielectric surface-relief gratings," J. Opt. Soc. Am. **72**, 1385–1392 (1982).
15. S. Teichmann, B. Chen, R. A. Dilanian, P. Hannaford, and L. Van Dao, "Experimental aspects of multiharmonic-order coherent diffractive imaging," J. Appl. Phys. **108**, 023106 (2010).
16. F. Pesty, P. Garoche, and S. Dorel, "Modulation of the beam intensity for high-dynamic-range low energy electron diffraction," J. Appl. Phys. **92**, 3021–3026 (2002).
17. R. L. Sandberg, A. Paul, D. A. Raymondson, S. Hädrich, D. M. Gaudiosi, J. Holtsnider, R. I. Tobey, O. Cohen, M. M. Murnane, H. C. Kapteyn, C. Song, J. Miao, Y. Liu, and F. Salmassi, "Lensless diffractive imaging using tabletop coherent high-harmonic soft-x-ray beams," Phys. Rev. Lett. **99**, 098103 (2007).
18. G. Langer, A. Hochreiner, P. Burgholzer, and T. Berer, "A webcam in bayer-mode as a light beam profiler for the near infrared," Opt. Lasers Eng. **51**, 571–575 (2013).

Simulation of optical diffraction properties of multi-microgratings

Christian A. Rothenbach and Mool C. Gupta*

Department of Electrical and Computer Engineering,

University of Virginia, Charlottesville, Virginia 22904, USA

Abstract

Modeling and simulation of the 1D and 2D diffraction patterns from complex periodic structures such as arrays of apertures or arrays of microgratings is presented. Two different approaches are analyzed. First, a mathematical model is derived from the Fraunhoffer intensity distributions of the diffraction patterns of periodic structures that can be used to simulate the diffraction patterns of highly periodic structures. Second, a graphical Fourier Transform approach is described, which overcomes certain limitations imposed by the intensity based approach. Simulated diffraction patterns obtained with the two methods are compared to the diffraction patterns of fabricated samples. It is found that the diffraction pattern of highly complex structures is generated by the combination of the different periodicities that compose the system, as those periodicities all contribute to their diffraction patterns, but it is also shown that the interaction between the different periodicities can give rise to highly sensitive cross terms.

Keywords: diffraction grating, grating array, Fourier transform, diffraction pattern simulation, micro-gratings

* Corresponding author, e-mail: mgupta@virginia.edu.

1. Introduction

Naturally occurring optical phenomena such as those found in moth eyes or butterfly wings have been studied in order to exploit their unique optical properties for different applications [1]. For example, studies of blue *morpho* butterfly wing scales, which are composed of optical structures akin to 3D photonic crystals, have been shown that the wings could be used in thermal and vapor sensing, high speed imaging and other applications [2–4]. It is, however, inconvenient to use actual wing scales due to their scarcity and brittle nature, so artificial fabrication of bio-inspired optical structures has become a growing field. Furthermore, complex 3D structures that mimic optical properties found in nature involve complicated and expensive fabrication procedures [5, 6]. Thus, devices with similar optical properties as bio-inspired structures that can be fabricated more easily and cost-effectively are desired.

One such approach to use an alternative method to produce devices with similar optical properties as those found in *morpho* wing scales was analyzed by Wong et al. [7]. The authors describe a planar array of multi-micrograting cells which consisted of hexagonally shaped individual microgratings in different orientations which used the effects of diffraction to produce a blue color that can be seen from different angles. Their periodic structures produced complex diffraction patterns and understanding how diffraction patterns are formed is the main focus of the current study. We have measured the optical diffraction properties of fabricated micrograting structures and results have been published [8]. In this manuscript, we focus on simulation of optical diffraction properties of multi-microgratings.

Micrograting cells of six possible grating orientations, can be grouped up together into a repeating cell as seen in Figure 1(a), with grating period d and hexagon side s. The repeating cell can be arrayed, resulting in a large area pattern that can be seen in Figure 1(b). Upon closer inspection, and also shown in Figure 1(b), the array can be described by a unit cell indicated by the red parallelogram with vectors $\vec{a}$ and $\vec{b}$. The vectors $\vec{a}$ and $\vec{b}$ can be used to translate the unit cell and produce the large areas.

The authors have previously used the indicated design for the fabrication and measurement of the optical properties of arrays of micrograting. A complex diffraction pattern

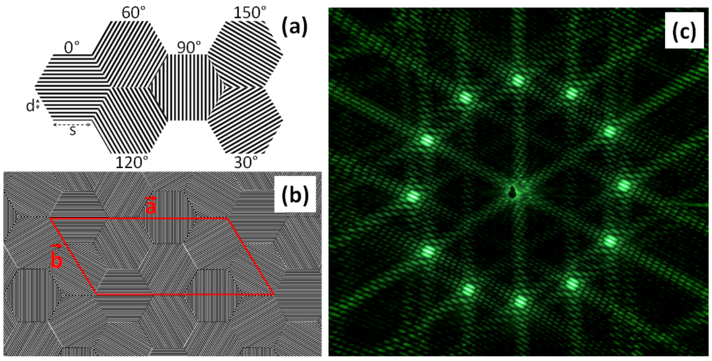

Fig. 1. (a) Micrograting repeating cell with six possible orientations. s is the hexagon side dimension and d is the grating period. (b) Array of multi-microgratings, with the red parallelogram defining the unit cell that was used to form the array, with sides a and b. (c) Photograph of screen projection of a normal incidence, optical diffraction pattern by multi-micgrograting array with d = 2 μm, and s = 20 μm and laser light wavelength λ = 532 nm.

was observed, such as the one seen in the photograph shown in Figure 1(c). This shows a screen projection of a diffraction pattern of a micrograting array with d = 2 μm, and s = 20 μm fabricated on silicon samples. The diffraction pattern produced by micrograting arrays can be very intricate, with several features with high and low intensity.

Optical diffraction occurs when a beam of light is incident on an aperture that has a wavelength comparable to the aperture size. The intensity distribution of the light after the aperture changes as a function of the aperture size and radial distance.

The grating equation, seen in Equation 1, describes a method to calculate the m^{th} order diffraction angle θ_d for a light beam of wavelength λ, incident at an angle of θ_i with respect to the grating normal.

$$d(\sin\theta_i + \sin\theta_d) = m\lambda \qquad (1)$$

The grating equation only provides the angular behavior of diffraction from simple 1D grating structures for a given set of parameters, with no information regarding light intensity anywhere on the pattern. Furthermore, it falls short when trying to explain more complicated periodic structures, such as two dimensional arrays of apertures or microgratings.

Because of the limitations imposed by the grating equation, there is a need to describe the complex diffraction patterns produced by multi-mcirogratings. The current work reports the origins of the features found in the diffraction patterns from multi-microgratings through simulation using analytical and graphical approaches. Such understanding can also be extended to explain the features in other periodic designs.

2. Simulation methods

2.A. Fraunhoffer intensity distribution approach to simulate 1D multi-microgratings

In the Fraunhoffer approximation, the angular intensity distribution of the diffraction patterns from several types of apertures, such as rectangular or circular and diffraction gratings have been formally described by solving the Kirchoff diffraction integral [9, 10]. Alternatively, if arranged properly, the diffraction integral can be seen as having the form of a Fourier Transform of the apertures and thus it is solved using a Fourier Transform technique.

The normalized diffraction intensity distribution for a 1D grating system consisting of n grating elements is made of two terms and is given by Equation 2, where $I(\theta)$ is the diffraction intensity as a function of the incident angle θ and I_0 is the intensity of the incident wave. The first term, also known as the diffraction factor, is the intensity distribution for a single aperture of width a and it acts as an envelope function. The second term, the interference factor, takes into account the contribution of different grating elements separated by the grating period d. A convolution of the two terms results in the diffraction intensity for a periodic diffraction grating, with the first term functioning as an envelope. Often, the interference is not considered when describing a diffraction pattern in order to be able to clearly distinguish weaker features that would otherwise be obscured by the envelope function.

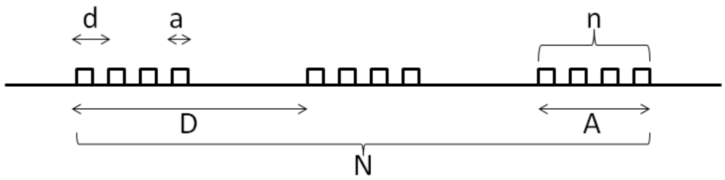

Fig. 2. 1D array of micrograting cells, with n grating lines of width a separated by period d; and N apertures of width A separated by D.

$$\frac{I(\theta)}{n^2 I_0} = \underbrace{[\mathrm{sinc}(a\nu)]^2}_{\text{Diffraction factor}} \cdot \underbrace{\left[\frac{\sin(nd\nu)}{\sin(d\nu)}\right]^2}_{\text{Interference factor}} \text{ where } \nu = \frac{\pi}{\lambda}\sin(\theta) \tag{2}$$

Interestingly, the solutions for the local maxima of Equation 2 can be found to be the angles described by the grating equation (Equation 1). Also, for $n = 1$, Equation 2 reduces to the intensity distribution of a single aperture.

The same analogy can be extended to explain systems with complex periodicities, in which the intensity distribution functions for the different periodicities can be convoluted with each other to obtain the overall system's intensity distribution. Arrays of multi-microgratings (similar to the one shown in Figure 2), in 1D, can be understood as the combination of the 1D pattern of the microgratings and the 1D pattern of the arrayed apertures. A 1D micrograting array is depicted in Figure 2, where d is the grating period, a is the grating line width, n is the number of periodic grating lines, D is the separation between different apertures, A is the aperture width and N is the number of different periodic apertures. Thus, in the general case, the 1D multi-micrograting diffraction intensity distribution function I_{mmg} can be interpreted as the convolution of the intensity distribution functions for the two individual periodic elements, and is shown in Equation 3.

$$I_{mmg} = I_{microgratings} \cdot I_{apertures} \tag{3}$$

The multi-micrograting intensity, I_{mmg}, is given by Equation 2. For the periodic aperture intensity, $I_{apertures}$, a similar function is derived for a system with N apertures with width A, separated by a distance D. Combining all the terms, the normalized Fraunhoffer intensity distribution for 1D multi-microgratings can be described as shown in Equation 4.

$$\frac{I_{mmg}(\theta)}{n^2N^2I_0} = [\mathrm{sinc}(a\nu)]^2 \cdot \left[\frac{\sin(nd\nu)}{\sin(d\nu)}\right]^2 \cdot [\mathrm{sinc}(A\nu)]^2 \cdot \left[\frac{\sin(ND\nu)}{\sin(D\nu)}\right]^2 \tag{4}$$

Equation 4 above will be used to simulate the diffraction pattern of an array of 1D microgratings, where Equation 4(b) represents the micrograting intensity and Equation 4(c) represents the aperture intensity.

2.B. Fraunhoffer intensity distribution approach to simulate 2D arrays of apertures

The previously presented method for simulating the diffraction patterns of 1D arrays of microgratings can be further extended to simulate 2D diffraction patterns of different aperture shapes. As long as the aperture shapes can be described mathematically, it is possible to simulate the diffraction patterns by convoluting the aperture functions in each independent direction. Mathematical descriptions for different types of apertures and their diffraction patterns have been reported [11–13].

Consider a single rectangular aperture with two independent dimensions x and y (with sides oriented at 0° and 90°). Its diffraction pattern is the the 2D intensity distribution given by θ_x and θ_y, and it is the convolution of the 1D intensities in in the x and y directions. This diffraction pattern has a rectangularly shaped central lobe (orthogonally rotated to the original aperture), and modulated tails that extend past the central lobe. The 0° sides of the rectangular aperture give rise to the diffraction pattern in the vertical (90°) direction, and the 90° sides of the aperture gives rise to the diffraction pattern in the horizontal (0°) direction. Additionally, due to the convolution of the two functions, weaker cross terms appear as well.

Now, consider a single hexagonal aperture (with sides oriented at 0°, 60° and 120°). Each of the side pairs acts as an aperture in at directions 30°, 90° and 150°, respectively. Therefore, the diffraction pattern of a hexagonal aperture has a hexagonally shaped center lobe, with tails extending from the center lobe sides in the 30°, 90° and 150° directions.

2.C. Graphical Fourier Transform approach to simulate diffraction from 2D arrays of apertures

As apertures become more complex, finding appropriate 2D mathematical descriptions of the apertures becomes cumbersome. However, as mentioned earlier, the solutions to the Kirchoff integrals can also be obtained by the Fourier Transform method. The diffraction integrals can be thought of as a coordinate transformation between the aperture plane (the functions that describe the apertures or gratings) and the image plane (where the diffraction pattern is projected). In other words, in the Fraunhoffer regime, the diffraction pattern can be described as the Fourier Transform of the aperture function. The same analogy applies to a graphical representation of the aperture or grating plane, with the resulting graphical Fourier Transform being the simulated diffraction pattern of the aperture [14–17].

Images of different aperture shapes can be described with a graphical Fourier Transform technique to obtain their diffraction patterns. By carrying out a FFT (Fast Fourier Transform) of the image of the aperture, the $x - y$ coordinates of the pixel locations in the image are transformed to $\theta_x - \theta_y$ space, obtaining the aperture's diffraction pattern. Spatial distance information from the original aperture image has to be used to calibrate the simulated diffraction pattern in angular space.

2.D. Finite-Difference Time-Domain (FDTD) method to simulate multi-microgratings

The FDTD method is a numerical analysis method that was first proposed by Yee to approximate the time-dependent Maxwell equations for electromagnetic fields [18, 19]. A two-dimensional model is devised, with an electromagnetic wave propagating in the XY plane, with a transverse component H_z [20]. The boundaries are defined to be absorbing with a perfectly matched layer (PML). The grating device is defined as a perfect electric conductor (PEC), by setting the electric field components to zero in those regions.

At each instant in time, the electric field vectors are solved first, followed by the magnetic field vectors in the next time iteration. The result is a time evolution of the electric field. Since the electric field is proportional to the intensity of the wave, then it can be used to understand how the electromagnetic wave interacts with the diffraction gratings. For the simulation, because of the short distances, the solved electric fields are in the near field. A spatial Fourier transform of the field is then used to approximate the intensity in the far field.

A MATLAB implementation of this method was created and the results are presented in the Results section. Since this method is computationally and memory intensive, the size of the grid was carefully chosen so as to be able to run the simulations in time-efficient manner. Due to its complexity, only a 1D model of a grating was solved for.

2.E. Multi-micrograting diffraction efficiency simulations

The diffraction efficiency, η, is defined as the ratio of the diffracted and incident powers of a wave that is incident on a diffraction grating. In other words, the diffraction efficiency is the proportion of the intensity that is distributed to each of the diffracted orders, as it can be seen in Equation 5:

$$\eta = P_{diffracted}/P_{incident} \tag{5}$$

Diffraction efficiency greatly depends on several parameters such as incident angle, substrate material, incident polarization, wavelength, grating period, depth, shape and duty cycle [21–24]. For large multi-micrograting arrays, the majority of the patterned sample surface area will consist of 1D gratings contained within the microgratings. Therefore, it is expected that the greatest contribution to diffraction efficiency will be from the 1D grating parameters in the microgratings.

In order to simulate multi-micrograting diffraction efficiency, commercial software (GSolver V52 Demo, Grating Software Development, Co.) was used to optimize the total diffraction efficiency for a normally incident plane wave of wavelength $\lambda = 532$ nm with transverse electric (TE) polarization. For samples with multi-micrograting patterns, 2 μm period rectangular gratings with 50% duty cycle on a silicon substrate were chosen to determine the optimal depth of the gratings in order to maximize first order diffraction efficiency. Total TE diffraction efficiency was then calculated by adding the calculated diffraction efficiencies for the first 4 orders.

A similar method was used to calculate the diffraction efficiency of samples with hexagonal apertures on silicon. With a 20 μm hexagon cell size, the period between adjacent hexagons was calculated to be 34.67 μm. A linewidth of 3.0 μm was selected for the width of the hexagon lines, which means the effective apertures were 31.67 μm in size. The distance between adjacent hexagons and the linewidth was used to approximate the hexagonal apertures as 1D gratings with a duty cycle of 0.087%. Due to the longer grating period, the first 50 orders were taken into account to calculate the total TE diffraction efficiency of samples with hexagonal apertures.

3. Simulation results

3.A. Simulation of diffraction patterns of 1D multi-microgratings

Equation 4 was used to simulate the diffraction pattern of 1D micrograting arrays, for a system with 1D gratings and large apertures at wavelength of $\lambda = 532$ nm. The diffraction factor was ignored in the interest of presentation and to normalize the intensity at different angular locations in the patterns.

The normalized intensity distribution for a 1D system with 1D gratings can be seen in Figure 3(a), with grating parameters: period d = 2.0 μm, width a = 1.0 μm and n = 5 lines. The normalized intensity distribution in 1D for the system with periodic apertures can be seen in Figure 3(b), with aperture parameters: period D =34.6 μm, A = 31.6 μm, N = 5 slits. Due to the fact that the diffraction factor was ignored in the interest of presentation, the 1D grating width a and aperture width A do not affect the patterns. Combining the two periodicities together, a micrograting array is formed and its diffraction pattern is shown in Figure 3(c).

As it can be seen, the diffraction patterns of the 1D grating system in Figure 3(a) and periodic aperture system in Figure 3(b) correspond to the 1D diffraction patterns for the given parameters. The areas of maximum intensity correspond to the angles calculated by the grating equation, and their angular separation is determined by the grating periods and aperture separation and the wavelength used. When the two functions are convoluted,

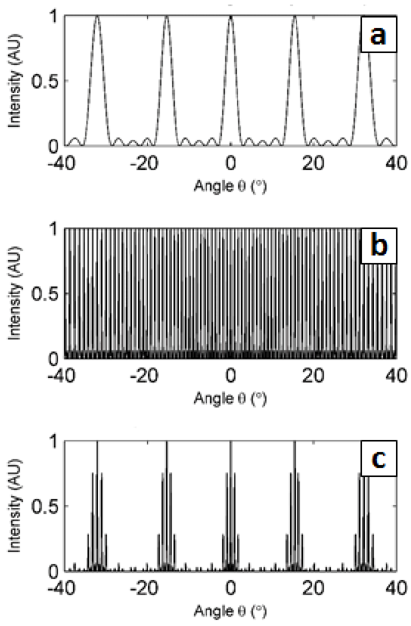

Fig. 3. Fraunhoffer intensity distribution based simulated diffraction pattern for a 1D array of microgratings. (a) Normalized intensity distribution for 1D gratings with d = 2.0 μm, a = 1.0 μm, n = 5 slits. (b) Normalized intensity distribution for periodic apertures with D =34.6 μm, A = 31.6 μm, N = 5 periodic apertures. (c) Normalized intensity distribution of combined 1D gratings and apertures with the respective parameters given in (c) and (d).

the 1D diffraction pattern of micrograting arrays is formed, which show very defined, sharp features from the periodic aperture system and their intensity determined by the 1D grating envelope.

3.B. Formation of the 2D diffraction pattern of arrays of hexagonal apertures

The formation of the 2D diffraction pattern of arrays of hexagonal apertures can be seen in the simulation results in Figure 4. The patterns were simulated using the Fraunhoffer intensity distribution method and the graphical Fourier Transform method. Hexagonally

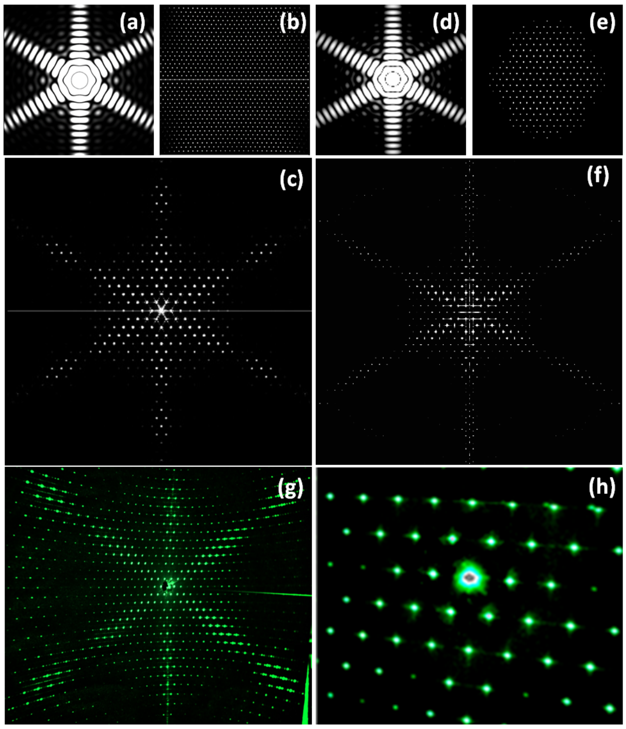

Fig. 4. Formation of the 2D diffraction patterns from arrays of hexgonal apertures with hexagon side of 20 μm and separation of 34.6 μm. (a-c) show simulations using the Fraunhoffer intensity distribution method and (d-f) using the graphical Fourier Transform method for a single hexagonal aperture, an array of honeycomb centers, and an array of hexagonal apertures respectively. (g) Experimental diffraction pattern of a fabricated array of hexagonal apertures in silicon, with the given dimensions, illuminated by 532 nm laser light and projected on a screen 20 cm from the sample. (h) Magnification of the central area of (g) by locating the screen 300 cm away from the fabricated sample.

shaped apertures with 20 μm hexagon side lengths were arrayed in a honeycomb lattice that separated the hexagonal aperture centers by a distance of 34.6 μm.

The diffraction pattern from hexagonal aperture arrays receives two main contributions. The first contribution is from the diffraction effects from the hexagonal aperture itself. Using an adapted mathematical representation of a 2D hexagonal aperture [11–13], a simulation of a single hexagonal aperture using the intensity distribution approach is shown in Figure 4(a). Alternatively, Figure 4(d) shows a simulated diffraction pattern using the graphical Fourier Transform approach, which was obtained by plotting the graphical Fourier Transform of the image of a hexagonal aperture. As it can be seen in the figures, the two methods that were used to predict the diffraction patterns of single hexagonal apertures present nearly identical results. A hexagonally shaped center lobe is formed with long, modulated tails emanating from the pairs of hexagon sides. These tails grow dimmer in intensity the further away from the center of the hexagon. They also have areas of high and low intensity. The diffraction effects from the three pairs of sides interact with each other, producing cross terms which exist in between the long diffraction tails.

The second contribution to the diffraction pattern of arrays of hexagonal apertures comes from the honeycomb array. The hexagon centers are located 34.6 μm from each other. Thus, taking just the coordinates of the centers of the each of the hexagons in the array, a rhomboidal unit cell is formed. In turn, when diffracted, they produce an array of equidistant spots in orthogonal directions. Figure 4(b) was created by plotting the diffraction intensity distribution of a 2D mathematical representation of a hexagonal (honeycomb) array. Such array can be formed by convoluting Equation 2 in three different angular directions, and letting n become large (n >20), resulting in delta-like points which locate the hexagon centers of the honeycomb array. In the interest of presentation, the simulation in Figure 4(b) used $n = 5$. Analogously, Figure 4(e) shows the simulated diffraction pattern of a graphical honeycomb array by the Fourier Transform method. As it can be seen in both simulated patterns, the rhomboidal unit cell that forms the honeycomb lattice produces a rotated honeycomb lattice in the diffraction pattern.

By combining the two contributing effects of hexagonal apertures and honeycomb array, the diffraction pattern of arrays of hexagonal apertures was simulated and it can be seen in Figures 4(c) and (f), respectively via the intensity distribution and graphical Fourier Transform methods. The two simulations appear to be very similar. The diffraction pattern consists of a honeycomb array of spots shaped by the envelope of the hexagonal aperture patterns. Some graphical artifacts are observable in both simulated patterns, but their general shape is very similar.

For comparison, Figure 4(g) shows an experimentally photographed diffraction pattern produced by illuminating a fabricated silicon sample with a hexagonal array of apertures with laser light of $\lambda = 532$ nm as projected on a screen located 20 cm from the grating surface. The hexagons had 20 μm sides and were separated by 34.6 μm. Figure 4(h) shows the central area of the experimental diffraction pattern in Figure 4(g), projected at 300 cm instead to show the distribution of the spots. Both simulated patterns appear to be very similar to the observed diffraction patterns, predicting the existence of the different features.

3.C. Formation of the diffraction pattern of multi-microgratings

To understand how the diffraction pattern from multi-microgratings is formed, it is necessary to understand how each of the periodicities in the array contributes to the whole diffraction pattern. A graphical Fourier Transform approach was used. Revisiting Figure 1(a) and (b), micrograting array parameters are set as follows: hexagon side dimension s = 20 μm, micrograting period d = 2.0 μm, vector $\vec{a}$ = 120 μm at 0° and vector $\vec{b}$ = 60 μm at 120°, wavelength $\lambda = 532$ nm.

First, it is necessary to understand the various contributions to the diffraction pattern of the microgratings. The difraction pattern of each micrograting cell receives contributions from the two elements that form it: the 1D grating element of each micrograting and the hexagonal shape of that micrograting. Figure 5 shows the simulated patterns of the apertures with microgratings shown as the insets via the graphical Fourier Transform approach. Figures 5(a) and (b) show the simulated pattern for a micrograting cell with a grating oriented at 90° and 30°, respectively. As expected, the 1D grating orientation produces positive and negative orders, arranged radially outward along direction perpendicular to each orientation (0° and 120°). Orders $m = 1$ and $m = 2$, labeled as A and B in Figures 5(a) and (b), are found to correspond to the angular position that is described by the grating equation. A and B both have the same shape as the diffraction pattern

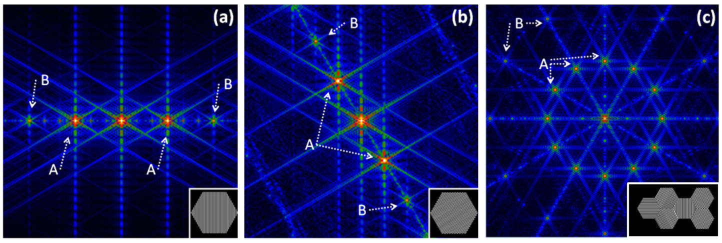

Fig. 5. Graphical Fourier Transform simulations of micrograting diffraction patterns for (a)single micrograting oriented at 90°,(b)single micrograting oriented at 30° and (c)collection of six migratings. Insets shown are the images used to simulate diffraction patterns. Labels A and B indicate first and second orders respectively.

of a single hexagonal aperture (described earlier in Figure 4). Thus, it is shown that the diffraction pattern of each micrograting cell is formed by the convolution of the diffraction patterns of 1D gratings and of hexagonal apertures.

Figure 5(c) shows the simulated diffraction pattern of the six combined micrograting cells. This diffraction pattern has a central spot, surrounded by a ring of 12 first order spots, labeled A. For simplicity, it is possible to refer to the 12 spots as the hours in a clock. Radially outward from each of the 12 spots in the ring are 12 more spots, of lower intensity, forming a second ring, labeled B. Each spot in the rings is equidistant to the center spot. The two rings of spots, A and B, correspond to the first and second orders, respectively, for each of the micrograting orientations. Given that there are six possible angular orientations of the grating periods within the micrograting cells, then each angular orientation produces diffracted spots in the corresponding perpendicular direction. For example, for micrograting orientations of 0°, spots are produced in a vertical (90°) direction, or the spots in the 12 and 6 o'clock positions (one being the positive first order, and the other the negative). For a grating orientation of 30°, the spots lie in a line that is oriented at 120°, or the 5 and 11 o'clock spots. A similar analysis can be carried out for the other micrograting orientations, thus resulting in the twelve visible spots for the first order (negative and positive) spots and 12 more for the second order if the grating equation is satisfied for that particular order.

Now, in order to generate large area arrays of microgratings, the unit cell described by Figure 1(b) is used, adding the periodicity of the array itself. Figure 6(a) shows the simulated diffraction pattern via graphical Fourier Transform of a large area array of microgratings. Figure 6(b) shows the magnified image of one of the 12 spots in Figure 6(a). Figure 6(c) shows detail of one of those spots in 6(a). As it can be seen, the diffraction pattern of a large array of microgratings becomes the convolution of the diffraction pattern of a six micrograting array, such as that in Figure 5(c), and that of a set of multiple apertures separated by vectors $\vec{a}$ and $\vec{b}$. The diffraction pattern from the array formed by vectors $\vec{a}$ and $\vec{b}$ is manifested by the white parallelogram inscribed in Figure 6(c), which has vectors orthogonal to $\vec{a}$ and $\vec{b}$ at 90 ° and 30° respectively. For comparison, Figure 6(d-f) show experimental diffraction patterns captured for micrograting arrays at similar magnifications.

It can be seen that the experimentally observed diffraction patterns of arrays of microgratings are very similar to their simulated patterns, confirming that their diffraction pattern is formed by the different periodicities found in the arrays. The micrograting period forms positive and negative orders around the central spot. Due to the hexagonal shape of the micrograting, each of the positive and negative spots are shaped like the diffraction pattern of a hexagonal aperture. Finally, the vectors used to create the array of microgratings appear in the diffraction pattern, giving rise to an array of spots in a grid like fashion, described by a rhomboidal unit cell.

In summary, it is possible to understand diffraction patterns from multi-microgratings and other periodic structures by breaking the patterns down to their individual optical periodic components and studying their diffraction properties as sequential optical elements. For 1D gratings, the incident beam encounters the periodic lines and thus is diffracted into a reflected or transmitted order $m = 0$ beam and $m = \pm 1$, ± 2, ± 3, ± 4... orders. Figure 7(a) has a schematic diagram of what happens to a beam that is incident on a sample with 1D diffraction gratings. In the case of an array of hexagonal apertures, the diffraction pattern can be understood as the diffraction from a single hexagonal aperture, which reshapes the beam into the shape of the diffraction pattern of a hexagonal aperture but does not break the beam up into diffracted orders. The beam gets modified

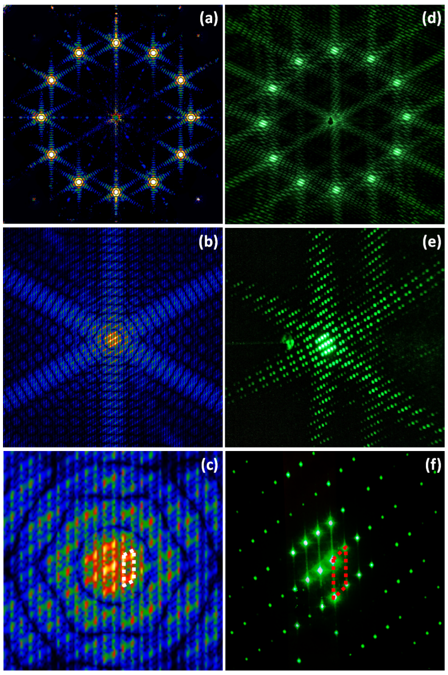

Fig. 6. Simulated via graphical Fourier Transform and observed diffraction patterns of an array of hexagonally shaped microgratings with $s = 20$ μm, $d = 2.0$ μm, vector $\vec{a} = 120$ μm at 0° and vector $\vec{b} = 60$ μm at 120°, wavelength $\lambda = 532$ nm.(a) The 12 spots shown correspond to the positive and negative orders of each micrograting orientation. (b) Magnification of one of the 12 spots seen in (a). (c) Higher magnification of a spot in (a), showing the periodic nature of the small features produced by the large area array. (d-f) Experimentally observed diffraction patterns at similar magnifications as those in (a-c).

by the periodic hexagonal apertures. It is, thus, further diffracted into orders $M = 0$ and closely-spaced, multiple $\pm$ higher orders due to the longer period between adjacent hexagons. This phenomenon is schematically described in Figure 7(b). Finally, when a light beam is incident on multi-microgratings, the diffraction pattern can be understood as the light first encounters the 1D grating and is separated into orders m =0, ±1, ±2,

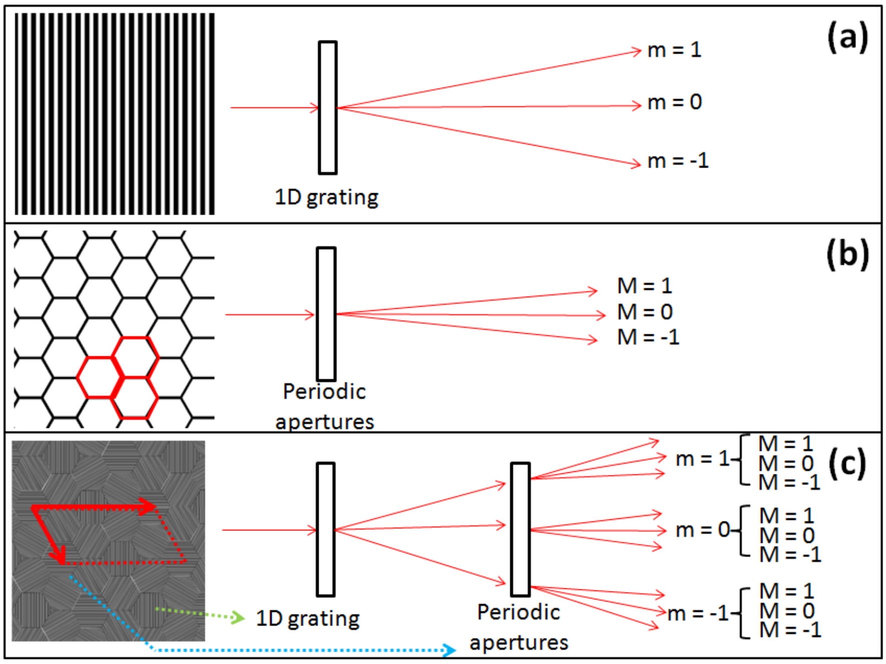

Fig. 7. (a) Distribution of light in a sample with 1D diffraction grating. (b) Distribution of light in a sample with periodic apertures.(c) Distribution of light in a sample with multi-microgratings.

±3, ±4.... Each of those orders then interact with the single hexagonal aperture of the micrograting, and are reshaped to look like the diffraction pattern of a hexagonal aperture. Furthermore, the m^{th} order diffracted beams then encounter the periodicity of the nearest similarly oriented microgratings, and are further diffracted into $M = 0$, ±1, ±2, ±3, ±4... orders. This is exemplified in Figure 7(c).

3.D. FDTD simulations of multi-microgratings

FDTD simulations were carried out to study the time-dependence of the electric field along the z direction, E_z, for a monochromatic sinusoidal electromagnetic wave incident on diffracting apertures defined by PECs.

with , to interact with the sinusoidal EM wave with 532 nm wavelength in vacuum with .

The following parameters were used to simulate the interaction of a multi-micrograting with an EM wave of 532 nm wavelength: 2.0 μm grating period, 1.0 μm grating width, 5 slits, 4 micrograting cells separated by 34 μm, a grid size of 50 nm, electric permittivity ε_0 of $0.0278 * 10^{-9} F/m$ and magnetic permeability μ_0 of $12.56 * 10^{-7} H/m$. The results are shown in Figure 8(a). Each micrograting produces diffracted beams that travel parallel to the diffracted beams of the other microgratings. Since they are parallel, diffracted beams of a particular order (m = 1 for example) produced by different microgratings will not interfere with each other. However, as it can be seen from the figure, there are areas where the diffracted beam of the left most micrograting interacts with the zeroth order beam from the second micrograting at a Y distance of 200 μm. The same can be said more of the beams at particular distances. In those locations, the interference of those beams would be manifested as interference fringes which will have a fringe period related to the angular separation of the interfering beams. After those regions of interference, the beams continue to propagate to the far field. If one were to place a screen in those locations were the beams overlap, the interference fringes would become visible.

Since the FDTD simulations depict the intensity at the near field, the field distribution of E_z as a function of x for a fixed y is Fourier Transformed to obtain the far field pattern. The far field pattern is shown in Figure 8(b), centered around the zeroth order max. In the case of the multi-microgratings, the intensity can be seen to be further distributed to higher orders as well. The far field pattern can be compared to the Fraunhofer intensity distributions shown in Figure 3, which are the exact solutions to the multi-micrograting diffraction pattern.

3.D.1. FDTD simulations of interference

One of the biggest advantages of the FDTD method is that it can also simulate interference effects between plane waves, which is an effect that would happen with multi-microgratings. Referring back to Figure 8, it was possible to see that the diffracted beams from a micrograting can interact with the diffracted beam from a different micrograting.

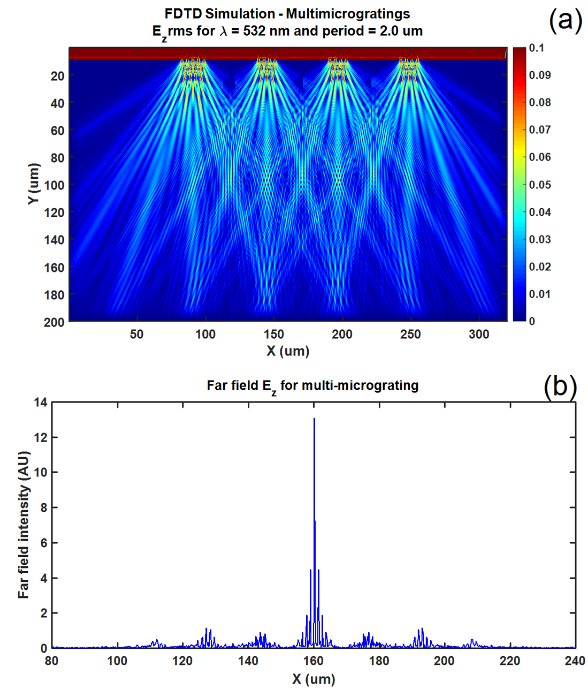

Fig. 8. (a) FDTD simulation of electric field $E_z rms$ of the interaction of 1D multi-micrograting (2.0 μm grating period, 1.0 μm grating width, and with 34 μm micrograting cell separation) and EM wave of 532 nm wavelength. (b) Far field distribution of $E_z rms$.

Conceptually, the two diffracted beams can be considered monochromatic plane waves traveling at angles $\pm\theta_{int}/2$ and that intersect at an angle θ_{int}. In the region of intersection, interference fringes would be produced with a fringe period d_f given by Equation 6.

$$d_f = \frac{\lambda}{sin\theta_{int}} \tag{6}$$

An FDTD simulation was carried out that simulates two interacting beams separated by 30 μm, traveling downwards at angles $\theta_{int}/2 = \pm 20^\circ$ with a wavelength of 532 nm.

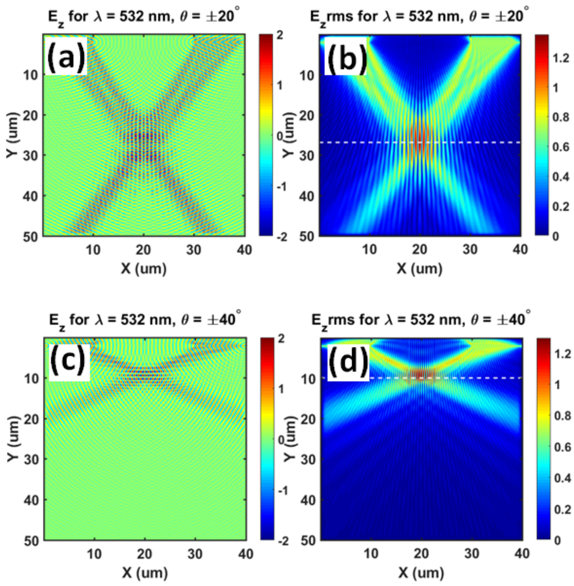

Fig. 9. FDTD simulation of interfering beams (30 μm separation, 532 nm wavelength). (a) Electric field E_z and (b) RMS electric field $E_z rms$ at angles $\theta_{int}/2 = \pm 20°$. (c) Electric field E_z and (d) RMS electric field $E_z rms$ at angles $\theta_{int}/2 = \pm 40°$.

The steady state electric field E_z field is shown in Figure 9(a), and the steady state RMS electric field $E_z rms$ is shown in Figure 9(b). The beam on the left is traveling at angle $\theta_{int}/2 = 20°$ and the one on the right at angle $\theta_{int}/2 = -20°$ and they intersect at an angle of 40°. As it can be seen from both plots, interference fringes are formed along the white line plotted in Figure 9(b). The same simulation was carried out for two beams traveling at angles $\theta_{int}/2 = \pm 40°$. E_z and $E_z rms$ for this case can be seen in Figure 9(c) and (d).

As it is seen in Figure 9, if the interference angle increases, the fringe period decreases. To better visualize this effect, the profiles of the RMS fields of Figure 9(b) and (d) are plotted along the white lines and are shown in Figure 10(a) for the 20° case and (b) for

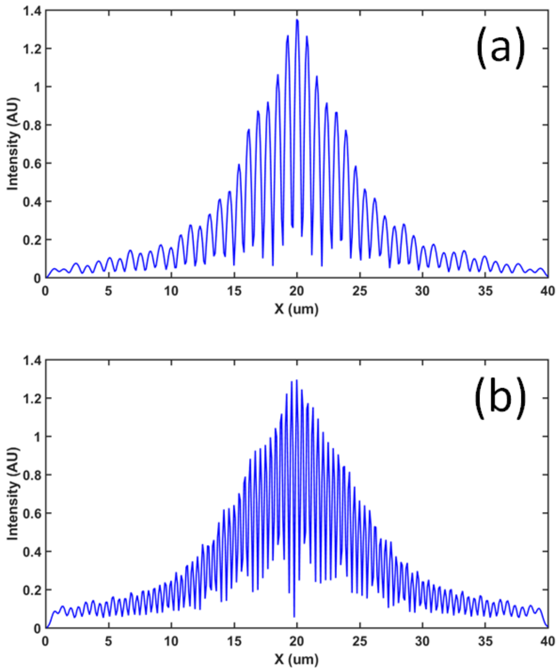

Fig. 10. Line profiles of the RMS electric fields from Figure 9(b) and (d).

the 40° case. It is possible to see how the interference fringe period changes dramatically.

The FDTD simulations presented complement and corroborate the results shown for the predicted patterns of multi-microgratings that were calculated with the Fraunhofer intensity approach and with the graphical Fourier Transform method. These simulations also predict interference fringes forming in the regions where multi-micrograting diffracted beams overlap with one another.

3.E. Results of diffraction efficiency simulations

For samples with multi-microgratings, a depth of 0.95 μm was calculated to maximize the first order diffraction efficiency for the parameters listed earlier. This resulted in a

Table 1. Design parameters and calculated diffraction efficiencies

Design type	Grating period or cell size (μm)	Etch depth (μm)	Calculated total TE diffraction efficiency (%)
1D gratings	2.0	0.95	31.5
Hexagonal apertures	20.0	1.95	8.7
Multi-micrograting	2.0	0.95	31.5

1D grating TE diffraction efficiency of 14.1% for the first order, and a total diffraction efficiency of 31.5%. Most of the light gets diffracted to the ± 1 order (28.2%), and a smaller portion (3.3%) is distributed to the higher orders.

For samples with hexagonal apertures only, a depth of 1.95 μm was selected since it provided a maximum in the efficiency calculations. The total diffraction efficiency for periodic hexagonal apertures was calculated to be 8.7%. Due to the longer period, the incident light is diffracted into a higher number of spots. The efficiency of individual diffracted spots was considerably reduced. Additionally, due to a non-ideal duty cycle, efficiency was further decreased.

As reported separately [8], the measured total diffraction efficiency for samples with multi-microgratings with the given parameters was measured to be 32.1%, which is close to the calculated values. For hexagonal aperture samples, a total diffraction efficiency of 23.7% was measured, which was higher than the calculated since the samples were coated with 80 nm of Al. The addition of Al to the samples was determined to increase the diffraction efficiency by a factor of about 2.2 - 2.3 for all other samples, so the measured total diffraction efficiency for uncoated hexagonal apertures is estimated to be 10.3%, which is also close to the calculated values. Table 1 summarizes the selected depths for each of the sample designs as well as the calculated total TE diffraction efficiency.

4. Conclusions

The optical diffraction properties of multi-microgratings have been simulated. Simulated diffraction patterns of arrays of hexagonal apertures and arrays of microgratings were compared to the experimental diffraction patterns of silicon fabricated structures and found to be in agreement. The diffraction pattern of arrays of hexagonal apertures receive contributions from the hexagonal aperture, the honeycomb array and their interaction. The diffraction pattern of arrays of microgratings are the combination of the diffraction pattern from hexagonal shape of the micrograting cells, the periodic nature of the gratings within each cell and the grid-like structure that is formed by the vectors that array the microgratings into large areas.

It has been shown that complex periodic structures can be broken down into their constituting elements for easier understanding of how their diffraction patterns are formed, but suggesting that there is a strong interaction between the different periodic elements. The interaction gives rise to areas of high intensity appearing highly defined and with sharp features. These features could prove to be very sensitive to changing conditions in the samples themselves. Such idea can be exploited in multiple applications such as strain or temperature sensing where both anisotropic and isotropic changes in the sample dimensions could lead to very defined changes in a diffraction pattern and its intensity.

Three simulation approaches were presented. A Fraunhoffer intensity distribution approach was developed in order to mathematically explain structures with multiple periodic elements. This approach is useful when mathematical expressions of the apertures can be easily derived, such as regularly shaped aperture arrays. Also, the simulations can be targeted to only display areas of interest with great detail, allowing for high resolution images of any area of the simulated diffraction pattern. A different, graphical Fourier Transform approach was implemented to simulate the diffraction patterns of more complex structures. Diffraction patterns of such structures can be simulated by obtaining their graphic Fourier Transform, but the diffraction patterns must be spatially calibrated. Furthermore, such technique only applies to square images with pixel counts that are in powers of 2. Simulations have to be obtained for the whole structure, not just a portion of it. This approach has been proven to be a very useful tool to explain the formation of diffraction patterns of complex periodic structures like arrays of hexagonal microgratings, but it is also possible to use such approach to simulate the diffraction patterns of quasi-periodic and non-periodic structures as well. A third approach was implemented to simulate the optical properties of multi-microgratings that is based on the FDTD method.

The method can be used to observe other optical effects, such as interference between the different microgratings. The model can be further specialized to incorporate different materials with distinct refractive indices, different incidence angles, etc.

5. Acknowledgements

The authors would like to thank NSF I/UCRC and NASA Langley Professor programs for the partial financial support to this project.

References

[1] A. R. Parker and H. E. Townley. Biomimetics of photonic nanostructures. *Nature Nanotechnology*, 2(6):347–353, 2007.

[2] R. A. Potyrailo, H. Ghiradella, A. Vertiatchikh, K. Dovidenko, J. R. Cournoyer, and E. Olson. Morpho butterfly wing scales demonstrate highly selective vapour response. *Nature Photonics*, 1(2):123–128, 2007.

[3] R. A. Potyrailo, Z. Ding, M. D. Butts, S. E. Genovese, and T. Deng. Selective chemical sensing using structurally colored core-shell colloidal crystal films. *IEEE Sensors Journal*, 8(6):815–822, 2008.

[4] A. D. Pris, Y. Utturkar, C.l Surman, W. G. Morris, A. Vert, S. Zalyubovskiy, T. Deng, H. T. Ghiradella, and R. A. Potyrailo. Towards high-speed imaging of infrared photons with bio-inspired nanoarchitectures. *Nature Photonics*, 6(3):195–200, 2012.

[5] S. Zhu, D. Zhang, Z. Chen, J. Gu, W. Li, H. Jiang, and G. Zhou. A simple and effective approach towards biomimetic replication of photonic structures from butterfly wings. *Nanotechnology*, 20(31):315303–1–315303–8, 2009.

[6] K. Watanabe, T. Hoshino, K. Kanda, Y. Haruyama, T. Kaito, and S. Matsui. Optical measurement and fabrication from a morpho-butterfly-scale quasistructure by focused ion beam chemical vapor deposition. *Journal of Vacuum Science & Technology B: Microelectronics and Nanometer Structures*, 23(2):570–575, 2005.

[7] T. H. Wong, M. C. Gupta, B. Robins, and T. L. Levendusky. Color generation in butterfly wings and fabrication of such structures. *Optics Letters*, 28(23):2342–2344, 2003.

[8] C. A. Rothenbach, I. I. Kravchenko, and M. C. Gupta. Optical diffraction properties of multi-microgratings. *Manuscript submitted to Applied Optics*, 2014.

[9] K. K. Sharma. *Optics: Principles And Applications*. Elsevier/Academic Press, 2006.

[10] M. Born. *Principles of optics: electromagnetic theory of propagation, interference and diffraction of light*. Cambridge University Press, Cambridge ; New York, 7th expanded ed edition, 1999.

[11] Y. Takano, K.N. Liou, and P. Yang. Diffraction by rectangular parallelepiped, hexagonal cylinder, and three-axis ellipsoid: Some analytic solutions and numerical results. *Journal of Quantitative Spectroscopy and Radiative Transfer*, 113(14):1836–1843, 2012.

[12] J. Komrska. Fraunhofer diffraction at apertures in the form of regular polygons. II. *Optica Acta: International Journal of Optics*, 20(7):549–563, 1973.

[13] R. C. Smith and J. S. Marsh. Diffraction patterns of simple apertures. *Journal of the Optical Society of America*, 64(6):798–803, 1974.

[14] D. G. Voelz. *Computational fourier optics: a MATLAB tutorial*. SPIE Press, Bellingham, Wash, 2011.

[15] G. O. Reynolds, DeVelis J.B. Parrent, G. B., and B. J. Thompson. *The New physical optics notebook: tutorials in Fourier optics*. SPIE Optical Engineering Press, Bellingham, Wash., USA, 1989.

[16] J. W. Goodman. *Introduction to Fourier optics*. Roberts & Co, Englewood, Colo, 3rd ed edition, 2005.

[17] A. R. Weeks. *Fundamentals of electronic image processing*. SPIE/IEEE series on imaging science & engineering. SPIE Optical Engineering Press ; IEEE Press, Bellingham, Wash., USA : New York, 1996.

[18] Kane Y. Numerical solution of initial boundary value problems involving maxwell's equations in isotropic media. *IEEE Transactions on Antennas and Propagation*, 14(3):302–307, 1966.

[19] J Frances, M Perez-Molina, S Bleda, E Fernandez, C Neipp, and A Belendez. Educational Software for Interference and Optical Diffraction Analysis in Fresnel and Fraunhofer Regions Based on MATLAB GUIs and the FDTD Method. *IEEE Transactions on Education*, 55(1):118–125, 2012.

[20] C Calderón-Ramón, JF Gómez-Aguilar, M Rodríguez-Achach, LJ Morales-Mendoza, JR Laguna-Camacho, M Benavides-Cruz, MI Cruz-Orduna, M González-Lee, H Pérez-Meana, M Enciso-Aguilar, et al. Use of the perfect electric conductor boundary conditions to discretize a diffractor in fdtd/pml environment. *Revista mexicana de física*, 61(5):344–350, 2015.

[21] M. C. Gupta and S. T. Peng. Diffraction characteristics of surface-relief gratings. *Applied Optics*, 32(16):2911–2917, 1993.

[22] M. G. Moharam and T. K. Gaylord. Rigorous coupled-wave analysis of planar-grating diffraction. *Journal of the Optical Society of America*, 71(7):811–818, 1981.

[23] M. G. Moharam and T. K. Gaylord. Rigorous coupled-wave analysis of metallic surface-relief gratings. *Journal of the Optical Society of America A*, 3(11):1780–1787, 1986.

[24] M. G. Moharam and T. K. Gaylord. Diffraction analysis of dielectric surface-relief gratings. *Journal of the Optical Society of America*, 72(10):1385–1392, 1982.

Multi-microgratings for high sensitivity temperature sensing

Christian A. Rothenbach and Mool C. Gupta*

Department of Electrical and Computer Engineering,

University of Virginia, Charlottesville, Virginia 22904, USA

Abstract

Development of non-contact, fast, accurate temperature measurements of surfaces is necessary in production and development environments in order to increase processing throughput and yields. Optical temperature measurement methods offer possible solutions, but are often slow, depend on surface conditions and have limited ranges. A temperature measurement method based on optical diffraction of highly-periodic multi-micrograting structures is presented and compared to similar methods that use conventional one-dimensional gratings. The system is shown to have a temperature resolution 300 times better than with 1D gratings, and is capable of resolving changes in temperature of <0.1°C using inexpensive equipment and simple alignment.

Keywords: diffraction grating, grating array, Fourier transform, microgratings, optical temperature sensing, temperature measurement

* Corresponding author, e-mail: mgupta@virginia.edu.

1. Introduction

In production environments, accurate temperature measurement of materials and substrates is very critical due to the multitude of different processes. The most common temperature measurements methods are direct contact measurements such as those with thermocouples, which require physical contact between the probe and the material being measured. Physical contact is not always feasible in certain processing configurations and also thermocouples are highly susceptible to contamination. For example, many processes require temperature monitoring while under vacuum or in locations where contact is not possible, so non-contact temperature measurements are necessary such as those implemented by optical techniques.

Conventional, optical noncontact measurement techniques such as pyrometers, which measure blackbody radiation from a surface, are relatively accurate; however, they are highly dependent on surface and material properties (i.e. emissivity, roughness) and offer poor spatial resolution and have slow acquisition times [1]. Newer methods for temperature sensing, such as microbolometers, thermal bimorphs, thermal buckling based sensor arrays, Fabry-Perot structures and cantilevers have poor spatial resolution and narrow operating ranges [2]. Some novel designs, such as thermally actuated interferometric sensors, have been reported based on device fabricated with PDMS [3], long period fiber sensors with high temperature sensitivity [4, 5] and designs with photonic crystals [6, 7] and plasmonic nanostructures [8]. These novel designs are complicated to fabricate and difficult to align and may not be suitable for a simple, quick temperature measurement.

An alternative method for optical temperature measurements is using diffraction gratings. One dimensional gratings have been proposed as method for temperature measurements, using diffracted beam angular measurement changes due to thermal expansion of the grating substrates, like PDMS, silicon carbide, silicon and gallium arsenide [9–11]. Results are promising, but they lack a high spatial resolution and low sensitivity. Low-cost, simple methods such as those described in [3, 10] based on thermal expansion of diffraction gratings offer a fast method to measure temperature. The angular deflection of diffracted beams was monitored for position changes due to increases in temperature in Si-C ($\alpha = 6.5\cdot 10^{-6}$ °C^{-1}) and PDMS ($\alpha = 277\cdot 10^{-6}$ °C^{-1}) substrates. The studies reported sensor configurations capable of resolving $\Delta T = 5°C$ and 0.01°C respectively. While α plays a big role in the sensitivity of the system, for a Si ($\alpha = 2.6 \cdot 10^{-6}$ °C^{-1}) substrate [12], sensitivity in the order of a few °C can be expected. To obtain better resolution (0.3-0.6°C), more complicated configurations can be used, such as those described in [1, 9]. Two independent probing beams at different incident angles were made incident on Si substrates with diffraction gratings so that their diffracted beams travel parallel to each other to a sensor. The difference in centroid position of the individual beams was monitored and used to measure changes in temperature and rotation. While this configuration offers a higher resolution, it has a complicated optical configuration that is very sensitive to alignment. Albeit for different applications, interferometric measurement methods using expansion of gratings can obtain further improvements in resolution, which also require complicated setups with critical alignment, cost and operation [13–16]. It follows then that using interferometric measurements would then improve the resolution of optical temperature measurement methods using thermal expansion of gratings.

In previous work [17, 18], we designed and studied the optical properties of multi-periodic structures defined as multi-microgratings. We showed that multi-microgratings have complex diffraction patterns that arise from the interaction of the multiple periodic elements that are present in the multi-micrograting design. These diffraction patterns are formed by the combination of the effects of periodic grating lines, single and multiple apertures as well as the arrangement of those apertures. Hence, the diffraction patterns contain information regarding the interaction between the individual periodic elements that form the multi-microgratings. These cross-term interactions between the different periodicities and interference between diffracted beams opens the opportunity for novel sensor applications.

1.A. Background on multi-microgratings

Six hexagonal micrograting cells, of six possible grating orientations, can be grouped up together into a repeating cell as seen in Figure 1(a), which shows the six cells with the respective grating orientations, grating period d and hexagon side s. That repeating cell can be arrayed together, resulting in a large area pattern that can be seen in Figure 1(b).

Upon closer inspection, and also shown in Figure 1(b), the array can be described by a unit cell described by the red parallelogram with vectors $\vec{a}$ and $\vec{b}$. In other words, the vectors $\vec{a}$ and $\vec{b}$ can be used to translate the unit cell and produce the large area arrays.

We used the indicated design to try to understand the optical properties of arrays of micrograting cells through fabrication and observation of their complex diffraction patterns, such as the one seen in the photograph shown in Figure 1(c), which shows a screen projection of a diffraction pattern of a micrograting array pattern with $d = 2$ μm, with $s = 20$ μm fabricated on silicon samples. The diffraction pattern produced by multi-micrograting arrays can be seen to be very intricate, with several features with high and low intensity. It can be explained as the convolution of the different periodicities that form the arrays. It appears to have a spatial hierarchy for the existence of these cross terms. The smallest observable features in the diffraction pattern (the lattice described by the red parallelogram in Figure 1(b)), which corresponds to the largest feature in the multi-micrograting array design (the unit cell that forms the arrays), is convoluted with the diffraction pattern of individual hexagonal apertures, thus creating the pattern seen in Figure 1(c). In turn, the pattern seen in Figure 1(b) is then convoluted with the 1D diffraction grating spot locations, creating the large and complex diffraction pattern of multi-microgratings seen in Figure 1(c).

In 1D gratings, the intensity is distributed between the 0th order and a few higher order diffracted beams, which occur at very localized and discrete angular positions. In the case of multi-microgratings, a significant portion of the intensity is also distributed into multiple higher order diffracted beams, due the shape of the micrograting apertures and into the periodic nature of the apertures.

Thus, by monitoring the position and intensity of the diffracted beams, the overall diffraction pattern characteristics and intensity distribution from multi-microgratings can be shown to be more sensitive to changes. Furthermore, as it was shown earlier, multi-micrograting beams tend to be slightly narrower than their 1D grating counterparts [17]. Also, depending on the sensing configuration, they also interfere with each other at the sensor plane, producing highly defined interference patterns.

Overall, the purpose of this paper is to describe a feasibility study of possible ap-

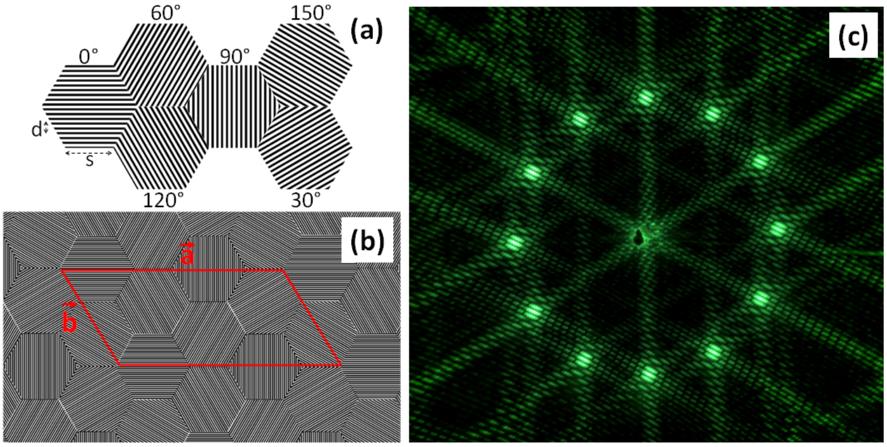

Fig. 1. (a) Micrograting repeating cell with six possible orientations. s is the hexagon side dimension and d is the grating period. (b) Array of multi-microgratings, with the red parallelogram defining the unit cell that was used to form the array, with sides a and b. (c) Photograph of screen projection of a normal incidence, optical diffraction pattern by multi-micgrograting array with $d = 2$ μm, with $s = 20$ μm and laser light with $\lambda = 532$ nm.

plications of multi-microgratings which exploit the differences between 1D gratings and multi-microgratings. A method that utilizes the complex multi-micrograting diffraction patterns and their interference is described in the framework of temperature sensing, which can also be further extended for other sensor applications such as strain/stress sensing, vapor concentration detection and nanometrology, etc.

2. Temperature sensing method with multi-microgratings

As the temperature of a solid is changed its physical dimensions are also affected. The coefficient of thermal expansion (CTE), α, is a characteristic of each material and it is a measure of the magnitude of the thermally induced change in dimensions [19]. This coefficient is also dependent on temperature itself. The change of dimensions of an object, ΔL, is given by Equation 1. The equation states that the change in length of an object

ΔL is proportional to the change in temperature ΔT, where L is the initial length and the proportionality constant α is the coefficient of thermal expansion.

$$\Delta L = \alpha * L * \Delta T \quad (1)$$

When surface relief gratings are present on the substrate, thermal expansion of the substrate can induce changes in the periodicity of the gratings. A change in this periodicity will result in a change in the diffracted angles, and thus, this technique can be used to measure changes in temperature. The change in the periodicity (Δd) of a grating with period d is given in Equation 2.

$$\Delta d = \alpha * d * \Delta T \quad (2)$$

A change in temperature of the substrate will induce a change in the periodicity of the micro-multigratings, and it will be dependent on the material itself (by means of the coefficient of thermal expansion) and the change in temperature. If the grating periodicity is changed, then it follows that the diffraction angle will also have to change. The accuracy at which that angular deflection can be measured determines the measurable sensitivity of the temperature change.

The mechanism showing the thermally induced changes in the diffracted angles is shown in Figure 2. If temperature increases from T to T', this will cause a linear expansion in the grating periodicity from d to d'. In other words, as ΔT increases, Δd will also have to increase. An increase in the grating periodicity will mean that the diffracted beams will shift towards the 0th order. Since the thermally induced changes in the grating periodicity will be relatively small, accurate measurement of the position of diffracted beams becomes very important.

In order to measure the changes in the diffracted angles, Δd, a screen can be placed at a distance D from the grating sample as seen in the schematic diagram in Figure 3.

The diffracted orders will be projected onto the screen, and the distance between the central beam and each diffracted spot will be given by s. The relationship between the diffracted angle θ_d, the distance to the screen D and the separation between the 0th order and the diffracted order can be described by $tan(\theta_d) = s/D$. As the distance to the screen

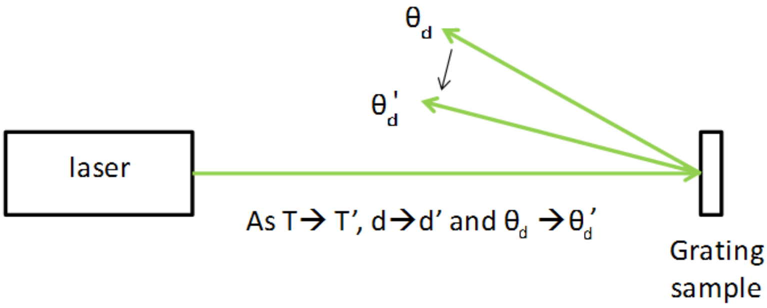

Fig. 2. Visualization of changes in diffracted angle caused by thermally induced periodiciy changes that affect the diffracted angle.

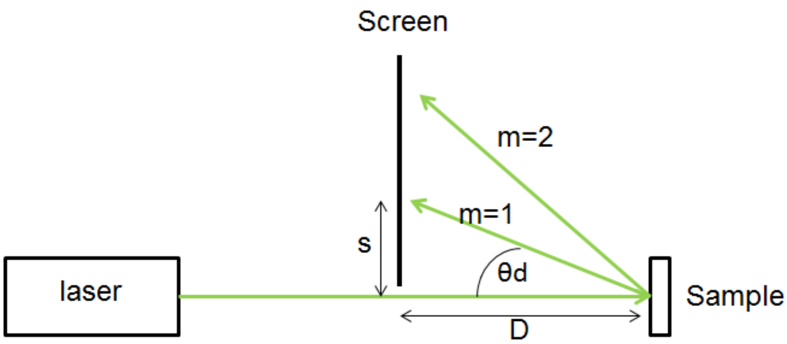

Fig. 3. Schematic of screen projection of diffraction patterns.

D is moved further away, the separation of the diffracted order and the 0th order on the screen, s, will also increase. Thus, the measurements are more accurate as D increases.

The change in displacement Δs can be measured, and an accurate way of measuring that change is by monitoring the displacement using a CCD camera. The resolution of the system is going to depend on the resolution of the optical elements and the ability of the system to resolve displacement. Arbitrarily long sample to sensor D distances can be used to make a small change in the diffracted angle be equivalent to a large change in the spatial shift, at a cost of range in the measurement and vice versa. Angular shift, $\Delta\theta_d$, is however fixed. Angular shift is also proportional to the change in temperature and the reference angular position, so for a given change in temperature, a larger θ_d is preferable, which can be achieved by using higher order diffracted beams or large angle of incidence θ_i of the probing beam.

Use of multi-micogratings allows measurement of several parameters. If multi- micogratings are present on the surface of a substrate, the absolute temperature of a substrate can be determined using the CTE of the substrate and the periodicity of the multi-micograting. Changes in the angular position of the diffracted orders can then be used to determine changes in the periodicity, which in turn can be used to determine the overall change in temperature of the substrate. This can be realized with gratings of single orientations, but there are advantages to having multi-micogratings of multiple orientations. By monitoring the diffracted angles, in the case of multi-micogratings, it is possible to determine the spatial variation of temperature. Additionally, it is possible to simulatenously record temperature at different locations and obtain spatial temperature information from a substrate with multi-microgratings, which would not be possible with 1D gratings.

The size of the probing beam has a large impact on the measurement of this method. If the probing beam is large in diameter but smaller than the overall size of the multi-micrograting pattern, the diffraction pattern will be the result of the contribution of all the multi-micogratings. However, a smaller beam can probe the area covered by the repeating unit of six hexagons. This pattern provides local information on the scale of the repeating cell. If the probing beam is even smaller in diameter, it can be focused to only be incident on a single hexagon, thus being able to determine the temperature of that particular area. The spatial resolution of this method will be in part dependent on the individual size of the hexagonal gratings. For probing beams that are larger than the muti-micrograting pattern itself, and at the right sample to detector position, interference effects could be observed which will create sharp, highly defined features.

With an arbitrarily long patterned sample, the diffracted beam from one micrograting would interfere with the zeroth order of several other microgratings. A schematic diagram

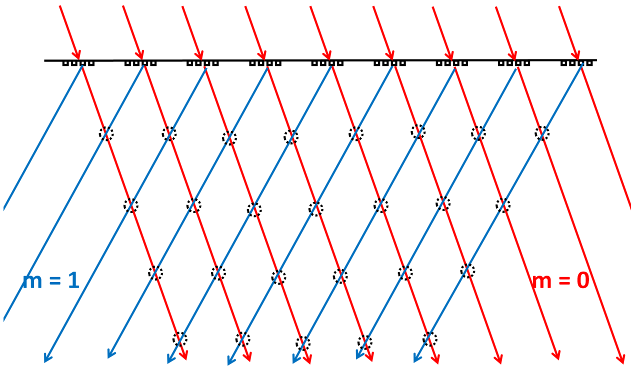

Fig. 4. Schematic diagram that illustrates multiple interference locations of first order diffracted beams and zeroth order beams .

of this concept is shown in Figure 4. The paths for the zeroth order and first diffracted order are shown and their intersections are marked to illustrate the regions where the beams would interfere. At all the marked locations, the beams would interfere, producing interference fringes.

In addition to being narrower, under certain conditions, the multi-micrograting diffracted beams can be allowed to interfere at the sensor plane, producing high contrast, sharp fringes. Figure 5 illustrates this effect. If we assume a 1D grating diffracted beam of FWHM = 560 μm as the black line in Figure 5(a), a typical 45 μm displacement in the sensor plane can be measured. One way to quantify that measurement is to look at the differential signal DS given by Equation 3, where T1 and T2 are the original and shifted signals respectively. The differential signal of Figure 5(a) can be seen in Figure 5(b). A maximum change of around ±11% is observed in the differential signal.

$$DS = 100\% * (\frac{T2}{T1} - 1) \tag{3}$$

For comparison, if the beam were instead narrower, that maximum change in the differential signal would be greater, such as in the case for multi-microgratings. Also, if the beam that is probing the grating sample is expanded so that it is larger than the total grating size, at a similar sample to sensor distance and due to their proximity, multi-

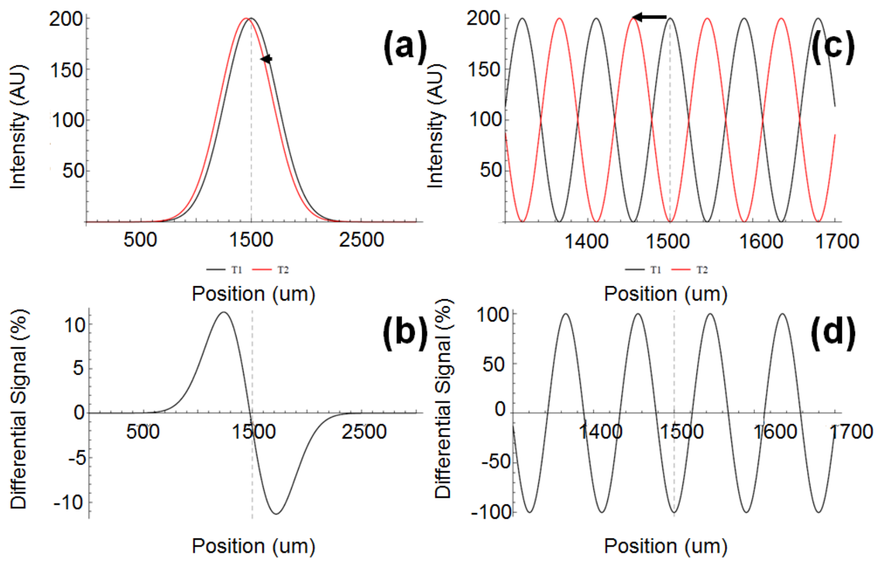

Fig. 5. Simulated 45 μm displacement/shift in (a) 1D grating Gaussian signal and (c) multi-micrograting signal with interferometric fringes with 90 μm periodicity. (b) and (d) represent differential changes in the signal to visualize strenght of measurement.

micrograting beams are observed to interfere with one another, producing fringes. Figure 5(c) simulates interference fringes with equal contrast but much narrower fringe widths than the beam of Figure 5(a), with 90 μm period and it is represented by the black T1 line. In the ideal case, a half period displacement of 45 μm (T2, as exemplified by the red curve) would produce the maximum change in the system's differential signal, as it can be seen in Figure 5(d). The differential signal can be found to have a maximum change of 100%. While this is an ideal case scenario, it is clearly observable how utilizing the interference effects observed on multi-micrograting diffraction patterns, which do not appear on 1D grating diffraction patterns, can much more readily utilized to carry out measurements.

To more accurately measure changes in displacement using interference fringes, a phase can be calculated for the reference image at T1 and at T2 for the example seen in Figure 5. The computed phase difference, $\Delta\phi$, can be used as a metric for calibration or measurement. As it can be seen from Figure 5(c) and (d), since a half period was chosen as the displacement, the phase difference between T1 and T2 is π. A short simulation was written in MatLab that calculates the phase difference $\Delta\phi$ [20]. To obtain the phase, Fourier Filters were applied to isolate one of the periodic frequencies of curves T1 and T2, a wrapped phase is calculated and unwrapped and the difference in phase between the reference image and the changed image are calculated. Since the fringe period was chosen to be displaced by a half period, the calculated phase is π.

Further simulations were designed, implementing the finite-difference time-domain (FDTD) method, to simulate 1D multi-micrograting structures . A two-dimensional model is devised, with an electromagnetic wave propagating in the XY plane, with a transverse component H_z [21]. The boundaries are defined to be absorbing with a perfectly matched layer (PML). For simplicity, a screen aperture or grating is defined as a perfect electric conductor (PEC), by setting the electric field components to zero in those regions. A sinusoidal electromagnetic source of a particular wavelength is then defined at a particular location inside the model volume and is allowed to propagate in the XY plane in a particular direction, by iterating over time until steady state is achieved. The sinusoidal source interacts with the aperture that was defined. At each instant in time, the electric field vectors are solved first, followed by the magnetic field vectors in the next time iteration. The result is a time evolution of the electric field. Since the electric field is proportional to the intensity of the wave, then it can be used to understand how the electromagnetic wave interacts with the diffraction gratings.

As an example, an FDTD simulation is carried out that simulates two interacting beams separated by 30 μm, traveling downwards at angles $\theta_{int}/2 = \pm 20°$ with a wavelength of 532 nm. The steady state RMS electric field $E_z rms$ is shown in Figure 6(b). The beam on the left is traveling at angle $\theta_{int}/2 = 20°$ and the one on the right at angle $\theta_{int}/2 = -20°$ and they intersect at an angle of 40°. As it can be seen from both plots, interference fringes are formed along the white line plotted in Figure 6(a). To better visualize this effect, the profile of the RMS fields of Figure 6(a) is plotted along the white line and is shown in Figure 6(b). It is possible to see how the interference fringe period changes

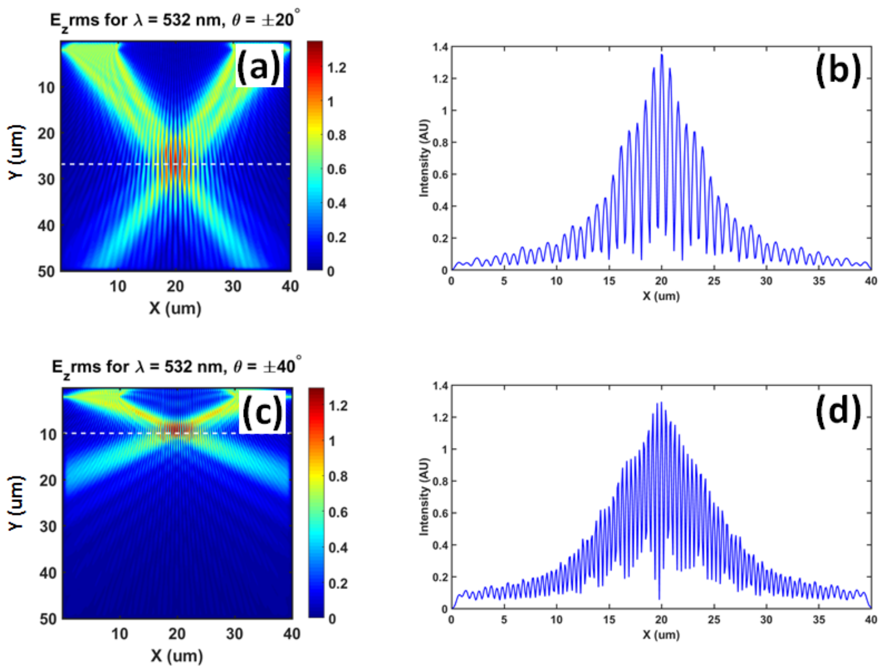

Fig. 6. FDTD simulation of interfering beams (30 μm separation, 532 nm wavelength). (a) RMS electric field $E_z rms$ at angles $\theta_{int}/2 = \pm 20°$. (b) Line profile of $E_z rms$ for (a). (c) RMS electric field $E_z rms$ at angles $\theta_{int}/2 = \pm 40°$. (d) Line profile of $E_z rms$ for (c).

dramatically. The same simulation was carried out for two beams traveling at angles $\theta_{int}/2 = \pm 40°$. $E_z rms$ for this case can be seen in Figure 6(c), and its profile in Figure 6(d).

Similar simulations are carried out for multi-microgratings with 2 μm grating period and 30 μm micrograting separation, which produce diffracted beams at angles of ±32°. The illuminating source was light with 532 nm wavelength. The diffracted angle θ_d (or interference half-angle $\theta_{int}/2$, as they can be shown to be the same angles) was simulated to increase from 32° to higher angles at different increments, as if temperature were decreasing in the sample. The FDTD simulations were allowed to run and reach steady

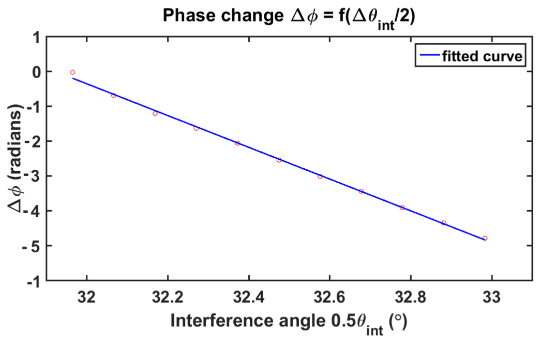

Fig. 7. Effects of decreasing temperature, causing an increase in the diffracted angle (or interference half-angle) from 32 to 33°, shown as red circles fitted to a blue best fit line.

state. Instead of looking at how much the fringes are moving, the phase change $\Delta\phi$ is calculated with respect to the reference beams at 32.0° ($\Delta\phi$=0). The phase change is calculated for each increment of 0.1° up to 33.0°. The plot for the phase change $\Delta\phi$ as a function of the interference half-angles is shown in Figure 7 as the red circles fitted to a blue linear trend. The initial condition at a half-angle of 32° is on the top left corner of the plot, and as temperature decrease is simulated, the phase change moves downwards to the right.

While the trend shown is very clearly linear, a change in the interference half-angle of a whole degree, and assuming a silicon sample, corresponds to a change in temperature ΔT of over 1100°C, which is not very useful. However, this technique can be shown to be very sensitive. Different increments in interference half-angles $\Delta\theta_{int}/2$ were selected to understand the sensitivity of the phase change technique and the results are plotted in Figure 8 for increments (a) $\Delta\theta_d$ = 1x10$^{-4\circ}$, (b) 1x10$^{-5\circ}$ and (c) 1x10$^{-6\circ}$. The R^2 values for the fitted curves are shown as well. The linear trend remains for all cases. The R^2 are for the two increments in Figure 8(a) and (b) are very high, indicating a good fit of the trend to the data. It can be said that differentiating two adjacent measurements at these deltas would accurately differentiate them from one another. In the third case, for $\Delta\theta_{int}/2$=1x10$^{-6\circ}$, the actual captured values (red circles) are seen to be deviating from the

Table 1. Summary of phase changing technique sensitivity

$\Delta\theta_d$ (°)	ΔT (°C)	$\Delta\phi$ per step (rad)	R^2
10	1100	-0.4	1
$1*10^{-4}$	1.1	-0.0004	0.99929
$1*10^{-5}$	0.11	-0.00004	0.99792
$1*10^{-6}$	0.011	-0.000004	0.94576

linear trend. At this point, it is still possible to differentiate two adjacent measurements. At lower values of $\Delta\theta_{int}/2$, the ability to distinguish two adjacent measurements would be lost. The resolving capabilities of this method are summarized in Table 1.

Due to the nature of the process, an ambiguity as to the direction of the phase shift is introduced since the phase shift is periodic and a 2π shift is the same as a $0\ \pi$ shift. Due to that ambiguity, errors can be made when calculating the phase. In this example, a 2π shift corresponds to a full 90 μm shift, but the calculated phase can result to be multiples of $\pm 2\pi$.

A solution is proposed, which uses both the high dynamic range and low resolution of 1D grating displacements and also the low dynamic range, high resolution of the phase change mechanism of the interference fringes caused by the multi-microgratings to obtain a high dynamic range, high resolution sensing method that would otherwise be impossible with just 1D gratings.

In summary, because multi-micrograting optical properties are the combined effect of the elements that compose them, the sensing current method shares some of the conventional 1D grating advantages as well as helps mitigate some of the issues. The advantages of using multi-microgratings is summarized below, which set them apart from other optical temperature measurement techniques.

1. Noncontact and real-time.

2. High dynamic range/ high resolution by combining displacement measurements of large features that behave as 1D grating spots and sharp features present from

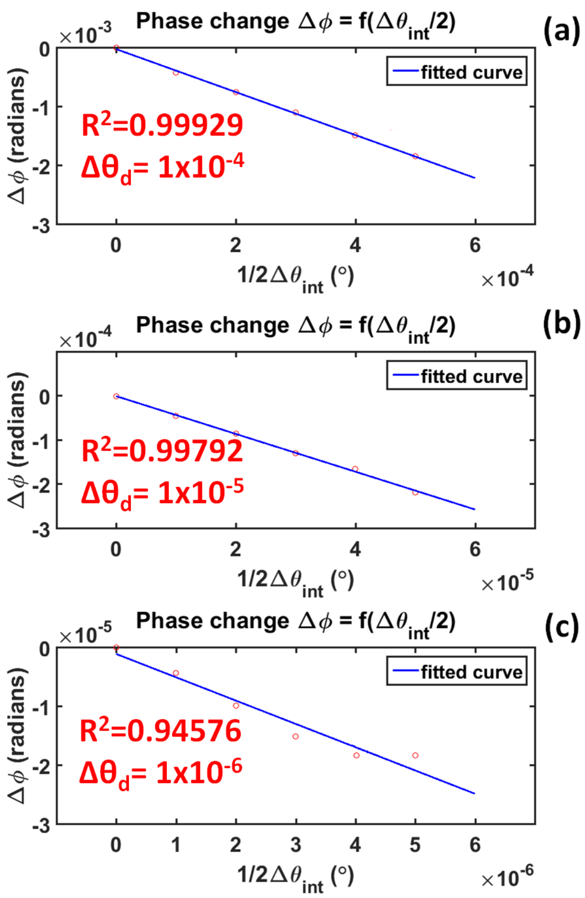

Fig. 8. Simulation of effects of decreasing temperature, causing an increase in the diffracted angle (or interference half-angle) at three different $\Delta\theta_{int}/2$ separating each measurement step, of (a) 1x$10^{-4\circ}$, (b) 1x$10^{-5\circ}$ and (c) 1x$10^{-6\circ}$.

allowing multi-micrograting beams to interfere with each other.

3. Capable of localized micron scale measurements by probing different areas of multi-microgratings.

4. Simple architecture and alignment, requiring only a laser, a substrate with multi-micrograting patterns and a camera.

5. Capable of measuring changes in variety of substrates that could be changing due to processing parameters such as transparent and opaque with low or no susceptibility to surface emissivity or conditions, flat or curved as long as periodic elements remain unchanged.

6. Analogous technique can easily be adapted for stress/strain, displacement or rotation measurements.

3. Experimental

Figure 9 shows the experimental setup used to test the feasibility of temperature sensing using multi-microgratings. 1D grating and multi-micrograting samples with 2 μm periodicities were placed on a hot plate and slowly heated to different temperatures to observe changes in the diffraction pattern as a function of temperature. The incident angle and sample to sensor positions were estimated from photographs of the experimental setup. The optional beam expander was used to modify the incident beam size so that adjacent beams in multi-microgratings could interfere with each other.

The diffracted beams were captured by the CCD sensor and analyzed for spatial changes. To measure beam profiles and beam positions, costly CCD sensors are typically employed. A cost-alternative method to measure beam profiles and positions [22] is adapted using a very inexpensive ($15) USB webcam (Intel CS110). The webcam housing was dismantled and the focusing lens removed to reveal the CCD sensor. The active area of the sensor has dimensions of 2.84 x 2.33 mm and an active area of 352 x 288 pixels. Square pixel pitch is measured to be 8.08 μm. Commercial software (QCFocus v2.1) is used to capture the images from the CCD webcam. Intensity values between 0 and 255 are captured by each pixel of the webcam. In order to prevent sensor saturation, the diffracted beam power is controlled by a combination of a rotating polarizer and neutral density (ND) filters. A notch filter (ThorLabs FB550-40) is used to prevent any stray light from reaching the sensor.

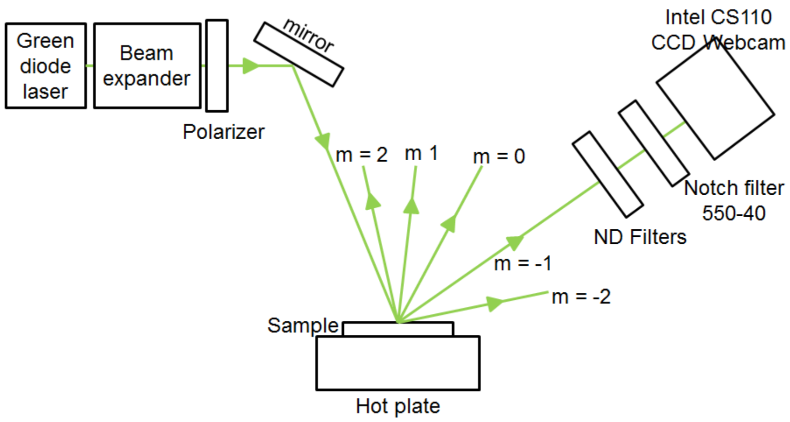

Fig. 9. Experimental setup for temperature change experiments.

As the laser beam is incident on the samples, the diffracted beam for order m = -1 is directed to the CCD webcam and beam profiles are extracted from the images at different temperature conditions using commercial software (ImageJ). Beam profiles are smoothened with a 5 pixel Gaussian filter to remove noise from the beam profiles. Average RMS noise of the CCD sensor was measured using MatLab by analyzing the mean and standard deviations of several captured signals and it was found to be 5.9%, with a range between 4.5% to 10.4%. It is established that if a measured signal is below the average noise of the sensor (SNR$\leq$1), then a change cannot be resolved.

Temperature of the hot plate (Corning Digital Hot Plate) was calibrated to the nominal reading in the device controls with a k-type thermocouple over several cycles. Additionally, a pyrometer based infrared thermometer (Fluke 568) was used on the hot plate to verify temperature readings. During experiments, temperature was carefully monitored with the attached thermocouple and infrared thermometer.

4. Results

In order to calculate system resolution and to visualize how using multi-microgratings would be beneficial in the sensor configuration described, images of displaced diffraction beams of similar displacement changes are shown in Figures 10 and 11 for two cases. Case 1 is with a measurement using a 1D grating and Case 2 is using multi-microgratings. Displacement in both cases is measured to be 65 μm, in order to be able to compare the measurement methods. It must also be noted that the sample to sensor distances was also different for each of the two cases, as it will be discussed below.

4.A. Case 1: 1D gratings, beam not expanded

Figure 10(a) and (b) shows the first order diffracted beam positions at temperatures of 30°C and 60°C for a sample with 1D gratings at a sample to sensor distance of 48 cm. The reference (30°C) beam is shown as the solid line in Figure 10(c). The displaced beam is shown in Figure 10(d) as the solid line and the reference beam appears as the dotted line. The differential change produced by the measurement can be seen in Figure 10(e). A maximum change of 12.6% was observed, which is still above the measured 5.9% average noise in the sensor. The effective observed change which can be seen to be high enough to resolve the temperature measurement when compared to the average noise (5.9%) of the sensor. The SNR is calculated to be 2.13. Under these parameters, a minimum displacement of 30.43 μm would be necessary in order to resolve the measurement, which corresponds to a 14.04°C minimum resolvable temperature.

4.B. Case 2: Multi-microgratings, expanded beam

Similarly, a sample with multi-micrograting patterns was exposed to temperature variations and the first order diffracted beam using an expanded probing beam can be seen in Figure 11(a) for room temperature (30°C) and (b) 100°C at a sample to sensor distance of 20 cm. As it can be seen, diffraction fringes that are produced by expanding the probing beam cause the diffracted beams to interfere with each other, producing the high contrast

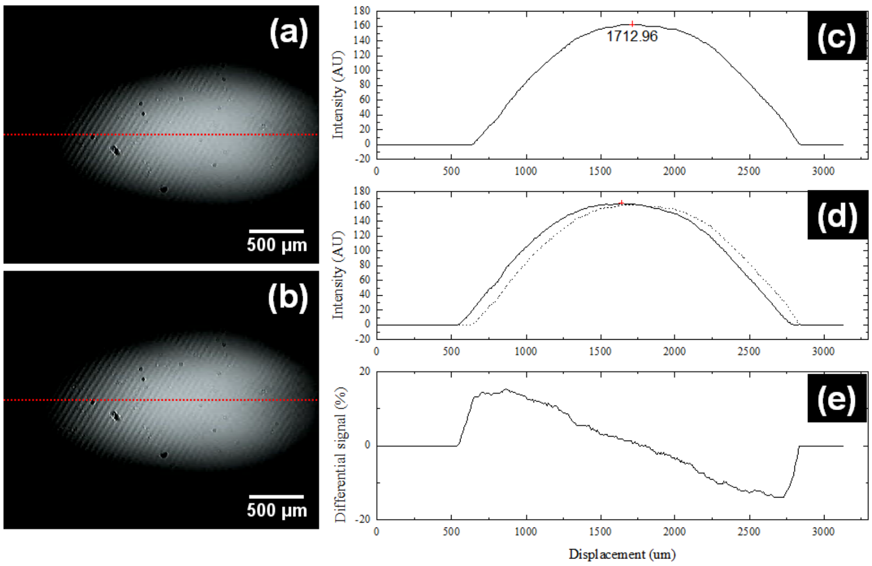

Fig. 10. Diffraction beam displacement for 1D gratings at (a) 30°C and (b) 60°C. (c) shows the reference beam profile and (d) shows the displaced beam as the solid line and reference as the dotted line for clarity. (e) shows the differential signal that results.

lines in the regions of overlap. Due to the sharpness of the feature, a smaller change can be more readily resolved, as compared to the 1D grating case. Figure 11(c) shows the profile of the room temperature measurement as the solid line, which has been smoothed (Gaussian filter) to more easily visualize the fringes and their periodic nature. Figure 11(d) shows the displaced diffracted beams at a temperature of 100°C as the solid line, while the dotted line represents the room temperature reference measurement. Arrows are added to clarify how the displacement occurred. The differential signal produced by this measurement is shown in Figure 11(e), where the maximum observable change can be seen to be produced at a position around 300 μm in the sensor, and it is around 51%. The SNR is calculated to be 8.6, which is much higher than that for 1D gratings. Under

Table 2. Summary of results for 1D gratings and multi-microgratings

Parameters	Case 1 (1D Gratings)	Case 2 (Multi-microgratings)	Case 3 (Multi-microgratings with interference)
Contrast (AU)	0.988	0.990	0.990
SNR (AU)	2.13	8.6	8.6
Sample-sensor distance (cm)	48	20	10
ΔT (°C)	30	70	<0.1
Adjusted min. resolvable ΔT (°C)	33.6	8.07	<0.1
Improvement (AU)	NA	4.2x	300x

this configuration, the sensor would be able to resolve a minimum displacement of 7.5 μm, which corresponds to a minimum ΔT of 8.07°C. A phase change $\Delta\phi$ is calculated to be 1.52, which corresponds to the expected $\pi/2$ shift for this particular displacement. A phase calculation can easily assign a numerical value to the displacement and can be used for alignment and characterization purposes.

Due to the different sample to sensor distance in Case 1, the resolution measurement of Case 1 is normalized to the sample to sensor distance of 20 cm and it is calculated to be 33.6°C, while for Case 2 it remains as 8.07°C. Case 2 shows to have a resolution that is 4.2 times higher than that for Case 1. The range of such a system under this configuration, normalized to a sensor to sample distance of 20 cm, is between 30 and 140 °C.

Table Table 2 summarizes the parameters and results of the results for Cases 1 and 2.

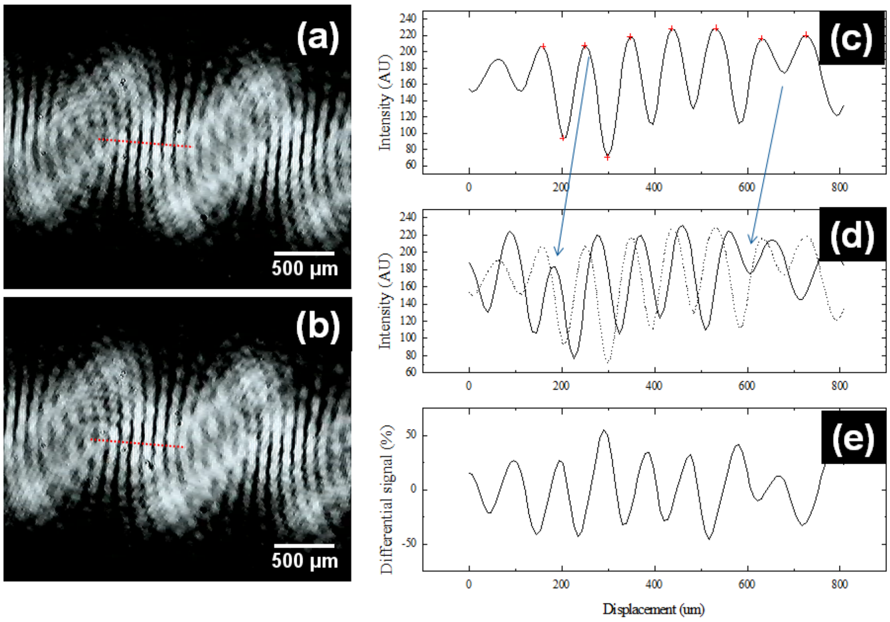

Fig. 11. Diffraction beam displacement for multi-microgratings at (a) 30°C and (b) 100°C. (c) shows the reference beam profile and (d) shows the displaced beam as the solid line and reference as the dotted line for clarity. (e) shows the differential signal that results.

5. Conclusions

A method that uses the thermal expansion of 1D gratings and multi-microgratings was described to demonstrate the advantages of using multi-microgratings over 1D gratings. Several key aspects show these clear improvements. Beams that are narrower for multi-microgratings allow for a theoretical better sensor resolution. High contrast fringes that are produced only in the case of multi-micrograting diffraction patterns can be used to increase the resolution of the system by 4.2 times. The improvement in resolution can be achieved without a decrease in the dynamic range of the sensor configuration. With 1D gratings, in order to improve the resolution of a system with a similar configuration it would require the sample to sensor distance to be increased, at the cost of a reduced field of view (range). In the case of the interferometric measurement using multi-microgratings, the same range can be achieved but at a much higher resolution 300 times higher, capable of resolving $<0.1°$C.

Furthermore, the tested configuration is simple and cost-effective. A simple webcam is sufficient to capture the diffracted beams. No critical alignment is necessary, which is often the case with interferometric setups requiring multiple beams. A low power laser beam (5 mW) can be used as the probing light source. One can argue that instead of using multi-microgratings, a large period 1D grating could be used in order to have multiple diffracted beams. A 1D grating with a period of 10-20 wavelengths ((i.e. d = 50-100 μm) would produce multiple diffracted orders that could be interfered on the sensor plane, but since the diffraction efficiency of higher order 1D grating beams is much lower, a higher power laser may be necessary for proper sensor operation. One of the key advantages of multi-microgratings is the fact that the diffraction efficiency can be tailored to be enhanced for larger angles because of the multi-micrograting low period (i.e. 2 μm), which has a diffraction efficiency that distributes most of the power to the area of the pattern that corresponds to first order diffracted beam, but which is further separated into more spots because of the periodic nature of the apertures.

Further improvements could be made by using a better, lower noise camera with a larger sensor and higher dynamic range, with more robust alignment techniques. Since the thermal expansion method measures changes in the diffracted angle due to induced changes in dimensions by temperature differences, the method can easily be extended for sensing displacement, stress/strain and rotation. Micro-multigratings can be incorporated into substrates using different methods. Using photolithography, for example, these structures could be made out of photoresist or etched onto the substrates surface and the temperature could easily be determined. Also, the probing area could be made out of polymers that contain the micro-multigratings, such as PDMS, that could be glued or attached to the surface of the substrates easily, and temperature measurements could be carried out.

6. Acknowledgments

The authors would like to thank NSF I/UCRC and NASA Langley Professor programs for the partial financial support to this project.

References

[1] M. K. Lang, G. W. Donohoe, S. H. Zaidi, and S. R. J. Brueck. Real-time image processing techniques for noncontact temperature measurement. *Optical Engineering*, 33(10):3465–3471, 1994.

[2] A. D. Pris, Y. Utturkar, C.l Surman, W. G. Morris, A. Vert, S. Zalyubovskiy, T. Deng, H. T. Ghiradella, and R. A. Potyrailo. Towards high-speed imaging of infrared photons with bio-inspired nanoarchitectures. *Nature Photonics*, 6(3):195–200, 2012.

[3] B. A. Grzybowski, S. T. Brittain, and G. M. Whitesides. Thermally actuated interferometric sensors based on the thermal expansion of transparent elastomeric media. *Review of Scientific Instruments*, 70(4):2031, 1999.

[4] S. Chaubey, P. Joshi, M. Kumar, R. Arya, A. K. Nath, and S. Kher. Design and development of long-period grating sensors for temperature monitoring. *Sadhana*, 32(5):513–519, 2007.

[5] M. Smietana, W. J. Bock, and P. Mikulic. Temperature sensitivity of silicon nitride nanocoated long-period gratings working in various surrounding media. *Measurement Science and Technology*, 22(11):115203, 2011.

[6] J. Ballato and A. James. A Ceramic Photonic Crystal Temperature Sensor. *Journal of the American Ceramic Society*, 82(8):2273–2275, 2004.

[7] H. Fu, H. Zhao, X. Qiao, Y. Li, D. Zhao, and Z. Yong. Study on a novel photonic crystal temperature sensor. *Optoelectronics Letters*, 7(6):419–422, 2011.

[8] B. Paivaranta, H. Merbold, R. Giannini, Luca Buchi, S. Gorelick, C. David, J. F. Loffler, T. Feurer, and Y. Ekinci. High Aspect Ratio Plasmonic Nanostructures for Sensing Applications. *ACS Nano*, 5(8):6374–6382, 2011.

[9] C. Huang. Optical temperature measurement by grating expansion for rotating semiconductor wafers. *Journal of Vacuum Science & Technology A: Vacuum, Surfaces, and Films*, 14(2):271, 1996.

[10] G. L. DesAutels, P. Powers, C. Brewer, M. Walker, M. Burky, and G. Anderson. Optical temperature sensor and thermal expansion measurement using a femtosecond micromachined grating in 6h-SiC. *Applied Optics*, 47(21):3773, 2008.

[11] J. A. Rogers, R. J. Jackman, O. J. A. Schueller, and G. M. Whitesides. Elastomeric diffraction gratings as photothermal detectors. *Applied Optics*, 35(34):6641, 1996.

[12] M. Jones and S. Jones. Basic Mechanical and Thermal Properties of Silicon. *Technical publication of Virginia Semiconductor, Inc.*

[13] Z. He and X. Liu. A high precision displacement sensor based on dual-gratings interference. In *2011 International Conference on Electric Information and Control Engineering (ICEICE)*, pages 997–1000, 2011.

[14] C. Feng, M. Kajima, S. Gonda, K. Minoshima, H. Fujimoto, and L. Zeng. Accurate measurement of orthogonality of equal-period, two-dimensional gratings by an interferometric method. *Metrologia*, 49(3):236, 2012.

[15] M. Mino. Position Sensing Grating Interferometer for a Specular Object. *Optical Review*, 5(3):191–195, 1998.

[16] S. Zhao, C. Hou, J. Zhang, J. Bai, and G. Yang. A high-resolution displacement sensor based on a grating interferometer with the phase modulation technique. *Measurement Science and Technology*, 23(10):105102, 2012.

[17] C. A. Rothenbach, I. I. Kravchenko, and M. C Gupta. Optical diffraction properties of multimicrogratings. *Applied Optics*, 54(7):1808–1818, 2015.

[18] C. A. Rothenbach and M. C Gupta. Simulation of optical properties of multi-microgratings. *Submitted for publication in Applied Optics*, 2016.

[19] D. Halliday, R. Resnick, and J. Walker. *Fundamentals of Physics*. Wiley, 9th edition, 2010.

[20] M. Mora-Gonzalez, J. Munoz-Maciel, F. J., F. G., R. Chiu-Zarate, and H. de Guevar. Image Processing for Optical Metrology. In Clara Ionescu, editor, *MATLAB - A Ubiquitous Tool for the Practical Engineer*. InTech, 2011.

[21] C Calderón-Ramón, JF Gómez-Aguilar, M Rodríguez-Achach, LJ Morales-Mendoza, JR Laguna-Camacho, M Benavides-Cruz, MI Cruz-Orduna, M González-Lee, H Pérez-Meana, M Enciso-Aguilar, et al. Use of the perfect electric conductor boundary conditions to discretize a diffractor in fdtd/pml environment. *Revista mexicana de física*, 61(5):344–350, 2015.

[22] G. Langer, A. Hochreiner, P. Burgholzer, and T. Berer. A webcam in Bayer-mode as a light beam profiler for the near infra-red. *Optics and Lasers in Engineering*, 51(5):571–575, 2013.

Appendix B

Additional Work

This appendix includes the first pages of additional work authored and co-authored while completing the degree:

1. Research at Corning, Inc. Publication: A Comparative Study of Femtosecond and Picosecond Laser Interactions with Fused Silica

2. High resolution, low cost laser lithography using a Blu-ray optical head assembly

3. Self-organized 2D periodic arrays of nanoprotrusions in silicon with nanosecond laser irradiation

4. Diode Pumped Solid State Lasers for Surface Microtexture

A Comparative Study of Femtosecond and Picosecond Laser Interactions with Fused Silica

Yang Shen,[1] Christian A. Rothenbach,[1] Anping Liu,[2,*]
Barada K. Nayak,[2] David A. Pastel,[2] and Mool C. Gupta[1,*]
[1]*Department of Electrical and Computer Engineering, University of Virginia, Charlottesville, Virginia 22904, USA*
[2]*Science and Technology, Corning Inc., Corning, New York 14831, USA*

Abstract

The surface and bulk damage induced by femtosecond and picosecond IR laser pulses in fused silica is investigated. Low power femtosecond and picosecond laser pulses are used to study the initial changes in bulk. A long, conically shaped laser affected zone is observed with a diameter slightly larger than the focused spot size. Filamentation is observed in the region surrounding the laser affected zone, inducing small void formation and porosity for both femtosecond and picosecond pulses. However, it is determined that to achieve high aspect ratio drilling of fused silica, laser energy above a certain threshold is required. For higher picosecond pulse energies, ablation is observed that extends more than 500 μm deep into the sample, achieving depth to diameter aspect ratios of over 20:1. Laser induced surface and bulk damage for different repetition rates and pulse energies are compared. The thermal diffusion length is estimated for various laser repetition rates. In the high repetition rate cases, fused silica remains in a molten state between each delivered laser pulses, while in the low repetition rate case the material remains in a solidified state.

OCIS codes: picosecond laser femtosecond laser laser-induced damage, fused silica, laser processing

http://dx.doi.org/10.1364/XX.99.099999

* Corresponding authors: liua4@corning.com; mgupta@virginia.edu. The first two authors contributed equally in this work.

Optics and Lasers in Engineering 50 (2012) 900–904

Contents lists available at SciVerse ScienceDirect

Optics and Lasers in Engineering

journal homepage: www.elsevier.com/locate/optlaseng

High resolution, low cost laser lithography using a Blu-ray optical head assembly

Christian A. Rothenbach, Mool C. Gupta *

Charles L. Brown Department of Electrical and Computer Engineering, University of Virginia, Charlottesville, VA 22904, USA

A R T I C L E I N F O

Article history:
Received 8 September 2011
Received in revised form
8 December 2011
Accepted 9 December 2011
Available online 6 February 2012

Keywords:
Laser applications
Photolithography
Blu-ray

A B S T R A C T

We present a novel, cost-effective laser lithography system capable of producing periodic and non-periodic patterns with sub-micrometre feature sizes and periodicities. The optical head assembly of a Blu-ray disc recorder containing a 405 nm semiconductor diode laser and 0.85 NA objective lens was mounted on a motion stage and it was used to expose silicon samples covered with a mixture of SU-8 photoresist and photoinitiating chemicals. Experiments were carried out to demonstrate the lithographic capabilities of the system, and a smallest feature size of 450 nm was obtained. Grating structures were fabricated in order to demonstrate system capabilities.

1. Introduction

One of the most common lithography systems is optical projection, which uses an advanced optical design to expose a pattern onto a photoresists using a mask. It is capable of exposing large areas of resist and offers great repeatability, but its resolution is limited by the wavelength of light being used. Excimer lasers are the current standard, and feature sizes have reached dimensions below 100 nm [1]. Similar dimensions have been fabricated using X-ray sources instead of coherent light as the source of energy for these systems [2]. Masked systems tend to be expensive, so there is always a need for maskless, low cost, high resolution lithographic systems. Ion and electron beam lithography have been shown to produce features in the order of 10 nm, but their high complexity, high cost and low throughput limit their wider applications [3]. Another way of fabricating devices using maskless lithography is to use a laser source and scan it across the photoresist covered sample, or direct laser write. The resolutions that can be achieved with this technique are in the range of 0.5–1 μm depending upon the wavelength and focusing optics, and it has a high throughput and relatively lower cost.

The resolution in a direct laser write lithographic system is determined by the spot size of the beam, which is determined by the type of lens being used and the wavelength of the light, and is proportional to

$$\text{Spot size} = \frac{\lambda}{\text{NA}}, \tag{1}$$

where λ is the wavelength and NA is the numerical aperture of the lens [4].

The wavelength of the light is an important factor. Lower wavelengths can provide better resolution. Objective lenses with high numerical apertures are able to tightly focus the beam. The spot size is smallest at the focal spot, and the distance between the lens and the substrate must be accurately controlled. Just a few microns away from the focal spot in either direction causes the beam to become larger, thus, reducing the resolution of the system.

The cost of semiconductor laser diodes has decreased significantly in the last few years due to technological developments and also due to mass production and availability of shorter wavelengths in the UV-blue region. There are several uses for these diodes, but one of the most common is as light sources for reading and writing optical media such as compact discs (CD), digital video discs (DVD) and now Blu-ray discs (BD). The main difference between these media is their storage capacity, which is given by the size of the marks that are written onto the substrates. As marks get smaller, the storage capacity of the discs increases. However, in order to be able to read the data encoded in the smaller marks, lower wavelengths are necessary. The laser diodes went from 780 nm in wavelength for CDs, to 650 nm for DVDs and to 405 nm for BDs. The lower wavelength, combined with a high numerical aperture lens, allow BDs to store over 25 GB of information, compared to the 0.7 GB capacity for CDs and 4.7 GB capacity for DVDs [5–7].

The standard adopted for BD technology is to use objective lenses with 0.85 NA. This yields spot sizes of around 480 nm for a 405 nm wavelength, which highly correlates to the feature size that can be exposed on a resist. Objectives with higher numerical aperture reduce the tolerance for disc fluctuations and laser sources below

* Corresponding author. Tel.: +1 434 924 6167; fax: +1 434 924 8818.
E-mail address: mgupta@virginia.edu (M.C. Gupta).

0143-8166/$ - see front matter © 2012 Elsevier Ltd. All rights reserved.
doi:10.1016/j.optlaseng.2011.12.004

Self-organized 2D periodic arrays of nanostructures in silicon by nanosecond laser irradiation

Barada K. Nayak, Keye Sun, Christian Rothenbach, and Mool C. Gupta*

Charles L. Brown Department of Electrical and Computer Engineering, University of Virginia, Charlottesville, Virginia 22904, USA

*Corresponding author: mgupta@virginia.edu

Received 13 December 2010; revised 30 March 2011; accepted 30 March 2011; posted 31 March 2011 (Doc. ID 139526); published 20 May 2011

We report a phenomenon of spontaneous formation of self-organized 2D periodic arrays of nanostructures (protrusions) by directly exposing a silicon surface to multiple nanosecond laser pulses. These self-organized 2D periodic nanostructures are produced toward the edge as an annular region around the circular laser spot. The heights of these nanostructures are around 500 nm with tip diameter ~100 nm. The period of the nanostructures is about 1064 nm, the wavelength of the incident radiation. In the central region of the laser spot, nanostructures are destroyed because of the higher laser intensity (due to the Gaussian shape of the laser beam) and accumulation of large number of laser pulses. Optical diffraction from these nanostructures indicates a threefold symmetry, which is in accordance with the observed morphological symmetries of these nanostructures.

OCIS codes: 310.6628, 220.4241, 040.6040, 140.0140, 350.3390.

1. Introduction

Laser interaction with matter leading to formation of various kinds of surface structures, such as ripples [1–4], surface waves [5,6], and micro/nano structures [7–17] has been widely reported for semiconductors [1–4,7], metals [3,10–12], and insulators [18,19]. These surface structures are usually formed inside the laser irradiated spot and have semiperiodicity from hundreds of nanometers to several micrometers in length. For instance, the ripple structures usually show the period in the order of the laser wavelength and their formation mechanism has been attributed to the interference between parts of the incident laser beam with the scattered light from material surface. It has been shown that the orientation of ripples is dependent on laser polarization and their periods can also be affected by laser fluence, wavelength, and angle of incidence. On the other hand, the periodicity of other structures such as micro/nanostructures and concentric ringlike morphological structures formed after the femtosecond and picosecond laser irradiation process on silicon show no direct wavelength dependence [6]; rather, their periodicity is more likely dependent on thermal processes involved in laser–matter interaction.

Recently, another type of laser-induced periodic surface structure has been reported—periodic arrays of nanoprotrusions or dots [20–24]. Like ripples, these periodic arrays of dots or protrusions show remarkable order and periodicity close to the wavelength of the laser. Guan *et al.* reported the observation of 2D-ordered nanoprotrusions in silicon [20] and ordering of nickel catalyst [21] by using a Lloyd mirror setup. Longstreth-Spoor *et al.* produced periodic nanostructures on Co coated Si by a two-beam interference technique [22]. Nishioka and Horita produced Si and Ni dots by directly exposing thin films of Si and Ni deposited on SiO_2 to laser beams [23]. After a ripple structure was generated due to melting and surface tension, they rotated the sample by 90° and exposed again to create 2D periodic structures. Very recently, Xiao *et al.* created 2D-ordered gold nanostructures by direct laser exposure through a mask [24]. Lu *et al.* reported nanosphere enhanced periodic nanopatterning of silicon surface by laser

0003-6935/11/162349-07$15.00/0

JLMN-Journal of Laser Micro/Nanoengineering Vol. 8, No. 2, 2013

Diode Pumped Solid State Lasers for Surface Microtexture

Mool C. Gupta, Longteng Wang, Christian Rothenbach and Keye Sun

Department of Electrical & Computer Engineering, University of Virginia, Charlottesville, VA 22904
E-mail:mgupta@virginia.edu

Surface microtexture has been observed under nanosecond pulsed laser irradiation of silicon and metals. Diode pumped solid state lasers with pulse width in the nanosecond regime can provide a low cost method for fabrication of large area microtextured surfaces. Results are presented on control of microtexture height using laser processing parameters and mechanism of microtexture formation is described. Microtexture height can be controlled from less than a micron to tens of microns with multiple laser pulse irradiation. The reflectivity of the microtextured surface in the visible spectrum was reduced to lower than 5%.

Keywords: lasers, microtexture, solid state lasers, nanosecond, silicon, metals

1. Introduction

Currently there is a significant interest in understanding the mechanism of microtexture formation under femtosecond laser irradiation [1-5]. Several research groups have reported results on microtexture fabrication, characterization, mechanism of formation and their applications with primary focus using femtosecond and excimer lasers. Ultrafast laser generated microtextured surfaces have applications in photovoltaics [6, 7], photodetectors [8, 9], water repellant surfaces (superhydrophobic) [10] etc. Few research papers have reported similar microtexture formation in silicon using excimer laser [11]. However, the difficulty with femtosecond and excimer lasers for surface microtexture has been that it is not practical to produce large area in a cost effective manner.

We have carried out experiments using high repetition rate diode pumped solid state lasers which can provide a low cost method for fabrication of large area microtextured surfaces. Diode pumped solid state lasers with pulse width at around 10 ns are well suited for surface microtexture formation. The reported laser pulse width for microtexture formation ranges from about hundred femtosecond (for femtosecond lasers) to about 10 ns (for excimer lasers) as longer pulse width causes significant thermal diffusion and inhibits the formation of microtextures. When laser pulse widths are longer than about 10 ns, surface microtexture formation is not reported. The laser induced microtexture has been obtained on a variety of surfaces including dielectrics, semiconductors, metals and polymers [11-14]. In this paper we provide results on dependence of microtexture height on nanosecond pulsed laser processing parameters and mechanism of microtexture formation is described.

2. Experimental

The surface microtexture experiments were carried out using three lasers: a diode pumped solid state laser from Quantel Lasers (model Ultra 50), fiber laser from IPG Photonics (model YLP-G-10) and Nitrogen laser from Stanford Research Systems (model NL-100). Samples were placed in a vacuum chamber mounted on a high-precision,

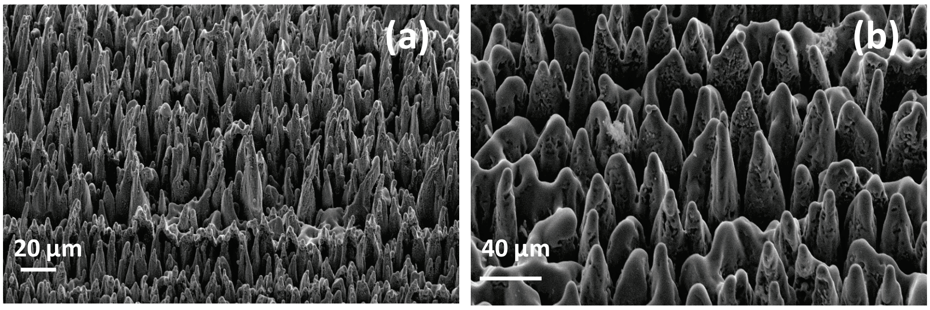

Fig. 1. SEM micrographs of microtextured Si sample. (a) Scan speed = 0.08 mm/s, equivalent to about 100 overlapping laser pulses at each point. (b) Higher magnification image of (a).

Appendix C

List of publications

1. B. K. Nayak, K. Sun, C. Rothenbach, and M. C. Gupta. Self-organized 2D periodic arrays of nanostructures in silicon by nanosecond laser irradiation. Applied Optics, 50(16):23492355, 2011.

2. C. A. Rothenbach and M. C. Gupta. High resolution, low cost laser lithography using a blu-ray optical head assembly. Optics and Lasers in Engineering, 50(6):900904, 2012.

3. M. C. Gupta, L. Wang, C. Rothenbach, and K. Sun. Diode pumped solid state lasers for surface microtexture. Journal of Laser Micro/Nanoengineering, 8(2):124130, 2013.

4. Y. Shen, C. A. Rothenbach, A. Liu, B.K. Nayak, D. Pastel, and M. C. Gupta. A comparative study of femtosecond and picosecond laser interactions with fused silica. Manuscript in preparation, 2013.

5. C. Rothenbach, I. Kravchenko, and M. Gupta, "Optical diffraction properties of multimicrogratings," Appl. Opt. 54, 1808-1818 (2015).

6. C. A. Rothenbach and M. C. Gupta. Simulation of optical diffraction properties of multi-microgratings. Manuscript in preparation, 2016.

7. C. A. Rothenbach and M. C. Gupta. Multi-microgratings for high sensitivity temperature sensing. Manuscript in preparation, 2016.

Bibliography

[1] A. R. Parker and H. E. Townley. Biomimetics of photonic nanostructures. *Nature Nanotechnology*, 2(6):347–353, 2007.

[2] P. Vukusic, R. Sambles, C. Lawrence, and G. Wakely. Sculpted-multilayer optical effects in two species of papilio butterfly. *Applied Optics*, 40(7):1116–1125, 2001.

[3] K. Watanabe, T. Hoshino, K. Kanda, Y. Haruyama, T. Kaito, and S. Matsui. Optical measurement and fabrication from a morpho-butterfly-scale quasistructure by focused ion beam chemical vapor deposition. *Journal of Vacuum Science & Technology B: Microelectronics and Nanometer Structures*, 23(2):570–575, 2005.

[4] R. A. Potyrailo, H. Ghiradella, A. Vertiatchikh, K. Dovidenko, J. R. Cournoyer, and E. Olson. Morpho butterfly wing scales demonstrate highly selective vapour response. *Nature Photonics*, 1(2):123–128, 2007.

[5] A. D. Pris, Y. Utturkar, C.l Surman, W. G. Morris, A. Vert, S. Zalyubovskiy, T. Deng, H. T. Ghiradella, and R. A. Potyrailo. Towards high-speed imaging of infrared photons with bio-inspired nanoarchitectures. *Nature Photonics*, 6(3):195–200, 2012.

[6] R. A. Potyrailo, Z. Ding, M. D. Butts, S. E. Genovese, and T. Deng. Selective chemical sensing using structurally colored core-shell colloidal crystal films. *IEEE Sensors Journal*, 8(6):815–822, 2008.

[7] G. England, M. Kolle, P. Kim, M. Khan, P. Munoz, E. Mazur, and J. Aizenberg. Bioinspired micrograting arrays mimicking the reverse color diffraction elements evolved by the butterfly Pierella luna. *Proceedings of the National Academy of Sciences*, 111(44):15630–15634, 2014.

[8] T. H. Wong, M. C. Gupta, B. Robins, and T. L. Levendusky. Color generation in butterfly wings and fabrication of such structures. *Optics Letters*, 28(23):2342–2344, 2003.

[9] C. Palmer and E. Loewen. *Diffraction Grating Handbook*. Newport, 6th edition, 2005.

[10] J. W. Goodman. *Introduction to Fourier optics*. Roberts & Co, Englewood, Colo, 3rd ed edition, 2005.

[11] K. K. Sharma. *Optics: Principles And Applications*. Elsevier/Academic Press, 2006.

[12] R. Blandford and K. Thorne. *Applications of classical physics*. Caltech, 2006.

[13] M. Born. *Principles of optics: electromagnetic theory of propagation, interference and diffraction of light*. Cambridge University Press, Cambridge ; New York, 7th expanded ed edition, 1999.

[14] M. G. Moharam and T. K. Gaylord. Diffraction analysis of dielectric surface-relief gratings. *Journal of the Optical Society of America*, 72(10):1385–1392, 1982.

[15] M. G. Moharam and T. K. Gaylord. Rigorous coupled-wave analysis of planar-grating diffraction. *Journal of the Optical Society of America*, 71(7):811–818, 1981.

[16] M. G. Moharam and T. K. Gaylord. Rigorous coupled-wave analysis of metallic surface-relief gratings. *Journal of the Optical Society of America A*, 3(11):1780–1787, 1986.

[17] Mool C. Gupta and S. T. Peng. Diffraction characteristics of surface-relief gratings. *Applied Optics*, 32(16):2911–2917, 1993.

[18] D. A. Pommet, M. G. Moharam, and Eric B. Grann. Limits of scalar diffraction theory for diffractive phase elements. *Journal of the Optical Society of America A*, 11(6):1827–1834, 1994.

[19] S. Rutishauser, M. Bednarzik, I. Zanette, T. Weitkamp, M. Börner, J. Mohr, and C. David. Fabrication of two-dimensional hard x-ray diffraction gratings. *Microelectronic Engineering*, 101:12–16, 2013.

[20] M. Paturzo, F. Merola, and P. Ferraro. Multi-imaging capabilities of a 2d diffraction grating in combination with digital holography. *Optics letters*, 35(7):1010–1012, 2010.

[21] J. Liu, Z. Zhang, Z. Lu, G. Xiao, F. Sun, S. Chang, and C. Flueraru. Fabrication and stitching of embedded multi-layer micro-gratings in fused silica glass by fs laser pulses. *Applied Physics B*, 86(1):151–154, 2007.

[22] Z. Qi, N. Pei-Gen, M. Qing-Bo, C. Bing-Ying, and Z. Dao-Zhong. Tow-dimensional micro-grating formed by polystyrene spheres. *Chinese Physics Letters*, 20(8):1290, 2003.

[23] J. Gjessing, E. Stensrud Marstein, and A. Sudbø. 2d back-side diffraction grating for improved light trapping in thin silicon solar cells. *Optics express*, 18(6):5481–5495, 2010.

[24] M. Riahi and H. Latifi. Fabrication of a 2d thermally tunable reflective grating for measuring a co 2 laser beam profile. *Optica Applicata*, 41(3):735–742, 2011.

[25] B. Senyuk, I. I Smalyukh, and O. Lavrentovich. Switchable two-dimensional gratings based on field-induced layer undulations in cholesteric liquid crystals. *Optics letters*, 30(4):349–351, 2005.

[26] B. Senyuk, I. Smalyukh, and O. Lavrentovich. Electrically-controlled two-dimensional gratings based on layers undulations in cholesteric liquid crystals. In *Optics & Photonics 2005*, pages 59360W–59360W. International Society for Optics and Photonics, 2005.

[27] P. Deguzman, Y. Cao, T. Suleski, M. Fiddy, R. Jones, R. TeKolste, and J. Morris. Wafer-based diffractive polarizer design for low-reflectivity applications. *Optical Engineering*, 46(3):038001–038001, 2007.

[28] B. Boruah. Zonal wavefront sensing using an array of gratings. *Optics letters*, 35(2):202–204, 2010.

[29] D. Fattal, Z. Peng, T. Tran, S. Vo, M. Fiorentino, J. Brug, and R. Beausoleil. A multi-directional backlight for a wide-angle, glasses-free three-dimensional display. *Nature*, 495(7441):348–351, 2013.

[30] A. Cronin, J. Schmiedmayer, and D. Pritchard. Atom interferometers. *arXiv preprint arXiv:0712.3703*, 2007.

[31] X. Yue, Y. Zhai, Z. Wang, H. Xiong, X. Chen, and X. Zhou. Observation of diffraction phases in matter-wave scattering. *Physical Review A*, 88(1):013603, 2013.

[32] H. Hamam. Lau array illuminator. *Applied optics*, 43(14):2888–2894, 2004.

[33] Y. Hua, J. Yong Suh, W. Zhou, M. Huntington, and T. Odom. Talbot effect beyond the paraxial limit at optical frequencies. *Optics express*, 20(13):14284–14291, 2012.

[34] M. Kim, T. Scharf, C. Menzel, C. Rockstuhl, and H. Herzig. Talbot images of wavelength-scale amplitude gratings. *Optics express*, 20(5):4903–4920, 2012.

[35] K. Chen and J. Kuo. Diffraction angle prediction of surface micromachined planar curved grating and crossed grating. In *Nano/Micro Engineered and Molecular Systems, 2009. NEMS 2009. 4th IEEE International Conference on*, pages 363–366. IEEE, 2009.

[36] G. Granet. Analysis of diffraction by surface-relief crossed gratings with use of the chandezon method: application to multilayer crossed gratings. *JOSA A*, 15(5):1121–1131, 1998.

[37] E. Popov, D. Maystre, R.C. McPhedran, M. Nevière, M.C. Hutley, and G.H. Derrick. Total absorption of unpolarized light by crossed gratings. *Optics express*, 16(9):6146–6155, 2008.

[38] N. Yoshimizu, A. Lal, and C. R. Pollock. MEMS diffractive optical nanoruler technology for tipbased nanofabrication and metrology. *IEEE 22nd International Conference on Micro Electro Mechanical Systems, 2009. MEMS 2009*, pages 547–550, 2009.

[39] N. Yoshimizu, A. Lal, and C. R. Pollock. Nanometrology optical ruler imaging system using diffraction from a quasiperiodic structure. *Optics Express*, 18(20):20827–20838, 2010.

[40] N. Yoshimizu, A. Lal, and C. R. Pollock. Nanometrology using a quasiperiodic pattern diffraction optical ruler. *Journal of Microelectromechanical Systems*, 19(4):865–870, 2010.

[41] Kane Y. Numerical solution of initial boundary value problems involving maxwell's equations in isotropic media. *IEEE Transactions on Antennas and Propagation*, 14(3):302–307, 1966.

[42] J Frances, M Perez-Molina, S Bleda, E Fernandez, C Neipp, and A Belendez. Educational Software for Interference and Optical Diffraction Analysis in Fresnel and Fraunhofer Regions Based on MATLAB GUIs and the FDTD Method. *IEEE Transactions on Education*, 55(1):118–125, 2012.

[43] C Calderón-Ramón, JF Gómez-Aguilar, M Rodríguez-Achach, LJ Morales-Mendoza, JR Laguna-Camacho, M Benavides-Cruz, MI Cruz-Orduna, M González-Lee, H Pérez-Meana, M Enciso-Aguilar, et al. Use of the perfect electric conductor boundary conditions to discretize a diffractor in fdtd/pml environment. *Revista mexicana de física*, 61(5):344–350, 2015.

[44] D. G. Voelz. *Computational fourier optics: a MATLAB tutorial*. SPIE Press, Bellingham, Wash, 2011.

[45] G. O. Reynolds, DeVelis J.B. Parrent, G. B., and B. J. Thompson. *The New physical optics notebook: tutorials in Fourier optics*. SPIE Optical Engineering Press, Bellingham, Wash., USA, 1989.

[46] A. R. Weeks. *Fundamentals of electronic image processing*. SPIE/IEEE series on imaging science & engineering. SPIE Optical Engineering Press ; IEEE Press, Bellingham, Wash., USA : New York, 1996.

[47] Y. Takano, K.N. Liou, and P. Yang. Diffraction by rectangular parallelepiped, hexagonal cylinder, and three-axis ellipsoid: Some analytic solutions and numerical results. *Journal of Quantitative Spectroscopy and Radiative Transfer*, 113(14):1836–1843, 2012.

[48] J. Komrska. Fraunhofer diffraction at apertures in the form of regular polygons. II. *Optica Acta: International Journal of Optics*, 20(7):549–563, 1973.

[49] R. C. Smith and J. S. Marsh. Diffraction patterns of simple apertures. *Journal of the Optical Society of America*, 64(6):798–803, 1974.

[50] W Wang, W Zhang, J Gu, Q Liu, T Deng, D Zhang, and H Q Lin. Design of a structure with low incident and viewing angle dependence inspired by morpho butterflies. *Scientific reports*, 3:3427, 2013.

[51] P. Rai-Choudhury. *Handbook of Microlithography, Micromachining, and Microfabrication: Microlithography*. SPIE Press, 1997.

[52] J. A. R. Samson and D. L. Ederer. *Vacuum ultraviolet spectroscopy II*. Academic Press, 1998.

[53] C. P. Fucetola, H. Korre, and K. K. Berggren. Low-cost interference lithography. *Journal of Vacuum Science & Technology B: Microelectronics and Nanometer Structures*, 27(6):2958, 2009.

[54] I. Byun and J. Kim. Cost-effective laser interference lithography using a 405 nm AlInGaN semiconductor laser. *Journal of Micromechanics and Microengineering*, 20(5):055024, 2010.

[55] A. Langner, B. Päivänranta, B. Terhalle, and Y. Ekinci. Fabrication of quasiperiodic nanostructures with euv interference lithography. *Nanotechnology*, 23(10):105303, 2012.

[56] H. Solak, C. David, J. Gobrecht, V. Golovkina, F. Cerrina, S.O. Kim, and P.F. Nealey. Sub-50 nm period patterns with euv interference lithography. *Microelectronic Engineering*, 67:56–62, 2003.

[57] H. Solak. Space-invariant multiple-beam achromatic euv interference lithography. *Microelectronic engineering*, 78:410–416, 2005.

[58] J.A van Kan, J.L Sanchez, B Xu, T Osipowicz, and F Watt. Micromachining using focused high energy ion beams: Deep Ion Beam Lithography. *Nuclear Instruments and Methods in Physics Research Section B: Beam Interactions with Materials and Atoms*, 148(1-4):1085–1089, 1999.

[59] S. Teichmann, B. Chen, R. A. Dilanian, P. Hannaford, and L. Van Dao. Experimental aspects of multiharmonic-order coherent diffractive imaging. *Journal of Applied Physics*, 108(2):023106–023106–6, 2010.

[60] F. Pesty, P. Garoche, and S. Dorel. Modulation of the beam intensity for high-dynamic-range low energy electron diffraction. *Journal of Applied Physics*, 92(6):3021–3026, 2002.

[61] R. L. Sandberg, A. Paul, D. A. Raymondson, S. Hdrich, D. M. Gaudiosi, J. Holtsnider, R. I. Tobey, O. Cohen, M. M. Murnane, H. C. Kapteyn, C. Song, J. Miao, Y. Liu, and F. Salmassi. Lensless diffractive imaging using tabletop coherent high-harmonic soft-x-ray beams. *Physical Review Letters*, 99(9):098103–1–098103–4, 2007.

[62] G. Langer, A. Hochreiner, P. Burgholzer, and T. Berer. A webcam in Bayer-mode as a light beam profiler for the near infra-red. *Optics and Lasers in Engineering*, 51(5):571–575, 2013.

[63] P. O. Caffrey, B. K. Nayak, and M. C. Gupta. Ultrafast laser-induced microstructure/nanostructure replication and optical properties. *Applied Optics*, 51(5):604–609, 2012.

[64] B Farshchian, S Park, J Choi, A Amirsadeghi, J Lee, and S Park. 3d nanomolding for lab-on-a-chip applications. *Lab on a Chip*, 12(22):4764, 2012.

[65] D Lee, H Pan, A Sherry, S Ko, M Lee, E Kim, and C P Grigoropoulos. Large-area nanoimprinting on various substrates by reconfigurable maskless laser direct writing. *Nanotechnology*, 23(34):344012, 2012.

[66] A E Grigorescu and C W Hagen. Resists for sub-20-nm electron beam lithography with a focus on HSQ: state of the art. *Nanotechnology*, 20(29):292001, 2009.

[67] A Babinet. Mémoires doptique météorologique. *Compt. Rend. Acad. Sci*, 4:638, 1837.

[68] J. R. Jimnez and E. Hita. Babinets principle in scalar theory of diffraction. *Optical Review*, 8(6):495–497, 2001.

[69] N. V Tkachenko. *Optical spectroscopy: methods and instrumentations.* Elsevier, 2006.

[70] M. K. Lang, G. W. Donohoe, S. H. Zaidi, and S. R. J. Brueck. Real-time image processing techniques for noncontact temperature measurement. *Optical Engineering*, 33(10):3465–3471, 1994.

[71] B. A. Grzybowski, S. T. Brittain, and G. M. Whitesides. Thermally actuated interferometric sensors based on the thermal expansion of transparent elastomeric media. *Review of Scientific Instruments*, 70(4):2031, 1999.

[72] S. Chaubey, P. Joshi, M. Kumar, R. Arya, A. K. Nath, and S. Kher. Design and development of long-period grating sensors for temperature monitoring. *Sadhana*, 32(5):513–519, 2007.

[73] M. Smietana, W. J. Bock, and P. Mikulic. Temperature sensitivity of silicon nitride nanocoated long-period gratings working in various surrounding media. *Measurement Science and Technology*, 22(11):115203, 2011.

[74] J. Ballato and A. James. A Ceramic Photonic Crystal Temperature Sensor. *Journal of the American Ceramic Society*, 82(8):2273–2275, 2004.

[75] H. Fu, H. Zhao, X. Qiao, Y. Li, D. Zhao, and Z. Yong. Study on a novel photonic crystal temperature sensor. *Optoelectronics Letters*, 7(6):419–422, 2011.

[76] B. Paivaranta, H. Merbold, R. Giannini, Luca Buchi, S. Gorelick, C. David, J. F. Loffler, T. Feurer, and Y. Ekinci. High Aspect Ratio Plasmonic Nanostructures for Sensing Applications. *ACS Nano*, 5(8):6374–6382, 2011.

[77] C. Huang. Optical temperature measurement by grating expansion for rotating semiconductor wafers. *Journal of Vacuum Science & Technology A: Vacuum, Surfaces, and Films*, 14(2):271, 1996.

[78] G. L. DesAutels, P. Powers, C. Brewer, M. Walker, M. Burky, and G. Anderson. Optical temperature sensor and thermal expansion measurement using a femtosecond micromachined grating in 6h-SiC. *Applied Optics*, 47(21):3773, 2008.

[79] J. A. Rogers, R. J. Jackman, O. J. A. Schueller, and G. M. Whitesides. Elastomeric diffraction gratings as photothermal detectors. *Applied Optics*, 35(34):6641, 1996.

[80] M. Jones and S. Jones. Basic Mechanical and Thermal Properties of Silicon. *Technical publication of Virginia Semiconductor, Inc.*

[81] Z. He and X. Liu. A high precision displacement sensor based on dual-gratings interference. In *2011 International Conference on Electric Information and Control Engineering (ICEICE)*, pages 997–1000, 2011.

[82] C. Feng, M. Kajima, S. Gonda, K. Minoshima, H. Fujimoto, and L. Zeng. Accurate measurement of orthogonality of equal-period, two-dimensional gratings by an interferometric method. *Metrologia*, 49(3):236, 2012.

[83] M. Mino. Position Sensing Grating Interferometer for a Specular Object. *Optical Review*, 5(3):191–195, 1998.

[84] S. Zhao, C. Hou, J. Zhang, J. Bai, and G. Yang. A high-resolution displacement sensor based on a grating interferometer with the phase modulation technique. *Measurement Science and Technology*, 23(10):105102, 2012.

[85] D. Halliday, R. Resnick, and J. Walker. *Fundamentals of Physics*. Wiley, 9th edition, 2010.

[86] J. Enguita, I. Alvarez, C. Fraga, J. Marina, and Y. Fernandez. Improving signal processing performance on a conoscopic holography-based profilometer with phase-shifting interferometry algorithms. *Optical Engineering*, 46(9):093605–093605–9, 2007.

[87] E. W. Weisstein. Fringe Visibility – from Eric Weisstein's World of Physics, 1996.

[88] M. Mora-Gonzalez, J. Munoz-Maciel, F. J., F. G., R. Chiu-Zarate, and H. de Guevar. Image Processing for Optical Metrology. In Clara Ionescu, editor, *MATLAB - A Ubiquitous Tool for the Practical Engineer*. InTech, 2011.

[89] Ilya Shadrivov. Spotlight on Optics: Highlighted Articles from OSA Journals. *Applied Optics*, 2015.